UNIVERSITAT POLITÈCNICA DE VALÈNCIA

Human body scattering effects at millimeter waves frequencies for future 5G systems and beyond

Departamento de comunicaciones moviles o Instituto de Telecomunicaciones y Aplicaciones Multimedia iTEAM

Universitat Politècnica de València

A thesis submitted for the degree of

Doctorado Industrial por la Universitat Politècnica de València

Valencia, Junio 2022

Author:
Johan/Jhoan Samuel Romero Peña

Supervisors:
Prof. Narcís Cardona Marcet

To God,
My beautiful and smart wife :),
my parents ,
my beautiful sister(Bee),
my friends.

Abstract

Future mobile communications are expected to experience a technical revolution that goes beyond Gbps data rates and reduces data rate latencies to levels very close to a millisecond. New enabling technologies have been researched to achieve these demanding specifications. The utilization of mmWave bands, where a lot of spectrum is available, is one of them.

Due to the numerous technical difficulties associated with using this frequency band, complicated channel models are necessary to anticipate the radio channel characteristics and to accurately evaluate the performance of cellular systems in mmWave. In particular, the most accurate propagation models are those based on deterministic ray tracing techniques. But these techniques have the stigma of being computationally intensive, and this makes it difficult to use them to characterize the radio channel in complex and dynamic indoor scenarios. The complexity of characterizing these scenarios depends largely on the interaction of the human body with the radio environment, which at mmWaves is often destructive and highly unpredictable.

On the other hand, in recent years, the video game industry has developed powerful tools for hyper-realistic environments, where most of the progress in this reality emulation has to do with the handling of light. Therefore, the graphic engines of these platforms have become more and more efficient to handle large volumes of information, becoming ideal to emulate the radio wave propagation behavior, as well as to reconstruct a complex interior scenario. Therefore, in this Thesis one has taken advantage of the computational capacity of this type of tools to evaluate the mmWave radio channel in the most efficient way possible. This Thesis offers some guidelines to optimize the signal propagation in mmWaves in a dynamic and complex indoor environment, for which three main objectives are proposed.

The first objective has been to evaluate the scattering effects of the human body when it interacts with the propagation channel. Once evaluated, a simplified mathematical and geometrical model has been proposed to calculate this effect in a reliable and fast way. Another objective has been the design of a modular passive reflector in mmWaves, which optimizes the coverage in indoor environments, avoiding human interference in the propagation, in order to avoid its harmful scattering effects. And finally, a real-time predictive beam steering system has been designed for the mmWaves radiation system, in order to avoid propagation losses caused by the human body in dynamic and complex indoor environments.

Resumen

Se espera que las futuras comunicaciones móviles experimenten una revolución técnica que vaya más allá de las velocidades de datos de Gbps y reduzca las latencias de las velocidades de datos a niveles muy cercanos al milisegundo. Se han investigado nuevas tecnologías habilitadoras para lograr estas exigentes especificaciones. Y la utilización de las bandas de ondas milimétricas, donde hay mucho espectro disponible, es una de ellas. Debido a las numerosas dificultades técnicas asociadas a la utilización de esta banda de frecuencias, se necesitan complicados modelos de canal para anticipar las características del canal de radio y evaluar con precisión el rendimiento de los sistemas celulares en milimétricas. En concreto, los modelos de propagación más precisos son los basados en técnicas de trazado de rayos deterministas. Pero estas técnicas tienen el estigma de ser computacionalmente exigentes, y esto dificulta su uso para caracterizar el canal de radio en escenarios interiores complejos y dinámicos. La complejidad de la caracterización de estos escenarios depende en gran medida de la interacción del cuerpo humano con el entorno radioeléctrico, que en las ondas milimétricas suele ser destructiva y muy impredecible. Por otro lado, en los últimos años, la industria de los videojuegos ha desarrollado potentes herramientas para entornos hiperrealistas, donde la mayor parte de los avances en esta emulación de la realidad tienen que ver con el manejo de la luz. Así, los motores gráficos de estas plataformas se han vuelto cada vez más eficientes para manejar grandes volúmenes de información, por lo que son ideales para emular el comportamiento de la propagación de las ondas de radio, así como para reconstruir un escenario interior complejo. Por ello, en esta Tesis se ha aprovechado la capacidad computacional de este tipo de herramientas para evaluar el canal radioeléctrico milimétricas de la forma más eficiente posible. Esta Tesis ofrece unas pautas para optimizar la propagación de la señal en milimétricas en un entorno interior dinámico y complejo, para lo cual se proponen tres objetivos principales. El primer objetivo es evaluar los efectos de dispersión del cuerpo humano cuando interactúa con el canal de propagación. Una vez evaluado, se propuso un modelo matemático y geométrico simplificado para calcular este efecto de forma fiable y rápida. Otro objetivo fue el diseño de un reflector pasivo modular en milimétricas, que optimiza la cobertura en entornos de interior, evitando la interferencia del ser humano en la propagación. Y, por último, se diseñó un sistema de apuntamiento del haz predictivo en tiempo real, para que opere con el sistema de radiación en milimétricas, cuyo objetivo es evitar las pérdidas de propagación causadas por el cuerpo humano en entornos interiores dinámicos y complejos.

Resum

S'espera que les futures comunicacions mòbils experimenten una revolució tècnica que vaja més enllà de les velocitats de dades de Gbps i reduïsca les latències de les velocitats de dades a nivells molt pròxims al milisegundo. S'han investigat noves tecnologies habilitadoras per a aconseguir estes exigents especificacions. I la utilització de les bandes d'ones millimètriques, on hi ha molt espectre disponible, és una d'elles.

A causa de les nombroses dificultats tècniques associades a la utilització d'esta banda de freqüències, es necessiten complicats models de canal per a anticipar les característiques del canal de ràdio i avaluar amb precisió el rendiment dels sistemes cellulars en millimètriques. En concret, els models de propagació més precisos són els basats en tècniques de traçat de rajos deterministes. Però estes tècniques tenen l'estigma de ser computacionalment exigents, i açò dificulta el seu ús per a caracteritzar el canal de ràdio en escenaris interiors complexos i dinàmics. La complexitat de la caracterització d'estos escenaris depén en gran manera de la interacció del cos humà amb l'entorn radioelèctric, que en les ones millimètriques sol ser destructiva i molt impredicible.

D'altra banda, en els últims anys, la indústria dels videojocs ha desenrotllat potents ferramentes per a entorns hiperrealistes, on la major part dels avanços en esta emulació de la realitat tenen a veure amb el maneig de la llum. Així, els motors gràfics d'estes plataformes s'han tornat cada vegada més eficients per a manejar grans volums d'informació, per la qual cosa són ideals per a emular el comportament de la propagació de les ones de ràdio, així com per a reconstruir un escenari interior complex. Per això, en esta Tesi s'ha aprofitat la capacitat computacional d'este tipus de ferramentes per a avaluar el canal radioelèctric millimètriques de la manera més eficient possible.

Esta Tesi oferix unes pautes per a optimitzar la propagació del senyal en millimètriques en un entorn interior dinàmic i complex, per a la qual cosa es proposen tres objectius principals. El primer objectiu és avaluar els efectes de dispersió del cos humà quan interactua amb el canal de propagació. Una vegada avaluat, es va proposar un model matemàtic i geomètric simplificat per a calcular este efecte de forma fiable i ràpida. Un altre objectiu va ser el disseny d'un reflector passiu modular en millimètriques, que optimitza la cobertura en entorns d'interior, evitant la interferència del ser humà en la propagació, per a així evitar pèrdues de propagació addicionals. I, finalment, es va dissenyar un sistema d'apuntament del feix predictiu en temps real, perquè opere amb el sistema de radiació en millimètriques, l'objectiu del qual és evitar les pèrdues de propagació causades pel cos humà en entorns interiors dinàmics i complexos.

Acknowledgements

First of all, my most humble gratitude to God for giving me the opportunity to face this challenge in my life, which has been important to continue strengthening my character and to learn to know Him and myself better, and to understand that as one goes deeper into real scientific questions, the more I am aware that we are and will continue to be complete ignorant in the immeasurable and perfect creation of God.

So I thank Narcis Cardona for giving me the opportunity and freedom to develop this interesting research, which will be a small grain of sand for technological advances that could be of great benefit to humanity.

I thank Dr. Paolo Grazioso, Dr. Slawomir Jerzy Ambroziak and Dr. Silvia Ruiz Boqué for their work as reviewers of the Thesis.

Finally, I would like to express my enormous gratitude to my clan, who have always been there when I have needed them the most, despite the distance that separates us, their love and support has never ceased, I love them very much. I would also like to express my great appreciation to my friends, who despite knowing that I am a little irreverent, have had the patience to continue being my friends and accompany me on this journey.

Thank you all very much.

Jhoan/Johan Samuel Romero Peña

Table of contents

Acronyms

3GPP Third Generation Partnership Project

5G Fifth Generation

ACIS 3D ACIS Modeler

ANSYS High-frequency structure simulator

AP Angular Profile

BTS Base Station

CA Carrier Aggregation

CST Computer Simulation Technology

D2D Device-to-Device

DKED Double Knife Edge Diffraction Model

EM ElectroMagnetic

FDD Frequency Division Duplexing

GO Geometrical Optics

GTD General Theory of Diffraction

H2D Human-to-Device

H2H Human-to-Human

IMT International Mobile Telecommunications

IMT-Advanced International Mobile Telecommunications Advanced

ACRONYMS

ITU International Telecommunications Union

ITU-R ITU Radiocommunications Sector

KPI Key Performance Indicator

LOS Line-of-Sight

LSP Large Scale Parameter

MATLAB MATrix LABoratory

METIS Mobile and wireless communications Enablers for Twenty-twenty Information Society

MIMO Multiple-Input Multiple-Output

MiWEBA Millimeter-Wave Evolution for Backhaul and Access

MKED Multiple Knife Edge Diffraction Model

MLFMM Multilevel method solver

mMIMO massive MIMO

mmMagic Model created by mmMagic Project

MMSE Minimum Mean Squared Error

mMTC massive Machine Type Communications

mMTC massive Machine Type Communications

mmWave Millimeter Wave

MoM Method of Moments

MPC MultiPath Components

NLOS Non-Line-of-Sight

NR New Radio

NYUSIM NY University model

O2I Outdoor to Indoor

O2O Outdoor to Outdoor

PBA Perfect Boundary Approximation

PCB Printed Circuit Board

PDP Power Delay Profile

PEC Perfect electrical Conductor

QuaDRIGa QUAsi Deterministic RadIo channel GenerAtor

RAN Radio Access Network

SL Spatial Lobe

SSP Short Scale Parameter

STMKE Truncated Multiple Diffraction Model

TCSL Time Cluster Spatial Loop

TDD Time Division Duplexing

TST Thin Sheet Technique

UE4 Video Game Platform called Unreal Engine 4

UMi Urban Micro-cell

uMTC ultra-reliable Machine Type Communications

Unity Video Game Platform Engine

UTD Uniform Theory of Diffraction

UV UV mapping is the 3D modeling process of projecting a 2D image to a 3D model's surface for texture mapping

V2V Vehicle-to-Vehicle

V2X Vehicle-to-anything

VNA Vector Network Analyzer

VSWR Voltage Standing Wave Ratio

WINNER Wireless World Initiative New Radio

WRC World Radiocommunication Conference

xMBB extreme Mobile Broadband

Chapter 1

Introduction

Nowadays, due to the constantly changing requirements and expectations of users and operators, mobile wireless communications are continuously evolving. The last 20 years have seen remarkable technological developments, particularly with the rapid adoption of wide-band services.

These services have reached a saturation point in developed countries, with more mobile phones than fixed lines in most countries. Mobile data traffic is expected to overtake the fixed internet service soon, because people tend to be more connected to the internet network from their mobile devices than from fixed ones, for reasons of mobility and convenience.

In addition to this trend of increasing Internet usage, in the early 2020s, the demand for data traffic increase even more due to the implementation of teleworking, videoconferencing, mail transfers, etc, due to the health crisis that forced nearly everyone to work from home; for instance, in the case of Spain the increase of telework increased by 216% compared to 2019 [1].

Therefore, due to this sharp increase in bandwidth needs, there is a need to use the millimeter spectrum to offer higher bandwidth in mobile services. But the use of this spectrum region brings with it many technical challenges. The most unpredictable is the scattering effects of the human body that cause considerable propagation losses.

This Thesis presents the results of the research effort focused on studying the harmful effects of signal propagation at mmWave frequencies in indoor environments and how to avoid them.

The effect that is most emphasized throughout this work is the effect of human body scattering at mmWaves, because it is the most relevant non-stationary obstacle in the propagation channel in this frequency range.

Therefore, throughout the Thesis different approaches were investigated, aiming to determine how to address this phenomenon to characterize and adequately mitigate its effect.

Hence, human body and channel modeling techniques were developed in real time simulation indoor environments, in order to figure out how to reduce the human body effects for Fifth Generation (5G) system at mmWaves.

This chapter contains the frame of reference on which the research carried out in the Thesis is based, as well as the scope and methodology used for the execution of this research.

In order to better structure the information, this chapter has been divided into the following sections:

- Section 1.1 discusses the most important radio channel concepts in the context of this Thesis while also presenting the historical backdrop of mobile communications.
- Section 1.2 defines the technical starting points to be developed throughout the Thesis.
- Section 1.3 defines the research hypoThesis and outlines the primary issue that drives this Thesis.
- Section 1.4 defines the research objectives of this Thesis.
- Section 1.5 outlines the Thesis organizational framework while summarizing the key points of each chapter.
- Section 1.6 lists publications associated with this Thesis, including journals, conferences and patents.

1.1 Technical and Historical Background

This section presents the framework of communications systems and the standardization process from 5G to 6G and the main concepts of Millimeter Wave (mmWave) propagation models and strategies that could potentially be used in the industry.

1.1.1 Why is 4G not enough?

Over the decades, the mobile communications technology sector has been characterized as one of the fastest growing technology sectors, due to its usefulness and great acceptance among people. For this reason, bandwidth requirements have been increasing dramatically over the years, both for users and operators.

This growth is due to the increasing need to digitize various basic services, such as health services, public utilities, banking services, video conferencing services, etc.

In addition, there has also a great need for video-on-demand entertainment services, video games, as well as social networks, which require much more bandwidth than essential services for their proper functioning.

Additionally, due to the health circumstances that have been experienced in 2020/2021, the demands for broadband services have increased substantially as it was not foreseen. Therefore, there is an urgency to offer higher throughput, hence it becomes imperative to increase the operating frequencies of mobile systems in order to guarantee the throughput demanded by the current requirements.

Because it is essential to increase bandwidth, it is equally important to do so in an organized and regulated manner. The main global entities in charge of regulating telecommunications standards for 5G mobile systems are the International Telecommunications Union (ITU), with its Radiocommunications segment (ITU-R), as well as the Third Generation Partnership Project (3GPP):

- The ITU-R, which is one of the three main sectors of the ITU, is responsible for managing the radioelectric spectrum at international level. Therefore, one of its main objectives is to develop standards for all radiocommunication systems that use the electromagnetic spectrum. For this reason, this entity has been in charge of the standardization of 3G/4G mobile communications and has been a fundamental part in the standardization of 5G mobile communications systems in the mmWave band.

- The 3GPP is an international organization that, under its leadership, organizes different regional and industry mobile communication standards, in order to have a standard common to all that allows the best intercompatibility of technology worldwide. The 3GPP's responsibilities are to standardize three segments of mobile communications: radio access networks, services and systems, and central networks and terminals.

- The Third Generation Partnership Project (3GPP) consists of seven regional telecommunications organizations, along with market representative partners, as a mobile standards body. Three areas make up its work: radio access networks, services and system components, and central networks and terminals. A brand-new radio access technology termed 5G NR is being proposed by the 3GPP as part of the 5G standardization process. In 2017, the initial iteration of the 5G NR specification was finished. In fact, the 3GPP released Release 15 in 2019 that details Phase 1 of the 5G standard.

In 2012, the ITU-R developed initial recommendations to standardize the technological framework based on the global objectives for the further implementation of International Mobile Telecommunication systems (IMT) by 2020 [2]. Therefore, when the term IMT-2020 is mentioned, it will be used as a simplification to make reference to the 5G standards stipulated by ITU-R. The recommendations proposed in the IMT-2020 standard were the first step in structuring the vision of the future 5G technology in terms of its technical challenges.

This vision showed a system that allows full connectivity, so that any mobile device (Mobile Terminal, Tablet, SmartWatch, etc) can be connected anytime and anywhere, without altering its performance of maximum data rate and minimum latency, remaining stable over time [3][4].

Indeed, the implementation of full 5G technology will be a paradigm shift that will have major consequences for industry and society. 5G will enable active interaction between humans and their environment (Internet of Things IoT) to achieve this. In addition, it will increase the interaction of Human-to-Human (H2H), Human-to-Device (H2D) and Device-to-Device (D2D), which implies having real-time positions of people and devices [5].

The recommendation [2] above identifies the main trends at user, technology and application level. It also proposes a reference framework to address the technical feasibility for the correct use of spectrum in the 6 to 100 GHz bands. This recommendation considers three fields of action for the correct use of 5G capacity [6]:

- **extreme Mobile Broadband (xMBB)**: It offers extreme data speeds, low latency communications and wide coverage. This optimises the user experience by offering stable tariffs within the service area. Its applications are focused on the average user to enable easy access to multimedia content, data and services.

- **massive Machine Type Communications (mMTC)**: Provides wireless connectivity to many millions of networked devices. Connectivity adapts to the number of devices in a given area. Coverage is more important than high data rates. This scenario only considers H2H and D2D communications. This context is ideal for use cases that require low latency, high reliability and high availability.

- **ultra-reliable Machine Type Communications (uMTC)**: This context provides ultra-reliable, low latency communications to services and high availability. It focuses on D2D communication, which has a large number of connected devices and low delay, sensitivity and battery

life. It is ideal for industrial processes for communication with robots (industry 4.0).

1.1.2 Technical guidelines for the 5G implementation

The ITU Radiocommunications Sector (ITU-R) has continued the standardisation process by determining the requirements and their evaluation methods for IMT-2020 systems[2]. These are the Key Performance Indicators (KPIs), which were used to establish the key technical parameters, defining the scope of the technology:

- **Peak Data Rate [Gbps]**: Maximum data rate that a user or device can achieve in a lossless environment.
- **User Experienced Data Rate [Mbps or Gbps]**: Data rate present in a coverage radius, useful for the mobile device.
- **Latency [ms]**: The time it takes for a radio network to send a packet from the source until it reaches the destination.
- **Mobility [km/h]**: Maximum speed that the terminal can have between base stations to achieve minimum Quality of Service (QoS).
- **Connection Density [#devices/km^2]**: The number of mobile terminals connected in each coverage area.
- **Network Energy Efficiency [bit/Joule]**: Energy efficiency is referred to as the number of bits of information transmitted or received from users, per unit of radio access network (RAN) energy consumption.
- **Reliability [%]**: The success rate of a connection over a period of time.
- **Area Traffic Capacity [Mbps/m^2]**: Traffic throughput per geographical area.

The proposed IMT-2020 standardization was supposed to provide a user experience like fixed networks. This improvement implies increased data rates, increased spectrum efficiency, increased mobility, and reduced latency.

Figure 1.1 shows graphically the proposed IMT-2000 requirements for 5G systems and their comparison with International Mobile Telecommunications Advanced (IMT-Advanced) capabilities. The proposed KPIs do not have equal importance for all use cases according to their field of action. The level of importance (xMBB-mMTC-uMTC) of each requirement will depend on the needs of each use case.

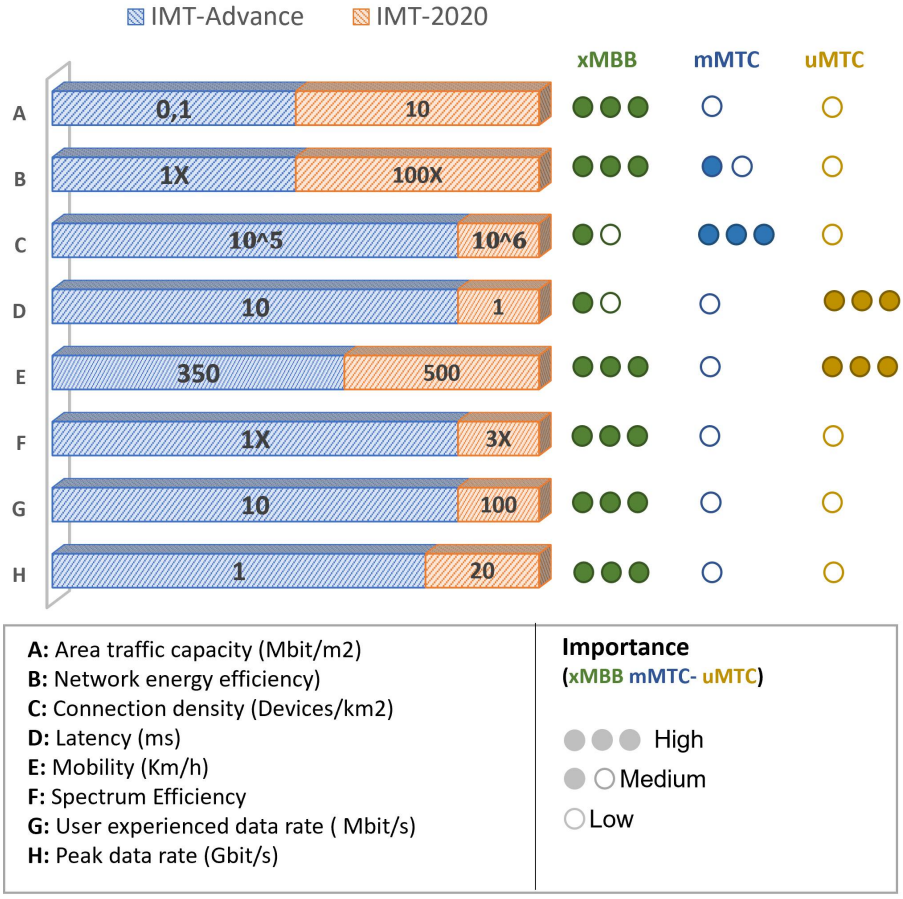

Figure 1.1: 5G KPI defined by ITU and ITU-R [7][8].

1.1.3 5G Use Cases

The main characteristics of 5G systems include the high data transfer speed, the large number of supported devices and the ultra-low latency. The idea of the 5G network is that it should be flexible enough for a wide range of use cases. Mobile network operators (MNOs) must build a dense network that includes a large number of network nodes. This will be the basis of the 5G infrastructure. Initially the use cases will be focused where communications are most critical [9], such as in the case of public health, security and industrial automation.

These are the most important technical and business use cases for 5G [10]:

- **Mobile Broadband**: Mobile broadband is more than just Internet access. It includes a number of new services that require high-speed Internet and real-time (RT) response. In addition, it supports Augmented Reality and Virtual Reality (VR) and these services are increasingly in demand nowadays due to the incursion into the Metaverse of companies as big as Meta (Facebook), so these kind of solutions will be indispensable in the near future.

- **Vehicular Communications**: Vehicle-to-Vehicle (V2V) and Vehicle-to-anything (V2X) communications will make transport safer, more comfortable, more secure and environmentally responsible. This technology will enable massive connectivity between vehicles, roads and infrastructures in a constant and reliable way. Latency should therefore be minimal. This sector has a lot of potential because the aim is to have smarter cities, where energy resources are prioritised, therefore more efficient transport will have to be guaranteed.

- **Industrial Sector**: Reliability and ultra-low latency are crucial criteria for communication between equipment in the production chain in the industrial sector. With complete visibility, real-time control, and intelligent data analysis, industrial sector automation aims to enable intelligent and adaptable production processes, boost production efficiency, and bring manufacturing closer to end users. A latency of less than 8 ms and a dependability of 99.3% are specifically needed for real-time control. In some situations, ultra dense D2D connections with vast access capabilities and extremely low terminal power consumption will be necessary for the collecting and reporting of data from industrial meters and sensors.

- **Healthcare Sector**: In this use case all healthcare models will be customer-centric and will aim to provide quality care at an affordable cost. It is therefore a priority to maximize the medical human resources that have been so depleted after the health crisis. Consequently, many hospitals and medical centers have opted to encourage remote medical consultations in order to streamline patient care. This is where the new 5G technology will help to meet these new needs.

- **Smart Cities**: This use case addresses the connectivity needs of urban residents to improve their quality of life. The 5G will combine dense networks of wireless sensors into a smart grid to provide a holistic solution in various sectors, such as security, energy saving and transportation. Therefore, these smart grids will be designed to manage, control and optimize these resources.

1.1.4 Technical strategies to address 5G requirements

The ITU identified the key technologies that enable the successful implementation of the 5G standard requirements as follows [11]:

- **Advanced Modulation and Coding Schemes**: The number of applications that 5G supports is enormous, so the criteria used to select modulation and coding schemes fit the type of use case. For example, a strong and low-power link is necessary for M2M communications. Whereas, for real-time communication, a high bandwidth and high frequency band should be used to prioritize the data rate, where the recommended frequency band should be the mmWave band. The 5G modulation schemes include filter bank multi-carrier (FBMC), Universal Filtered Multi-Carrier (UFMC), Generalized Frequency Division Multiplexing (GFDM), and Filtered OFDM (f-OFDM).

- **Dynamic Beam-Forming**: Current cellular base station (BS) networks have antennas with fixed radiation patterns along the horizontal axis. This system has worked well so far, because the operating frequency was low for 4G and earlier systems. But in the case of 5G systems the operating frequency is considerably higher. Therefore, the wave propagation is more complicated to characterize, so the radiation pattern of the antennas cannot be simplified as it has been done. It is therefore essential that the radiation pattern of base stations (BS) be dynamically adapted to each environment [12], in order to acomplish with the quality standards proposed by the ITU.

- **Massive MIMO**: The main difference between traditional MIMO and Massive MIMO systems is the number of antenna elements that both base stations and mobile terminals will have. With mMIMO, significant gains will be obtained by having a more directive antenna with higher gain, also increasing spectral efficiency [13] and spatial diversity [14]. Although it sounds good in theory, in practice Massive MIMO brings with it a host of technical challenges that do not existed in previous technologies.

- **Dynamic Spectrum Usage**: According to the 5G standard, flexible spectrum usage is necessary to meet the traffic demand in the different IMT-2020 scenarios. Flexible spectrum usage optimizes spectral efficiency through the use of cognitive radio techniques, authorized shared access, joint management of multiple radio access technologies (RATs), discontinuous band carrier aggregation and inter-band carrier aggregation. This could enable the joint operation of time division duplexing (TDD) and frequency division duplexing (FDD).

- **5G Full-duplex**: This technique increases the spectral efficiency and capacity of the cellular network and reduces latency. Full-duplex communication theoretically allows a node to transmit and receive simultaneously in the same frequency band. One of the limitations of full-duplex is self-interference. But with the proposed spatial diversity (Massive MIMO) for this new technology, this interference can be mitigated. Full-duplex communications is considered a key technique for 5G systems because it doubles the speed and allows reusing the spectrum to connect many clients simultaneously [15].

- **Dynamic Backhaul**: This technology improves the spectral efficiency and performance of point-to-point and point-to-multipoint links. It is mainly used in industrial and enterprise applications. It allows dynamic management of network resources, adapting to different traffic levels and capacities, and efficient use of the electromagnetic spectrum [16].

- **Flexible Radio Access Network (RAN)**: In this new generation, the wireless devices can operate in a dual mode, so a mobile terminal can act as a base station. With this approach the mobile handset will have the ability to manage radio resources locally, in order to optimize connectivity to a base station or to another mobile handset.

- **Dynamic Beam-Steering**: This technology aims to redirect the radiation pattern of the base station or mobile terminal to reach a specific receiver, so the Beam-Steering is achieved by changing the phase of the antenna elements [17]. This strategy is one of the most ambitious because the antenna must dynamically calculate the direction in which to send the signal. Therefore, the device must have characterized its environment prior to redirect the radiation.

- **Dynamic Beam-Switching**: This technique is complementary to Beam-Steering techniques, where according to a previously established Beam-Forming, the system will have the ability to dynamically switch between radiating beams according to coverage needs. This technique is usually more efficient than Beam-Steering techniques because it is faster to switch between beams than to reorient a complete beam [18].

- **Technologies to improve network energy efficiency**: Provide a signaling and control information system to ensure low latency and reliability in the link, as well as dynamically manage spectrum, modulation and control information, support a wide variety of devices with different hardware capabilities, as well as various types of radio environment [19].

1.1.5 Spectrum management in 5G

Previous mobile cellular generations have operated in the sub-6 GHz bands. On the other hand, new 5G networks will also have to operate in frequencies above 6 GHz to meet IMT-2020 requirements. According to the 5G standard, the lower bands will be used for long range solutions (xMBB-uMTC). As opposed to the upper bands, which will operate in the mmWave range, to be used for medium and short range solutions for bandwidth-intensive applications (mMTC) [20, 21].

The 5G higher frequency bands should be used exclusively for short distance communications [22], due to the high propagation losses in line of sight (LOS) and even higher losses in case of no line of sight (NLOS) due to blocking elements in the environment like people, furniture etc. This effect is more pronounced in the mmWave frequency band, because the obstacles are more obstructive at higher frequencies compared to bands below 6 GHz. On the other hand, in the frequency bands below 6 GHz the spectrum is already saturated, which is not used for high transfer rates, but where wide coverage is required. Many mmWave band frequencies are used for short-range and backhaul services. However, its use in mobile communications is still under study.

According to [23], spectrum selection is affected by three factors: first, the spectral range must be accessible in all regions of the world. Second, the spectrum range must be contiguous to ensure more flexible spectrum management. And the final requirement is that the spectral range meets the requirements for cellular mobile communications [24].

ITU is a leader in radio spectrum management and development of internationally applicable standards for IMT-2020. Therefore, the ITU conducted the World Radiocommunication Conference 2019 (WRC), where they identified the target frequency bands for the 5G standard below 6 GHz.

Within all bands, the following bands of special interest for the 5G standard were found [22]: First, there is a global band that has been identified in many countries but neither in Europe nor in North America within the frequency range 3300-3400 MHz. Second, there is a global C-band for all countries between 3400-3600 MHz. Third, a global C-band is identified in many countries, but not in Africa nor in some Asia-Pacific regions at 3300-3400MHz. Finally, there is a C-band band that has been identified for some countries in Asia-Pacific at 4800-4990 MHz. C-band will provide adequate bandwidth per operator and meets the traffic demands of the 5G standard in highly populated urban coverage [23].

On the other hand, there has been great interest in using the 700 MHz band to offer high coverage services. Although this implies additional work on the

part of governments and companies to free up this spectrum range and migrate some existing services [20].

One of the central topics in the discussion of spectrum management proposed at WRC 2019 was to finalize the definition of the frequency ranges above 6 GHz for the 5G standard, where they were initially defined at WRC 2015. These were the main bands that were proposed: 24.25-27.5 GHz, 37-43.5 GHz, 45.5-47 GHz, 47.2-48 GHz, , and 66-71 GHz.

WRC-2019 has identified a 17.25 GHz spectrum, compared to a 19 GHz bandwidth proposed in WRC-2015. Of the 17.25 GHz, 85% has been harmonized globally.

In this Thesis the research has been focused on the study of the radio channel behavior in the band above 6 GHz, especially in the mmWave band range (24 GHz to 40 GHz). From the three approaches for spectrum management in 5G, (i) global availability of access, (ii) bandwidth in a contiguous spectrum, (iii) optimal radio propagation, this Thesis focuses on the latter aspect, where it is key that the radio propagation must be characterized, in order to use the radio resources properly, both from the mobile device and the base station.

1.1.6 5G Propagation Channel Model

This section explains briefly what a channel propagation modeling for 5G is, its requirements, and the most important scenarios in which it is necessary to correctly characterize the propagation models to provide the expected capabilities in 5G.

There are two main factors that influence channel propagation modeling according to [25]: the first factor corresponds to the requirements that the new channel propagation model must meet in order to operate in the upper 5G frequency bands (up to 71 GHz). Such requirements are based on the existing models already proposed by 3GPP to meet this new technical challenge, where some of these requirements are shown below:

- The new channel propagation model must support large antenna arrays, especially at high frequencies in mmWave bands, to compensate propagation losses with antenna directivity gain and take advantage of massive MIMO (mMIMO) capabilities.
- The radio channel model must be flexible enough to support a wide range of frequencies up to 71 GHz, mainly in the mmWave range because it is more complicated to model stochastically.
- To evaluate multiband operation it is important to include the characteristics of joint propagation across different frequency bands. As in carrier

aggregation configurations (CA) from 24 GHz to 71 GHz in the mmWave range.

- The channel model must allow mobility. In particular, it must allow speed up to 500 km/h, according to ITU-R.
- The mobility channel model should allow scenarios such as vehicle-to vehicle (V2V) and device-to-device (D2D), because a network node will not always be available close to the mobile device and the relay effect in information exchange can be exploited.
- This new channel approach recommended by ITU-R must ensure temporal stability as well as spatial and frequency coherence.
- The model proposed should be flexible enough to evaluate various states of the link between network node (BTS) and mobile device. For example, when the mobile device is in direct line-of-sight (LOS) or not (NLOS).

The propagation environment or scenario is the second factor influencing channel propagation modeling. The propagation scenarios of the 5G standard are determined according to the use cases described in section 1.1.3. The following classification of scenarios where the radio channel is intended to be modeled has been proposed by the ITU according to the report [2]:

- **Backhaul** (Distribution Network): This type of scenario refers to the connection between network nodes (Base Stations). Normally this type of scenario has a point-to-point connection with highly directive antennas and simple stochastic models are used. But in 5G standard, there will be more concentration of network nodes, where a simple point-to-point communication might not be the best option, so properly characterizing this type of outdoor environment is vital in order not to reduce network performance [26].
- Urban Micro-cell (**UMi**): This type of scenarios are densely populated with maximum coverage of 90 meters. Because the network nodes are located at mid-height of the surrounding buildings, this makes signal propagation very difficult, especially in the mmWave band range. This type of scenario is usually stochastically characterized due to its complexity and the type of connections it establishes are Outdoor to Outdoor (O2O) and Outdoor to Indoor (O2I) [27].
- Urban Macro-cell (**UMa**): Similar to Urban Micro-cell (UMi), this scenario has the base station located on top of the surrounding buildings. This scenario covers an average distance of over more than 100 meters [27].

- **Indoor**: In this scenario the base station is usually located within a building. This scenario covers a variety of environments, including offices, malls, Conference centers, etc. The average height of the base station ranges between 2 to 3 meters. In this scenario, modelling the propagation channel is particularly complex, because the base station antenna is at low height. This implies that the radiation emitted by the base station will be prone to be constantly obstructed by people in the environment.

- Device to Device (**D2D**): This type of scenario refers to communication between devices, without the need to establish a link with the base station. In this approach each device will bridge the link with the base station [28]. This is the most complex propagation model to characterize because the interaction of the mobile terminal with the human body becomes very relevant.

This Thesis focuses on propagation models in indoor and D2D environments. Therefore, emphasis has been placed on modeling the human body correctly, because it is the most obstructive element in this type of environments. The scattering effect of the human body in the mmWave band can be characterized according to the model proposed by 3GPP in TR-38.901 - Release 14 [29]. This effect has been included in a propagation model using ray tracing techniques, to evaluate a complex indoor scenario as a whole (people, furniture and architectural structure), where both LOS and NLOS zones are considered.

1.2 State of the Art Analysis

This section provides an overview of the status at the PhD start date, based on a summary review of the literature. This review is divided into three areas. The first area is a review of the mathematical models used to characterize the scattering effect of the human body. The second area presents the reflector antenna designs used to increase the propagation diversity of the radio channel. The third area presents the concepts of propagation modeling for 5G in the mmWave band with ray-tracing techniques.

1.2.1 Human Blockage Models

Mathematical models in the literature consider that human body blockage in mmWave propagation can be defined through its morphology and material. The blocking loss of the human body is evaluated by simple mathematical formulas, most of which are driven by the diffraction of plane waves as they impact

the boundaries of blocking objects. These proposed models are physically valid, if their parameters, such as shape, dimension and material, are statistically defined in order to adjust the models to reproduce realistic losses measured in the laboratory. Therefore, one of the most arduous tasks in modeling the blocking effect of the human body is to calculate statistically reasonable properties to obtain reliable results. This section reviews the models available for human blocking, considering different geometrical shapes, which emulate the morphology of the human body, as well as dielectric properties that simplify human body tissues in order to estimate propagation losses and scattering phenomena.

1.2.2 Absorbing Screen Models

Double Knife-Edge Diffraction (DKED) Model

Traditionally in the scientific community, the human body has been modeled as an absorbing screen. The screen's simplest shape is a vertically infinitesimal strip. It is also known as a Double Knife-Edge model (DKED) [30], as shown in figure 1.2. It is feasible to obtain good estimates of the received electromagnetic field (RX) behind the human body using double-edged diffraction (DKED) of the absorbing screen. The diffracted fields from two wedges sides (Ⓐ and Ⓑ) of the absorbing screen are included. First, starting from a half-plane absorbing screen with a point source of transmission (TX) and a receiving point (RX), whose positions are shown in figure 1.3, the RX field is given by (1.1).

$$E_{RX} = \left(\frac{1+j}{2}\right)\left[\left(\frac{1}{2} - C(v)\right) - j\left(\frac{1}{2} - S(v)\right)\right] * E_0 \tag{1.1}$$

where E_0 is the RX field when there is no absorbing knife edge; $C(v)$ and $S(v)$ are cosine and sine Fresnel integrals given by 1.2.

$$C(v) + jS(v) = \int_0^v exp(j\frac{\pi}{2}t^2)dt \tag{1.2}$$

Where in the (1.4) indicates the wave propagation velocity in the path (1.3) from the TX to the corner of the obstacle to the RX.

$$\Delta d_n = (d_{TX\to n} + d_{n\to RX}) - (d_{TX} + d_{RX}) \tag{1.3}$$

$$v = \pm\sqrt{\frac{2k_o\Delta d_n}{\pi}} \tag{1.4}$$

Where n can be any of the positions of the edges of the obstacle, as in figure 1.2, can be the distance to position A or B.

The diffraction estimate of the incident field is not affected by the polarization states, so this effect is not included in the mathematical model. Fresnel integrals (1.2) can be easily solved with numerical methods, which are available in all scientific libraries.

The DKED model has a higher accuracy under the following conditions: $d_{TX}, d_{RX} >> \lambda$ and $d_{TX}, d_{RX} >> h_A + h_B$. The simplification proposed by the model is critical because it limits the applicability of this model to evaluate obstacles such as the human body. Therefore, it is one of the research objectives proposed in the Thesis.

The sign of the variable v is defined by the degree of obstruction between the TX and the RX (See figure 1.3). In the situation where there is a total visibility blockage (NLOS), V would be positive and in the opposite case where there is a partial obstruction without loss of visibility (LOS), V would be negative if it has a separation greater than the first Fresnel zone and zero if it is equal to the Fresnel radius with regard to the relative position between the TX and the RX.

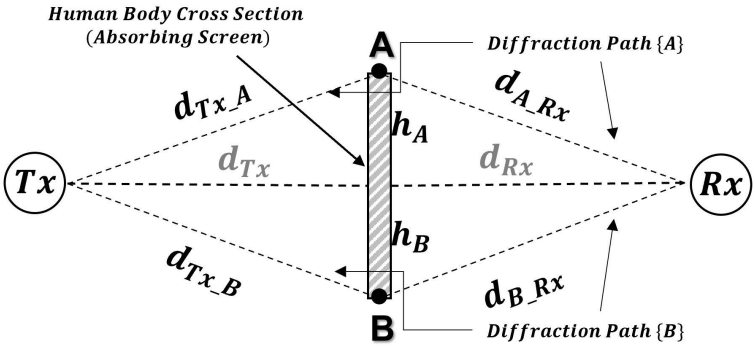

Figure 1.2: (DKED) Double Knife-Edge Diffraction model [30].

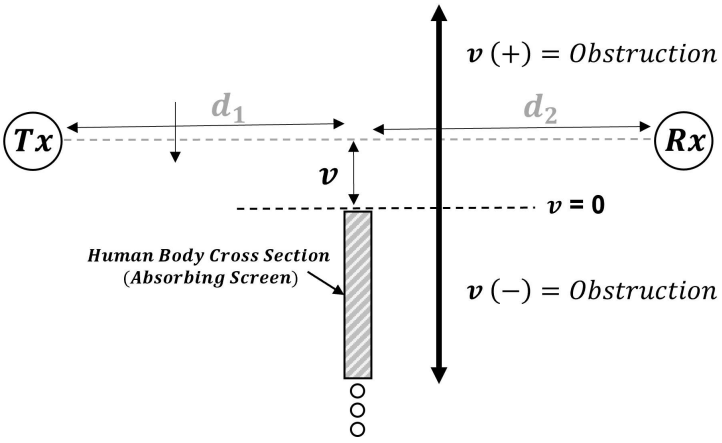

Figure 1.3: Half-Plane absorbing screen.

The relative RX field strength across the absorbing screen can be calculated by considering the DKED approach of figure 1.2 as two independent sub-problems, where each field estimation only takes into account one of the two edges of the absorbing screen, and each edge is bounded by the screen contours of the half-plane screen. Therefore, the final diffracted field is calculated by the sum of the two field contributions according to equation (1.1), wherein the line-of-sight field is given by (1.5).

$$E_o = \frac{\lambda}{4\pi(d_{TX} + d_{RX})} exp(-j2\pi \frac{d_{TX} + d_{RX}}{\lambda}) \tag{1.5}$$

The final field in the RX is given by the sum of the two sub-problems associated with each side (Ⓐ + Ⓑ) of the absorbing screen, and is expressed as 1.6.

$$E_T = E_A + E_B = E_{RX_A} exp(-j2\pi \frac{\Delta d_A}{\lambda}) + E_{RX_B} exp(-j2\pi \frac{\Delta d_B}{\lambda}) \tag{1.6}$$

Note that the Fresnel integral (1.2) is not strictly valid at low radio frequencies, since the conditions $d_{TX}, d_{RX} >> \lambda$ and $d_{TX}, d_{RX} >> h_A + h_B$ are not satisfied. Because of its simplicity, the DKED model of a single human body is also useful for predicting the link attenuation when multiple human bodies block a propagating path [31], [32]. To estimate the human blockage attenuation more accurately, [33] modifies DKED to consider the radiation patterns of the transmitting TX and RX antennas.

Multiple Knife-Edge Diffraction (MKED) Model

Unlike DKED models, in which the human body is represented as a simple infinitesimal absorbing screen along one axis, more sophisticated human body blocking models consider not only the human torso, but also the shoulders and the head [34]-[35], and are commonly referred to as MKED models.

These are also absorbing screen models, and take into account the diffraction field of each edge of the absorbing screen to calculate the total blocking loss. Furthermore, depending on the orientation of the human body, the blocking losses will change radically. [34] evaluates human blocking by assuming that the human body can be simplified with only two truncated vertical absorbing strips; where on one side a human head is assembled to consider its effect [35], see figure 1.5. The two screens cross orthogonally and are representative of the thickness and width of a human body, see figure 1.4.

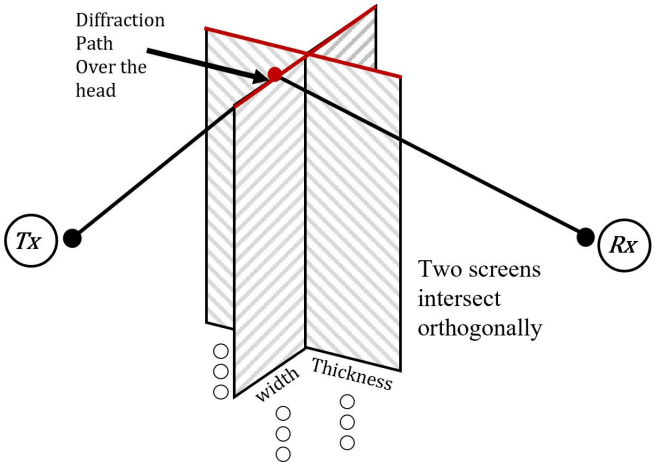

Figure 1.4: Half-Plane absorbing screen.

Depending on the orientation of the two screens, only the one with the bigger cross section, as perceived from the TX/RX link, is used to compute the diffracted trajectories. A diffracted path from the top edge of the screen is considered in addition to the diffracted paths from the sides. Therefore, this mathematical methodology is called the truncated multiple diffraction model (STMKE) (see 1.7).

When multiple diffraction from multiple edges of an absorbing screen is considered, any extra diffraction contribution must be calculated using (1.1)

and added to (1.6). For example, as in the case of STMKE, the RX field is determined by (1.7).

$$E_{STMKE} = E_{DKED} + E_h exp(-2\pi f \frac{\Delta d_h}{c}) \tag{1.7}$$

where $\Delta d_h = d_{THR} - d_1 - d_2$, and d_{THR} is the 3-D distance between the TX source and RX observation point through the top edge of the half-plane vertical absorbing screen. While applying 1.1 to compute the diffraction from each edge, the height h, distances d_1 and d_2 in 1.1 can be set by $h = h\prime cos(\alpha)$, $d_1 = D_{TP} \pm h\prime sin(\alpha)$, and $d_2 = D_{RP} \pm h\prime sin(\alpha)$ for $h\prime = h_{b1}, h_{b2}, h_{s1}, h_{s2}$ for $-\pi/2 \leq \alpha \leq \pi/2$ as defined in figure 1.5. If the human body orientation is perpendicular to the TX - RX line, i.e., $\alpha \sim \pm\pi/2$, where the thickness of the human body depends on the orientation of the cross-section of the geometrical model of the body, depending on the positions of the TX and RX.

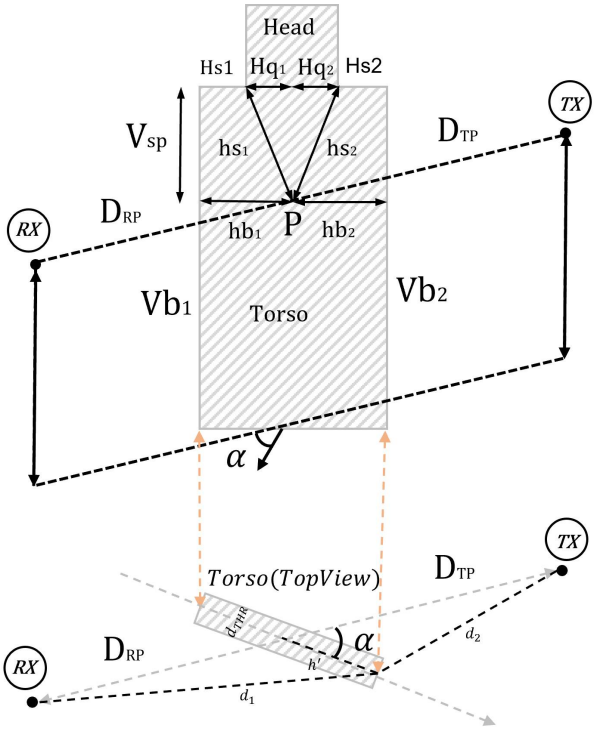

Figure 1.5: Multiple knife-edge model with head and shoulders.

The diffraction coefficients do not depend on the polarization of the wave, because the human body is modeled as an absorbing screen, so no induced currents are modeled on the surfaces that are modified by the polarization of the incident wave. The MKED models provide greater consistency with measurements when the orientation of the human body is arbitrary and when the heights of the mobile and base station antennas are significantly different. These are significant features in mobile cellular links and this methodology allows to model more complex environments.

Conducting Screen and Wedge Models

This model estimates the diffraction coefficients of each edge of a finite conducting screen in a similar manner to the DKED model, assuming that each edge is a zero-angle wedge [36]. Compared to the MKED model, this one does not consider the screen as an absorbing material but as a conductor or insulator. In this approach, the uniform theory of diffraction (UTD) is used to obtain the RX field [37]. Given the wedge geometry shown in figure 1.6, the diffracted field is defined by (1.8).

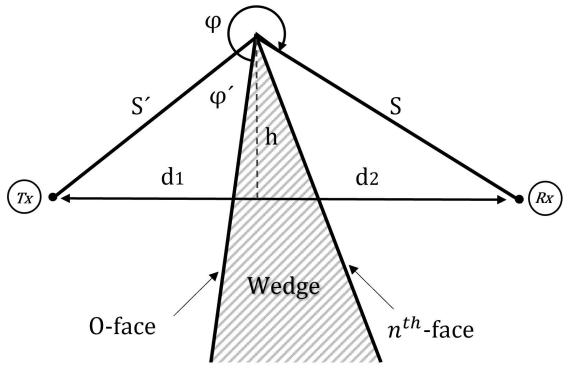

Figure 1.6: Wedge between two points of TX and RX.

$$E_W = E_0 \frac{e^{-jkS\prime}}{S'} D^{\perp\parallel} \sqrt{\frac{S'}{S(S'+S)}} e^{-jkS} \tag{1.8}$$

where the polarization dependent diffraction coefficient for a finitely conducting wedge is given by (1.10), where $D^{\perp\parallel}$ is the diffraction coefficient of

parallel and perpendicular polarizations. The function $F(*)$ is the Fresnel integral defined in equation (1.9).

$$F(x) = 2j\sqrt{x}e^{jx}\int_{\sqrt{x}}^{\infty} e^{-j\tau^2 d_\tau} \tag{1.9}$$

$$\begin{aligned} D^{\perp\parallel} &= \frac{-e^{-j\pi/4}}{2n\sqrt{2\pi k}}x \cdot cot\left(\frac{\pi + (\phi - \phi\prime)}{2n}\right)F(kLa^{+}(\phi - \phi\prime)) \\ &+ cot\left(\frac{\pi - (\phi - \phi\prime)}{2n}\right).F(kLa^{-}(\phi - \phi\prime)) \\ &+ R_0^{\perp\parallel}cot\left(\frac{\pi - (\phi + \phi\prime)}{2n}\right)F(kLa^{-}(\phi + \phi\prime)) \\ &+ R_n^{\perp\parallel}cot\left(\frac{\pi + (\phi + \phi\prime)}{2n}\right)F(kLa^{+}(\phi + \phi\prime)) \end{aligned} \tag{1.10}$$

and furthermore, in (1.11),

$$L = \frac{SS'}{S + S'} \tag{1.11}$$

$$a^{\pm}(\beta) = 2cos^2\left(\frac{2n\pi N^{\pm} - \beta}{2}\right) \tag{1.12}$$

$$\beta = \phi \pm \phi' \tag{1.13}$$

where n defines the exterior wedge angle to be $n\pi$ and $N\pm$ are the integers that satisfy the following two equations:

$$2\pi nN^{+} - \beta = \pi, 2\pi nN^{-} - \beta = -\pi \tag{1.14}$$

Finally, $R_0^{\perp\parallel}$ and $R_n^{\perp\parallel}$ are the polarimetric Fresnel reflection coefficients of a plane wave at $0-$ and $n - face$, where incident and reflecting angles are given by $\phi\prime$ and $N\pi - \phi$, respectively. There are no cotangent functions in 1.8 around the reflection and shadowing boundaries is mitigated through the approximation given by 1.15.

$$\cot\left(\frac{\pi \pm \beta}{2n}\right)F(kLa^{\pm}\beta) \simeq n\left(\sqrt{2\pi kL}.sgn(\epsilon) - 2kL\epsilon e^{j\pi/4}\right)e^{j\pi/4} \tag{1.15}$$

with ϵ defined by (1.16).

$$\beta = 2\pi n N^{\pm} \mp (\pi - \epsilon) \tag{1.16}$$

In this way, it is possible to consider the realistic conductivity and permittivity of the real human body. To enhance the estimation of the diffracted field of right-angle wedges, [38] suggests diffraction coefficient using the inverse problem theory to improve the estimation. It should be noted that wedge diffraction becomes a thin screen when $n = 2$, which allows to calculate the blocking loss due to finite conducting screens using (1.8). The diffraction coefficient for a finitely conducting wedge can also be applied to shadow objects other than humans, e.g. corners of buildings [39].

1.2.3 Cylinder Models

Circular Cylinder Model

Cylinder-based human blocking models have also been popularly discussed in the literature [40–43]. When a cylinder is a perfect electrical conductor (PEC) and its cross section is circular, the mathematical model can derive exactly diffracted polarimetric fields based on the geometrical theory of diffraction (GTD) [44]. Consider a circular cylinder of radius α as shown in figure 1.7. The detected field at point P2 is determined as a sum of the diffracted trajectories from the two sides of the cylinder, given by 1.17.

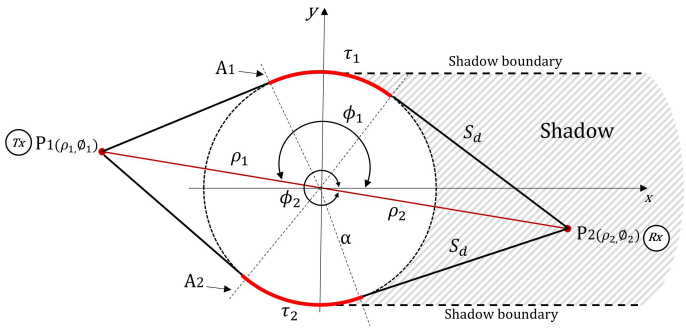

Figure 1.7: Circular model illustration for link blockage.

$$E_z = \sum_{n=1}^{\infty} D_n^e E_i \left[exp(-(jk + \Omega_n^e)\tau_1) + exp(-(jk + \Omega_n^e)\tau_2)\right] \frac{exp(-jks_d)}{\sqrt{8j\pi ks_d}} \tag{1.17}$$

where two propagation paths are of distances τ_1 and τ_2 and attenuated according to a constant Ω_n. For the electric field, this constant is given by 1.18.

$$\Omega_n^e = -\frac{q_n}{a} M e^{j\pi/6} \tag{1.18}$$

where $q_n = -\alpha_n$ indicate the nth root (zero) of the Airy function $Ai(*)$ [45]. Finally, D_n and M are given by 1.19 and 1.20.

$$D_n = 2MAi\prime(q_n)^{-2} e^{j\pi/6} \tag{1.19}$$

$$M = \frac{ka}{2} \tag{1.20}$$

where Ai' indicates as the derivative of the Airy function [45], and $k = 2\pi/\lambda$ is the wavenumber. It should be mentioned that GTD solutions have uniqueness around the transition region between the illuminated and shadow regions. Analytical UTD methods for a conductive cylinder are limited, for example, to a thin coating of lossy material [46], and are only valid at RX positions of the cylinder [47]. Reference [42] also discussed the impact of clothing on blocking loss and concluded that clothing could affect the blocking loss under specific conditions, and is susceptible to the thickness of the clothing layer. This is another of the topics analyzed throughout the development of the Thesis, in order to clarify whether or not clothing has any effect on the blocking of the human body at mmWaves.

Elliptical Cylinder Model

In this mathematical model a cylinder with elliptical cross section is considered. It is assumed that the center of the ellipse coincides with the $z - axis$ of the Cartesian coordinate system [48]. The distance between the two focal points of the ellipse is assumed to be $2h$. The elliptical coordinates on the horizontal plane, defined by $\xi - \eta$ domain as depicted in figure 1.8, have a relationship with the Cartesian $x - y$ coordinates as in equations 1.21 and 1.22.

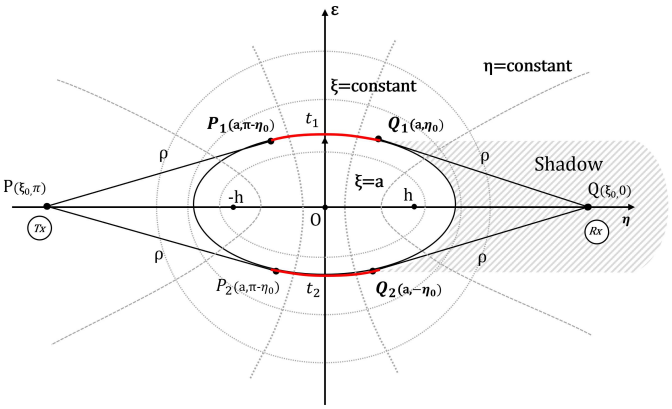

Figure 1.8: Elliptical model illustration for link blockage.

$$x = hCosh(\xi)Cos(\eta), \tag{1.21}$$

$$y = hSinh(\xi)Sin(\eta) \tag{1.22}$$

In figure 1.8, the locations are represented on the elliptic coordinate system as, e.g., $P(\xi, \eta)$. The ellipse representing the human cross section is given by $\xi = a$. The TX and RX antennas are located at $P(\xi_0, \pi)$ and $Q(\xi_0, 0)$, respectively. Two diffracting rays symmetric to the horizontal axis exist from the TX antenna at P to the RX antenna at Q. The points of tangency where the two rays impact and leave the cylinder are $P_1(a, \pi-\eta_0)$, $Q_1(a, \eta_0)$, $P_2(a, \pi+\eta_0)$ and $Q_2(a, \eta_0)$. The radial distance from the points of tangency to the TX and RX is $P \rightarrow P_1 = Q \rightarrow Q_1 = P \rightarrow P_2 = Q \rightarrow Q_2 = \rho$. The following derives the total field at the RX E_z for vertical polarization. First, the diffracted field at the RX due the ray PP_1Q_1Q is given by 1.23.

$$\begin{aligned} E_{1z} =& A_0\rho^{-1}exp[jk(\rho + t_1)] \\ & \sum_{n=0}^{\infty} B_n(np)B_n(nQ)exp[jk^{1/3}\tau_n\alpha(t_1)]. \\ & .[1 - exp(jkT + jk^{1/3}\tau_n\alpha(T))]^{-1} \end{aligned} \tag{1.23}$$

where $\xi P = \pi$ and $\eta Q = 0$ are the η coordinates corresponding to the TX and RX locations P and Q, respectively; t_1 denotes the arc length from the

P_1 to Q_1 and T is the total arc length of the ellipse, A_0 is a constant given by 1.24.

$$A_0 = \frac{e^{j\pi/4}}{2\pi}\sqrt{\lambda} \tag{1.24}$$

$B_n(\eta)$ represents the diffraction coefficient

$$B_n(\eta) = \pi^{3/4}2^{1/4}6^{-2/3}e^{j\pi/24}k^{-1/12}b^{1/6}(\eta)[Ai'(q_n)]^{-1} \tag{1.25}$$

where q_n is the same as used in [43]; $b(\eta)$ refers to the radius of the ellipse on the major axis as

$$b(\eta) = h.(Cosh(a)Sinh(a))^{-1}.(Sinh^2(a) - Sin^2(\eta) + 1)^{3/2} \tag{1.26}$$

Furthermore, in [37], $a(x)$ is

$$\alpha(x) = \int_0^x b^{-2/3}(\eta)d\eta \tag{1.27}$$

and τ_n is

$$\tau_n = e^{j\pi/3}6^{-1/3}q_n \tag{1.28}$$

The diffracted field E_{2z} due to the ray PP_2Q_2Q can be evaluated in the same way as E_{1z}. Now the total diffracted field at the RX as a combination of the diffracted fields from the two sides of the elliptic cylinder is given as $E_z = E_{1Z} + E_{2Z}$.

The two mathematical models in which the equivalent of the human body was considered as a circular or cylindrical object, only work for a normal incidence of a plane wave, which only allows to analyze the problem of scattering in two-dimensional space. When the scattering problem is extrapolated to 3-D, with an oblique plane wave incidence, in scenarios with different TX and RX heights, there are no closed-form solutions in the literature to determine the scattering field. In this situation it is required to resort to a numerical solver of the electromagnetic (EM) field [49] and a more extensive numerical integration [50], which in most cases is very computationally expensive, due to the complexity of the morphology of the human body and the relative electrical size of the human body in the mmWave range.

1.2.4 Other Heuristic Models

Human blocking models have been described as estimating the blocking loss by determining the diffracted field around objects. The analytical methods for estimating diffracted fields, using GTD or UTD solutions, can be used for simple objects such as absorbing screens, conductive edges and PEC cylinders. These methods involve using Fresnel integrals (see equation 1.2), which can be calculated as integrated functions available in scientific tools and mathematical libraries. However, this type of approach is too complex to implement in more complex simulations where not only a single person but several people and their environment need to be characterized. Alternatively, with the heuristic modeling approach, GTD and UTD solutions can be simplified with approximations of the formulas involved, observations and measurements.

Measurement-Based Models

The models based on mmWave frequency measurements include, for instance, [51], that characterizes the signal level attenuation caused by human shadowing observed on short-range 60 GHz radio links employing a Gaussian probability distribution. In the research presented in [43], authors propose a linear approximation where the concealment of the human body is random in time in a 60 GHz band, in order to statistically predict how the radio channel would behave in a highly crowded scenario. The scattering caused by the human body is emulated as a decreasing slope in the received intensity as the link becomes progressively obstructed, and as an increasing slope when the person is no longer obstructing the link. In spite of its simplistic approach, results obtained with this methodology show good agreement with measurements, considering that measurement campaign used a point to point link, where the TX and RX antennas are at the same height as the torso of an average person. The research conducted in [52] models fast fading due to pedestrian crowds, using a measurement-based Markov process in a dense urban environment at 73.5 GHz.

3GPP-mmMagic Model

In the European Union H2020-5GPPP project mmMagic [53], a simplified blocking model based on the GTD is proposed, which is the improvement of the blocking model adopted by 3GPP version 14 TR-38.901 [54]. It is classified as a heuristic model because the formulas for predicting losses include approximations that do not strictly follow the physical behavior of wave propagation. The equivalent geometry used by the mathematical model representing the blockage of the human body is shown in figure 1.9, where the side and top views of the

geometry are drawn. The blocking object is an infinitesimally thick rectangular screen that floats in the air, and is claimed to be large enough to simulate different physical objects over the entire human body. By considering that the screen floats in the air, only the blocking of the object of study is analyzed, without taking into account external elements such as the floor. The diffraction losses in the screen are determined by the mathematical formula 1.29.

$$E_{mmMAGIC} = \left[1 - \prod_{i=1}^{2}\sum_{j=1}^{2} S_{ij}\left(\frac{1}{2} - \frac{ph_{ij}}{Ph}F_{ij}\right)\right]E_0 \tag{1.29}$$

where,

$$F_{ij} = \left[\frac{1}{2} - \frac{1}{\pi}tan^{-1}\left(\frac{\nu_{ij}\pi}{2}\right)\right]cos\psi_{ij} \tag{1.30}$$

$$\nu_{ij} = \sqrt{\frac{\pi}{\lambda}(D1_{ij}^{proj} + D2_{ij}^{proj} - r_i^{proj})} \tag{1.31}$$

$$ph_{ij} = exp\left[\frac{-j2\pi}{\lambda}(D1_{ij} + D2_{ij})\right] \tag{1.32}$$

$$Ph = exp\left[\frac{-j2\pi}{\lambda}r\right] \tag{1.33}$$

Finally, S_{ij} is a sign parameter, which is 1 if the non-line-of-sight (NLOS) condition is in projection i_m while $s_{ij} = sgn(D1_{ij} + D2_{ij} - D1_{ik} - D2_{iK})$ if the line-of-sight (LOS) condition is in projection i, where $k = mod(j, 2) + 1$. It is important to emphasize that the multiplication of the fields from different sides of the absorbing screen in [48] is an approximation that is not physically accurate for wave propagation, and therefore, this model is considered heuristic.

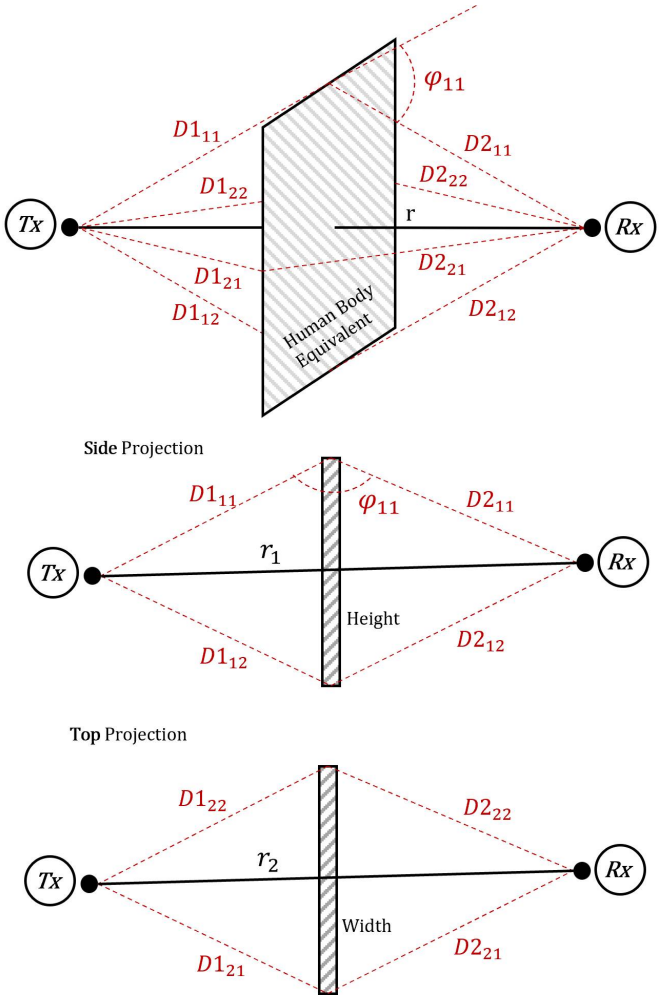

Figure 1.9: 3GPP-mmMAGIC model geometry.

The terms $cos\psi_{ij}$ in F_{ij} account for the increase in shadowing loss in the shadowed zone behind the screen. For long distances with respect to the screen, this parameter can be ignored. The formulation satisfies Babinet's principle that different shapes of blocking objects like a truck [53] can be simplified by combining multiple screens.

1.2.5 Reflector Antennas

Since the discovery of electromagnetic wave propagation by Hertz in 1888, reflector antennas have been used in some form to optimize wave propagation. However, the sophisticated art of designing and analyzing reflectors, considering many different geometrical shapes, did not emerge until the beginning of World War II, where one of their benefits was to enhance the newly invented military radar applications. After the war, reflectors were increasingly in demand for applications in radio astronomy and microwave communication, as well as for tracking balloon satellites, because there was a need for long distance communication, where large antennas were required to establish the wireless link between the TX and RX. Therefore, the most practical way to have electrically large antennas with high gain was through reflectors. This boosted the development of analytical and experimental techniques to optimize reflector surfaces to maximize their gain and optimize their coverage.

In most cases, reflectors operate in the high frequency range. Consequently, the propagating waves behave like an electromagnetic wave in the light range. This implies that the design of the reflector can be realized by a projection of incident rays on a polished surface, similary to the ray tracing techniques that will be discussed throughout the progress of the Thesis, not exclusively for reflector design but also to analyze radio channel propagation in complex indoor scenarios in the mmWave band.

There are many configurations of reflector antennas. However, the most common shapes are corner, flat and curvilinear reflectors figure 1.10(a-b-c-d).

The analysis of reflectors is not always done with geometrical optics (ray tracing), but only in those cases where the surface is smooth and the operating frequency is quite high, as in the classical cases of figure 1.10(a-b-c-d). This means that other techniques cannot be used to emulate the effect of an electrically large reflector. Another alternative to an electrically large antenna is to use several smaller antennas in an array [55]. Nowadays most antenna arrays are built of microstrips, a technology proposed by Deschamps in 1953 [56], which has many advantages such as low cost, small size, compact structure, simple manufacturing process and ease of configuration. Since then, microstrip antenna arrays have played an essential role in modern phased-array systems. While reflectors and arrays continue to race for the largest apertures, a new generation of high gain antennas has emerged in recent years, which have attracted increasing interest from the antenna/electromagnetic science community due to their low profile, low mass and, in many cases, low cost characteristics. These antennas are a hybrid of these two previously antagonistic technologies, now known as reflectarray antenna [57]-[58]-[59], see figure 1.10(e).

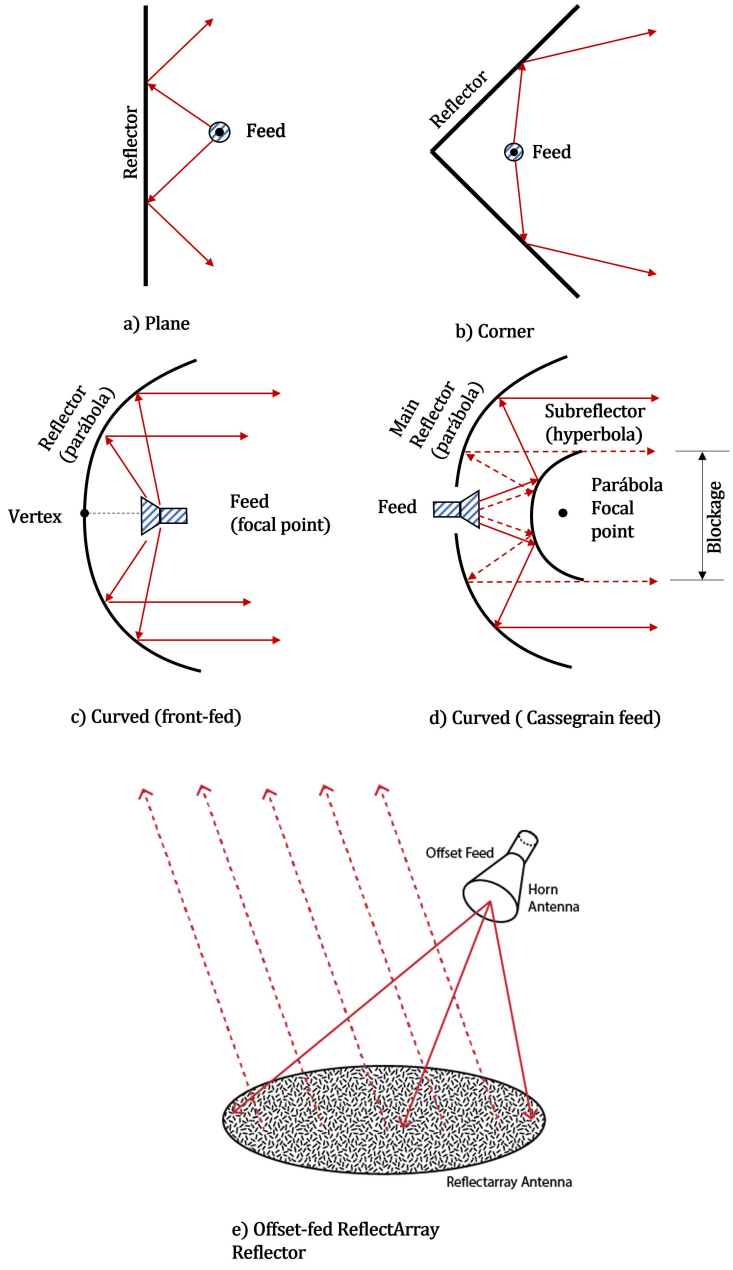

Figure 1.10: Geometrical configuration for some reflector systems.

Plane Reflector

The most simple type of reflector is a flat reflector used to direct the energy in a specific direction. Antenna theory has shown that the polarization and position of the radiating source with respect to the reflecting surface can be used as controls on the radiating properties (patterns, impedance, directivity, etc.) of the entire system. With this basic type of reflectors, image theory has been used to analyze the radiation characteristics of the entire system as a whole. Mathematically it is often assumed that the flat reflector has infinite dimensions; this assumption is valid when designing reflectors that are electrically large, which is the case study of this Thesis, where the operating frequency is the mmWave band. In the opposite case, when the reflecting surface is not electrically large enough, the geometrical diffraction theory can be used [60].

Corner Reflector

To better concentrate the radiation energy in the forward direction, it is essential to change the geometrical shape of the flat reflector itself to avoid radiation in the rear and lateral directions. A configuration that achieves this consists of two flat reflectors joined together in the form of a corner, as shown in figure 1.11(b). and in 1.11(a).

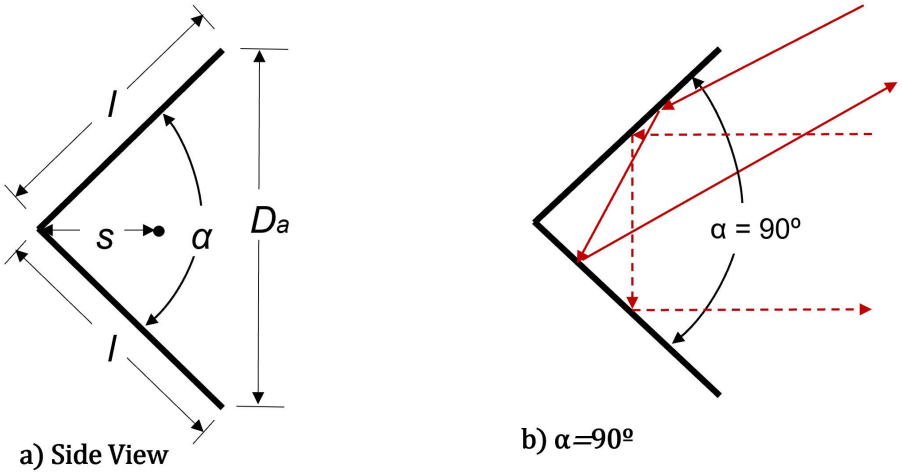

Figure 1.11: Side views of solid corner reflector.

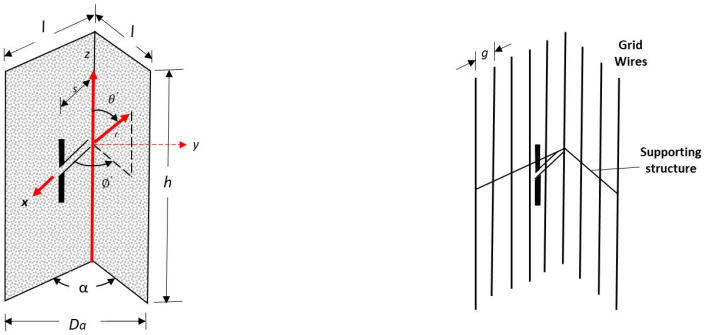

a) Perspective view

b) Wire_grid arrangement

Figure 1.12: Perspective views of solid and wire-grid corner reflectors.

This type of reflector is known as the corner reflector. Its design is simple and has many unique uses. If the reflector is used to transmit a communication or radar signal, it will return it exactly as it received it, even if its angle is 90°. This geometrical premise is illustrated in the figure 1.12(b). This unique property makes possible to design ships and military vehicles with a minimum of sharp corners to reduce their detection by enemy radars. As receiving devices for television, corner reflectors are frequently used. In most practical applications, the angle formed by the reflectors is usually 90°; however, other angles are sometimes used. For the reflector to work at its best efficiency, the distance between the vertex and the feed must increase as the included angle of the reflector decreases, and vice versa. Reflectors with infinite size have a greater gain when the angle between the planes is smaller. Therefore, the higher the operating frequency of the system, the higher the gain in the reflector, because it will be electrically larger. However, this is not true for reflectors of finite size. For simplicity, it will be assumed that the reflectors have infinite extent ($l = \infty$). However, since in practice the dimensions must be finite, guidelines will be provided for aperture size (D_a), length (l) and height (h).

The feed component of a corner reflector is almost always a dipole or an array of parallel dipoles placed parallel to the vertex at a distance s, as shown in a perspective view in figure 1.12(a). A higher bandwidth is obtained when the feed is a set of cylindrical dipoles instead of thin wires, because it has a larger surface in the reflector, therefore it obtains a higher gain by concentrating more energy.

A higher bandwidth is obtained when the feed is a set of cylindrical dipoles instead of thin wires, because more energy is incident on a larger surface area

in the reflector, thus obtaining higher gain. In many applications, particularly when the wavelength is large compared to tolerable physical dimensions, the corner reflector surfaces are commonly made of mesh wires instead of solid sheet metal, as shown in figure 1.12(b). One of the reasons to manufacture it this way is to have more wind resistance, less weight and lower system cost. The separation (g) between the wires must be a small fraction of the wavelength (usually $g \leq 10\lambda$). Reflectivity of the grid-wire surface is equal to that of a solid surface for wires parallel to the length of their dipoles, as in figure 1.12(b). The corner reflector aperture (Da) is usually made between one and two wavelengths ($\lambda < D_a < 2\lambda$). The length of the sides of a 90° corner reflector is at least in practice twice the distance from the vertex to the feed ($l \simeq 2s$). For reflectors with small angles α, the sides of each reflector have to be larger. The distance between the feed and the vertex (s) is suggested to be between $\frac{\lambda}{3}$ and $\frac{2\lambda}{3}$ ($\frac{\lambda}{3} < s < \frac{2\lambda}{3}$).

There is an optimum separation between the feeder and the vertex for each reflector. If the separation (s) is too small, the losses increase, because all the reflected contributions are canceled by being in counter-phase, so the loss becomes comparable to the loss due to the resistance of the system, resulting in a useless antenna. For a very large separation s, the system generates undesirable multiple lobes and loses its directional features. Experimentally, it has been demonstrated that increasing the lateral dimensions does not significantly affect the beam-width or directivity, but increases the bandwidth. For reflectors of finite dimensions, the main lobe is slightly wider than for those with infinite dimensions. To reduce back radiation, the height (h) is typically between 1.2 to 1.5 times the length of the feed elements [61].

Parabolic Reflector

The general radiation performance (antenna pattern, antenna efficiency, polarization discrimination, etc.) of a reflector can be improved by changing its surface structural configuration. Geometrical optics shows that when a beam of parallel rays is incident on the surface of a parabolic reflector, most of the energy will be concentrated at a point called the focal point. Similarly, if a point source is positioned at the focal point, the rays reflected by a parabolic reflector will exit as a parallel beam. This is called the reciprocity principle and is demonstrated through geometrical optics graphically in the figure 1.10(c). The symmetric point of the parabolic surface is known as the vertex. Rays emerging in a parallel forming are commonly referred to as collimated. The collimation is frequently used to describe the highly directional characteristics of an antenna even though the radiating rays are not exactly parallel. If the

TX/RX is located at the focal point of the parabola, this type of configuration is usually referred to as front-fed.

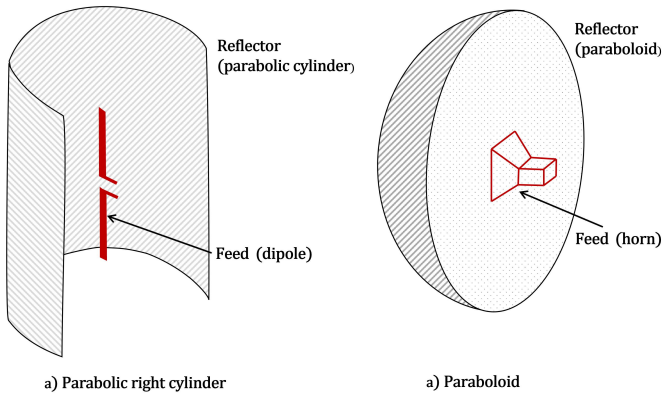

Figure 1.13: Parabolic right cylinder and paraboloid.

The drawback of the front-feed setup is that it requires the transmission line to reach the TX and RX equipment. This equipment is typically located behind or below the reflector. This may require the use of long transmission lines where losses cannot be tolerated in many applications, especially in low-noise receiving systems. In some applications, the Tx or RX equipment is positioned at the focal point to avoid the need for long transmission lines. However, in some of these applications, these may require large amplifiers and low noise receiving systems, where cooling and weatherproofing may be mandatory. The equipment may be too heavy and bulky, resulting in undesirable blocking. Another setup that eliminates the need to place the feeder (TX and/or RX) at the focal location is commonly known as Cassegrain feeder see figure 1.10(d).

Thanks to geometrical optics, a famous astronomer named Cassegrain proved that parallel incident rays can be focused to a point using two reflectors. This requires that the main reflector be a parabola and the secondary reflector a hyperbola. The feeder should be placed along the parabola's axis, usually at the vertex. This design was used by Cassegrain to create optical telescopes. Later, his design was used for RF systems. In this configuration, the rays leaving the feeder, incident on the subreflector, are reflected back to the primary reflector, as if originating from the focal point of the parabola. The primary reflector then reflects the rays and converts them into parallel rays. The interaction between the primary and secondary reflector is not perfect, so

it is necessary to analyze the diffractions produced at the edges of the reflectors and in the reflector structure, in order to determine the overall radiation pattern of the system, in order to avoid unwanted radiation that affects the proper antenna performance [62], [63]. The Cassegrain feed setup allows the TX or RX equipment to be placed behind the primary reflector device. This configuration facilitates maintenance and adjustment of the system.

A parabolic reflector can be of two basic geometrical shapes. One shape is that of the parabolic cylinder (figure 1.13(a)), whose energy is collimated in a line parallel to the axis of the cylinder which is its focal point. The most commonly used feed for this type of reflector is a linear dipole, a slotted waveguide or a linear array. The other type of reflector is shown in figure 1.13(b). Where the surface is formed by rotating the parabola around its axis, and is called a paraboloid or parabola of revolution. Typically, pyramidal or conical horn antennas are used as the TX or RX of this type of configuration.

There are many kinds of reflectors, the analysis of which has been widely documented in the literature [64]-[65]-[66]. The spherical reflector has been used for radio astronomy and ground station applications, because by being able to change the position of the feed, the received signal can be scanned more easily.

An example of this approach is the 305 m diameter spherical reflector in Arecibo, Puerto Rico [67], whose surface is built on the ground and the beam is scanned by feed motion. This radio telescope has recently ceased operation due to a structural problem where the feed has fallen off. But it has been replaced by another larger radio telescope called FAST located in China with a diameter of 500m [68]. In the case of spherical reflectors, the feeder will substantially block radiation, resulting in unacceptable minor lobe levels, in addition to imminent gain decrease and regular cross-polarization discrimination. In order to eliminate the inherent problems of symmetrical reflectors such as those mentioned above, offset parabolic reflector designs have been developed for single- and dual-reflector systems [65].

Due to the asymmetry of the reflector, evaluating the resulting radiation is more complex. However, with the increase in computing power, it has been possible to model and optimize these reflector designs for maximum performance. Such offset reflectors reduce aperture blockage and VSWR and they allow the use of larger f/d ratios while preserving the structural rigidity of the antenna, making it possible to design customized radiation patterns to take full advantage of this type of reflectors, thereby reducing the cross-polarized radiation generated by the feed. However, this kind of reflector doesn't have only advantages, because this type of displaced reflectors generate a cross-polarized radiation when illuminated by a linearly polarized power supply. Therefore, it is suggested to use circularly polarized feeders in order to eliminate depolar-

ization, but this causes cross-polarization of the main beam. In addition, the structural asymmetry of the system is often considered a major drawback if the reflector is very large.

Paraboloid reflectors, which are large-aperture ground-based antennas, are the most popular [66]. The 100 m diameter radio telescope of the Max Planck Institute for Radio Astronomy (West Germany) was the largest fully steerable reflector of the time [69]. The 64 m reflector at Goldstone (California) was built primarily for deep "space" applications [70]. Paraboloid reflectors can produce a pencil beam with high gain and low sidelobes when fed from the focal point. They also have good cross-polarization discrimination properties. This antenna is popular for low-noise applications such as radio astronomy and is considered to be a good compromise of cost and performance. A large reflector will require a substantial financial investment, as well as a complex structural undertaking. It must be able to withstand extreme weather conditions.

Cassegrains design with Dual reflector surface are used for applications that require pattern control, such as globe satellite ground system systems. This reflector design has an radiation efficiency of 65-80%. This design outperforms the classic front-fed reflector design by approximately 10%. Thanks to geometrical optics, Cassegrain reflectors are designed to achieve a uniform phase front at the main reflector aperture. This design can be used to achieve less overflow and uniform illumination of the main reflector by using good feed designs. Slight shaping of one or both surfaces of the dual reflector can create a uniform amplitude or phase aperture, with significant gain enhancement [14]. These reflectors are also known as shaped reflectors. Dual reflectors used in ground station applications have used shaping techniques. Radio astronomy and ground station applications have led to significant effort in the development of more efficient feeds that can illuminate the main reflector and subreflector. Wave horns, which can support hybrid mode fields (combination of TE/TM modes), can be used to realize more desirable feeds. By matching the feed to the reflector surface, cross polarization is reduced [61].

1.2.6 Reflectarray antenna

The reflectarray is a hybrid design, combining many favorable features of reflectors and printed arrays, and as such can provide advantages over the two conventional large-aperture antenna configurations (arrays and reflectors). Parabolic reflectors are often difficult to fabricate due to their curved surface, which demands costly custom molds; this difficulty increases when higher frequencies are used. While antenna arrays have the advantages of flexible design freedom, flexible radiation performance, and a simple-to-manage feed network, the cost of T/R modules [14] for phased active arrays can be very expensive

for many applications. The reflectarray is fast becoming a popular alternative to more advanced technologies because it can mitigate the drawbacks of two high-gain antennas. A reflector antenna is an antenna that has a flat reflective surface and hundreds of elements in its aperture. It also includes an illumination feed antenna, as shown in figure 1.10(e). The feed antenna spatially illuminates the aperture. The elements reflect the incident field with specific phase shifts to reflect it. This allows the antenna to collimate its beam in the desired direction with the best radiation pattern shape. The synThesis of this type of antenna is similar to that of reflector antennas in terms of spatial illumination by geometrical optics, and is also similar to that of antenna arrays in terms of phase synThesis and beam collimation.

The advantages of reflectors, such as their low profile, light weight and shaped geometry, make them desirable for diverse communication systems, particularly for mobile platforms. Its uses in space exploration, satellite balloon communications, remote sensing and radar systems are growing in the last decade, and will continue to widen in the future. Moreover, the current PCB manufacturing technology and low-cost commercial laminates enable rapid production of prototypes at a low cost. This enables large-scale production and marketing of commercially useful reflective antennas. Reflectarrays for optical and terahertz communications are also very promising. Advances in manufacturing technology, such as 3D printing and nanotechnology, enable the practical implementation of low-cost THz and reflective optical designs. Reflectarray's full potential has yet to be fully tapped. New ideas and designs are constantly being presented by researchers in this field, where they make use of new materials for multifunctional systems. Over the next decade, this field is expected to remain an active area of research, and there is no doubt that reflectors will be a key focus within the antenna community.

Reflectarray element analysis and design

Reflectarray antennas consist of an array of elements in a conformal or planar configuration that is excited by a feed antenna. Figure 1.14 shows a typical reflectarray antenna. Each element is designed so that it reflects a specific phase when illuminated by the antenna feed. The phase distribution across the aperture of the reflectarray is then synthesized to allow it to realize a collimated beam or shaped beam in the required directions.

Therefore, the analysis and design of the reflectarray elements, usually called phase elements, is of great importance. Two steps are required in designing a reflectarray: the element design and the system design. But this chapter only explains the basics of the design of the phase distribution in the reflector aperture, which is key to determine the phase of each element individually,

according to the design parameters. In other words, we will describe how the individual elements should be designed to scatter the electromagnetic waves with the required phases.

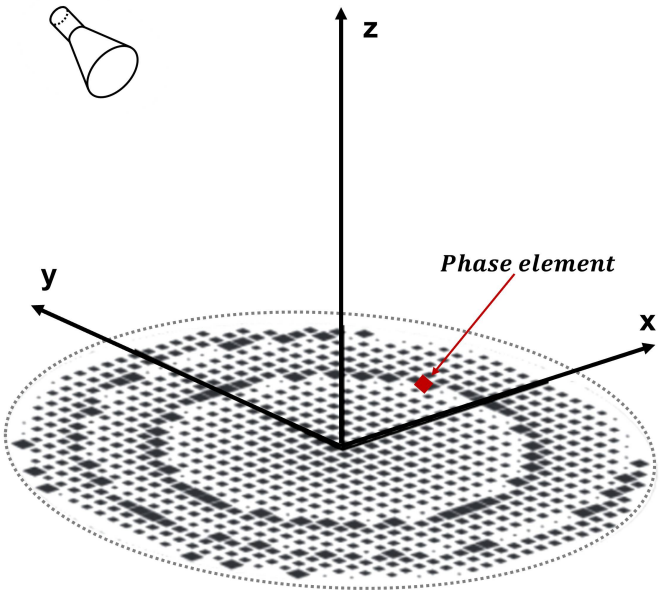

Figure 1.14: Show a typical geometry of a planar reflectarray antenna.

The classic planar antenna arrays will produce a collimated beam in broadside orientation if there is a uniform phase distribution at the aperture. This is normal to the array's plane. A progressive phase distribution is used to focus the beam in a specific direction [71], [72]. The basic operating principle for reflectarrays is the same, but one must also account for the position of the feed antenna [73]. Figure 1.15 shows that the feed antenna is at a specific position relative to the reflectarray coordinate systems. It is supposed that the elements of the reflecting network are typically in the far field of the feed antenna. Therefore, it is feasible to approximate the electromagnetic field incident on each element of the reflectarray by creating a plane wave that excites the element at a specific angle of incidence. Electromagnetic fields radiating from the feeder propagate as spherical waves that originate at the phase center of the antenna feeder. Electromagnetic fields incident on the reflectarray aperture are phased proportional to the path traveled, which is called spatial

phase delay. Therefore, to obtain a collimated beam, the phasing elements of the reflectarray have to compensate for this phase. figure 1.15 presents a geometrical model of the reflectarray system illustrating the position of the center of the feeding phase and the reflectarray coordinate system.

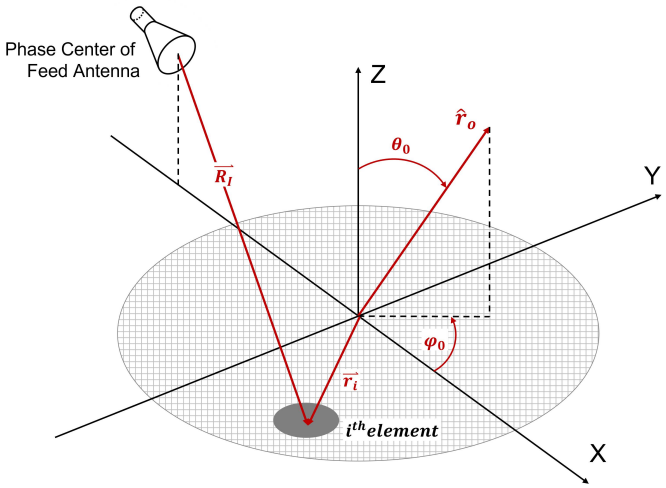

Figure 1.15: Show a typical geometrical parameters of a planar reflectarray antenna.

The spatial phase delay (spd), from the feed phase center to the element, must be compensated by the reflection phase of a reflectarray component. This is represented mathematically by 1.34.

$$\phi_{[spd]} = -k_o R_i \tag{1.34}$$

Where R_i is the distance from the feed phase center to the i^{th} element, and k_0 is the wavenumber at the center frequency. Such a phase convert the spherical wave radiated by the feed antenna, to a collimated beam in the broadside direction, that is, in the Z-direction with respect to figure 1.15. To scan this collimated beam in any direction, a progressive phase (pp) can be added to the aperture; its vector expression is given by (1.35).

$$\phi_{pp} = -k_o \vec{R_i} \hat{R_o} \tag{1.35}$$

Where $\vec{R_i}$ is the position vector of the i^{th} element, and $\hat{R_o}$ is the direction of the main beam as shown in figure 1.15. In the cartesian coordinate system

of previous figure, the position of each element can be described as (x_i, y_i), so for a beam directed in a certain spherical direction (θ_o, φ_0), this mathematical expression can be simplified to (1.36).

$$\phi_{pp} = -k_o(x_i sin\theta_o cos\varphi_0 + y_i sin\theta_o sin\varphi_0) \tag{1.36}$$

Therefore, the requested phase shift in the aperture of the reflective grid must compensate for the spatial delay (*spd*) and add the progressive phase to the aperture, which is given by 1.37.

$$\phi_{RA} = k_o(R_i - sin\theta_o(x_i cos\varphi_0 + y_i sin\varphi_0)) + \phi_0 \tag{1.37}$$

ϕ_0 is a phase constant that indicates the requirement for a relative phase in order to use reflectarray elements. Note that the necessary phase distribution given in (1.37) will create a pencil beam in the desired direction. However, for shaped beams, the progressive phase (1.36) should be replaced with an appropriate phase distribution. Furthermore, in any design, the phasing elements must compensate for the spatial phase delays related to the feed. The reflectarray antenna has a similar structure to a parabola reflector antenna. However, unlike the parabola it consists of a limited number of elements and is usually laid out in a Cartesian grid. Thus, the phase distribution in the reflectarray aperture is essentially subdivided in pixels, where each pixel modifies the phase individually over the incident radiation.

1.2.7 Radio Propagation Channel at mmWave for 5G

MmWave communications

Massive amounts of bandwidth are required to support 5G's high data transmission speeds and service ubiquity. Traditionally, wireless networks operate at bands below 6 GHz, which are very saturated. Traditionally, the radio access network (RAN) has not been using the unsaturated cmWave and mmWave bands, due to the higher propagation loss in these frequency bands and to their sensitivity to blocking effects. Therefore, these frequencies were not considered viable for medium and long distance communications, and so far they have been used only for short distance communications, essentially for indoor environments where there is high concentration of people with large bandwidth requirements, or in use cases for very specific applications such as telemedicine or industrial applications. The large amount of spectrum available at those bands has attracted the attention of scientists, with the challenge of mitigating the high propagation losses in the cm/mm wavebands, in order to increase bandwidth and decrease latency in radiocommunications.

As pointed out by the authors in [74], it is common knowledge that free space propagation losses increase in proportion to the square of frequency, but isotropic antennas with an effective aperture size of $(\lambda/2)$ equal to half the wavelength also follow this rule. The wavelength becomes shorter and the effective aperture area becomes less as the frequency increases. Furthermore, an antenna with a larger aperture will have a higher gain, since it can capture more energy.

Shorter wavelengths allow placing many independent antennas in the same effective aperture area. Several radiating elements make the antenna more directional, which means that the antenna can focus the energy in specific directions, forming lobes or beams dynamically. As a result, extra gain can be obtained from the antenna in the directions with maximum energy according to the propagation channel.

The combination of these two gains can compensate for free space propagation losses and additional losses from other physical phenomena that are not relevant at frequencies below 6 GHz, such as attenuation by human obstructions and furniture, in indoor scenarios. According to the studies performed in [75], it was experimentally demonstrated that losses due to human body obstruction can be very high, around 45 dB. This could make signal propagation unfeasible, because people will always be interacting with the mobile phone at close range.

According to [76], the authors consider high-gain directional antennas as an enabling technology for wireless communications in the mmWave spectrum.

To use this technology, it must be taken into account that the communication system must know where to focus the beam. This approach is not trivial and is one of the technical challenges that we will address in the work of this Thesis.

Radio Propagation Channel

The Radio Channel is the electromagnetic characterization of the environment through which radio waves propagate from a transmitter to a receiver. The radio channel analysis can be simple or complex, depending on the wave frequency and the complexity of the scenario, that creates multiple routes of wave propagation from TX to RX. This is known as the "multi-path radio channel". The figure 1.16 shows some of the major phenomena that affect mmWave radio propagation, including free space propagation losses, reflections, diffraction and scattering. The complexity of characterizing each of these phenomena is directly proportional to the frequency increase, because the objects on the scenario are electrically larger and therefore their influence will be greater.

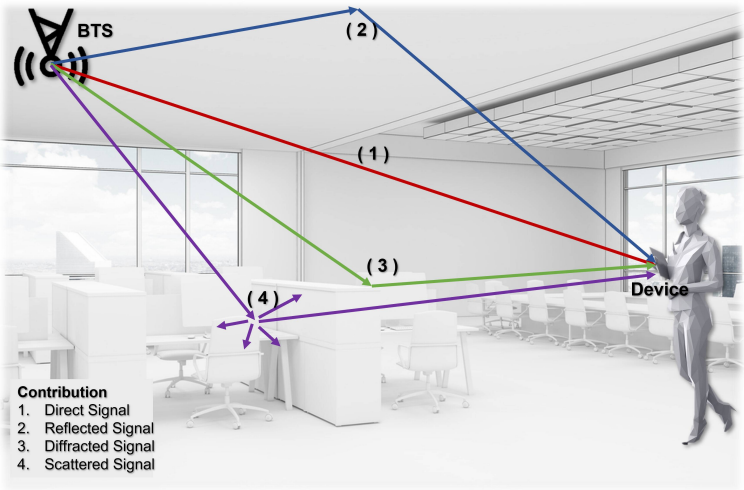

Figure 1.16: Multi-Path propagation contribution in indoor environments.

Each phenomenon induces alterations in the phase and power change of the radio waves that cause a variation of the channel in time, frequency and space. The frequency of the radio waves will determine the effects of each phenomenon. One of the major differences between frequencies below 6 GHz and mmWave is, for example, the sensitivity to signal blocking, which is significantly higher compared to sub-6 GHz bands.

Radio Propagation phenomena

Reflection is a physical phenomenon that happens when an electromagnetic wave is incident on an object that is larger than the wavelength [22]. The 5G networks working above 6 GHz in the mmWave range will cause radio waves to reflect over all objects due to their short wavelength. Multiple characteristics such as wave frequency, electrical and geometrical characteristics and angle of incidence are important in determining reflection behavior. Studies of reflections in the mmWave bands have shown interesting results. For example, in [77] an analysis of reflection and absorption is done for different materials that are commonly used in indoor and outdoor scenarios. Brick materials were more susceptible to penetration than other materials, with an average loss of 28.3 dB due to their porosity. Tinted glass showed no evidence of penetration. Other materials, such as clear glass, concrete, had penetration losses of 6.65 dB or 3.58 dB, respectively. Reflection is more important in materials with lower penetration attenuation, because most of the incident power on the material is reflected such as in the case of metallic materials. Tinted glasses have a higher reflection coefficient than drywall and transparent glass, but they are still highly reflective materials. [77] shows that indoor-to-outdoor penetration losses are high. However, indoor-to-indoor and outdoor-to-outdoor propagation are more feasible due to the strong reflectivity of outside building materials (except brick) and low attenuation of indoor materials.

Reflection studies extended to the 38 GHz band [76], concluded that in UMa or UMi scenarios, the power levels due to specular reflections are enough for propagation loss predictions. However, reflections can change considerably from one scenario to another depending on the complexity of the scenarios and the number of obstacles with reflective and/or absorbing materials. For the case of indoor environments, where wood is a predominant material in the manufacture of furniture, and according to [78], wood is a material with considerable penetration losses of 3.11 dB, due to their porosity and the denser it is the less losses it will have.

It is important to give a brief mathematical background of the specular reflection. A simple method for estimating the electric field of reflected rays is to solve Maxwell's equations and the boundary conditions. The electromagnetic characteristics of the materials where the ray is reflected are also to be considered, and the answer to this problem can be obtained from the Fresnel coefficients. The final electric field is split into three components: an incident beam part, a reflected beam part and a transmitted part through the material.

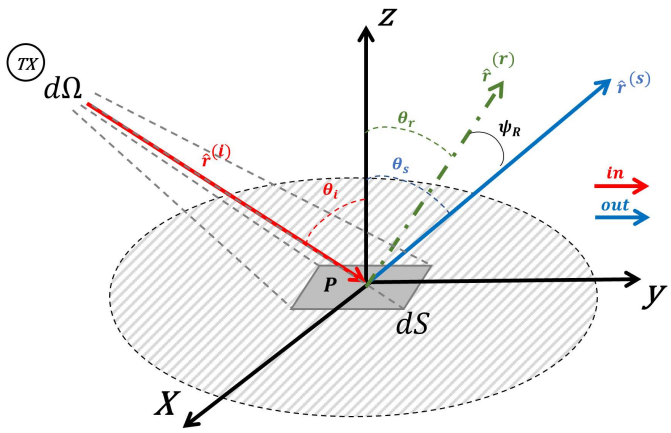

Figure 1.17: Generic geometric model of specular reflection and diffuse scattering.

The electric field of the reflected beam is given by 1.38

$$E = r_x \frac{e^{-\frac{j2\pi fd}{c}}}{d}, \tag{1.38}$$

where r_x would be r_h for the horizontal polarization and r_v for the vertical polarization, and d is the path distance for the reflected beam (from the TX to the reflection point).

$$r_h = \frac{\sin\psi - \sqrt{\varepsilon^* - cos^2\psi}}{\sin\psi + \sqrt{\varepsilon^* - cos^2\psi}} \tag{1.39}$$

and

$$r_v = \frac{\varepsilon^* \sin\psi - \sqrt{\varepsilon^* - cos^2\psi}}{\varepsilon^* \sin\psi + \sqrt{\varepsilon^* - cos^2\psi}} \tag{1.40}$$

Diffuse Scattering refers to a particular type of reflection, which occurs when a radio wave impacts irregular objects that are smaller than its wavelength. Although scattered rays usually have lower energy than the specularly reflected signal, they can contribute considerably to the total received power [79]. Diffuse scattering has been extensively studied for frequencies below 6

GHz. Therefore, for communications in small environments or with few obstacles, diffuse scattering elements are less dominant than specular ones [80].

However, bands above 6 GHz are more affected by diffuse scattering [81]. Usually, the Effective Roughness (ER) and Beckmann-Kirchhoff models are used to calculate diffuse scattering. ER introduces the Directive Model and the Lambertian Model as dispersion patterns. The Lambertian model gives the maximum power perpendicular to the reflection surface regardless of the direction of the incident waves [82]. This model introduces a coefficient S, referring to the amount of energy of the scattering component corresponding to the incident wave.

The Directional Model is analogous to the Beckmann-Kirchhoff Model in the sense that the maximum scattering lobe of the Directional Model is directed towards the direction of specular reflection. In [83], a study was done to estimate diffuse scattering characteristics at 60 GHz. A directive scattering loss parameter S was calibrated in this study for indoor scenarios, and small-scale parameters including diffuse scattering components were also calculated. The obtained results reveal a mean S of 0.5, a root mean square error (RMSE) of the delay estimate of 8.2%, and azimuth and elevation errors of 2.6° and 0.6°, respectively. Recent research on mmWave band frequencies has shown that diffuse scattering elements have a significant impact on NLOS communications [84].

It is also essential to provide a brief mathematical background for the diffuse scattering. The point P is where diffuse scattering happens (see figure 1.17), has attached a coefficient of dispersion S and a reflection coefficient Γ. In [85], two approximations of S are defined; a first one in which all the incident power is dispersed and radiated in all directions, and the second one where the scattering components are extended in all directions, but only consider the reflected energy. The first one, S is defined by 1.41.

$$S = \left.\frac{|\bar{E}_S|}{|\bar{E}_i|}\right|_{dS}, \tag{1.41}$$

where E_s is the electric field of diffuse scattering, E_i is the specular electric field. In [86] it is described the power balance of diffuse scattering, reflection, and transmission in P, and is defined by:

$$1 = \Gamma^2 R^2 + S^2 + \frac{P_p}{P_i}, \tag{1.42}$$

$$R \cong \sqrt{1 - \frac{S^2}{\Gamma^2}}. \tag{1.43}$$

Where R is the reflection loss factor, $0 < R < 1$, Γ and S are the reflection and scattering coefficient, respectively, P_p is the power that penetrates material and P_i is the incident power.

In the second approximation, S is defined by equation (1.44) and the power balance by equation (1.45).

$$S = \left.\frac{|\bar{E}_S|}{|\bar{E}_r|}\right|_{dS} \tag{1.44}$$

$$1 = \Gamma^2(R^2 + S^2) + \frac{P_p}{P_i} \tag{1.45}$$

With these two approximations, a function U is defined as follows:

$$U = \begin{cases} 1 & \text{if } S = |\bar{E}_S/\bar{E}_i| \\ \Gamma & \text{if } S = |\bar{E}_S/\bar{E}_R|. \end{cases} \tag{1.46}$$

Therefore, according to the approach to the coefficient of dispersion S, two diffuse scattering models are derived: the Lambertian model and the Directive model, as shown in figure 1.18.

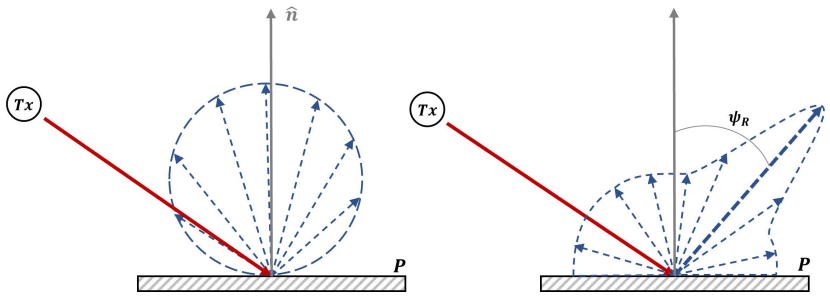

Figure 1.18: The Lambertian model and the Directive model.

Lambertian Model: In this model the energy is scattered in all directions centered in the normal to the point P and diffuse electric field is defined by:

$$|\bar{E}_S|^2 = \left(\frac{K_0 \cdot S}{r_i \cdot r_s}\right)^2 \cdot U^2 \cdot \frac{cos(\theta_i) \cdot cos(\theta_s)}{\pi} dS, \tag{1.47}$$

where r_i is the distance between the T_x and the point P, r_s is the distance between R_x and the point P. θ_i and θ_s are the incident and departure angles, and K_0,

$$K_0 = \sqrt{60 G_{TX}(\beta) P_{t_{ray}}}), \tag{1.48}$$

where $G_{RX}(\beta)$ is the antenna gain in β direction, and $P_{t_{ray}}$ is the ray power in W.

Directive Model: The directive model uses energy to scatter in directions around reflection angles. There are two versions: directive and directive with back scatter. The module for the electric field in directive model is provided by:

$$|\bar{E}_S|^2 = E_{S0}^2 \cdot \left(\frac{1 + cos\psi_R}{2} \right)^{\alpha_R}, \tag{1.49}$$

where ψ_R is the angle between the scattering and specular rays, the exponent α_R is related to the width of the scattering lobe. When the exponent (α_R) is higher, the lobe will become wider. E_{S0}^2 is defined by:

$$E_{S0}^2 = \left(\frac{SK_0}{r_i r_s} \right)^2 U^2 \frac{dScos(\theta_i)}{F_{\alpha_R}}, \tag{1.50}$$

where F_{α_R} is,

$$F_{\alpha_R} = \frac{1}{2^{\alpha_R}} \cdot \sum_{j=0}^{\alpha_R} \binom{\alpha_R}{j} \cdot I_j \tag{1.51}$$

and I_j is

$$I_j = \frac{2\pi}{j+1} \cdot \left[\cos\theta_i \sum_{w=0}^{\frac{j-1}{2}} \binom{2w}{w} \cdot \frac{\sin^{2w}\theta_i}{2^{2w}} \right]^{\frac{1-(-1)^j}{2}}. \tag{1.52}$$

Diffraction is based on Huygens' Law, which states that any point on an original wavefront can be treated as a source of secondary waves that propagate in all directions with exactly the same frequency and wavelength as the one from which they originate [87]. In general, the signal strength of diffracted rays will be lower than that of the reflected signals [88].

To understand the phenomenon of diffraction, a brief mathematical description is essential. This physical phenomenon is created by the incidence

of rays which impact the corners or edges. Both indoor and outdoor environments can be studied with the Geometrical Optics (GO) and Uniform Theory of Diffraction (UTD) algorithms.. The geometric connection between incident and diffracted rays is the basis of the algorithm of GO. The elevation view in figure 1.19.a, shows the incident ray reaching the diffracting edge with an angle. The diffracted moments are formed in the form Keller's cone in all directions [89].

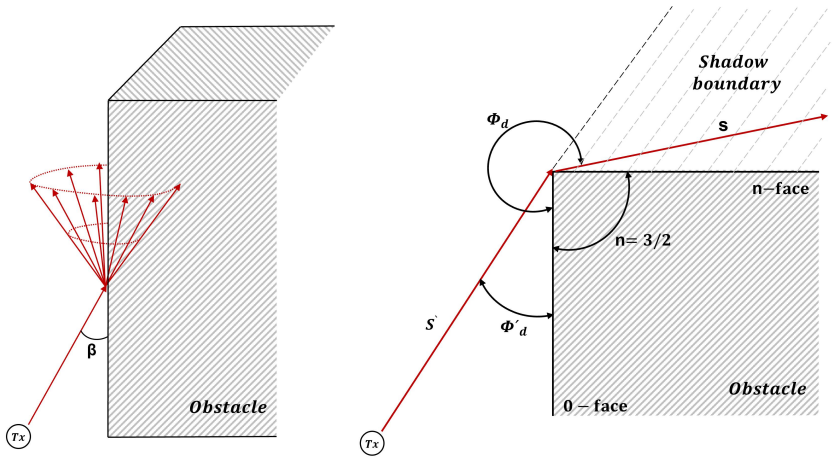

Figure 1.19: Elevation-Top view - Diffraction.

In the top view, figure 1.19.b, the geometric characteristics of diffraction are described with the angles ϕ'_d and ϕ_d for the outgoing beam, both with respect to face 0. These geometrical characteristics should be known to calculate the diffraction coefficient, D. If both the TX and RX points are known, the height of the intersection point can be calculated as:

$$h = \frac{h_T d_R + h_R d_T}{d_R + d_T}, \tag{1.53}$$

Where h_T and h_R are the TX and RX heights respectively, d_T is the distance between the diffraction point and the TX and d_R is the distance between the diffraction point and the RX.

The diffraction coefficient is calculated as:

$$D = \frac{-e^{-j\frac{\pi}{4}}}{2n\sqrt{2\pi k}\sin\beta} D_1 + D_2 + R_0 D_3 + R_n D_4, \tag{1.54}$$

where k is a wave constant. R_0 and R_n are the reflection coefficients on face 0 and face n respectively. The factor n is calculated by knowing the angle α of the edge $n = 2 - \frac{\alpha}{\pi}$.

The components of diffraction are defined as:

$$D_i = cot\left[\frac{\pi + (\phi_d - \phi'_d)}{2n}\right] F(kLa^{\pm}), \tag{1.55}$$

where $F(x)$ is the Fresnel transition function:

$$F(x) = 2j\sqrt{x}e^{jx}\int_{\sqrt{x}}^{\infty} e^{-j\tau^2}d\tau. \tag{1.56}$$

It is possible to simplify $F(x)$ with high values of x, with the following approximation:

$$F(x) \simeq 1 + j\frac{1}{2x} - \frac{3}{4}\frac{1}{x^2} - j\frac{15}{8}\frac{1}{x^3} + \frac{75}{16}\frac{1}{x^4}, \tag{1.57}$$

and for small values of x

$$F(x) \simeq \left[\sqrt{\pi x} - 2xe^{\frac{-j\pi}{4}} - \frac{2}{3}x^2 e^{\frac{-j\pi}{4}}\right] e^{j(\frac{-j\pi}{4}+x)}, \tag{1.58}$$

where the distance L is given by:

$$L = s \cdot sin^2(\beta), \tag{1.59}$$

and s is the distance between the RX and the diffraction point. The function $a^{\pm}$ is defined as:

$$a^{\pm}(\phi_d - \phi'_d) = 2cos^2\left[\frac{2n\pi N^{\pm} - (\phi_d - \phi'_d)}{2}\right], \tag{1.60}$$

where N^+ and N^- are closest integers that can satisfy the equations:

$$2n\pi N^{+/-} - (\phi_d - \phi'_d) = \pi \tag{1.61}$$

where a^+, N^+ are related with face n and a^-, N^- with the face 0. Finally, the diffracted electric field it is given by 1.62:

$$E_d = E_0 D A e^{jks}. \tag{1.62}$$

1.2.8 Propagation Models

The propagation channel models are essential for predicting interference, mapping frequency and defining cell parameters in mobile communication systems. In fact, radio channel knowledge allows proper planning of wireless networks [3]. Therefore, the implementation of new networks in the mmWave band must face new technical challenges due to the increase in frequency [5], so it is essential to have new reliable channel models, which allow to adequately characterize the radio channel in different scenarios [90], especially in indoor environments, where it is more feasible to implement this new technology.

Channel models can be divided into two groups: deterministic models and stochastic models. Deterministic models take into account the geometry and architectural structure of the propagation environment. Their objective is to reproduce all the electromagnetic and geometric components associated with a specific scenario, such as walls, ceiling, furniture and also dynamic environment, like humans. These deterministic models can be pure deterministic, such as the general ray-tracing model, or semi-deterministic, such as the map-based channel modeling of Mobile and wireless communication Enablers to Twenty-twenty Information Society (METIS) [25].

On the other hand, the stochastic models evaluate the propagation channel behavior from a statistical point of view according to the scenario features. Propagation models of this type are divided into two groups: the models based on the geometry of the environment and the pure probabilistic models, where geometrical characteristics where the radio signal propagates are unknown. The following describes the channel modeling process specific to each type of model and examples of models created by different institutions.

Stochastic Models

In the case of Stochastic Models, simple path loss models are basically probability functions that depend on the logarithm of the distance between the transmitter and the receiver, in addition to some constants. Depending on the channel model approach, the probability functions will be different for line-of-sight (LOS) and non-line-of-sight (NLOS) scenarios. In this model, depending on the type of scenario, for a fixed transmitter and receiver position, it can be determined whether the propagation channel is line-of-sight or not, according to probability functions. This applies mainly to model propagation in outdoor environments where the complexity of the scenario is usually less than in indoor scenarios [91]. Although this modeling approach may seem a bit simplistic, one of its great advantages is that it is computationally efficient. Although some of its disadvantages are its inaccuracy in propagation loss estimation, especially in indoor environments, in simple outdoor environments its results may be ac-

ceptable as a first approximation. In simple terms, stochastic models allow us to evaluate the chances of occurrence of events such as propagation losses, NLOS/LOS scenario type, delay spread, etc., which cannot be accurately predicted with so little information from the environment. The 3GPP model [92], mmMagic model [93] and WINNER+ model [94] are some examples of widely accepted stochastic models.

- **3GPP:** This model is also known as a geometric stochastic one. It separates large-scale parameters such as shadow fading, delay spreading and angular spread, from small-scale parameters such as delays, group powers and angles of departure and arrival. These two sets of parameters are tabulated in random probabilistic distributions. The large-scale parameters are the geometric positions TX and RX. They are used to model statistics for the small-scale parameters. The PDP and the angular profile (AP) are used to define channel behavior. This model was proposed in the 3GPP TR 138.901 technical report and it can operate in a wide frequency range from 6 to 100 GHz. This model can evaluate a variety of urban and rural environments. This model has been adapted to operate in 3D environments to take advantage of its capabilities to simulate Massive MIMO environments [95].

- **mmMagic:** The Millimetre-Wave Based Mobile Radio Access Network for Fifth Generation Integrated Communications (mmMagic) project proposes a stochastic propagation model that builds on the 3GPP model. Their objective is to improve the probability functions proposed by 3GPP with an intensive measurement campaign. It considers the same frequency ranges and the same use cases as 3GPP.

- **WINNER+:** One of the major limitations of the early geometry-based stochastic channel models is their inability to be used for 2D coordinates. Although this works for simple MIMO schemes, with this limitation is not possible to study the large-planar (full-dimensional) effects for 3D beam-forming approaches. For this purpose, a large number of additional measurements were required to obtain the necessary parameters for the model. After all, the new model required 18 additional parameters (50 in total, compared to 32 for the WINNER-II model [96]).

Deterministic Models

Deterministic models are based on a detailed description of the geometrical and electrical characteristics of the propagation environment. In addition to the parameters of the communication link such as operating frequency, bandwidth,

modulation, etc., deterministic models consider the characteristics of the antenna radiation pattern at the TX and RX. Therefore, deterministic models are geometrically complex, computationally slow and more difficult to implement, although they are the most accurate. For example, ray-tracing techniques are purely deterministic channel propagation models, in which it is essential to possess information about the geometrical structure of the room to be analyzed, such as the relative positions of walls, floors, doors, ceilings, structural columns, etc. In addition, the relative positions and dimensions of furniture and people, the electromagnetic properties of each of these scenario elements must be provided. It is an accurate model with detailed angular data and can be used for extensive estimation of channel variables for both small- and large-scale fading [97]. Because making use of this type of purely deterministic models is usually quite complex, and they are usually custom-designed for companies or universities for commercial or research purposes. The following deterministic propagation models were proposed to simplify the implementation for 5G systems in the mmWave band.

- **IEEE802.11ad:** This semi-deterministic model works for short-range communications at 60 GHz. To model the propagation loss, the specular component is estimated by ray-tracing algorithms. The components due to diffuse scattering, diffraction and transmission are stochastically combined.

- **MiWEBA:** The mmWave evolution for backhaul and access (MiWEBA) [98], is an extension of the IEEE802.11ad channel model. It is oriented to outdoor access, backhaul and D2D communications scenarios. The model uses both stochastic and deterministic models to simulate the specular parts. The models are useful in system-level simulations as well as in access network capacity analysis. This model assumes random arrival clusters with a Poisson distribution. The time intervals are exponentially distributed, while the random amplitudes obey Rayleigh distributions.

- **COST2100:** This model uses a cluster-level approach. Clusters interact with each other in a simulated setting. A visibility region is defined as an area that represents the spatial, temporal, and overall extent of multipath components presented at a common antenna. Spatial consistency is achieved using the visibility regions associated to each cluster of multipath elements. A cluster can be associated with one or more regions whose size changes with mobile terminal movement, allowing for spatial consistency within a simulated environment. However, this model does not take into account mobility at both ends of a link, so it cannot be applied for D2D.

- **METIS:** This model is semi-deterministic and map-based, developed upon measurement campaigns for the 6 GHz - 70 GHz bands [99]. The model uses ray-tracing techniques to determine the large-scale features of a given environment. It also uses measurements to calculate small-scale fading statistics. The 3GPP model and the Worldwide Initiative for New Wireless Radios (WINNER) are used to generate the small-scale statistics [97].

- **QuaDRiGa:** The QUAsi Deterministic RadIo channel GenerAtor (QuaDRiGa) channel model [100] is a significant extension of WINNER II/WINNER+, 3GPP-3D and 3GPP-3D models. It also includes some new features such as time evolution and scenario transitions. QuaDRIGa is capable of supporting any carrier frequency between 0.45 GHz and 100 GHz. The QuaDRIGa uses a geometry-based stochastic Channel modeling approach. QuaDRIGa modeling process is divided into two parts. The stochastic part generates and updates the large scale parameters (LSPs), while the geometry-based part calculates and updates the Short Scale Parameters (SSPs) based on the geometrical relationships between the receiver and transmitter. The channel parameters are subject to the statistical distributions that were determined from real-world channel measurements. For a given propagation scenario, the channel parameters are updated at every user location by a drifting process.

- **NYUSIM:** the model is capable of operating in a range of carrier frequencies from 0.5 to 100 GHz. This is based upon measurements at 28 to 140 GHz. NYUSIM is capable of supporting urban macrocell, rural macrocell, and urban microcell environments. New features include spatial consistency in the NYUSIM 2.01 version. It is now possible to generate the continuous time-variant channel coefficients, which allows for the reproduction of realistic scattering environments. The time cluster-spatial loop (TCSL) is used to determine the channel's temporal and spatial properties. Multipath components (MPC) which may be close in time, but have different directions of arrival, form a time cluster. The main directions of departure (or arrival) are represented by a Spatial Lobe (SL). A geometry-based reflection surface method, is also first adapted to update spatially and time-varying angular information along a user's trajectory.

1.3 Problem and Thesis Scope

The key to an optimal development of the Fifth Generation (5G) radio technologies and its evolution towards 6G, is to evaluate and solve the future problems related to its implementation in the mmWave band. Therefore, it is foreseen that one of the major problems for the implementation of this technology will be to deal with the excessive signal propagation losses due to the intrinsic behavior of the radio wave in such high frequency bands. For this reason, it will be essential to characterize signal propagation in complex and dynamic indoor environments, and to propose strategies to mitigate propagation losses proactively. In consideration of the problems presented, the following hypotheses are considered:

- **HypoThesis 1:** In indoor scenarios people cause a distortion in the radio propagation channel in the mmWave band.
- **HypoThesis 2:** Mathematical models evaluate the scattering effects of the human body in the mmWave band and adequately estimate propagation losses in non-line-of-sight (NLOS) areas.
- **HypoThesis 3:** The scattering effects of the human body can be modeled with a simplified morphology model to increase computational performance without losing scattering information.
- **HypoThesis 4:** Evaluating propagation losses in complex 3D environments, considering the scattering effects of the human body, improves the channel estimation in the mmWave band.
- **HypoThesis 5:** There are low-cost passive strategies that optimize signal propagation in the mmWave band and mitigate losses due to the scattering effects of the human body, so passive reflectors could be used to mitigate these effects in complex environments.
- **HypoThesis 6:** In short-range scenarios, stereographic video information can be used to deterministically estimate the radio channel in the mmWave band with ray tracing techniques.
- **HypoThesis 7:** The evolution of the propagation channel can be anticipated according to the prediction of the relative positions of moving objects, mainly humans, in indoor scenarios.
- **HypoThesis 8:** Open source video game engines allow to emulate and visualize the signal propagation in a 3D environment in real time.

1.4 Thesis Objectives

This Thesis focuses on the study of strategies to mitigate wireless propagation losses for 5G systems, taking into account the human body scattering effects in complex dynamic indoor environments. In addition, the Thesis aims to develop an interactive graphical tool where the propagation channel can be evaluated in a fast and predictive way, to reduce the uncertainty in the Radio Access Network (RAN) design at mmWaves.

The Thesis objective can be subdivided into the following sub-objectives:

- To investigate the propagation phenomenon of radio waves when they collide with the human body, in order to evaluate the scattering effects in the mmWave band.
- To propose a mathematical method to model the electromagnetic wave scattering phenomena when it impacts on the human body.
- To evaluate the performance of the proposed simplified geometric model of the human body, which is equivalent to its complex morphology in order to estimate its scattering effect.
- Design and validate the use of broadband modular passive reflectors to minimize propagation losses and maximize coverage.
- To explore the feasibility of using video game platforms to emulate mmWave band wave propagation in complex environments, considering the scattering effects of the human body with the proposed mathematical and geometrical model using with proprietary ray tracing techniques.
- Validate the use of stereoscopic cameras to analyze the environment in real time to determine the positions of all obstacles in the room, in order to evaluate the distortion of the radio channel in the mmWave band.
- Design and implement a ray tracing system on a video game platform that evaluates the radio channel in complex and dynamic scenarios, in order to propose antenna array orientations for RANs to improve coverage and minimize propagation losses.

1.5 Thesis Outline

This Thesis is organized in seven chapters and an appendix as described below:

Chapter 2 describes the proposed mathematical model used to characterize the scattering effects of the human body and its limits of applicability.

Chapter 3 describes the implementation of the double knife edge mathematical model in Unity, where the proposed mathematical and geometric simplifications are used for its efficient evaluation.

Chapter 4 describes the design and evaluation strategies of a diffuse reflector to optimize coverage in complex indoor areas.

Chapter 5 describes the methodology used to design the hexagonal passive modular reflector, explaining in detail the calibration process with simulation tools and the measurements performed.

Chapter 6 describes the design, implementation and validation of a predictive steering system based on video and depth information from stereographic cameras in complex and dynamic real-time environments.

Chapter 7 presents the conclusions of the Thesis and describes future lines of research.

Appendix A presents the description of the software used to carry out the research and implementation of the Thesis simulator.

1.6 Thesis Publications

The work developed during this Thesis made possible the following publications.

Conferences

[C1] **Romero-Peña, J. Samuel**, Cardona, Narcis, "Irregular MultiFocal Reflector for Efficient mmWave Propagation in Indoor Enviroments," *European Conference on Antennas and Propagation 2020 (EuCAP 2020)*, Mar. 2020, pp. 1-5.

[C2] **Romero-Peña, J. Samuel**, Cardona, Narcis, "Applicability Limits of Simplified Human Blockage Models at 5G mm-Wave Frequencies," *European Conference on Antennas and Propagation 2020 (EuCAP 2019)*, Mar. 2019, pp. 1-5.

[C3] **Romero-Peña, J. Samuel**, Cardona, Narcis, "Diffuse Modular Honeycomb Passive Reflector for Efficient mmWave Propagation in Indoor Environments," *2022 Joint European Conference on Networks and Communications - 6G Summit (EuCNC/6G Summit)*, Jun. 2022, pp. 1-5.

Patents

[P1] **Romero-Peña, J. Samuel**, Cardona, Narcis, "Reflector para ondas milimetricas" *Patent Number: ES202130068,PCT/ES2021/070909*, Jan. 2021

[P2] **Romero-Peña, J. Samuel**, Cardona, Narcis, "Procedimiento para analisis de la cobertura en espacios interiores para redes inalambricas" *Patent Number: P202130290, (In process)*, Feb. 2021

COST Technical documents

[TD1] **Romero-Peña, J. Samuel**, Cardona, Narcis, "Human Blockage Models at 5G mm-Wave Frequencies for indoor scenarios," *9th MC and Technical Meeting, European IRACON COST IC15104 action, Dublin - Ireland*, Jan. 2019

Research projects

[RP1] **WaveComBE**, Wave Communications in Built Enviroments

- Funding institution: Marie Skłodowska-Curie grant agreement No. 766231
- Start date: 01/07/2018
- Duration: 36 Months

Chapter 2

Mathematical model analysis to evaluate the RF scattering effects of blocking obstacles

This chapter presents the implementation of a proposed mathematical model to evaluate the scattering effects of the human body in the mmWave band. This analysis consists of evaluating the simplified mathematical model of Double Knife-Edge to evaluate the scattering effects of the human body in mmWave, and from the applicability of this it will be possible to model objects whose materials are totally absorbing or reflective in mmWave, independent of their geometrical morphology. As a result of this study, guidelines for the use of the mathematical model were established, not only to characterize the human body, but also for all types of obstacles in both indoor and outdoor environments.

To this aim, this chapter has been divided into the following sections:

- Section 2.1 presents a brief introduction.
- Section 2.2 presents the mathematical formulation of the Double Knife-Edge model to evaluate the scattering of absorbing objects.
- Section 2.3 presents validation strategies with measurements and simulation of the Double Knife-Edge model to evaluate the scattering effects of the human body

- Section 2.4 presents an analysis of the applicability limits for using the Double Knife-Edge model to characterize the scattering effects of the human body in mmWaves in a reliable way.
- Section 2.5 presents the conclusions of this chapter.

2.1 Introduction

The increasingly widespread use of the mobile technologies has created a progressive demand for higher bandwidths in the last few years, well above those used for the 4G standards or in the early 5G implementation.

Consequently, it was proposed to use the mmWave band (above 30 GHz) for mobile communications, mainly for indoor environments [76] [101].

The use of mmWave band in mobile terminals brings many technical challenges [102], especially on the characterization of the radio channel in indoor environments. Such scenarios are quite complex due to the large number of static and dynamic obstacles, like constantly moving people, which are electrically large and can produce significant alterations in the short-term and long-term fading radio channels [35].

Through the literature, several models with different mathematical formulations have been proposed to characterize the fading generated by the human body in mmWave bands, the most used of which are: Uniform Theory of diffraction - "UTD" [36], Geometrical Theory of diffraction - "GTD" [103], Method of Moments - "MoM" [49], numerical integration [50], measurement-based model [51] and mmMagic project model [53].

Despite using many different mathematical approaches, the concealment caused by the human body is modeled similarly for all the models publised in literature [104]. Because the whole human body has been modeled only with a simple geometric shape such as a cylinder or cube, models use to omit considering the head, arms and legs in its analysis.

Therefore, according to the analysis performed in [104], the simplest and most flexible mathematical model that characterizes the concealment of the human body is the Double Knife-Edge model "DKED". But because the DKE model is the simplest mathematical model, it is also the one with the most restrictions [30] at mmWaves. Nevertheless, the knife-edge model has been extensively used in the literature to characterize the dispersion of large-scale communication links [105].

Part of the objectives of this chapter are to quantify the DKED model restrictions, since in the literature [104], [30], [106] no specific limits have been defined, only very restrictive open limits, making it very uncertain under which circumstances it is valid to use this model.

Other objectives of this chapter are to analyze the viability of simplifying the morphology of the human body with basic geometric shapes, while considering all the relevant parts of the body. The aim is to easily implement this DKE model and reduce the computational load when it is applied to a large dynamic and complex environment.

The simplification morphology proposed is very useful in complex environments because the position of each person changes constantly and therefore the behaviour of the radio channel changes accordingly [52].

Another key contribution of this chapter was the study of the polarization effects of scattering on of the human body. This study is important because it has never been considered with mathematical model proposed in the literature [51] and especially with the DKE model.

2.2 Double Knife-Edge (DKE) Model to estimate Human Body scattering effects

The double knife-edge DKED model has been used to estimate the scattering propagation on the human body, since it is the simplest way to model the shadowing of such a complex morphology. As a result of this simplification, it has also been concluded throughout the literature [103] that the human body at millimeter-wave frequencies behaves as a fully absorbing material, according to the electromagnetic characteristics of human tissues in this frequency range.

In this section, only the basic behavior of the double-edge model has been analyzed, so the human body will be simplified as an absorbing screen of infinitesimal thickness (H_P). As depicted in figure 2.1 the equivalent width of the human body is given by (W_P) and its height by (L_P), and points Ⓐ and Ⓑ are the reference positions of the edges of the equivalent absorbing screen that will depend on the relative positions of the transmitter (T_x) and receiver (R_x). These two reference positions indicate the limits of the dimensions of the human body equivalent. These limits determine the relative concealment (visibility) between the transmitter (T_x) and receiver (R_x).

In summary, this mathematical model makes two key simplifications: the first is about the morphology of the obstacle, where it comes to be a two-dimensional obstacle, and the second is that the material of the obstacle must be completely absorbing at the operating frequency.

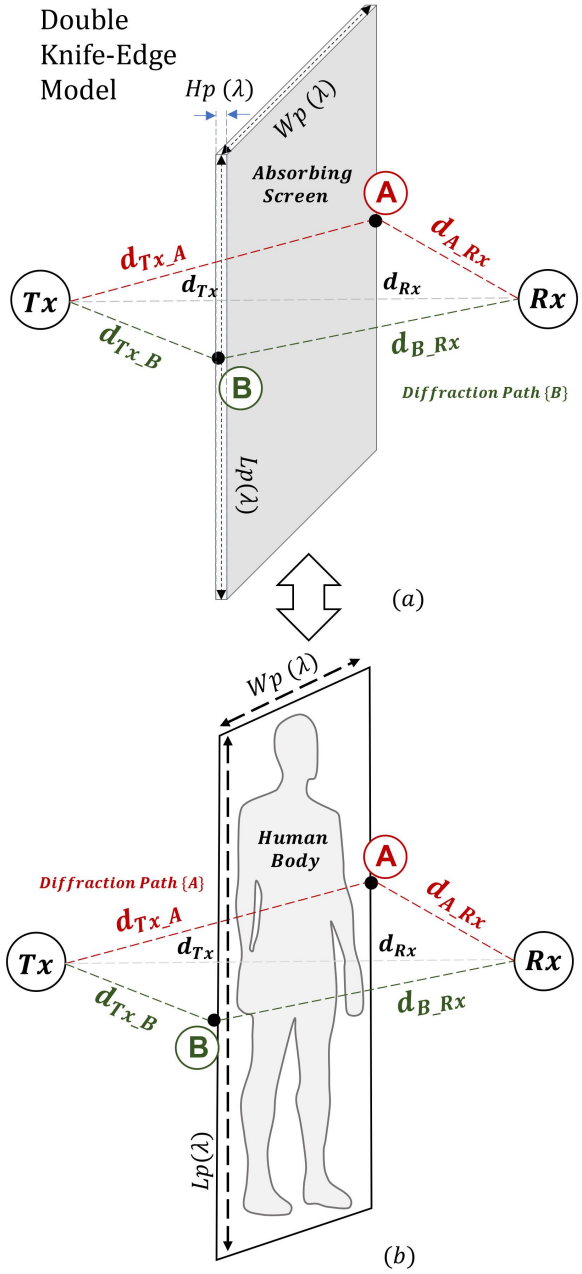

Figure 2.1: (a) Double Knife-Edge Model, (b) Human Body simplification to use the DKE.

The DKE model [30] considers only two contributions ($d_{T_x \to A/B}$ and $d_{A/B \to R_x}$) in two opposite points of the intersection plane between the screen "*Obstacle*" and the TX-RX path, as illustrated in figure 2.1. When the model refers to a "contribution" , it means that it is the route from the transmitter (T_x) to the edge (Ⓐ or Ⓑ) of the obstacle and from the edge (Ⓐ or Ⓑ) of the obstacle to the receiver (R_x), where each path has a phase component according to the path traveled.

According to [30] the DKE is only valid to model the concealment effect of any type of obstacle if the following restrictions are met:

- The electrical distance between the obstacle and the antennas (TX/RX) must be larger than the wavelength ($d_{TX}/d_{RX} >> \lambda$).
- The electrical dimensions of the obstacle must be much greater than the wavelength ($W_P/L_P >> \lambda$).
- The thickness of the obstacle must be much lower than the wavelength ($H_P << \lambda$).
- This DKE model is only valid to characterize the diffraction of symmetrical screens. It does not consider any other geometric shape.
- This DKE model does not consider the effects of polarization in its mathematical formulation, as the obstacle is assumed to be an absorbing screen.

Therefore, one of the main contributions of this chapter is to find out under which electrical circumstances "*quantified restrictions*", this model is valid to fully characterize the human body, avoiding excessive simplifications that are quite common in the literature. With this study, it will be possible to take into account all the parts of the body that are important for the radio channel at mmWave according to its electrical dimensions such as the arms, legs and head.

The DKE model calculates the normalized field diffracted at the RX location (diffraction loss).

$$E_{RX_n} = \frac{E}{E_o} = \left(\frac{1+j}{2}\right)\left[\left(\frac{1}{2} - C(v)\right) - j\left(\frac{1}{2} - S(v)\right)\right] \tag{2.1}$$

Where $C(v)$ and $S(v)$ are cosine and sine Fresnel integrals respectively, and the Fresnel parameter v is defined as the phase shift ratio between the paths from the T_x/R_x to the edges of the obstacle as quantifies the diffraction concealment according to the T_x/R_x visibility calculated in the equation (1.3) and (1.4) of the section 1.2.2.

where n is Ⓐ or Ⓑ for upper and lower paths, λ is the wavelength, d_{TX}/d_{RX} is the distance from the transmitter /receiver to the absorbing screen.

The Fresnel parameter v indicates how the incident field is diffracted according to the shadow generated by the obstacle. The sign uncertainty of v depends on the TX/RX visibility, being positive for LOS and negative in the NLOS case (See figure 2.2). This model can only be used if the obstacle is within the first Fresnel zone.

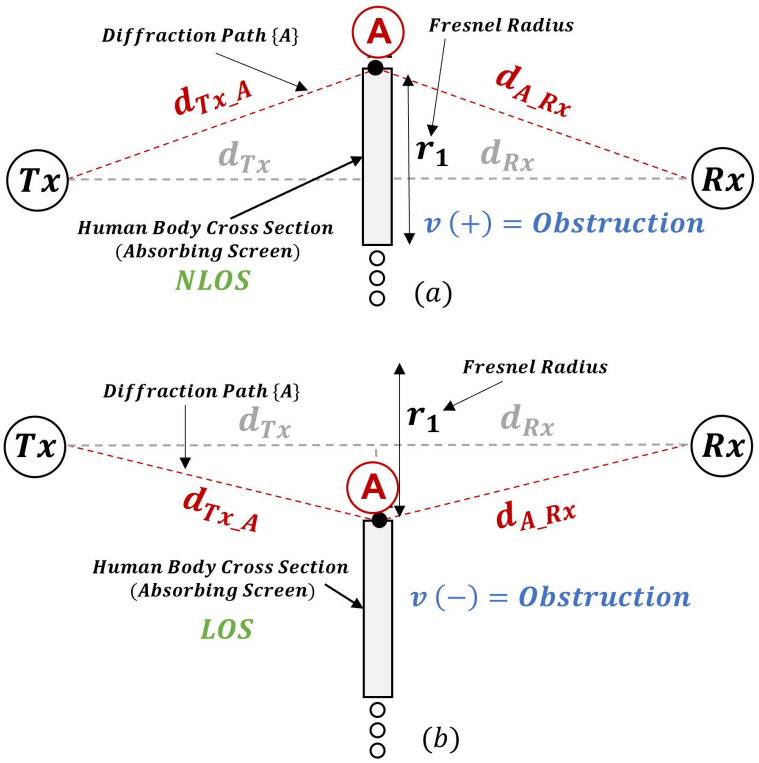

Figure 2.2: (a) Fresnel parameter $v(+)$ (NLOS), (b) Fresnel parameter $v(-)$ (LOS).

As shown in figure 2.1, the model is applied independently on each path. Therefore, the total losses are the sum of the two contributions of each path, being the reference line-of-sight field given by:

$$E_o = \frac{\lambda}{4\pi(d_{TX} + d_{RX})} e^{-j2\pi \frac{d_{TX}+d_{RX}}{\lambda}} \tag{2.2}$$

Thus, the total field at the receiver (RX) , is given by:

$$E_T = E_A + E_B = E_{RX_A} e^{-j2\pi \frac{\Delta d_A}{\lambda}} + E_{RX_B} e^{-j2\pi \frac{\Delta d_B}{\lambda}} \tag{2.3}$$

One of the advantages of the DKE model is its great versatility and, according to the simplifications and rules proposed in this chapter, to its being applicable to characterize the indoor radio channel more realistically.

2.3 DKE validation strategy

In the literature, the human body concealment analysis has been performed with different mathematical models, but all these mathematical approaches have given similar far-field behavior at the receiver. This is because in all the proposed mathematical approaches, the human body has been modeled with simple geometric shapes, such as cubes, planes or cylinders, omitting the geometry of the arms, legs and in some cases the head (See figure 2.3).

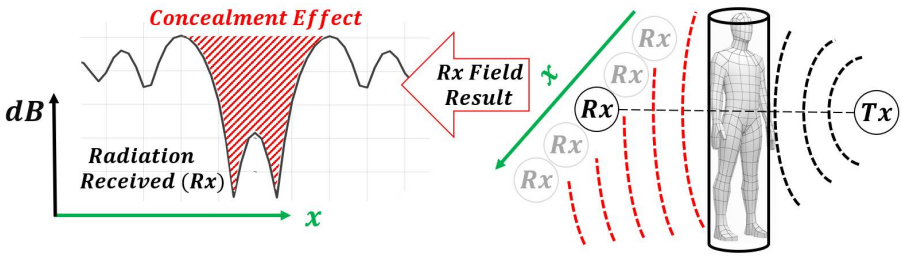

Figure 2.3: Scattering behaviour of the body with a simplified geometrical model.

Therefore, one of the objectives of this chapter is to identify which simplifications are valid based on the DKE model restrictions [30], in order to model the human body in the best way without ignoring details of its morphology that could significantly alter the fading of the signal.

For this reason, a double comparison strategy is proposed, where the diffraction losses obtained from the DKE model implemented in MATLAB will be compared with measurements and simulations, so to identify those restrictions that limit the use of the DKE model to correctly characterize the human body.

In all test scenarios, to compare and validate it with the far field results obtained with the DKE mathematical model implementation, the same set-up is used, i.e., materials, electrical dimensions, positions and geometrical shapes (See figure 2.4). It is worth noting that the material used for the obstacle in both cases (Simulation/Measurement) was a metal surface, so to emulate the absorption characteristics of the human tissue at mmWave [104] in the direction of concealment. The measurements and simulations were carried out considering the applicability rules proposed in [107], which indicate basic guidelines to avoid errors in the validation of the DKED model.

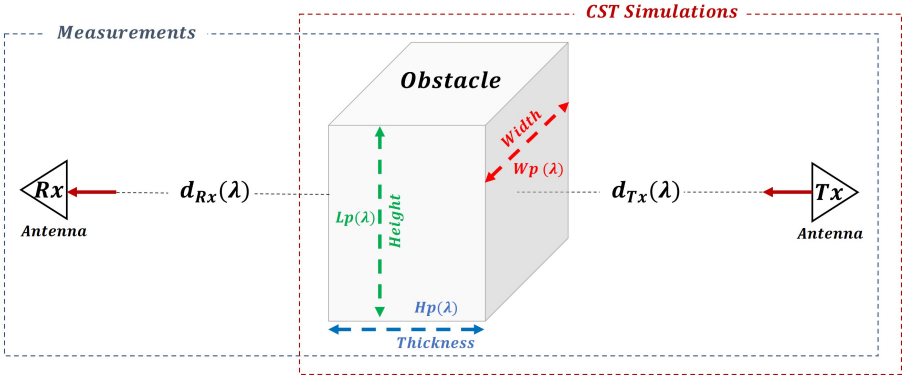

Figure 2.4: Simulation scenario Set-Up.

The approach used to obtain the resulting field behind the obstacle differs for measurements and simulations. Therefore, in the following subsections the procedure used for both measurements and simulations will be explained.

But first, the simulation platform CST Microwave Studio [108] used to perform the simulations is briefly discussed. This simulator is used both to determine the feasibility of characterizing the human body with the double knife edge model, and to characterize the passive reflector in millimeter waves, which is discussed in later chapters.

2.3.1 Simulation Set-Up in CST Microwave Studio

As mentioned above, the simulations have been carried out through the electromagnetic analysis tool (CST Microwave Studio). Within this tool the antenna simulation template was used, since this template is the most appropriate to

simulate the scattering effects on the radiation pattern of an antenna when it is obstructed by a totally absorbing element.

In our case the radiation source is a horn antenna operating in the Ka-band [109], and the obstacle is a basic geometric shape that may be either a plane, a cube, or cylinder. The dimensions of each geometric shape are variable (see figure 2.4) and depend on the type of simulation to be performed, which will depend on which of the constraints of the Double Knife-Edge model [30] is evaluated.

Both the material of which the radiating horn is composed and the obstructing object are a perfect electrical conductors (PEC). Recall that the objective of both simulations and measurements is to validate the usefulness of the Double Knife-Edge model to analyze the scattering behavior of the human body in mmWave.

The strategy used to simulate the radiation pattern scattered by an obstructive passive element was to place the obstacle at a distance (d_{TX}) (See figure 2.4), so that it is far away enough to be in the far field region of the radiating element, thus the incident radiation can be considered a plane wave.

In simulations a receiver antenna is not considered, as it does in the measurements, because CST calculates the final radiation pattern of the whole system (Horn + Obstacle). Therefore, to obtain the resulting field behind the obstacle it is not necessary to put a receiver that will move gradually, as it is the case of the measurements. This feature of the antenna templates in CST allows to save computational load, because when we do simulations in mmWave most of the objects are electrically very large.

Since simulations give the far field, it is possible to know which are the relative diffraction losses in each angular position behind the obstacle, according to the resulting radiation pattern. The transmitting antenna is the only source of energy and the obstacle should be located in front of the antenna, so that the most energy is incident on the obstacle.

Figure 2.5 shows the steps to be followed for each simulation. Initially, in **step one**, the type of validation to be performed is determined, depending on the type of geometric shape of the obstacle (Plane, Cube or Cylinder) and its dimensions (W_p, H_p, L_p), and the separation between the transmitting antenna and the obstacle (d_{TX}). In **step two**, this experiment is replicated in CST, taking into account the type of transient solver and its mesh resolution, in order to obtain the most accurate results in the simulation. In **step three**, the final radiated field of the whole system consisting of the radiating element (horn) and

the passive element (obstacle) is simulated. Finally, in **step four**, the results obtained from the radiation pattern are examined, where not only the result in three dimensions is analyzed, but also the cross sections of this radiation ($\theta = 90°$ and $\phi = 90°$), in order to determine how the obstacle scattered the radiation produced by the antenna.

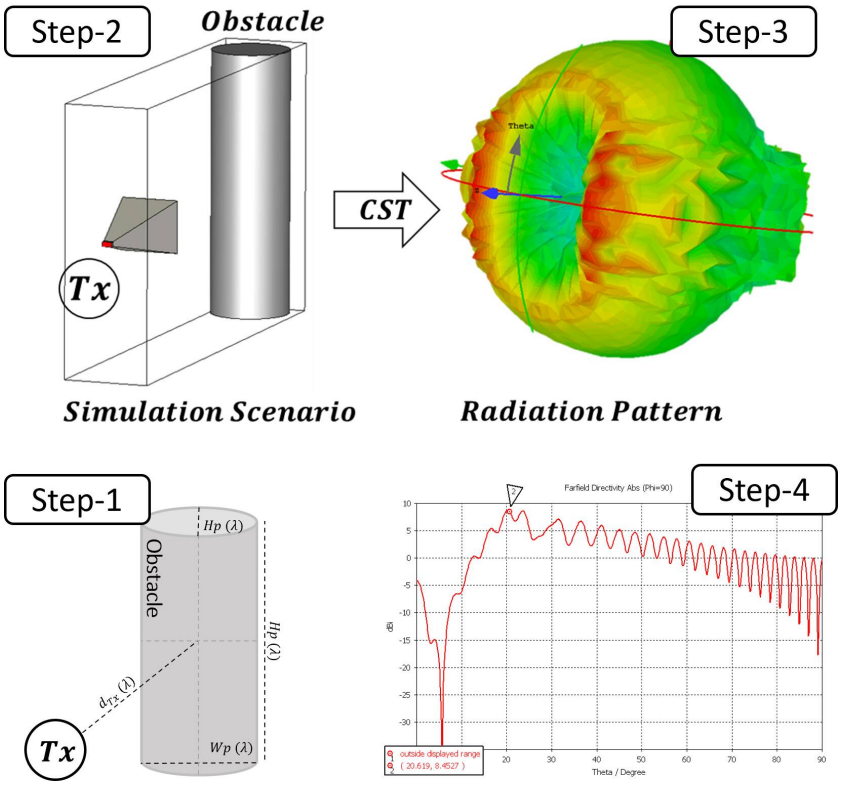

Figure 2.5: Simulation step to validate the DKE in CST.

2.3.2 Measurement Set-Up with VNA

The measurement campaign was carried out following the scheme shown in figure 2.6. The transmitter and receiver were equipped with the same horn antenna in Ka-band, which has been manufactured by Sagemillimeter, model WR-28, operating at frequencies from 26 to 40 GHz, with a nominal gain of 20 dBi [109]. The antenna 3 dB beamwidth is 18 degrees in both the vertical and horizontal planes.

The antennas of both the receiver and transmitter are connected to ports 1 and 2 respectively on the vector network analyzer (VNA) which is manufactured by Rohde-Schwarz and the model is the RS ZNB40. The measurement scheme is set up in an anechoic chamber, where the TX and RX antennas are oriented one in front of the other to minimize the path loss, and are separated by a distance ($2d_{TX}$).

The obstacle is located at a distance (d_{TX}) from both the receiver and the transmitter, and its dimensions depend on the experiment to be performed, as well as its geometric shape and material. The obstacle material is fully metallized to emulate one of the constraints of the DKE model, where it must be fully absorbing. As discussed in the subsection on the simulation setup, metallic materials are fully absorbing in transmission, which is similar to the behavior of human tissue at mmWave.

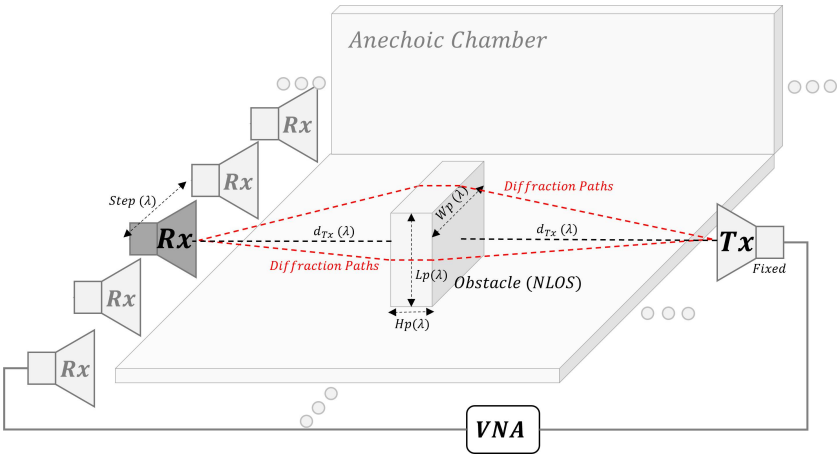

Figure 2.6: Measurement setup scheme for TX and RX positions.

In the measurement procedure the transmitting antenna remains fixed, while the receiving antenna is gradually moved in steps of 5cm along the orthogonal axis of the antennas orientation, where 30 receiver positions are considered for each measurement corresponding to a single sweep from left to right. Along the receiving antenna sweep, the channel frequency response or (S_{21};S_{12}) is measured at each receiver position. This procedure was carried out to measure the scattering field contributions when the receiver is at either a LOS or NLOS position.

These measurements are compared with the results obtained with the simulations and those obtained with the Double Knife-Edge model implemented in

Matlab, in order to validate its usefulness to describe the scattering effect of the human body. The measurement procedure is shown from another perspective in figure 2.7.a, and the set-up of the measurements in the anechoic chamber is shown in figure 2.7.b.

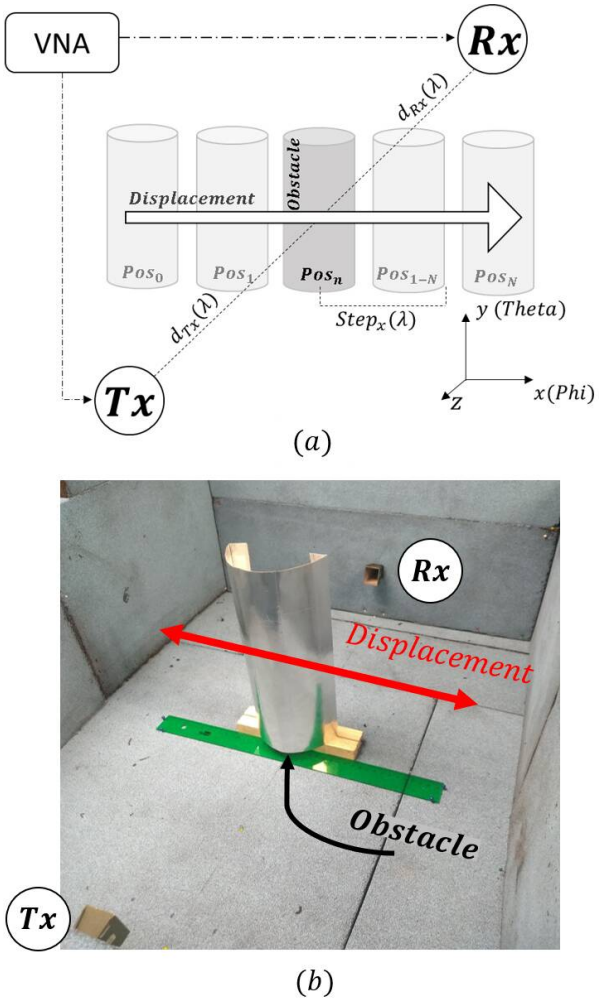

Figure 2.7: (a) Scheme of the movement of the obstacle in measurements (b)Measurement scenario in the anechoic chamber.

2.3.3 Decision criteria to compare the scattering results

The decision criterion for measuring the reliability of the proposed Double Knife-Edge mathematical model is based on the Minimum Mean Squared Error (MMSE), which has been widely used in the literature, especially in signal processing, when the aim is to compare the similarity between two functions or signals [110].

The objective of the MMSE estimator is to determine the error between the results obtained with the CST simulations and those measured with the results obtained with the DKE implementation in Matlab, taking into account the same scenarios, where each scenario is defined by the dimensions of the obstacle (W_p, L_p, H_p) and its separation to the antennas (d_{TX}).

MMSE in linear domain is given by:

$$MMSE = \sum_{i=0}^{N} \frac{(R_i - K_i)^2}{N(R_i \cdot K_i)} \tag{2.4}$$

Where R_i is the far-field received power (measured or simulated) at the location point i, K_i is the power level calculated for the same scenario but with the Double Knife-Edge (DKE) implementation in MATLAB, at the equivalent position point i, and N is the number of position samples between the point ① and ② of figure 2.8.

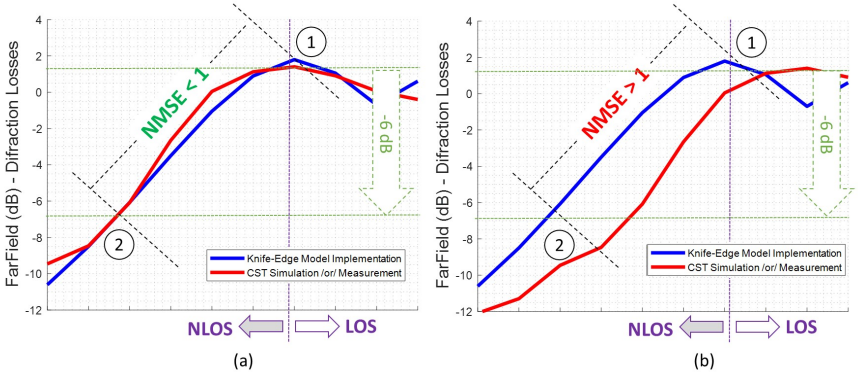

Figure 2.8: (a)MMSE Decision Factor < 1 (Point 1: Maximum Diffraction Gain – Point 2: -6dB in the shadow zone), (b) MMSE Decision Factor > 1 (worst adaptation).

The lower the MMSE value, the more accurate will be the estimation (more similar are the two sets of data compared). The decision threshold that has been chosen is $MMSE < 1$ for the data set in the range between the position with *maximum diffraction gain* ① to the -6 dB point of diffraction loss in the concealment zone ② (See figure 2.8), where the *diffraction gain* ① is the increased field power due to the scattering effects of the obstacle edge.

2.4 DKE Applicability Limits Analysis

As mentioned above, the human body has been modeled with simple geometric shapes in the literature [103], [49], [50], mainly due to the complexity of the body, although the larger electrical dimensions of the body have been maintained, as shown in figure 2.9.b.

But to our best knownledge, no model in literature has considered the geometric complexity of its morphology, due to the high computational cost that this would imply, and that for long links (several meters at mmWave band), this simplification is enough to evaluate the scattering effects of the human body. Such simplifications should not be made carelessly, because the arms, legs and head also play an important role in the dynamic behavior of the radio channel at short distance links in indoor scenarios. This is because body parts are electrically large in mmWave, and irremediably affect the propagation of the radio channel. This is even more relevant in uplink, because both the arms and the head interact directly with the cell phone due to their physical proximity. Legs also play an important role, because many of the multipath contributions arrive after having previously bounced on the ground, and because people are constantly moving, so the radio channel will be affected by the natural movement of the legs.

Therefore, the entire human body is a dynamic obstacle and not a rigid-static one as has been simplified in the literature. However, these simplifications were used as a reference (See figure 2.9.a) to analyze the constraints described in [30] on the proposed DKE model, and the analysis of each of these constraints with measurements and simulations will be carried out in detail throughout this section.

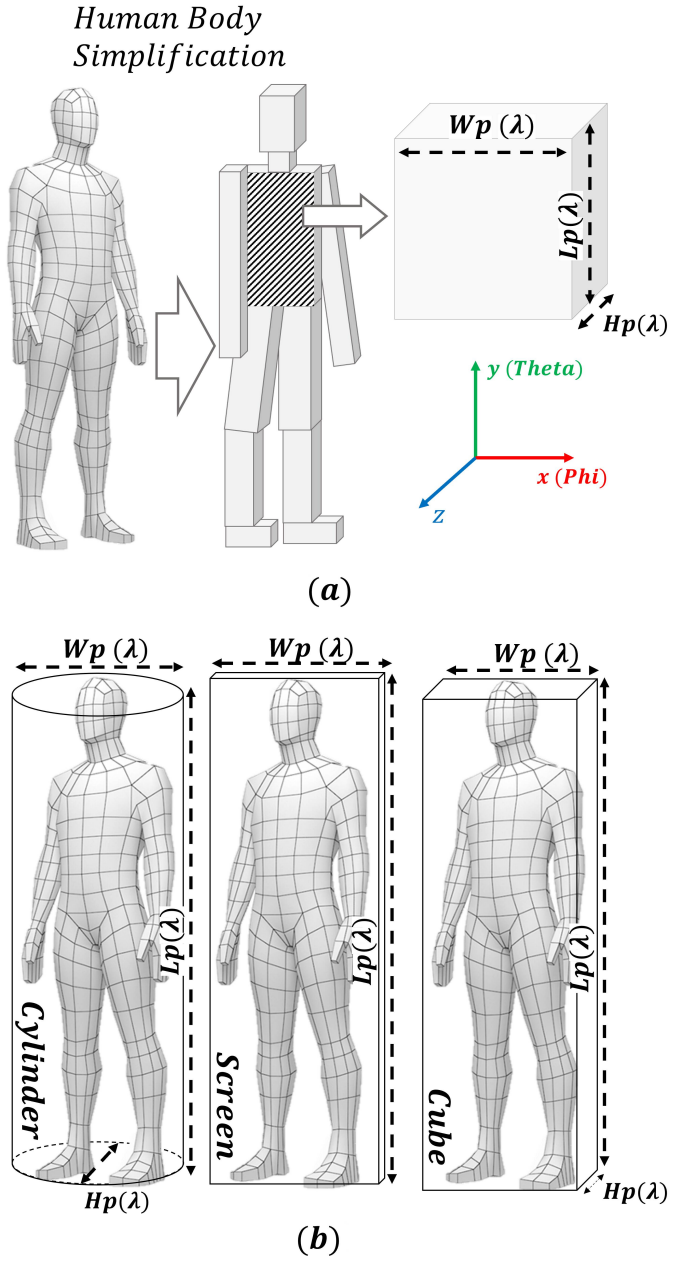

Figure 2.9: (a) Human Body geometrical simplification. (b) Geometric simplification in the literature.

The first simplification adopted is to assume that the human body can be characterized as a set of parallelepipeds, in the form of a robot model (see figure 2.9.a). The minimum dimensions that each parallelepiped should have to meet the constraints of the Double Knife-Edge model will be analysed, its width W_P, height L_P, and thickness H_P.

As mentioned above, the double knife edge model has a set of constraints that will be analyzed one by one to identify under which electrical dimensions of the obstacle (W_P, L_P, H_P) the DKE is applicable for each case study. That is, as the scattering characterization of each individual element of the robot model (See figure 2.9.a) is equivalent to evaluating the human body scattering, therefore all validations made on small scale on basic obstacles are extrapolated to higher electrical dimensions and more complex morphologies.

The applicability limits of the DKE model were determined by simulations and verified by measurements. The following subsections objectives will carry out the following analyzes:

- (SubSection 2.4.1): Determine the geometric limits of the obstacle height W_P and width L_P, regardless of the thickness H_P of the obstacle, because it is not a sensitive dimension for the obstruction, from the point of view of the TX and RX (See figure 2.4) and additionally it is part of the entry restrictions of the mathematical model [30].

- (SubSection 2.4.2): Determine the minimum distance d_{TX} between the obstacle and the antennas for which the proposed Double Knife-Edge (DKE) model approximation is valid for downlink or uplink scenarios according to its restrictions [30].

- (SubSection 2.4.3): Determine the truth of the assumption according to the restrictions [30], that the obstacle thickness does not influence the on the scattering phenomenon.

- (SubSection 2.4.4): Determine if there are different scattering effects, when the obstruction is modeled with different non-planar geometric shapes.

- (SubSection 2.4.5): Analyze the polarization effect on the scattering modeled, because according to limitations of the DKE model, this effect is not taken into account mathematically.

In order to evaluate the limits of applicability of the mathematical model, the following basic scheme was used (See figure 2.10), where the electrical dimensions of the obstacle, its separation relative to both the transmitter and the receiver, as well as the morphology of the obstacle are considered, thus using these simple variables the constraints of the DKE model are evaluated.

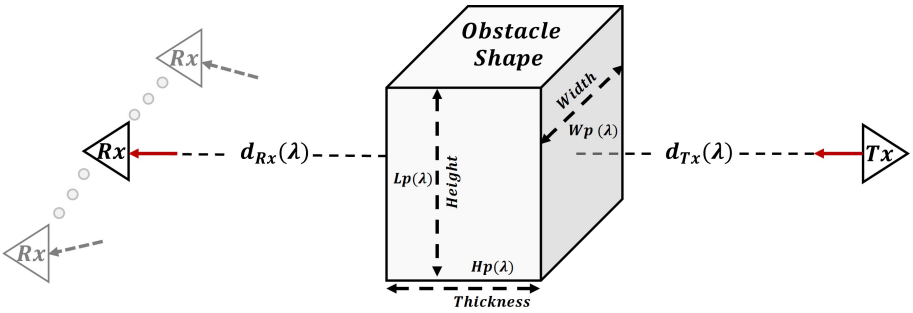

Figure 2.10: Simulation scenario Plan.

2.4.1 Analysis of the Electrical Dimensions of the Obstacle

In the present sub-section we determine the geometrical limits that an obstacle must respect for the DKE to be valid to model the scattering effect caused by this obstructive element. This is due to the fact that one of the first restrictions of this mathematical model, to be used properly, is that the cross-sectional dimensions of the obstacle must be much larger than the wavelength.

Therefore, the L_P dimension on the Y axis (See figure 2.10) has been set to $W_P = 80\lambda$ to satisfy all the proposed constraints [30], except for the W_P dimension. The W_P dimension is progressively scaled (3λ, 6λ, 10λ, 15λ, 20λ, 28λ at 30 GHz) along the X axis, in order to determine at what minimum dimensions of W_P the Double Knife-Edge model is valid for modeling its scattering effect, according to the quantitative comparison of the MMSE estimator, with simulations and measurements versus the results of the DKE model implemented in Matlab.

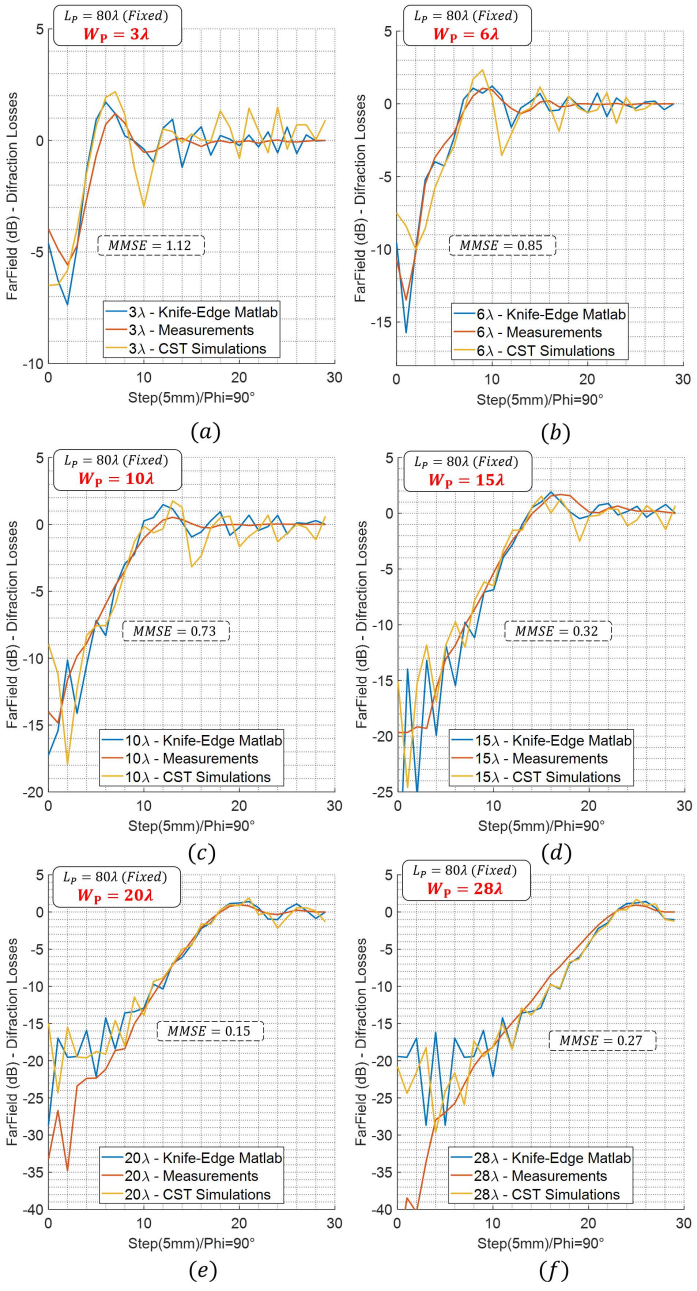

Figure 2.11: Diffraction Losses comparison in terms of blocking element width W_P:[(a):3λ, (b):6λ, (c)10λ, (d)15λ, (e)20λ, (f)28λ].

Electrical Dimensions Analysis	
W_P	**MMSE**
3λ	1.12
6λ	0.85
10λ	0.73
15λ	0.32
20λ	0.15
28λ	0.27

Table 2.1: Tabulated MMSE results of the analysis of the electrical dimensions with $L_P = 80\lambda$ and $d_{TX;RX} >> \lambda$ fixed.

The observed behavior of the far-field measurements and the radiation pattern simulated in CST are very similar to the Double Knife-Edge (DKE) diffraction loss implemented in MATLAB according to the MMSE estimator. Therefore, for obstacles with electrical dimensions larger than 6λ (MMSE=0.85) the Double Knife-Edge model can be used to evaluate the scattering behavior of the radiation field behind the obstacle. It should be noted that in this section all the measured and simulated obstacles are metallic screens without thickness, respecting the initial restrictions of the DKE [30].

2.4.2 Analysis of the Distance between the antenna and the obstacle

In the present analysis the minimum viable distance between the obstacle and the radiation source is analyzed, so that the Double Knife-Edge model can adequately calculate the scattering generated by the obstructive element.

This limitation is especially important in uplinks, because the mobile terminal is considerably close to the upper body (head, torso and arms), therefore it interacts in the signal propagation in a negative way. It is therefore important to know if this model can evaluate to evaluate this effect despite the proximity.

In this analysis the electrical distance d_{TX} will be varied between the obstacle and the antennas TX/RX ($5\lambda, 10\lambda, 15\lambda, 20\lambda, 25\lambda, 30\lambda$ at 30 GHz), keeping the physical dimensions $L_P = 15\lambda$ and $W_P = 15\lambda$ of the obstacle fixed, in agreement with keeping the limits identified in the previous subsection, where minimum dimensions must exceed 6λ.

In this case study, the model has been compared with the measures on the one hand and with CST simulations on the other, because the two types of results were obtained from different scenarios and methodologies.

The simulation results were obtained according to the methodology described in section 2.3.1, and the far field was calculated with a single transmitting antenna and an obstacle, where the separation distance between them was gradually changed from 5λ to 30λ.

On the other hand, in the methodology used for the measurements, only the relative distance between the TX-RX and the obstacle can be changed, being the distance between the TX and RX fixed to 70cm (70λ at 30 GHz), due to physical limitations of the cable used in the VNA and the anechoic chamber dimensions (See figure 2.10).

The figure below shows the results of the measurements according to their methodology and scenario.

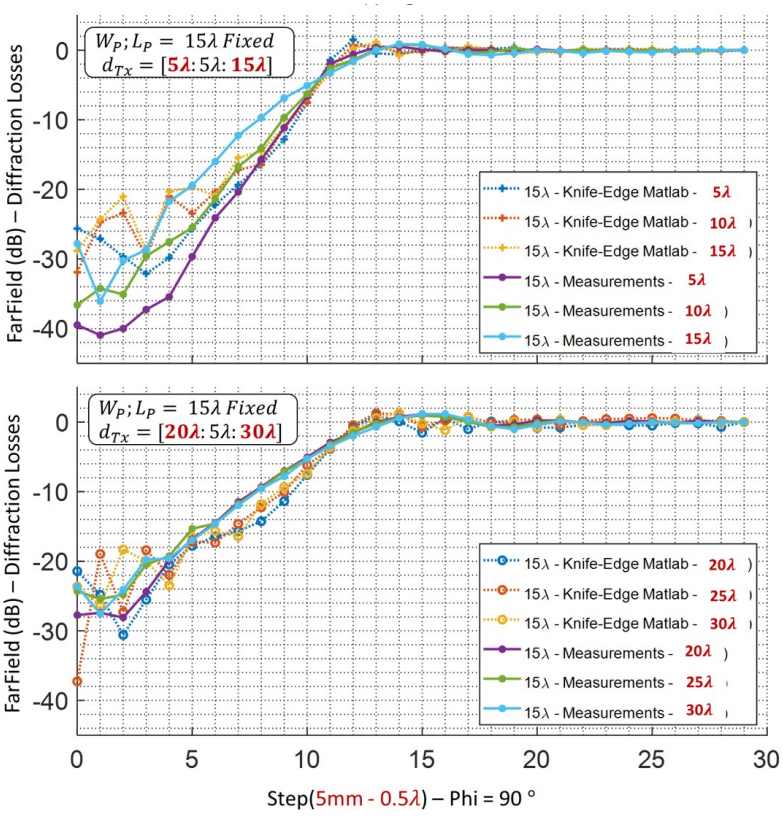

Figure 2.12: Equivalent far field concealment in terms of the distance between blocking screen and TX [d_{TX}] with DKE MATLAB implementation vs measurements.

According to the results observed in figure 2.12, it can be concluded that concealment will be similar regardless of the relative distance of the obstacle to TX and RX, because the distance between the TX and the RX is fixed to 70cm. According to the measurement results, the DKE model can be used from 10cm (10λ at 30 GHz) (MMSE=0.47). Note that the DKE model does not contemplate angles of incidence (See figure 2.1).

The figure below shows the results of the CST Simulation according to their methodology and scenario.

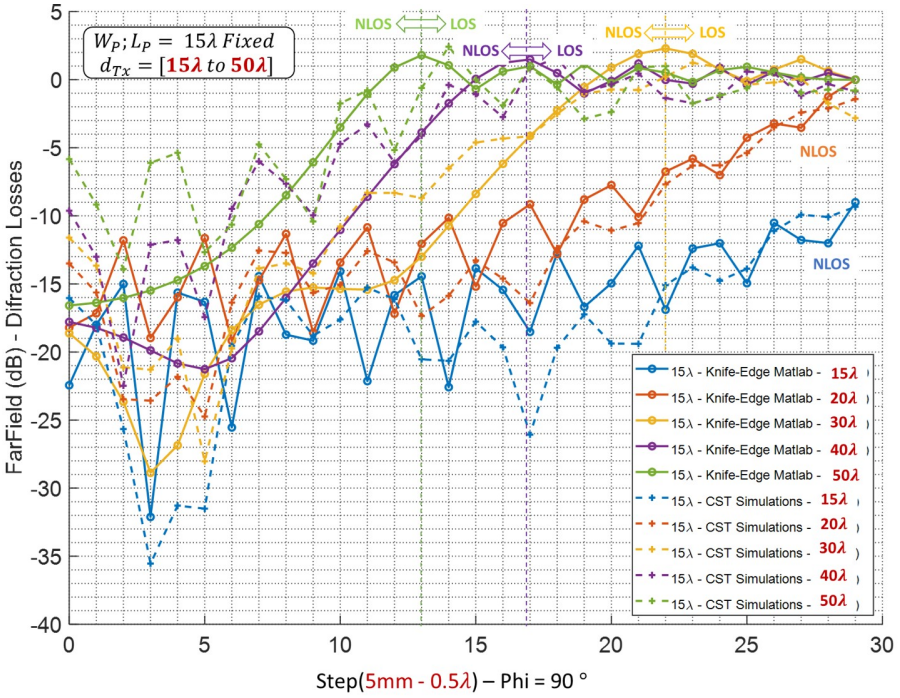

Figure 2.13: Equivalent far field concealment in terms of the distance between blocking screen and TX (d_{TX}) with DKE MATLAB implementation vs simulations.

Figure 2.13 shows the far field simulation results (dotted lines) compared to the DKE model implemented in MATLAB. The distance to transmitter is fixed, and represented in figure 2.21 for five values of d_{TX}, from 15 to 50 cm (15λ to 50λ at 30GHz). As the obstacle is moved away from the antenna, it becomes electrically smaller.

Electrical Distance Analysis		
d_{TX}	**MMSE Measurement**	**MMSE Simulation**
5λ	1.12	
10λ	0.47	
15λ	0.67	0.91
20λ	0.73	0.89
25λ	0.55	
30λ	0.58	0.88
40λ		0.98
50λ		1.1

Table 2.2: Tabulated MMSE results of the electrical distance from the TX to Obstacle, with obstacle dimensions of with $L_P; W_p = 15\lambda$ fixed.

According to the results, the DKE model can be used to characterize the concealment according to the CST simulations with electrical distances from 15 cm (15λ to 30 GHz) (MMSE=0.91), taking into account the smallest electrical distance for which the results of the DKE model are valid.

2.4.3 Obstacle Thickness Analysis

One of the main simplifications of the DKE model is that the absorbing screen is infinitesimally thin. In this section the influence of obstacle thickness will be analysed on the far field computation/measurement results. The most important restriction of the proposed mathematical model (DKE) is the assumption that the obstacle must be a screen "*without thickness*". Due to this DKE restriction [103], the thickness influence will be analysed according to the far field behaviour.

The simulation and measurement of the far field of the obstacle were made for obstacles of different thicknesses H_P ($0\lambda, 3\lambda, 6\lambda$ at 30 GHz), but with the same electrical dimensions $W_P = 15\lambda, L_P = 15\lambda$ and electrical distance $d_{TX} = 35\lambda$ for all the scenarios, respecting the applicability limits identified in the Section 2.4 in order to have reliable results,i.e electrical dimensions of $W_P, L_P > 6\lambda$ and $d_{TX/RX} > 15\lambda$ are considered.

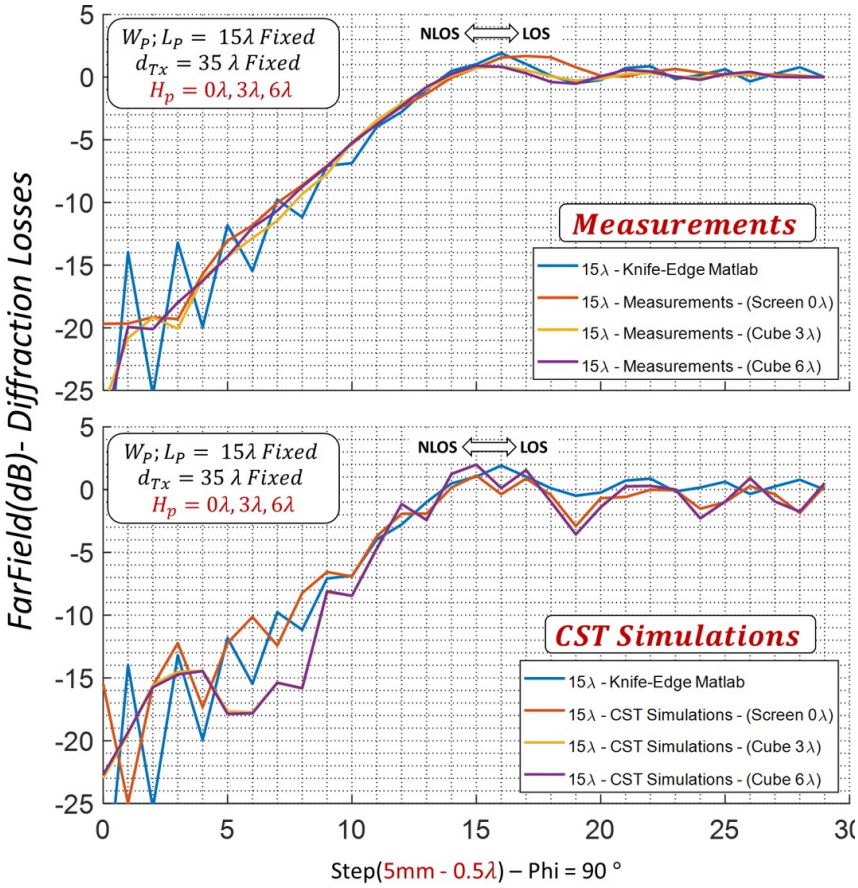

Figure 2.14: Equivalent far field radiation pattern (Screen Obstacle without thickness) vs blocking obstacle thickness (H_P) for measurements and CST simulations.

According to the results of the figure 2.14, it can be affirmed that the thickness of the obstacle has no influence on the behaviour of the concealment far field. The resulting far field (Measurements/Simulations) does not differ considerably from the field obtained by a completely flat obstacle without thickness that is used by the proposed DKE mathematical model. According to the MMSE estimator the worst results were MMSE=0.24 for Measurements and MMSE=0.78 for the CST Simulations in both cases the similarity condition is achieved satisfactorily.

2.4.4 Geometrical Shape Analysis

As discussed at the beginning of the section, the entire human body has been modeled in the literature with simplified geometric shapes as in figure 2.9.

But part of the objectives of this research is to avoid this type of simplification without justification. Therefore, in this subsection the scattering effects of different geometric shapes will be analyzed, to simplify as much as possible without omitting important effects that may affect the radio channel in mmWave frequencies.

We must take into account that the most common geometric shapes in the morphology of the human body are cylinders [104] so it is important to consider this geometric shape with different dimensions in order to evaluate its behavior.

Recall that according to the conclusions of the previous analysis, the thickness of a cubic obstacle is not relevant to the effect of far-field scattering, so analyzing a cylindrical shape is vital to fully validate the DKE model for characterizing the human body.

The geometric shapes that were used in the simulations and measurements are shown in figure 2.15 and figure 2.16, where, as a general rule, of them must have the same transverse electrical dimensions ($W_P(\lambda) - Width$, $L_p(\lambda) - Height$), while the geometric shape and thickness H_P variable.

This analysis in conjunction with the previous one, has the purpose of determining how to simplify the thickness H_P of the geometric model of the human body to be able to use DKE model correctly and efficiently.

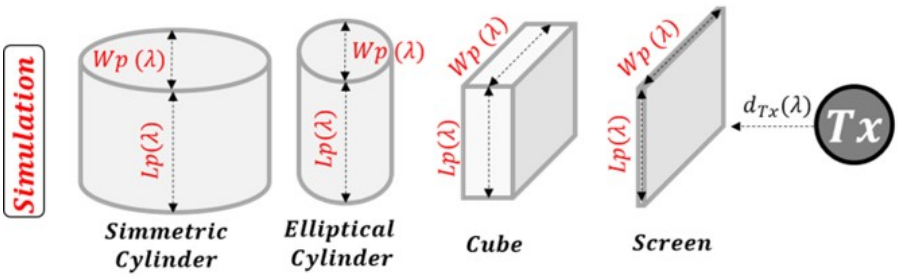

Figure 2.15: Scenario of geometric shapes in the simulation.

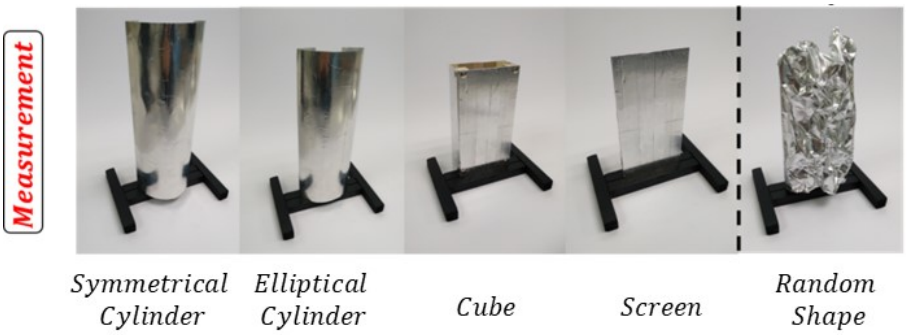

Figure 2.16: Scenario of geometric shapes in the measurements.

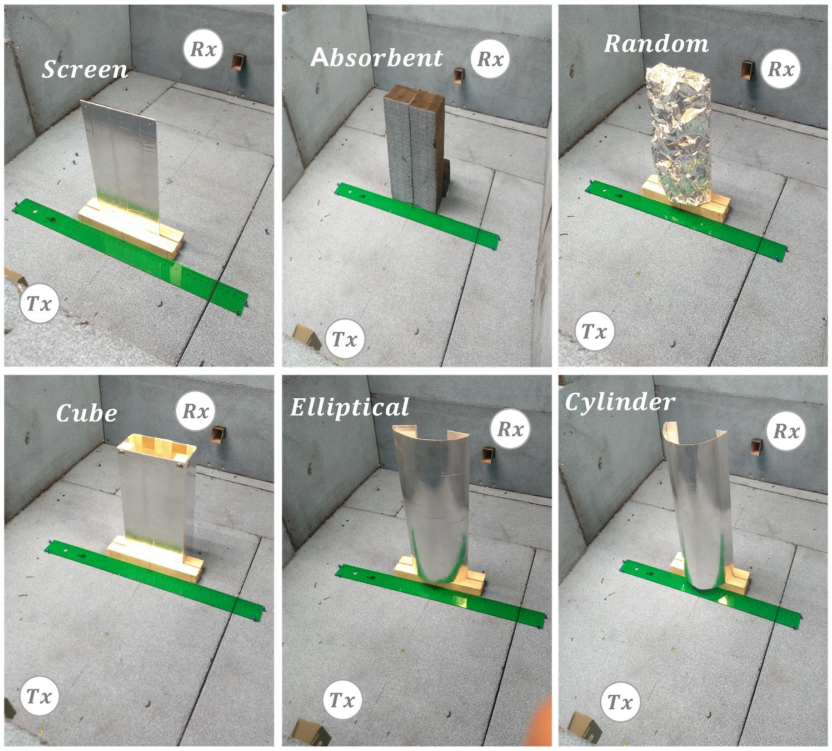

Figure 2.17: Measurement set-up with different geometrical shapes.

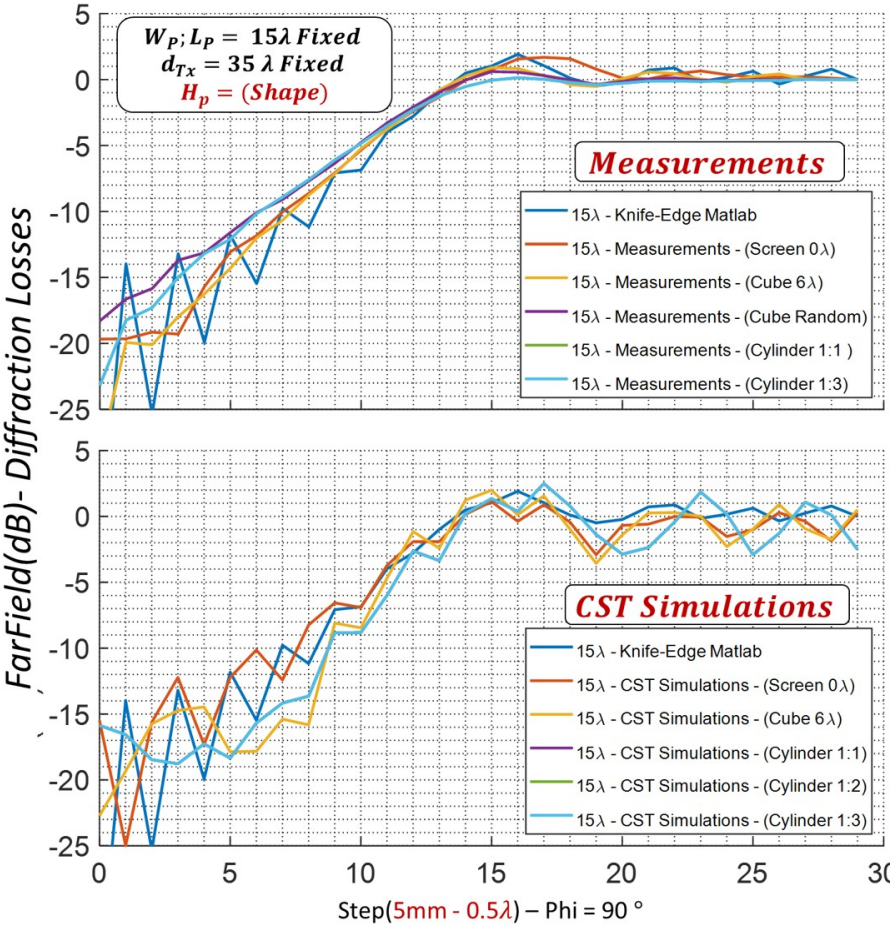

Figure 2.18: Equivalent far field radiation pattern (horizontal plane) for several shapes of the blocking (metallic) obstacle measurements and CST simulations.

According to the results observed in figure 2.18, the scattering losses calculated with the mathematical model implemented in MATLAB are very similar to the measured results, getting a MMSE estimator of 0.23, and also to the simulated ones (CST-Radiation pattern), with a MMSE estimator of 0.83, for different geometrical shapes (see figure 2.17), taking into account that the calculated MMSE estimator corresponds to the worst result obtained when testing with different morphologies.

Therefore, it can be affirmed that the geometrical shape of any obstacle does not affect the performance of the DKE model, only the equivalent contour of the original geometric shape. This issue is very important, because it simplifies the geometrical shapes to be characterized in such a way, that the DKE model can be directly implemented it in MATLAB or any other simulation tool. Additionally, it also simplifies the physical geometric models to perform measurements. Therefore, to apply the DKE model, it will only be required a screen completely absorbent or reflective with the same obstacle edge projection as shown in figure 2.19 in the "*Outline Model*".

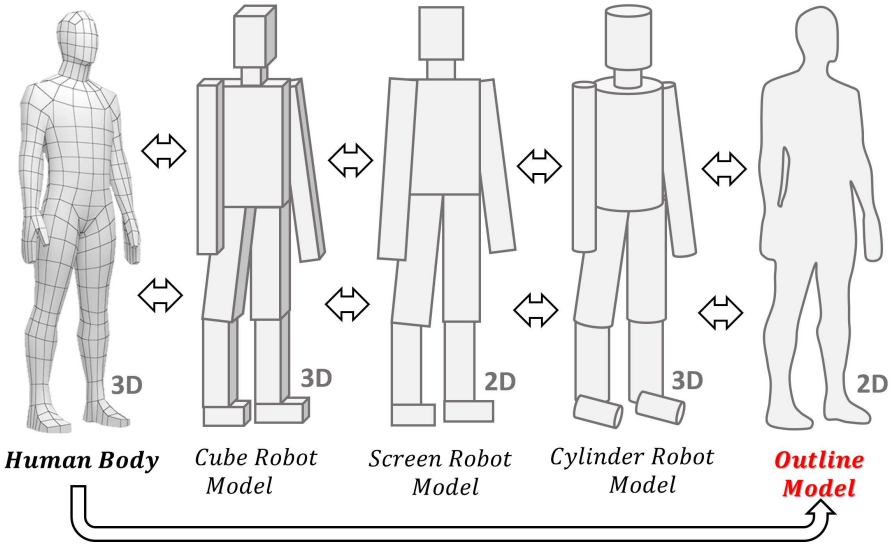

Figure 2.19: Geometrical Models Simplifications Evolution to the DKE Model.

2.4.5 Polarization Effect

Another significant contribution of this chapter is the analysis of the polarization effects on the implementation of the DKED model. This aspect is important because this mathematical model considers the obstacle as perfectly absorbing [103] which is valid in the case of the human body tissue at mmWave band. But because the obstacle is completely absorbing, the model does not consider the currents induced on the obstacle surfaces and therefore polarization effects are completely ignored in such a mathematical formulation, so it becomes a constraint.

Throughout the literature, when trying to characterize the human body, the effects of polarization have not been considered with simple mathematical models, and although its relevance has been confirmed in some works such as [36], its influence and how to avoid it have never been studied in depth. Therefore, the purpose of this analysis will be to identify the minimum electrical dimensions (W_P , L_P) in which the polarization effect has no influence and the DKE model can be applied directly.

In this study, only two types of polarization were taken into account: Vertical and horizontal polarization, alternating between them only by changing the rotation of the horn antenna, both in the simulation and measurement scenarios.

In this analysis, the L_p dimension on the $Y - Axis$ (See figure 2.10) has been fixed to $L_P = 15\lambda$ in order to satisfy all the restrictions proposed in the previous analysis, except for dimension W_P. The dimension W_P has to be changed progressively along the $X - Axis$ in order to quantitatively determine, by the MMSE estimator, from which electrical dimensions of W_P, the DKE correctly models the scattering effect, regardless of the disparity in the results of orthogonal polarizations in measurements and simulations.

In the following results an orthogonal polarization refers to a horizontally polarized incident wave (X-axis), because the predominant dimension of the obstacle is on the Y axis (L_p) while parallel polarization refers to a vertical polarization (Y-axis), because it is parallel to the orientation of the obstacle on the Y axis (L_p).

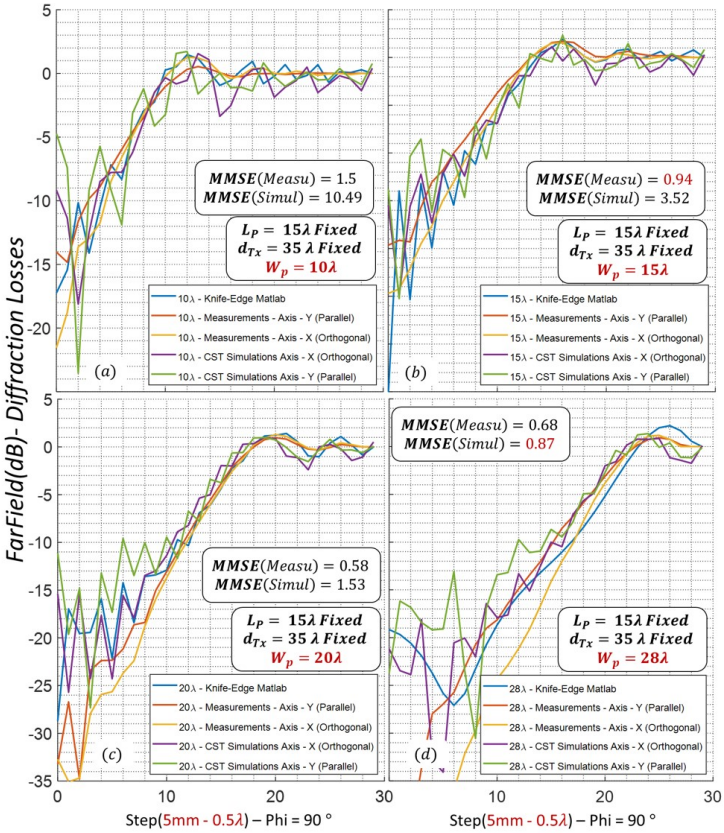

Figure 2.20: Far field comparison in terms of blocking element height W_P with orthogonal polarizations.

According to the results, it is concluded that in the case of the two studied polarizations, considering electrical dimensions of 15λ, and above, the diffraction losses can be characterized by the DKE mathematical model, without distinguishing between them. It is important to note that the polarization effects are more visible for electrical dimensions below 15λ if the incident polarization is parallel to the obstacle. Furthermore, it can be concluded that according to the measurements, the applicability limit of the model is less restrictive, being 6λ instead of 15λ. Therefore, the concealment effects of the human body can be characterized with a metallic screen without considering the polarization effects if the electrical dimensions are greater than 15λ reaching a MMSE estimator from simulation results of 0.87.

2.5 Conclusions

In this chapter the applicability limits of the DKE for modeling the scattering effect of the human body in mmWave frequencies have been verified. Throughout the development of this chapter, all the constraints of the Double Knife-Edge model [103] on the geometrical dimensions of any absorbing or reflecting obstacle have been analyzed. The geometrical limits where the DKED mathematical model can be applied have been found by analyzing measurements and simulations in CST.

According to the analysis of the obtained results, some simplifications on the morphology of the human body have also been proposed. These simplifications will facilitate the implementation of the DKE model in a complex simulation environment (Unity or Unreal Engine), where the objective will be not only to characterize a single human body, but several simultaneously in motion, as well as considering the effects of other obstacles within a complex indoor room.

Briefly, the applicability limits identified for implementing the Double Knife-Edge (DKE) model to characterize human body scattering at mmWave frequencies are:

- The minimum electrical dimensions of the cross section of any obstacle must be $W_P, L_P > 6\lambda$.
- The minimum electrical distance between the obstacle and the antennas must be $d_{TX/RX} > 15\lambda$.
- With the proposed geometrical simplifications, the scattering effects of the obstacle thickness H_P and the shape of its geometric volume can be ruled out if the edges projection to the obstacle from the TX/RX is known (see figure 2.19 "Outline Model").
- The wave polarization effect is relevant on the DKE implementation for low electrical dimensions (cross-section) of the obstacle, below 15λ.

These implementation rules and simplifications will be used in the next chapter to characterize the complex morphology of the human body, and to perform comparisons with measurements of the body shadowing in a real, dynamic indoor environment.

Chapter 3

Implementation of the human blockage simplified model at millimeter-wave frequencies

This chapter presents some evaluations of the applicability of the Double Knife-Edge (DKED) model, which was confirmed in the previous chapter to be potentially suitable to characterize the scattering effect of the human body. This assumption is verified by measurements with a reference person. And finally it is discussed how the model can be implemented in a 3D environment platform with proprietary ray-tracing techniques, developed throughout the Thesis research. These analyses confirmed the applicability of the DKED model to characterize the scattering generated by the human body in mmWaves. By using simulation tools, the DKED can be implemented quickly and without losing accuracy, taking into account the simplifications and rules proposed above.

To this aim, this chapter has been divided into the following sections:

- Section 3.1 presents a brief introduction.
- Section 3.2 presents additional analyses about the considerations that must be taken into account to use the Double Knife-Edge model to evaluate the human body.

- Section 3.3 presents the measurement campaign strategy used to validate the usefulness of the Double Knife-Edge model to characterize the scattering effects of the human body effect.

- Section 3.4 presents the video game platform used to implement the DKE model that emulates the scattering effects of the human body.

- Section 3.5 presents the implementation performed in the Unity simulation environment, where the DKE model was used to characterize the scattering effects of the human body in a complex simulation environment.

- Section 3.6 presents the conclusions of this chapter.

3.1 Introduction

As discussed in the state of the art and in the previous chapter, throughout the literature there have been quite a few mathematical models that have attempted to characterize the human body in this frequency band, among which some are more complex than others. But, regardless of the model used to characterize the human body, the residual field calculated by each model behind the blocking object is almost identical, because the complexity of the morphology of the human body is simplified with simple geometric shapes, hence their results [104].

Additionally, these models were verified with measurements, but having the radiating source electrically far away from the body, so this kind of simplifications are valid. This is not the case when the radiation source is close to the body, such as when a person holds a mobile phone in his hand.

Therefore, the objective of this chapter is to validate additional considerations on the implementation of the DKE model. One of them is to evaluate the concealment when the obstacle changes its cross section with respect to the relative positions of the transmitter and receiver, and an important additional consideration is to validate the DKE model in different frequency ranges, more specifically from 30 to 40 GHz.

With these additional considerations the aim is to characterize the scattering generated by the human body in the best possible way with simulation tools.

3.2 Additional Double Knife-Edge Model Considerations

Before presenting the additional considerations that have been taken into account to validate the double-knife edge model, we briefly review the basic concepts on which the DKE model is based to evaluate the scattering of the residual field behind the blocking object.

Recall that the mathematical formulation of the double-knife-edge model is determined by the calculation of the normalized field at the receiver position.

$$E_{RX_n} = \frac{E}{E_o} = \left(\frac{1+j}{2}\right)\left[\left(\frac{1}{2} - C(v)\right) - j\left(\frac{1}{2} - S(v)\right)\right] \tag{3.1}$$

$$v = \pm\sqrt{\frac{2k_o\Delta d_n}{\pi}} \tag{3.2}$$

$$\Delta d_n = (d_{TX\to n} + d_{n\to RX}) - (d_{TX} + d_{RX}) \tag{3.3}$$

Where $C(v)$ and $S(v)$ are cosine and sine Fresnel integrals that depend on the parameter v and this parameter defines the relationship between the transmitter and receiver visibility, and the relative distance to each of the equivalent edges of the obstacle. The equivalent edge is understood as the visible geometrical limits of the obstacle as seen from the point of view of the transmitter and receiver, like shown in figure 3.1 as points Ⓐ and Ⓑ.

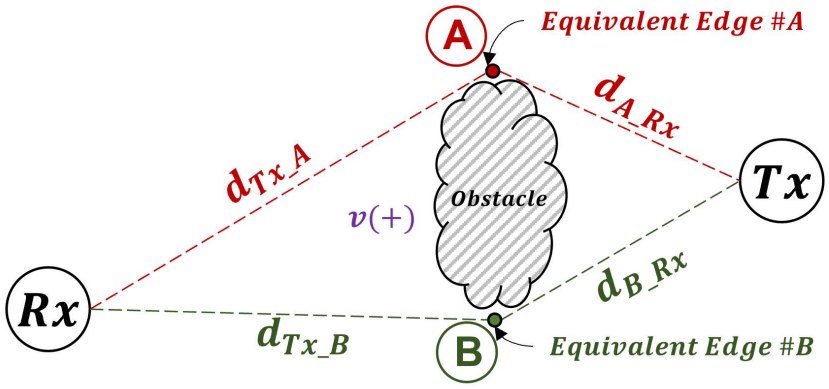

Figure 3.1: Simplified implementation at the DKE model.

Therefore, to implement the Double Knife-Edge model in a simulation environment only the relative positions of the transmitter and receiver, the relative distance (Δd_n) to the equivalent edges of the obstacle, the visibility within the first radius of the Fresnel zone and finally the applicability limits identified in the previous chapter must be taken into account.

The DKE model is relatively easy to implement and has very few input variables that depend on the electrical dimensions of the obstacle and ts relative concealment of the direct path between transmitter and receiver. It is important to evaluate how the electrical dimensions of the obstacle, and especially its orientation, affect the identification of the equivalent edges that define the electrical distance (Δd_n). Furthermore, it is worth considering how the frequency affects the scattered field produced by the obstacle in the concealing zone.

All the simulations and measurements carried out in this analysis follow the same methodology proposed in the previous chapter in section 2.3

3.2.1 Obstacle Cross-Section Analysis

In the present analysis the effect of changing the orientation of the obstacle is to be determined. The obstacle will always maintain the same electrical dimensions. It has to be taken into account that, according to the applicability limits of the DKE model, the thickness of the obstacle is not important, therefore, and according to this premise, the obstacle used for both measurements and simulations is a screen with thickness $H_P << \lambda$. The obstacle has a width $W_p = 15\lambda$ at 30 GHz and a separation distance between the antennas and the obstacle of $d_{TX/RX} = 35\lambda$.

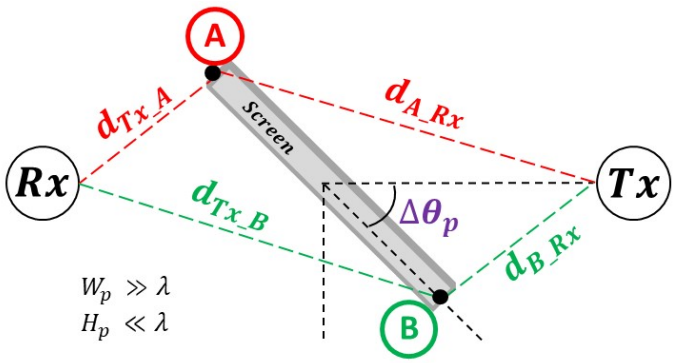

Figure 3.2: Simulation/Measurements set-up of rotation analysis.

In this analysis the obstacle is progressively rotated $\Delta\theta_P$ from 0° to 90°, with steps of 10°, along the orthogonal axis to the relative positions of the antennas, as shown in figure 3.2. Recall that the objective of this analysis is to determine the impact of changing the cross section of the obstacle as it is rotated. The following figure shows the set-up used to carry out the measurements, which is similar to that of the simulations.

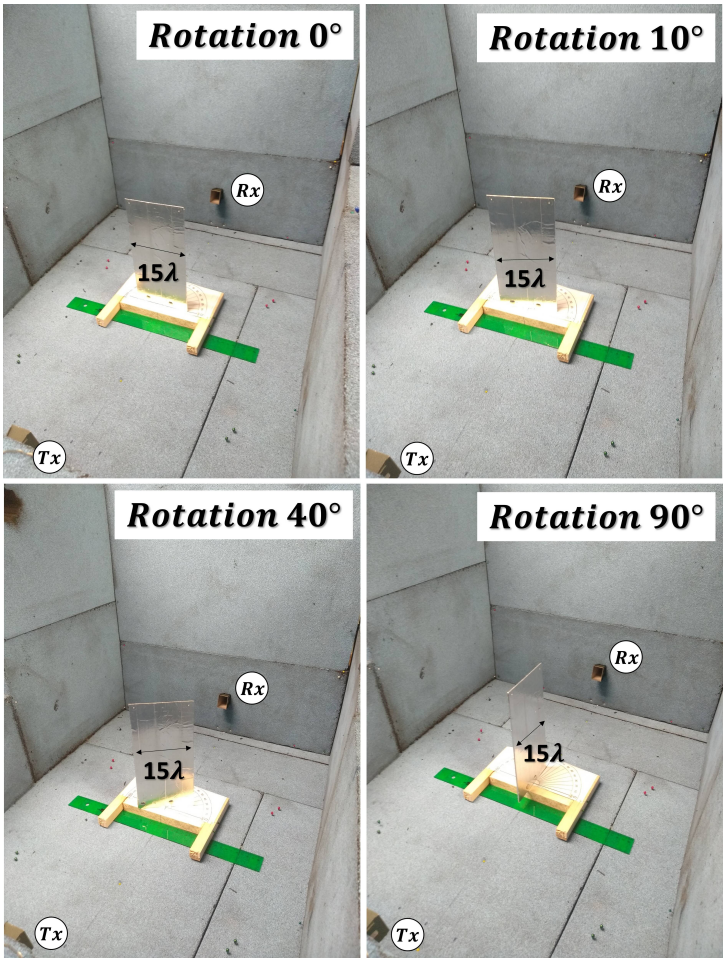

Figure 3.3: Measurements of a rotating flat obstacle to validate the DKE model.

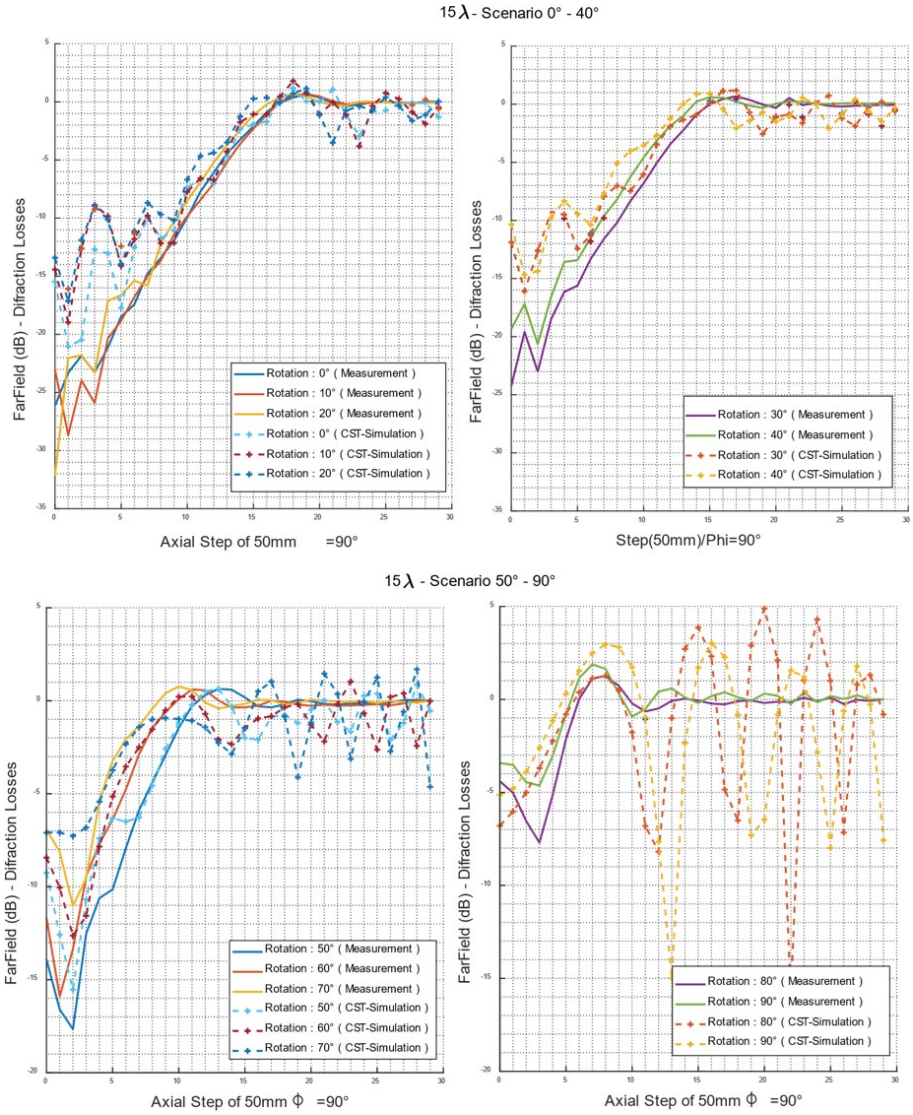

Figure 3.4: Normalized residual scattered field at the receiver with measurements and simulations. Obstacle dimension of 15λ, E Field with Polarization $\varphi = 90°$.

According to the results observed in figure 3.4, the simulation of the field dispersion in the angles between 80° and 90° is erroneous because it does not fit with the measurements, which is not critical because in the remaining slopes lower than 70° they agree. So the measurements match, taking into account the minimum mean square error (MMSE) parameter between two functions, which at 70° is MMSE = 0.96.

But the most important conclusion from the results is that, when the obstacle is rotated orthogonally to the orientation of the antennas, its occultation decreases as if it were electrically smaller from the point of view of the receiving antenna. This implies that the equivalent edge changes as a function of the obstacle orientation as can be seen in figure 3.5 where there are two obstacles, one of which has a considerably larger size (see figure 3.5.a) than the other (see figure 3.5.b).

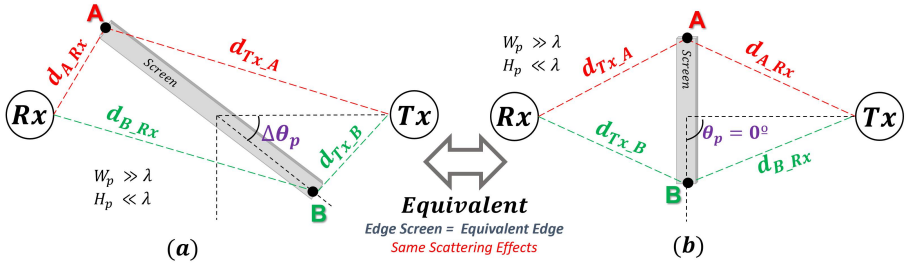

Figure 3.5: Equivalent concealment of two obstacles with different electrical dimensions.

But although the two obstacles have different electrical dimensions, their scattering effect on the residual field at the receiver is equal, and therefore their equivalent edges would be equal. Note that the DKE model only takes into account the distance to the visible boundaries of the obstacle. Therefore, when implementing this model, only the projection of the edges must be considered, which can vary drastically, depending on the relative position of the person in the indoor environment. Then, the complexity of implementing the DKE model comes from effectively identifying such equivalent edges.

3.2.2 Frequency Analysis

In the present analysis, the effect of the scattering caused by various obstacles with different electrical dimensions, measured and simulated at different frequencies, is evaluated in order to validate the Double Knife-Edge model in the bandwidth of interest from 30 to 40 GHz.

In these tests, the electrical dimensions of a flat obstacle are changed ($1\lambda, 3\lambda, 6\lambda, 10\lambda, 15\lambda, 20\lambda, 28\lambda, 40\lambda$ at 40 GHz) orthogonally to the positions of the transmitting and receiving antennas, with different target carriers (30 GHz, 32 GHz, 34 GHz, 36 GHz, 38 GHz and 40 GHz), separation distance between the antennas and the obstacle $d_{TX/RX} = 35\lambda$. Figures 3.6 and 3.7 show the results of the measurements performed.

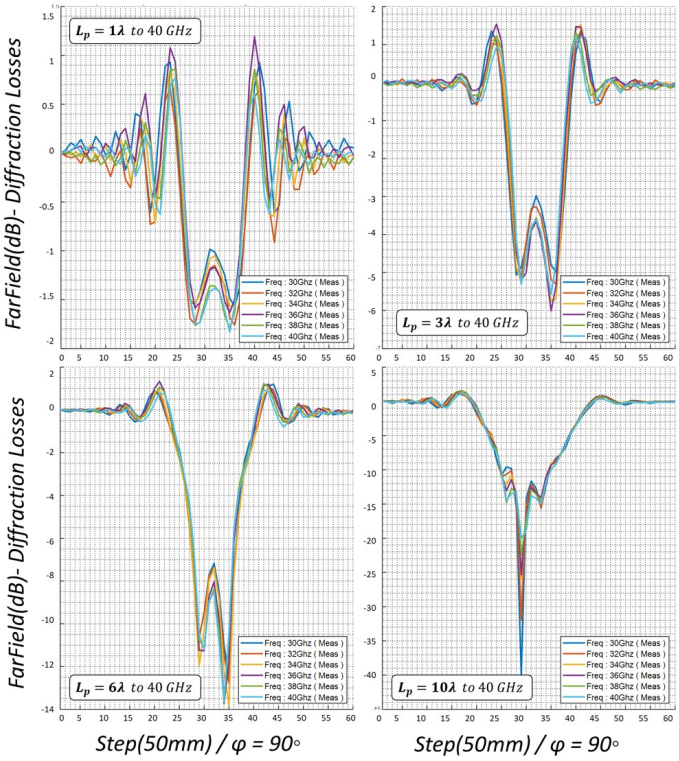

Figure 3.6: Residual scattered field by obstacles with electrical dimensions of ($1\lambda, 3\lambda, 6\lambda, 10\lambda$ at 40 GHz) in the frequency range from 30 GHz to 40 GHz.

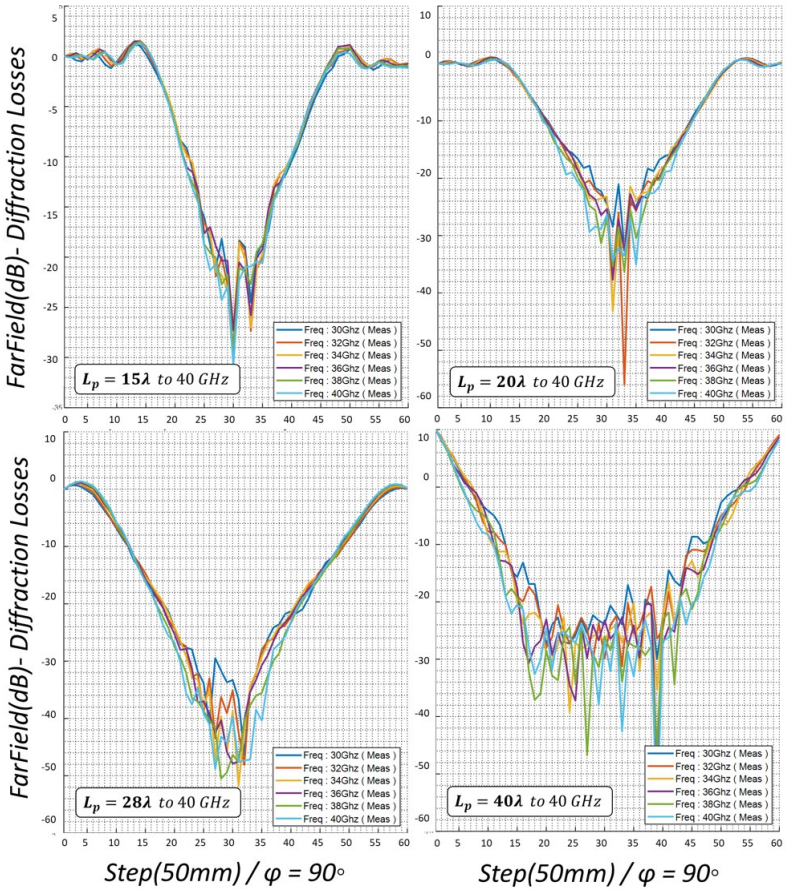

Figure 3.7: Residual scattered field by obstacles with electrical dimensions of $(15\lambda, 20\lambda, 28\lambda, 40\lambda$ at 40 GHz) in the frequency range from 30 GHz to 40 GHz.

According to the previous results, the residual scattered field measured with different dimensions of an obstacle at different frequencies at mmWave band is almost the same, therefore, the scattering in that frequency range has the same behavior, with a MMSE of 0.983.

Additionally, figure 3.8 shows the results of normalized scattering losses for a 15λ at 40 GHz obstacle, but compared to simulations and to the double Knife model implemented in Matlab.

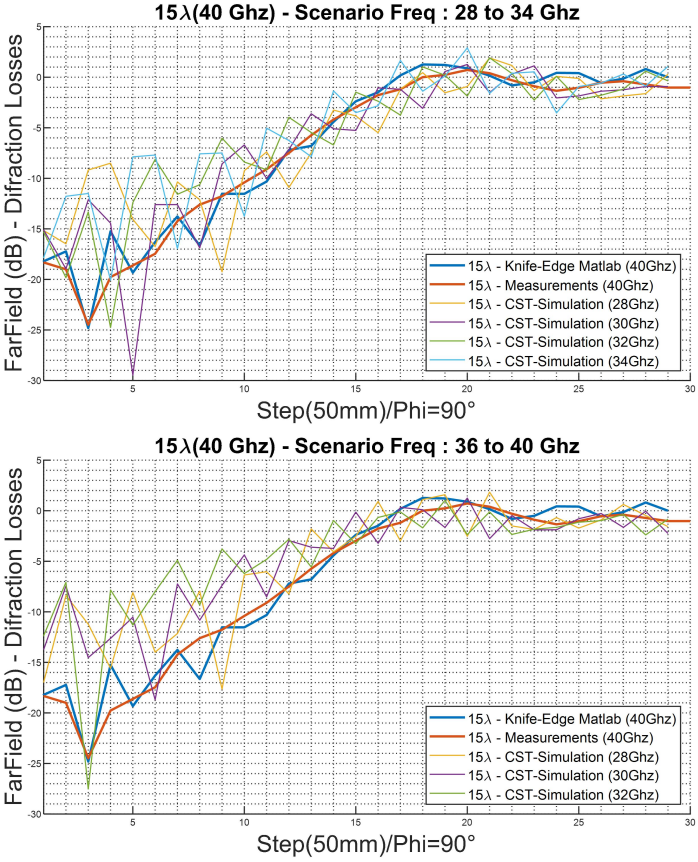

Figure 3.8: Residual scattered field simulated and measured by obstacle with electrical dimension of 15λ at 40 GHz compared with Double Knife-Edge implemented in Matlab.

Again after the last results in figure 3.8, it is reconfirmed that the DKE model is valid to characterize the obstacle masking at least in a bandwidth of 10 GHz, from 30 GHz to 40 GHz.

Recall that it is fundamental to be aware of the applicability limits of the DKE model discussed in the previous chapter, to characterize the scattering effect of the human body. The following section describes a measurement campaign carried out, in which simplifications of the morphology of the human body modelled with a flat metal obstacle were considered.

3.3 Measurement Campaign to Validate the DKE Model on the Human Body

Before starting to consider the measurement campaign on the human body, it is essential to briefly remember the applicability limits of the DKE model, which must be taken into account in order to model the scattering effect of the human body at mmWave, which are presented below:

- The minimum electrical dimensions of the cross section of the obstacle must be greater than 6λ .
- The minimum electrical distance between the obstacle and the antennas must be greater than 15λ
- With the proposed geometrical simplifications, the scattering effects of the obstacle thickness and the shape of its geometric volume can be ruled out if the equivalent edges to the obstacle from the TX/RX are known.
- The polarization effect on the scattering of the human body modelled by the DKE can be omitted if its electrical dimensions are greater than 15λ.
- The model is only validated for the frequency range of 30 GHz to 40 GHz, according to the measurements performed.
- The model is valid to characterize obstacles of totally absorbing materials at mmWave frequencies, or totally reflecting materials such as metallic surfaces.

The objective of identifying the applicability limits was not to confirm whether the model was valid for modeling the human body, because this hypoThesis had already been confirmed in the literature [30]. Rather, it was to know under what conditions this model would still be valid to characterize the human body in a complex dynamic environment, where people movement influences the radio channel, which would have to be constantly updated.

This constant updating implies running the model in a very efficient way, so, if the model can be simplified, it can be easily implemented in a simulation environment with proprietary ray-tracing techniques.

Therefore, in this section a set of measurements were carried out that confirmed the simplifications proposed to model the scattering effects of the human body with the DKE model.

3.3.1 Measurement Set-Up on the Human Body

The measurement campaign was conducted according to the set-up shown in the figure 3.9. The T_x and R_x were equipped with identical Ka-band horn antennas, manufactured by Sagemillimeter, model WR-28, operating at frequencies from 26 to 40 GHz, with a gain of 20 dBi [109]. The antenna 3 dB beamwidth is 18° in both the horizontal and vertical planes.

The R_x and T_x are connected to ports 1 and 2 respectively of the vector network analyzer (VNA) model is the RS-ZNB40. The measurements were carried out without using an anechoic chamber, because the T_x and R_x antennas are perfectly oriented facing each other to maximize their gain, and avoid external interference. T_x and R_x are separated by a distance of 100cm, and they move in steps of 1cm, until they cover 100cm, so for each T_x position it has been measured 100 R_x points.

Throughout the simultaneous sweep of the T_x and R_x antenna, the frequency response of the channel (S_{21};S_{12}) is measured over the entire bandwidth of interest from 30 GHz to 40 GHz at each position.

This process was performed to measure the scattered field contributions for both LOS and NLOS positions of T_x and R_x. The human body and its simplified geometric equivalent, is located halfway (50 cm) between the T_x and R_x antennas as shown in figure 3.9.

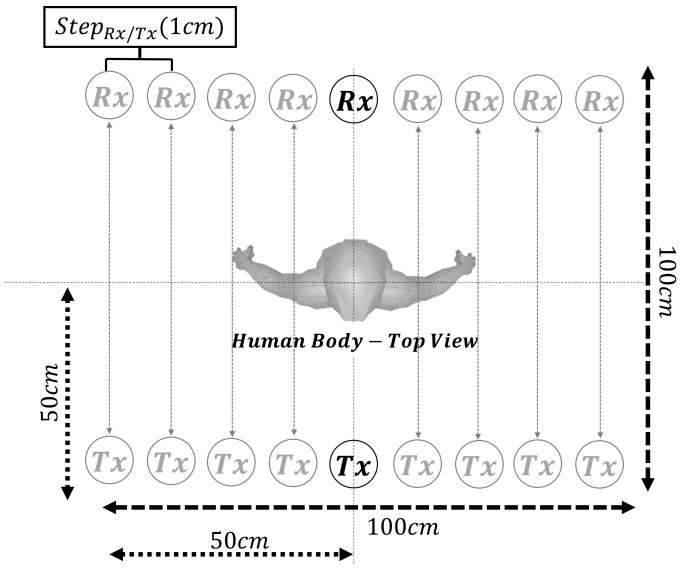

Figure 3.9: Setup scheme for the Human Body scattering effect measurement.

3.3.2 Analysis of Human Body Measurements

Before conducting the measurements it is important to remember one of the most important conclusions of the previous chapter, which is the simplification of the morphology of the human body: It can be affirmed that for using the DKED model the volumetric geometrical shape of any obstacle is not necessary if the equivalent contour of the original geometrical shape is available. Where the equivalent contour depends on the equivalent edges of the entire contour of the obstacle as seen in figure 3.10.

This statement is very important, because it allows to simplify the volumetric morphologies in such a way, that the DKE model can be implemented only knowing the relative distance to two edges of the equivalent contour, where the cross section depends on the positions of the antennas T_x and R_x as seen in figure 3.10.b.

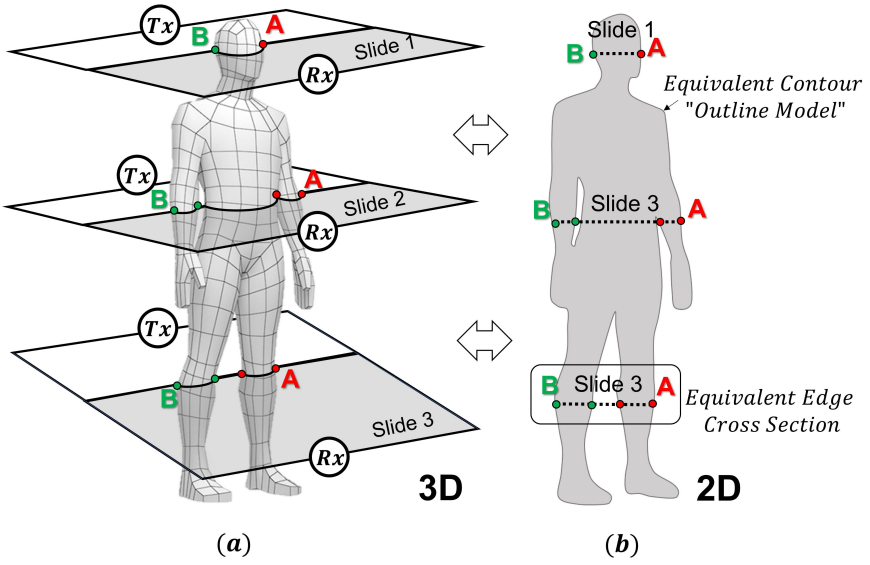

Figure 3.10: (a)Volumetric human body with cross-sections depending on TX and RX positioning, (b)Morphological equivalent of a volumetric human body (Outline Model).

With this in mind, the measurements were carried out in conjunction with the metallized flat geometric equivalent of the human body. And this must be metallized because it is the easiest way to emulate an absorbing material while transmitting at mmWaves.

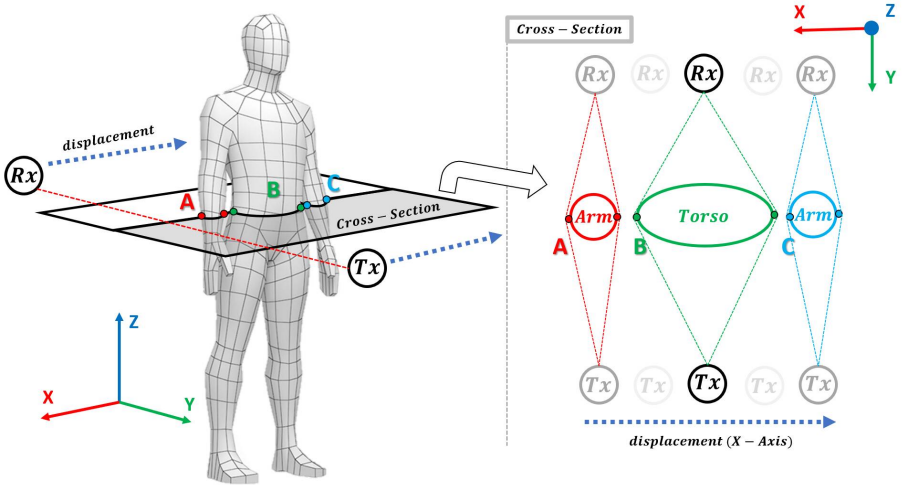

Figure 3.11: Equivalent edges of the human body cross-section in arms and torso.

According to the figure above it is important to note that only one obstacle at the time can obstruct the visibility of the transmitter and the receiver. Therefore, only two simultaneous equivalent edges per obstacle should be considered, where these edges delimit the region of concealment and how the DKED model is implemented.

For example, in figure 3.10.a, depending on the position of the TX and RX with respect to the human body, the concealment of the arm or torso will be considered independently or as the same obstacle. So, depending on the location of the TX/RX, different edges equivalent to the obstacles are considered, even when evaluating the scattering effects of the same human body.

The equivalent of the geometric contour of the person was made taking into account the outlines of the person. In order to accurately identify these contours, a shadow projection technique was used. This was carried out in a totally dark room, where a strong enough light source (10000 lumens flashlight) was projected towards the person, to delimit the equivalent contour of the person, and used to build our equivalent of the contour shape, which was built with cardboard and aluminum tape. Although it is a somewhat rudimentary procedure, it is precise enough to provide results almost identical to those measured directly with the human body, as can be seen in figure 3.12.

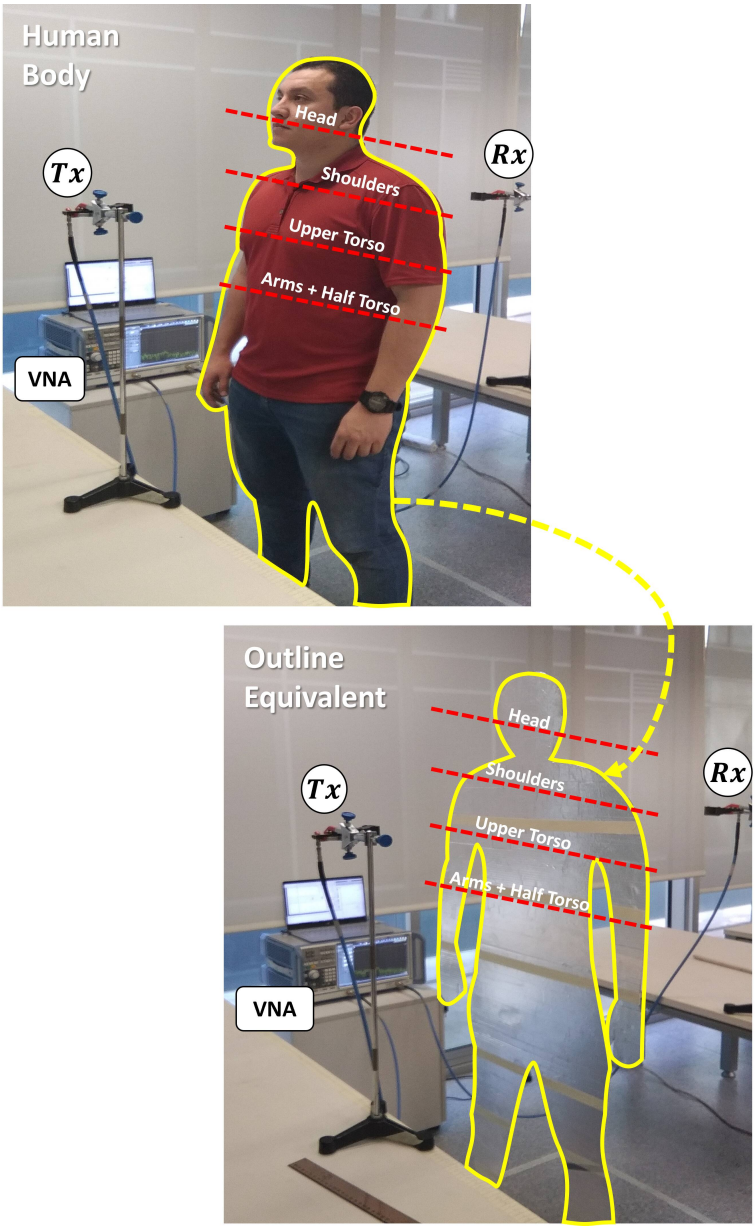

Figure 3.12: Photo of Real Measured Scenario.

The measurements were carried out for four different cross sections on the human body, at head, shoulder, upper torso, and half torso heights, with the arms separated from the torso, thus being two additional independent obstacles, as illustrated in figure 3.12. The measurements were performed on the same cross section for both the human body and its metallic flat outline equivalent, in order to compare how similar the scattered field measured by the obstacles is.

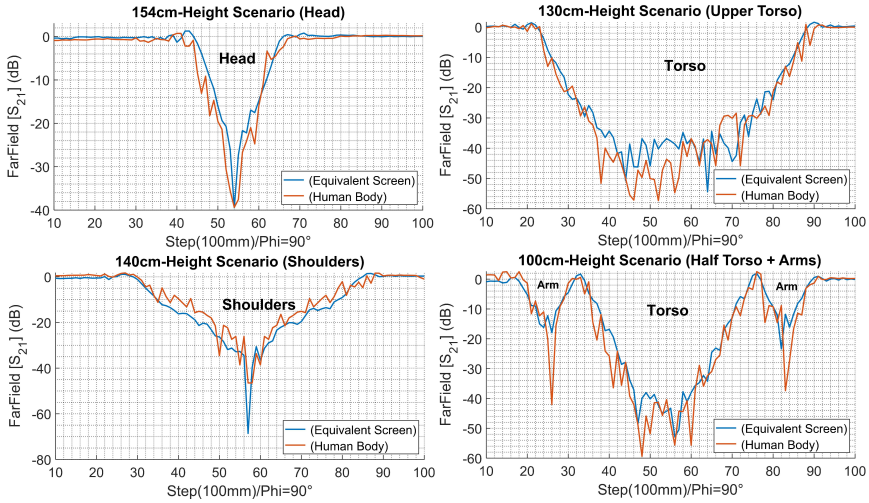

Figure 3.13: Measured scattered field of the human body with its contour equivalent.

According to the results obtained, it can be assured that the residual far field produced by the human body is almost identical to that produced by its equivalent contour. The simplification of the morphology confirms that applicability limits proposed in the previous chapter are valid, where only metallic objects were considered to carry out the measurements and simulation, due to the difficulty of having a material with the same electromagnetic characteristics as human tissues in mmWaves. Therefore, the feasibility of using the DKE model to characterize the scattering behavior of the human body is confirmed, with only information of its contour.

In addition to the measurements carried out previously, some other measurements were carried out using a metallized mannequin (See figure 3.14.a) instead of a person as a reference for measurements, in order to emulate the RF absorption of human tissues.

Together with the measurements of this mannequin, an equivalent of a metallized flat contour of the mannequin was created (See figure 3.14.b) n a way similar to the previous measurements that had been done on a person. One of the objectives of this measurement campaign is to confirm one of the most important premises of this study, i.e., that it is only necessary to have the equivalent edges of the obstacle to characterize its scattering effects by means of the DKE model. For this reason, it was intended to reconfirm what had already been concluded in the previous chapter, where the thickness of an obstacle, or in this case the thickness of the metallized mannequin, is not dependent on the equivalent edges, and therefore its residual scattered field will be exactly the same.

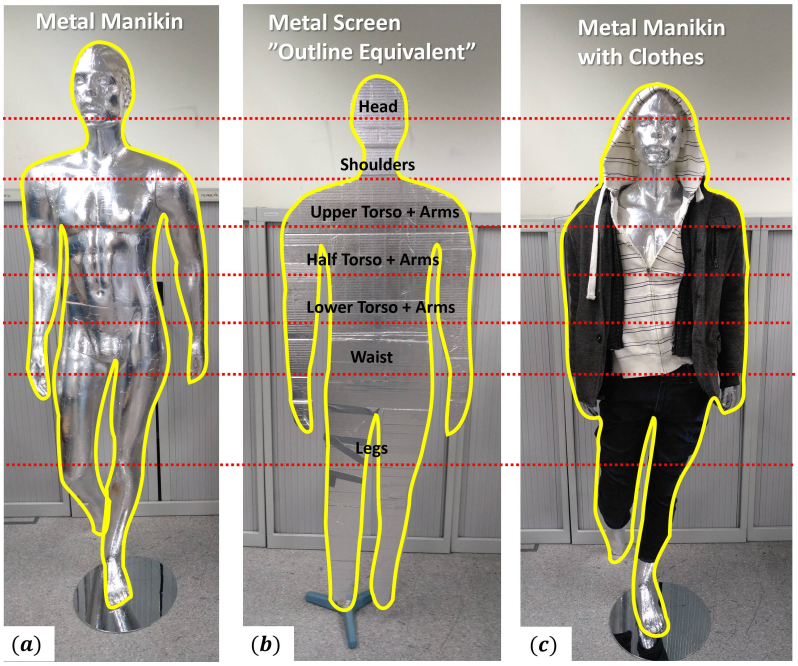

Figure 3.14: (a) Metallized mannequin emulating a person's morphology, (b) Metallic equivalent of the mannequin, (c) Metallized mannequin dressed with dense winter clothes.

Measurements were also made with a mannequin dressed with winter clothing, which is usually thicker, to identify which effect it has on the scattered field in mmWaves (See figure 3.14.c).

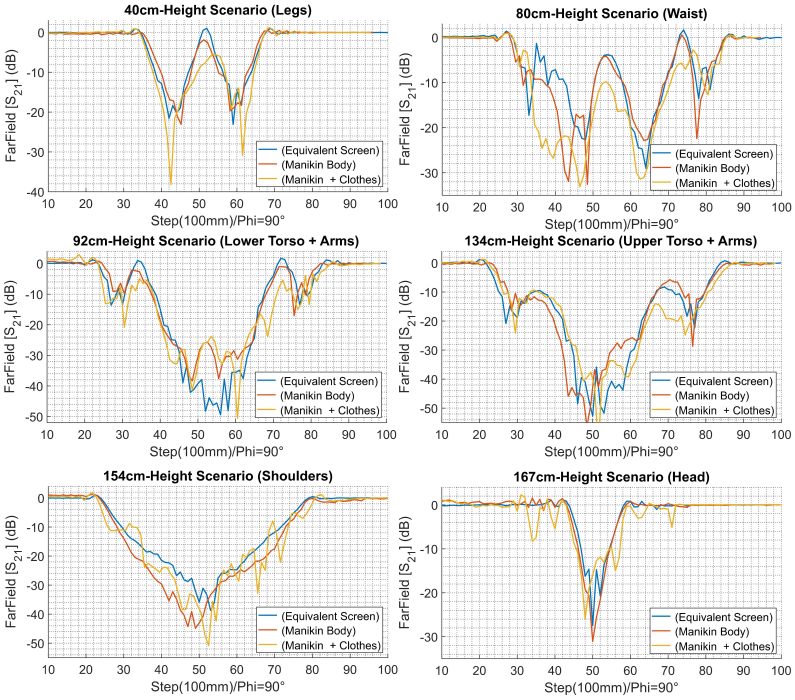

Figure 3.15: Measured scattered field of metallized mannequin with its equivalent contour with and without clothing.

According to the results obtained, it can be assured once again that the residual far field produced by the volumetric metallized mannequin is almost identical to that produced by its equivalent contour. Therefore, the simplification of the morphology is fully valid to simulate the scattering effects of the human body using the DKE model without having a reference person. This allows to conduct measurements in complex environments using only mannequins instead of people, which allows to do measurements with greater flexibility and more stability, since it will not be necessary to have one or more people in a fixed position at all times to evaluate their effect.

Additionally, the effect of clothing is negligible, because it is only appreciable in concealment zones with scattering losses above 20 dB, although in some cases, such as the cross section of the head measurement, its influence is more noticeable because the mannequin has the hood on. Therefore, due to the high randomness involved in characterizing a constantly moving clothing, the effect of the clothing can be omitted for practical purposes in mmWaves.

3.4 Game Engine Simulation Tool

The platform used to design a proprietary ray tracing system and simulate the scattering effect of the human body at mmWaves, with the DKE model, is called "Unity", which is a video game platform that is explained in detail in Annex 1 (Section A.3).

This video game software was only used to emulate the scattering effect of the Human Body without other external programs like Matlab, previously used to validate the DKE model with measurements and simulations. The simulations performed with Unity are totally different from those done in CST Microwave Studio, because in Unity the human body model was implemented from zero using exclusively ray-tracing techniques and the DKE model. Electromagnetic simulations of a radiation source being obstructed by various kinds of objects with electrical dimensions smaller than the human body morphology were carried out with CST in order to validate the applicability limits of the DKE model.

Therefore, characterizing the scattering effect of the human body was divided into two phases: (1)to design a ray-tracing system for Unity, and (2) to make use of that ray-tracing system to emulate the scattering effect on three-dimensional objects, where the main challenge is to identify the equivalent edge of any 3D mesh, independent of its position in space.

3.5 Simplified Ray-Tracing system to implement the DKE model

This section briefly describes the implementation of the proprietary ray-tracing tool that has been designed within Unity. Its objective is to implement the DKE model to characterize the scattering behavior of the human body scattering in three dimensions in a simulation environment.

Ray-tracing techniques are deterministic strategies for analyzing the radio channel in mmWaves. One of the advantages of using ray-tracing techniques over stochastic approaches is that a more complete study of the channel characteristics can be performed, although it is much more computationally costly.

But, although in our case the objective of this chapter is to predict the channel scattering exclusively over the human body, it would also apply to obstacles that meet the applicability limits of the DKE model.

The Ray-tracing techniques are based on Geometrical Optics (GO), and it has been shown that this deterministic technique is more efficient to characterize the radio channel compared to Finite Difference Time Domain (FDTD) approaches [111].

The Geometric Optics (GO) approach on which our Ray-tracing system is based is only applicable in those cases where the dimensions of the obstacles blocking the RF signal are much larger than the wavelength, and, according to the applicability limits, the obstacles to be analyzed will have to be at least 6λ.

Among the methods or procedures to obtain the different trajectories of the contributions that reach a receiver, we can mention the Virtual Imaging Method, and the method based on Ray Casting techniques, as described below.

- **Virtual Image Method**: This modeling technique consists of calculating the images of the receiver with the bigger walls, and floors, and then calculating the trajectories from the transmitter to each of the images. The dual method consists in calculating the trajectories from the transmitter to the receivers. This technique was first used in [112]. By having calculated the position of the transmitter and the images of the receivers (or vice versa), the trajectories of the optical rays that define the wavefront are perfectly defined, and can be accurately traced. For this reason, this technique is often referred to as Image Approach Method (IAM). In this technique the total received power can be obtained as the coherent sum of all the contributions, taking into account the phase, in addition to characterizing the impulse response of the channel. This method is inadvisable when the simulation environment is complicated, and especially when more than two reflections are to be considered, since the calculation time increases dramatically with the order of the reflections.

- **Method of Ray Casting**: The methods based on ray casting consist basically in launching uniformly from the transmitter a finite number of rays into space, thus covering the entire solid angle. For each ray cast, multiple reflections, transmissions and scatterings that may occur along its trajectory until it reaches the receiver are considered. The number of reflections or transmissions to be accounted for will depend on the attenuation level above which a contribution can be neglected, or may be limited at a given number of interactions with obstacles. All the settings of how the method should behave will depend on the developer. The method is very useful in complicated environments as it allows easy tracking of reflections, transmissions and diffractions if programmed for that purpose. In fact, if the trajectory of each ray is known, it will be easier for the developer to know where each contribution comes from and thus make a more detailed debugging process. Although this is usually quite computationally expensive, the advantages outweigh the complexity of it. This method of ray tracing is usually referred to in the literature as *Ray-Tracing* or *Ray-Launching* without further ado.

In this chapter, Ray-Tracing accounts for the contributions by reflections and diffractions. Diffractions will help us to determine the equivalent edges of an obstacle on which a ray has impacted, on which the DKE model will be applied.

The implementation of the ray-tracing system to apply the DKE model to characterize the scattering caused by the human body in a simulation environment consists of four clearly differentiated steps:

- Design of a transmission source.
- Analysis of the impact of each ray on an object.
- etermination of the output direction of each ray.
- Implementation of the DKE model according to the rays that have reached the receiver.

3.5.1 Design of a transmitter source

In the ray tracing technique what is done initially is to define a source of radiation, which in our case is determined by a "*GameObject*" in Unity that does not have any mesh, and therefore the physics collisions will not affect it. This is important because it will be a GameObject that will not interact with the other objects in the scenario.

The transmission source that is associated to a "*GameObject*" is treated as an infinitely small point from which rays emanate with the Unity command "Physics.Raycast" in all directions, if an omnidirectional antenna is simulated. In our implementation we simulated a horn antenna so that the number of rays in the scenario is lower, thus reducing the computational load.

Each ray emanating from the transmitter has a variable output angle in azimuth and elevation that will depend on the angular resolution of the radiation source (See figure 3.16). This angular resolution $(\triangle\theta, \triangle\varphi)$ is fully programmable and is adjusted for calibration purposes. It is determined empirically throughout the simulation and depends on the relative distance of the obstacle from the transmitter. For electrically small indoor scenarios a lower angular resolution is sufficient, while a higher resolution is required when the radio channel is evaluated in large scenarios or with electrically large objects.

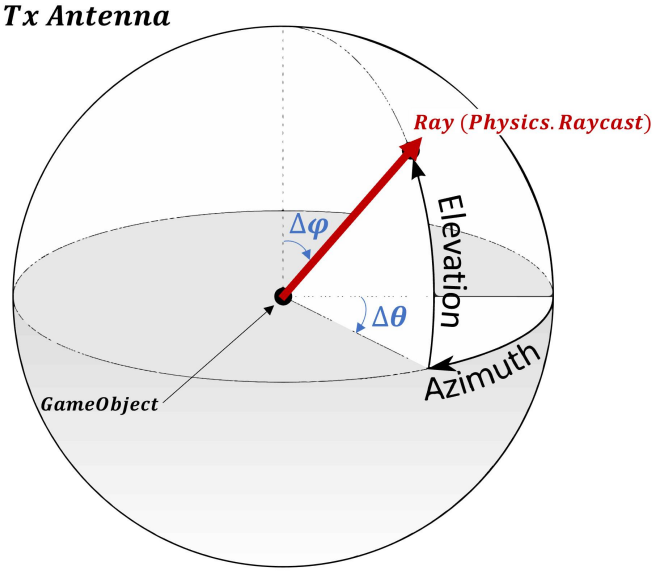

Figure 3.16: Emulated Transmitting Antena in Unity.

But this angular resolution $(\triangle\theta, \triangle\varphi)$ value is impossible to be obtained deterministically, since each scenario is different, and it will have to be evaluated individually. As an example of a simulation strategy, one can initially use an antenna with an angular resolution of 5° and progressively increase the resolution.

For instance, if with an angular resolution of 5°, there is a contribution that reaches the receiver with the transmitter output angle of θ=20°, φ=30°, when increasing the angular resolution to 0.1° we would likely have several contributions at θ = (19.1°: 0.1°: 21.0°) and φ = (29.1°: 0.1°: 31.0°). According to preliminary test simulations to calculate the effect of the DKE on Unity, the optimal antenna resolution will be 5° instead of 0.1°, Because simulating with an angular resolution of 0.1° will be computationally more expensive without any significant gain in accuracy. Therefore, a preliminary analysis must be done to know which is the optimal resolution of our antenna.

All the rays launched by the command *Physics.Raycast* interact in a three-dimensional scenario in Unity, where the position of the antenna will be the position of the *GameObject* associated to the antenna. The command statement is given by the following instruction:

public static bool Raycast(origin, direction, maxDistance, layerMask, QueryTriggerInteraction);

- **origin** (*Vector3*): The ray's origin in geographic coordinates.
- **direction** (*Vector3*): The direction of the ray.
- **maxDistance** (*float*): The greatest distance at which the ray should look for collisions.
- **layerMask** (*int*): Using a layer mask, it can be chosen which collisions to ignore when casting rays.
- **queryTriggerInteraction** (*QueryTriggerInteraction*): Indicates if this query should trigger any action.

3.5.2 Analysis of the impact of each ray on an object

To carry out the analysis of the impact on the objects, it must be considered that, once a ray leaves the antenna, it interacts with all the other objects of the scenario independently, and generates events on each *GameObject* impacted independently and sequentially.

In each obstacle *GameObject* there is a physical event called "*Collider.OnCollisionEnter(Collision)*". This event is triggered when a ray hits a specific GameObject and provides information about the object that hit it. This information contains the name of the object that hit, where it came from, and where it hit, among others.

By using this information each obstacle can know what is the output angle (azimuth and elevation) of the ray that has hit it, the output power of the ray, what is the position of the antenna *GameObject* that has launched the ray, etc.

This event was declared in Unity C# as follows:

```
using UnityEngine;
using System.Collections;

public class ExampleClass: MonoBehaviour
{
 void OnCollisionEnter(Collision collisionRay)
    {
    }
}
```

Where the variable that has the information is of type Collision and is called "*collisionRay*". This variable is *object* type and has the following properties (Information).

- **Collision**(properties):
  - *articulationBody*: The ArticulationBody of the collider that the GameObject collides with (Read Only).
  - *body*: The collider's rigidbody or articulation body that the component encounters (Read Only).
  - *collider*: A collider is hit (Read Only).
  - *contactCount*: The number of contacts for this collision is returned.
  - *gameObject*: The game object with whose collider is in contact. (Read Only)
  - *impulse*: The total impulse that was used to settle the collision between these contact points.
  - *relativeVelocity*: The two objects colliding at their respective linear velocities (Read Only).
  - *rigidbody*: The rigid body impacted (Read Only). If a collider without a rigidbody is struck, then this value is nil.
  - *transform*: The Object's Transform that is hit (Read Only).

With the "*Collision→collider*" variable, it can be determined which object is hit and where. With the information of the hit object, the treatment of each ray can be filtered. For example, when a ray hits an obstacle such as a wall, a ceiling, etc., this ray will be reflected specularly, without any additional treatment, but if the ray hits a human body obstacle, our algorithm displaces along the vertices of the mesh of the human body geometry a distance equal to the first Fresnel radius, as shown in figure 3.17.a.

This displacement helps to determine how close it is to an equivalent edge from which the ray hit the obstacle. At each displacement on the vertex our algorithm projects a ray with the same direction of arrival and, if it does not hit the same obstacle again, i.e. the human body, it means that the obstacle is on a potential equivalent edge (See figure 3.17.b). This equivalent potential edge will be the starting point to identify if there is a receiver nearby or not.

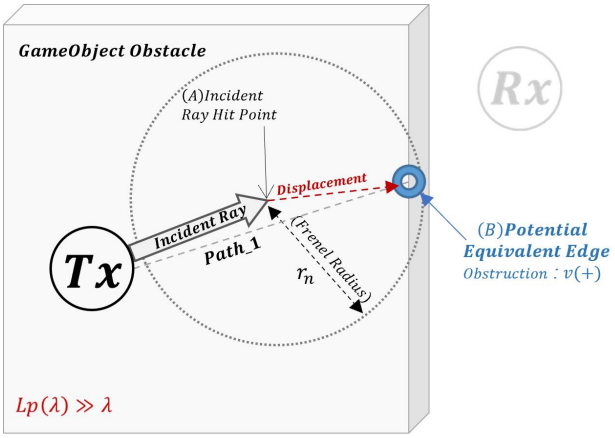

(*a*)

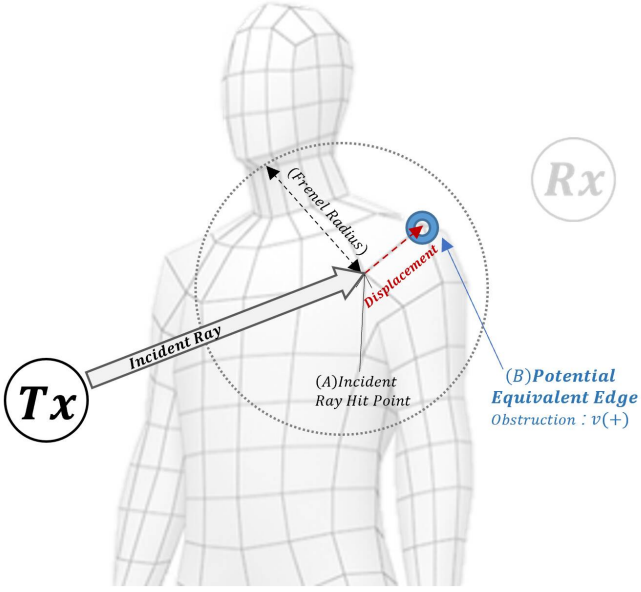

(*b*)

Figure 3.17: (a) Analysis of the equivalent edge on a basic obstacle, (b) Analysis of the potential equivalent edge on the mesh of the morphology of the human body.

3.5.3 Determination of the output direction of each ray

To carry out this analysis of the output direction of the ray that has previously hit an obstacle it is worth to classify whether the ray hits the scenario or whether it hits the morphological equivalent of the human body.

If the ray hits the furniture or the scenario(Walls, Ceiling, Floor), the output direction of this ray is specular to the normal of the surface where it hit. In Unity C# generating the direction of a specular reflection is relatively simple, and it is done by the following instruction:

Vector3 reflectVec = Vector3.Reflect(incomingVec, hitObstacle.normal);

Where this command is fed with two dimensional vectors: the first one "*incomingVec*" refers to the direction vector with which the "*hitObstacle*" obstacle has hit, and the second is the normal vector of the face from which the incident ray has hit. The result of this function is the three-dimensional vector "*reflectvec*", which is the resulting specular reflection after hitting the "*hitObstacle*" obstacle. With this simple command we can emulate specular directions in Unity C#.

Identifying the ray output direction in case it has hit the equivalent morphology of the human body is not as simple as in the previous case of specular reflection. In this case it is assumed that we have identified the position of the equivalent potential edge. In this position a decision cone is projected, which consists of casting a set of rays from the potential equivalent edge, and this decision cone has an opening angle of $\triangle p = 10^{o}$ in azimuth and elevation, taking as reference the direction of entry of the previously incident ray (See figure 3.18.a).

The objective of casting this set of rays is to identify if in the decision cone some of the rays hit the receiver. And, in case no ray hits the receiver, the potential equivalent edge is totally discarded, and will not be part of the further analysis of the DKE model. But in the case that any ray of the decision cone hits the receiver, the edge ceases to be a potential equivalent edge, so the position of this edge is stored in a database of all the rays of the antenna that have hit the human body.

All this analysis summarizes that, depending on where a ray hits a three-dimensional geometrical model of the human body, equivalent edges are defined, which vary with the position of the receiver and transmitter.

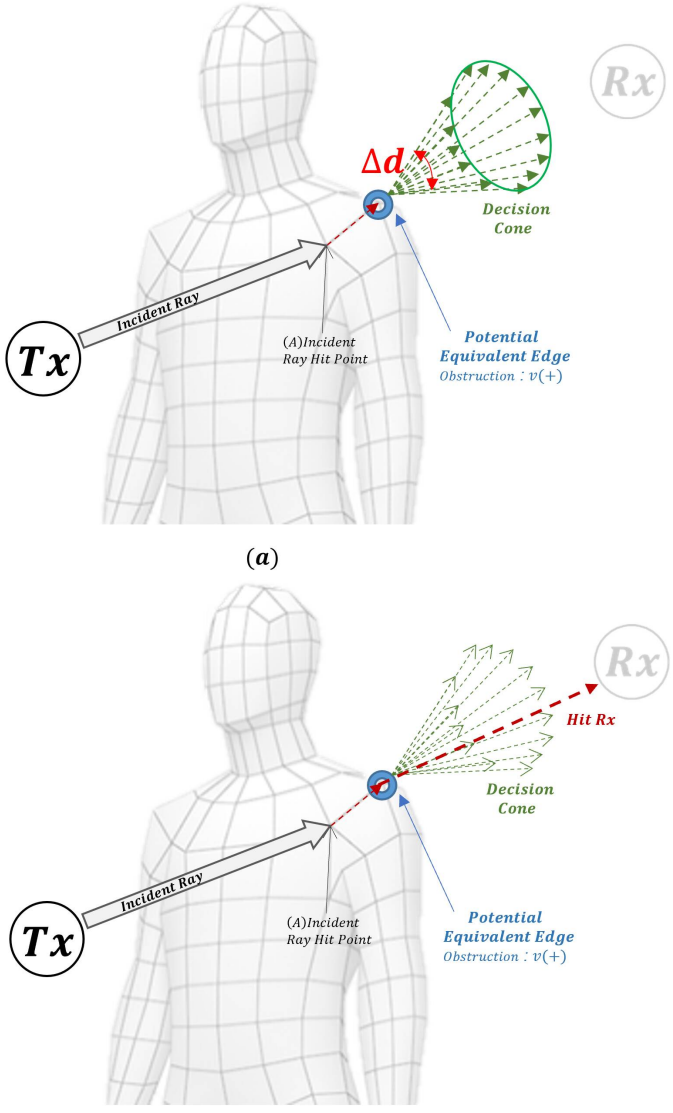

Figure 3.18: Decision cone on a potential equivalent edge on the morphology of the human body.

Figure 3.19 shows how the above analysis is performed in the Unity simulation environment, but only using one beam of the transmitting antenna.

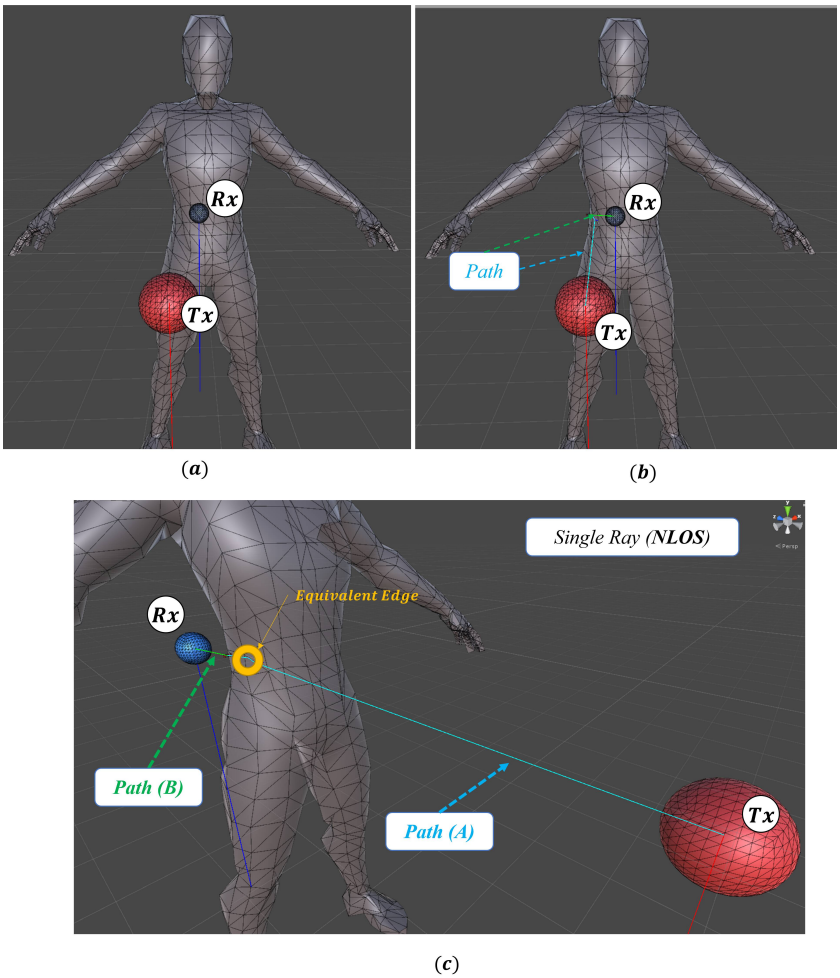

Figure 3.19: (a) Relative positions of the transmitter, body and receiver in the simulation environment without additional obstacles, (b) Front view of the simulation performed only considering a single antenna ray, (c) Side view of the simulation with the projection of the distance from the transmitter to the equivalent edge and from the equivalent edge to the receiver.

3.5.4 Implementation of the DKE model with Ray-Tracing

As seen in the previous sections, if the information about the equivalent edges of the human body is available, the DKE model can be implemented in a straightforward way. The complexity of implementing this model comes from the implementation of the Ray-Tracing techniques briefly explained above. The final result is shown in figure 3.22, where the ***path A*** is known because the position of the transmitting antenna and the position of the equivalent edge are known, and the ***path B*** is known because the position of the receiver and the position of the equivalent edge are known.

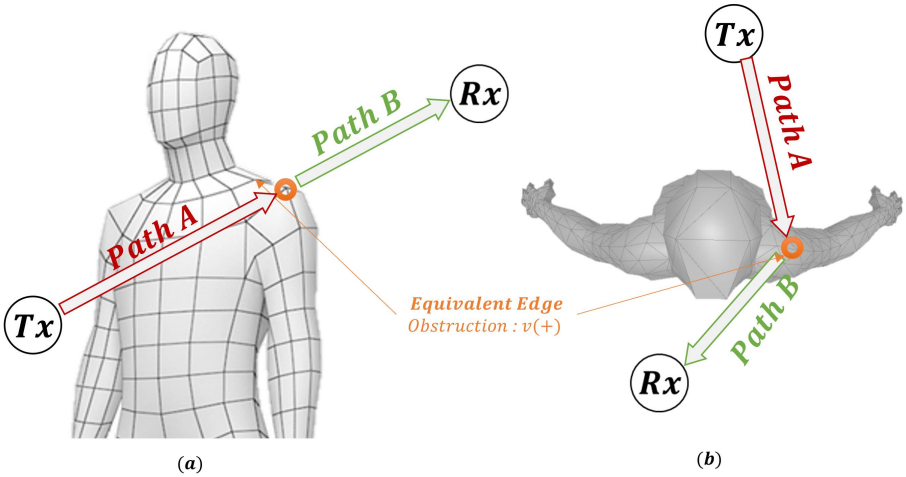

Figure 3.20: (a) Lateral view of the projection of the distances to the equivalent edge in the NLOS zone, (b) Zenith view of distance projection to equivalent edge.

Note that the example in figure 3.20 is only explanatory because only one ray is analyzed. In the simulations carried out we considered a horn antenna with hundreds of rays arising from it, since the analysis has to be performed considering a large number of rays that are potentially eligible to characterize the human body with the DKE model as seen in figure 3.21.a.

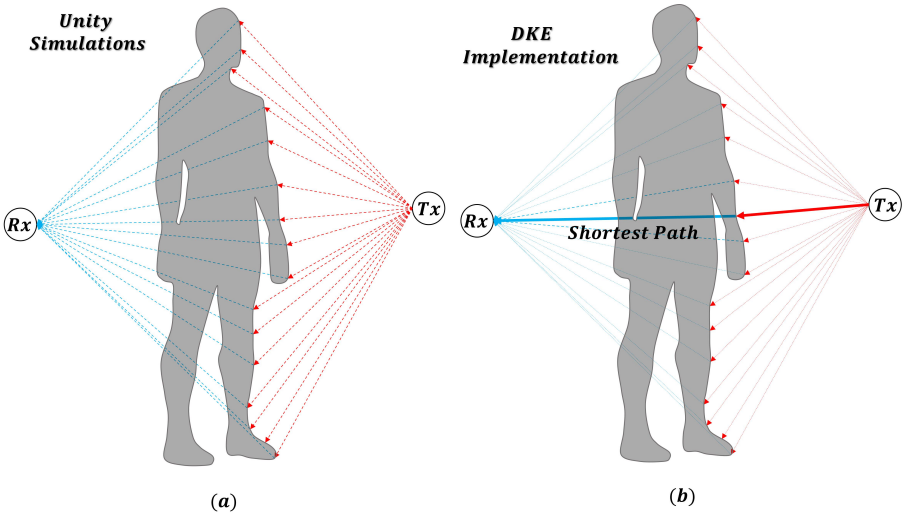

Figure 3.21: (a) Projection of all the equivalent edges identified by the simulation tool, (b) Choice of the equivalent edge with the shortest projection distance.

Then, to evaluate the scattering caused by the human body it is only necessary to consider at most two distances that delimit the obstacle, which in our case are defined by the equivalent edges explained above. Since only two distances can be applied to the DKE model, the shortest ones are chosen, those that delimit the concealment produced by the obstacle as shown in figure 3.21.b.

This approach is illustrated figure 3.22, which shows the simulator results, where in figure 3.22.a an antenna is designed with a single radiating beam along the X-axis, which only hits the human body along that axis and hence he ray-tracing algorithm designed in this PhD activity deduces the equivalent edges along that axis. At the end of the ray-tracing calculation, there are only two possible paths to the right side of the human body that depend on the relative positions of the transmitter and receiver, as shown in figure 3.22.b.

Note that not all rays incident on the geometrical model of the human body have potential paths to the receiver, because these paths depend on the parameters of the decision cone and the maximum distance through the vertices as a function of the first Fresnel radius.

This same example is also shown in figure 3.22.c-d but with an antenna radiating along the Y-axis, where all the rays are hitting on the right side of the human body and therefore there will be more alternative paths to the receiver compared to figure 3.22.a-b, but remember that only the shortest path on that

side will be taken into account to implement the DKE model. In addition to this single axis analysis, it has also been performed with a full antenna where both azimuth and elevation rays are considered to simulate a horn antenna, and the results are as shown in figure 3.22.e-f.

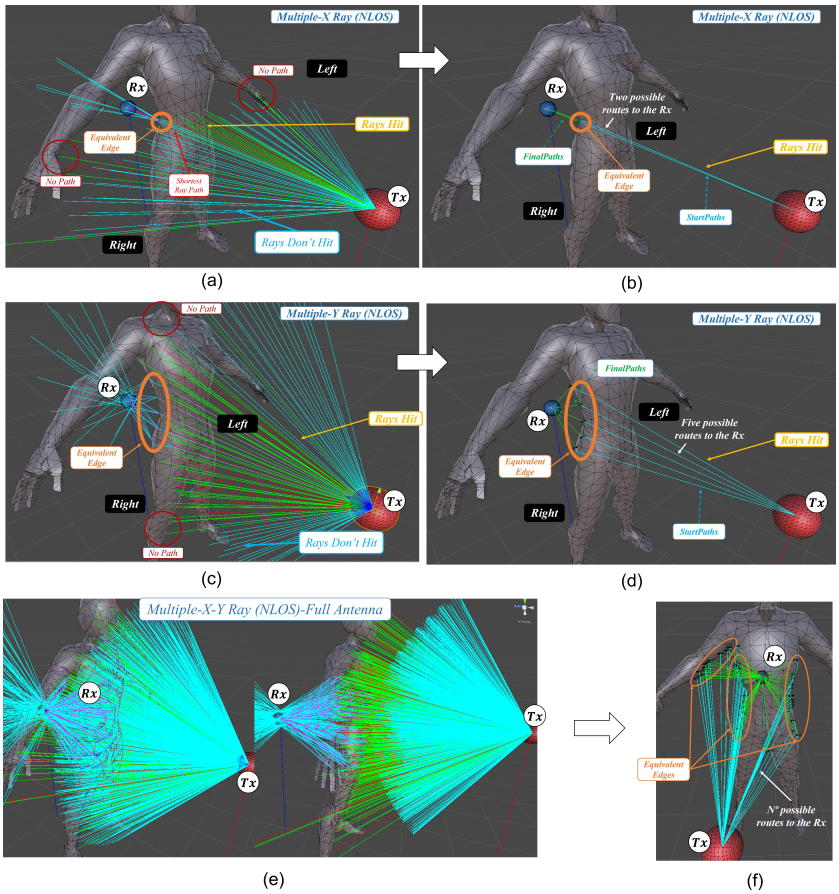

Figure 3.22: (a) X-axis ray casting, (b) Resulting paths to equivalent edges from X-axis, (c) Y-axis ray casting, (b) Resulting paths to equivalent edges from Y-axis, (e) Y-X-axis ray casting, (f) Resulting paths to the equivalent edges from a horn antenna with azimuth and elevation radiation.

Finally, the same analysis is made on the morphology of the human body both in a simple and in a complex indoor scenario, in which not all the rays

impacting the body come directly from the transmitting antenna but some come from the specular reflections of the environment. This makes the computation of the contributions much more complex, but it is also taken into account in the simulation tool (See figure 3.23).

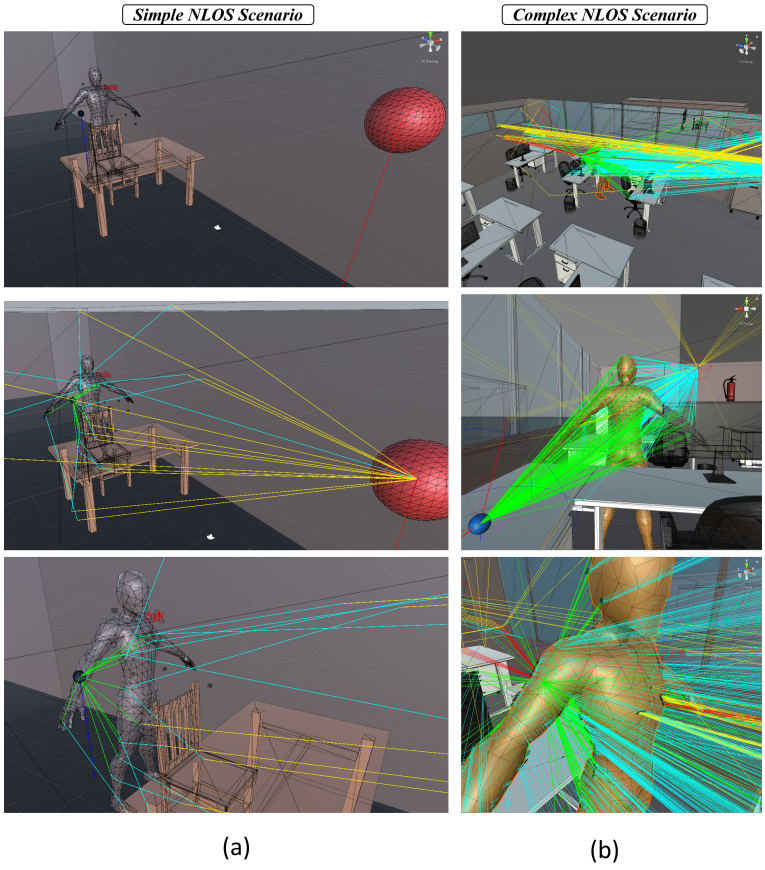

Figure 3.23: ((a) Simulation of the human body characterization in a simple indoor scenario, considering specular reflections. (b) Simulation of the human body characterization in a complex indoor scenario, considering specular reflections.

3.6 Conclusions

In this chapter the applicability limits proposed in the previous chapter to implement the Double Knife-Edge model were confirmed with measurements.

Evaluations were also made on the cross section of the obstacles when they change their orientation with respect to the transmitting and receiving antennas. This analysis was important because it reconfirmed that only the geometrical limits of the obstacle are required to characterize its scattering effect in mmWaves.

Furthermore, the effect of frequency on the scattering behavior of an obstacle was tested, and it was concluded that in the range of 30 GHz to 40 GHz the applicability limits are respected.

Finally, the implementation of the DKE model with proprietary Ray-Tracing techniques was addressed, where the biggest technical challenge to implement the model is to identify the geometrical limits of the obstacle, independently of its orientation with respect to the antennas.

Chapter 4

Diffuse multifocal flat reflector for coverage optimization

This chapter presents the development and design procedure of a diffuse reflector in the millimeter band, in order to optimize the radio access network (RAN) coverage and performance. The objective is to evaluate different geometrical structures with different types of rough surfaces, to emulate a diffuse reflection, with a parametrizable surface. Additionally, the feasibility of using a diffuse reflector to optimize coverage in non-line-of-sight (NLOS) areas in complex indoor environments with high propagation losses is evaluated. The methodology used to design a parametrizable rough surface using the 3D modeling tool Blender is also presented, as well as the simulation of this type of surfaces in the electromagnetic analysis software CST.

To this aim, this chapter has been divided into the following sections:

- Section 4.1 presents a brief introduction.
- Section 4.2 presents the technical basis on which the reflector is based to distribute the received energy.
- Section 4.3 presents the design guidelines expected in the reflector to operate in complex indoor environments.
- Section 4.4 presents the 3D modeling tool used to design the parametrizable diffuse reflector by using python code.

- Section 4.5 presents the simulation strategies used to evaluate each designed reflector using an iterative approach.
- Section 4.6 presents the setup used within the simulation tool to evaluate each designed reflector.
- Section 4.7 presents the measurement campaign used to validate the proposed reflector.
- Section 4.8 presents the conclusions of this chapter.

4.1 Introduction

As the number of wireless data services has increased dramatically in recent years, it is certain that the current mobile communication networks will reach their saturation point soon. Currently, much attention is being paid to wireless communication systems in higher frequency ranges because there is so much spectrum available. So mmWave communications, around 30 GHz, can support much higher data rates and much lower latency. For this reason, the use of this spectrum segment has been considered indispensable for the implementation of future fifth generation (5G) systems [90], [113], [114], [115].

Millimeter-wave communication is applicable to both indoor and outdoor environments, and its propagation has different characteristics compared to the propagation of today's cellular network. For example, it has very low dispersion and high penetration losses, both indoors and outdoors. These negative characteristics greatly limit the coverage of a millimeter-wave base station and drastically reduce the received power in non-line-of-sight (NLOS) areas. And, as concluded in the previous chapter, the human body will be one of the major impediments to proper propagation and characterization of the radio channel.

To increase the coverage area for mmWave communication systems, many solutions have been presented. Below, we list a brief literature survey:

- Reduced cell size [116]: The idea of this solution is to increase the number base stations in the area. This may improve link performance, especially at cell edge. However, it will also lead to a higher number of handovers between cells, which will make the RAN management algorithms more difficult.

- Increase of repeaters [117]: This method consists of multiple repeater nodes that can amplify and forward signals from a single base station. This can improve link performance in NLOS areas and increase the coverage area of a cell. The authors note that the node density should not be too high to achieve a significant increase in throughput. This will make systems more complicated and costly to maintain. In addition, too many repeater nodes are not energy efficient.

In this chapter we propose a new mmWave indoor coverage scheme. This scheme is based on diffuse passive reflectors. This scheme has many advantages over the other options, such as simpler structure, higher energy efficiency, installation flexibility and maintenance. It can also increase the coverage area of a mmWave base station. This premise has been confirmed by measurements with a flat specular reflector, according to the following studies [118] and [119], but only in an outdoor environment. The results obtained by these studies have shown that coverage can be increased up to 500 m using several passive specular reflectors.

It is important to note that the use of a specular reflector is not the best solution, because the radiation from the reflector is strongly influenced by the arrival angle of the radiation, as shown in figure 4.1(a). This solution is only valid for scenarios where all variables affecting signal propagation are controlled, because the location of the base station and the mobile terminals in the scenario are defined, in addition to knowing the geometrical composition of the scenario.

But in the case of real scenarios, the position of the base stations, the specular reflectors, and especially the positions of the mobile terminals, are unknown. This fact makes the implementation of the radio access network (RAN), with this type of reflectors, unfeasible.

Therefore, one of the purposes of this chapter is to design a diffuse reflector, which spreads the incident energy on a fixed spot homogeneously, being the radiation from the reflector independent as much as possible of the incidence angle, as shown in figure 4.1(b).

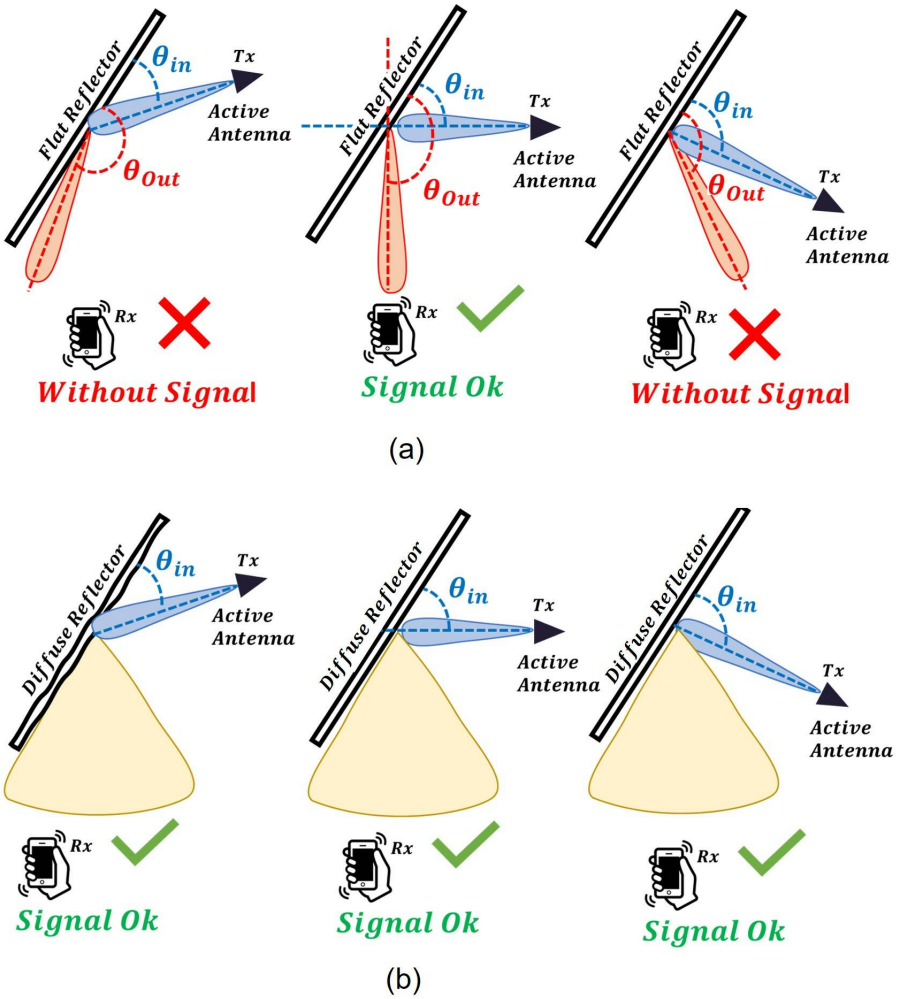

Figure 4.1: Specular reflector vs Diffuse reflector for mmWave coverage management in 5G Systems.

4.2 Passive reflector based system model

In this part we introduce the system model of our proposed approach. We briefly review the radar cross section (RCS) estimation approach because it is used in the passive reflector design process to get a notion of the reflector effective surface area. Therefore, initially the radio channel propagation model must be defined in a complex indoor environment, where the base station is located on top of a wall or at the ceiling of the room, and it is focused to a passive reflector. This strategy is used to avoid the high propagation losses caused by the people in the room as shown in figure 4.2.

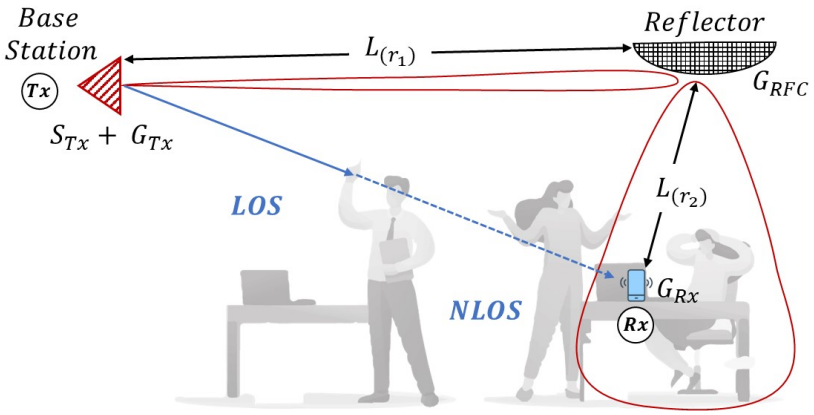

Figure 4.2: System model of reflectors-based mmWave link.

In our suggested strategy, we deploy a passive reflector over the user where coverage is intended to be increased. The radiation in the mmWave band is reflected from the base station to the position of the mobile user, therefore increasing the received power at the mobile user. The received power SRX [dBm] can then be expressed as:

$$S_{\mathrm{RX}} = S_{\mathrm{TX}} + G_{\mathrm{TX}} - L(r_1) + G_{\mathrm{RFC}} - L(r_2) + G_{\mathrm{RX}} \tag{4.1}$$

where S_{TX} [dBm] is the base station transmit power, G_{TX} [dBi] and G_{TX} [dBi] are the transmit and receive antenna gains, respectively, and $L(r_1)$ and $L(r_2)$ are the path losses between the BS and the passive reflector and between the passive reflector and the mobile user, respectively. The two path losses are calculated as follows:

$$L(r_k) = -27.55 + 20\log(r_k\ [\mathrm{m}]) + 20\log(f\ [\mathrm{MHz}]) \tag{4.2}$$

where r_k [km] represents the distances involved and f [MHz] the carrier frequency.

In 4.1, G_{RFC} indicates the reflection gain of the passive reflector given by

$$G_{\mathrm{RFC}} = \sigma\ [\mathrm{m}^2] \cdot 4\pi/\lambda^2 \tag{4.3}$$

where $\sigma\ [m^2]$ is the radar cross section (RCS) of the passive-reflector. RCS is defined as the ratio between the equivalent isotropic reflected power $4\pi R^2 \cdot |E_s|^2$ at a distance R from the reflector and the incident power density $|E_i|^2$ at the reflector, i.e.,

$$\sigma = 4\pi R^2 \cdot |E_s|^2 / |E_i|^2 \tag{4.4}$$

where $|E_s|^2$ is the reflected power density.

4.2.1 Radar Cross Section Estimation

The following is a discussion of the estimation procedure of the RCS (σ) according to equation 4.4. The calculation of the value of E_s is the essence of the estimation. For the calculation of this field power value, the Geometrical Optics (GO) approach in [120] is used, because the proposed passive reflector has dimensions larger than the minimum required wavelength of 0.01m at 30 GHz.

The scatter-wave power density in 4.4 is computed using the GO technique by integrating the generated current over the passive-illuminated reflector's surface. The electric and magnetic current on an illuminated surface produced by a perfect conductor is:

$$J_s(r') = 2\hat{n} \times H_i|_s; M_s = 0 \tag{4.5}$$

The electric and magnetic currents on the lighted surface of the target S are denoted by J_s and M_s, respectively. The dispersed fields in the distant field may be expressed as 4.6 using the Stratton–Chu equation [120].

$$E_s = \frac{jk}{4\pi} \frac{e^{-jkR}}{4\pi} \int_s \hat{s} \times (M_s + \eta_0 \hat{s} \times J_s) \exp[jkr' \cdot (\hat{s} - \hat{i})] ds' \tag{4.6}$$

where $\hat{i}$ and $\hat{s}$ denote the directions of the incident and scattered waves, r' denotes the vector from the center of the target to the surface spot ds', and η_0 denotes the free-space impedance. The integrals of 4.6 are difficult to compute, since the reflector surface is usually involved. To avoid this problem, we use the strategy provided in [121], which divides the surface of a reflector into N

small triangular facets. Assuming that N is large enough and that the incident wave is plane, the RCS in 4.4 can be approximated as follows.

$$\sigma = 4\pi R^2 \cdot \left| \sum_{j=1}^{N} E_{s,j}\left(r_j, \theta_j, \varphi_j\right) \right|^2 / |E_i|^2 \tag{4.7}$$

where $E_{s,j}\left(r_j, \theta_j, \varphi_j\right)$ is the jth triangular facet's dispersed field, r_j is the distance between the receiver and the jth facet, and θ_j and φ_j are the jth facet's vertical and horizontal coverage angles, respectively. After determining the RCS, we can calculate the reflection gain G_{RFC} in 4.3 and the received power S_{RX} in 4.1. With these two key parameters in mind, we have an initial design basis, whereby if we seek to maximize the reflector gain we must maximize its RCS as shown in figure 4.3. Therefore, the dimensions of the reflector will depend on the directivity of the radiation source, the spacing distance between them, and the angle of incidence of the radiation source.

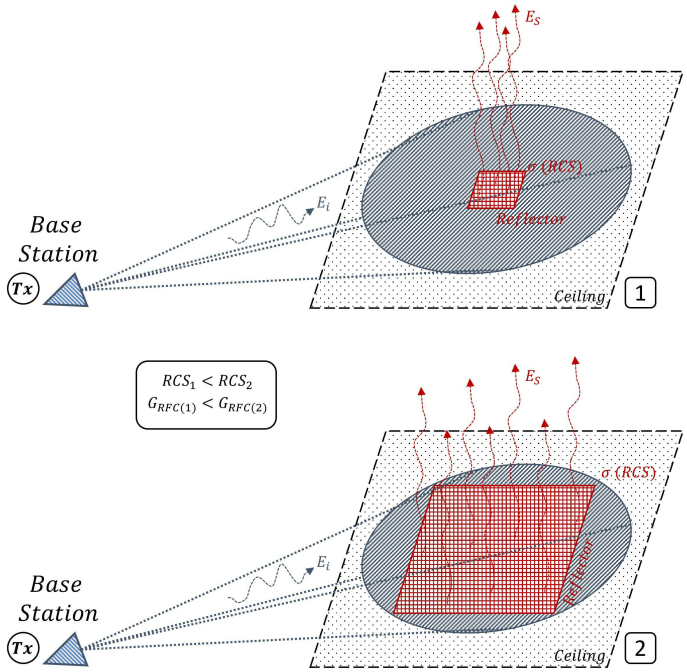

Figure 4.3: Gain evaluation as a function of RCS of passive reflectors.

4.3 Diffuse reflector design guidelines

Many existing physical objects, such as walls, windows and roofs, can act as reflectors in realistic environments. However, the associated G_{RFC} reflection gains associated with these everyday items are often insufficient to achieve adequate S_{RX} received power in non-line-of-sight (NLOS) areas. In addition, being completely flat objects, the resulting reflection has a strong specular behavior, which prevents in many cases to redirect the radiation towards areas of interest. It is therefore essential to create a passive reflector with a high G_{RFC} (reflection gain) value. According to equation (4.3), increasing the RCS is the key to achieving this. In addition to considering that the reflector has reflection surface as large as possible, it is also important to design the reflector with a volumetric surface that is as flat as possible, but not being completely flat to avoid specular components in the reflection. This approach in the design of this type of reflector will allow us to have sufficiently large reflecting surfaces, because it will allow us to build a large reflector with the union of several small reflectors, to have a good reflection gain, which allows to increase coverage as seen in figure 4.3.

This type of reflectors will usually be irradiated with highly directional beams, to compensate for the very high free space propagation losses in the millimeter range. Therefore, the angle of incidence on the reflector (θ_{in}) is a critical parameter to consider in the reflector design process, because the coverage area aperture angle ($\theta_{coverage}$) depends on it (See figure 4.4). One of the design objectives of this reflector is that this parameter ($\theta_{coverage}$) should be as independent as possible of the angle of incidence, at least in a certain input range (θ_{margin}).

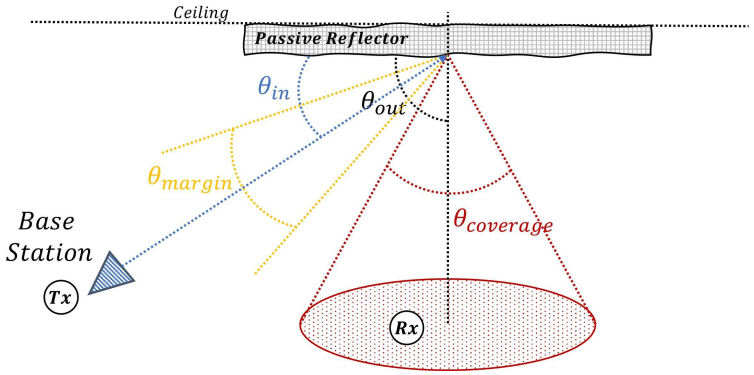

Figure 4.4: Passive Reflector Design Nomenclature.

In this type of proposed diffuse reflector, the power incident on the reflector is spread over the coverage area ($\theta_{coverage}$). We consider this phenomenon as dispersion losses (L_{spread}). This dispersion loss phenomenon is another important design parameter of the reflector, where these losses can be minimized by increasing the RCS of the reflector and limiting the coverage area ($\theta_{coverage}$).

Therefore, the design criteria is that the dispersion losses do not exceed 12 dB ($L_{spread} < 12dB$), with an angular coverage area of up to $\theta_{coverage} < 40°$, and an input margin of $\theta_{margin} \approx 20°$. It is important to note that this type of reflector will not have a fixed focal length, because it is designed to be as versatile as possible to be placed in any interior environment without considering the separation between the radiation source and the reflector. This approach is ideal for easy and fast implementation of 5G network infrastructure in the mmWave band.

One of the most important considerations in minimizing scattering losses is to ensure that the scattering produced by the reflector is as uniform as possible over the coverage area. Therefore, the fades of the reflector radiation pattern should not be greater than 6dB, as shown in figure 4.5. The operating bandwidth of the reflector is proposed to be between 30 GHz and 40 GHz which for design reasons, covering most of the operating range for the radio access network (RAN) in the mmWave band for 5G systems.

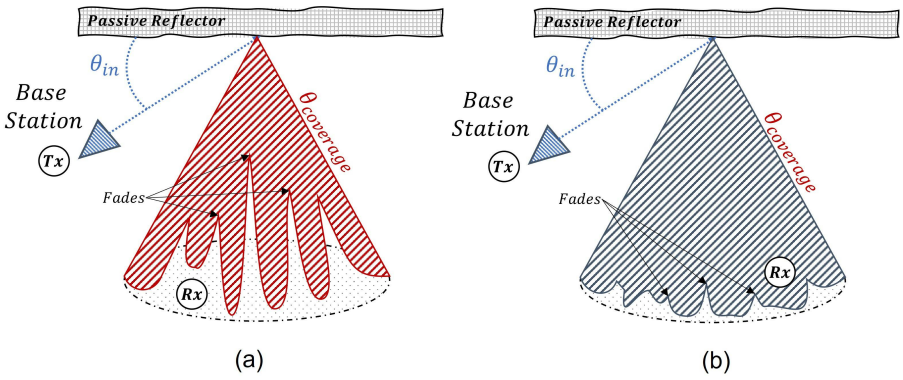

Figure 4.5: (a)Non-homogeneous dispersion with strong fades, (b)Homogeneous dispersion with slight fading.

4.4 Computer graphics Design Tool

In this section the design of the reflector surface is presented using the 3D modeling platform called Blender, presented in Annex, section A.2. It was used to build and parameterize different types of potential reflector surfaces.

This 3D modeling platform was the only tool used to create the reflector surface. The design of the reflector consisted of two phases, which were carried out in an interactive way, as different types of surfaces with different geometric shapes were evaluated.

The first phase consisted of creating a diffuse surface, testing different types of geometric shapes that can generate a diffuse reflection.

The second phase consisted of electromagnetically simulating this surface to evaluate its electrical properties, according to the design parameters proposed in the previous section.

In this section is described in detail the 3D modeling tool used and the methodology used to design and create each of the evaluated surfaces through the Python programming language in Blender.

4.4.1 Reflector Design with Python API in Blender

In order to design various types of reflectors, some primitive geometries of Blender were used, which are the sphere, the cone and the grid. In order to manipulate each of these primitives it is essential that the vertices, edges and faces of the 3D model have a consistent numbering to their relative location.

In Blender the numbering of each of these elements that compose a 3D model is stored in an array that describes the model itself. Therefore, once the primitive is created, it must be guaranteed that the nomenclature of each of these elements has an order relative to its location in the mesh of the object.

For example figure 4.6.a shows how the numbering of vertices does not maintain a coherence with respect to their relative position in the object, while in the opposite case in figure 4.6.b, the numbering of vertices follows an ascending order in radial clockwise direction.

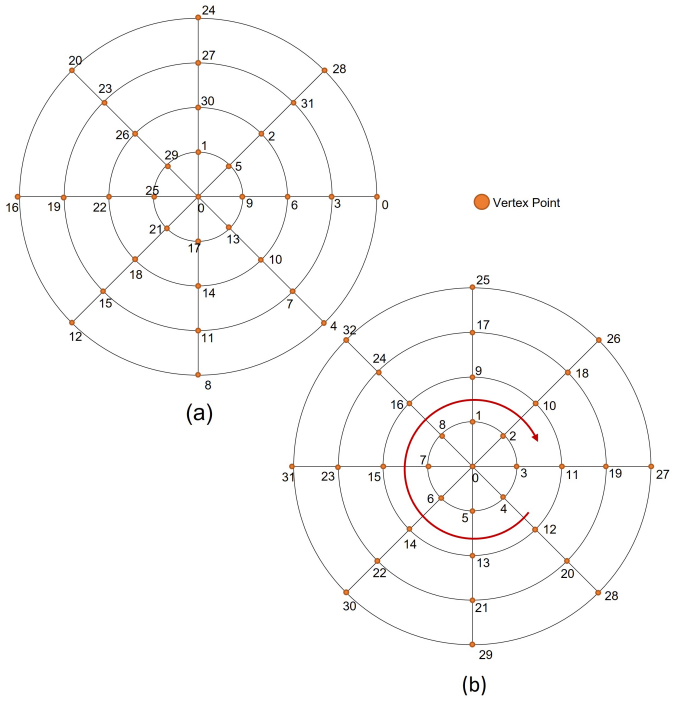

Figure 4.6: (a) Vertices without numerical consistency, (b) Vertices with numerical consistency.

Once it has been guaranteed that the mesh has a numerical coherence in vertices, edges and faces, as in figure 4.6.b, we may proceed to create a Python API code that allows us to parameterize a pseudo-random rough surface from which we can obtain a diffuse reflection. The strategy used for the design of the reflector was to scale, rotate and translate each of the vertices, of each mesh, and of each of the three base primitives separately, and in some cases to do a fusion of different primitives to create a single reflector, because with this we achieve more geometrical diversity in the reflector structure. (See figure 4.7).

One of the objectives of designing the geometric surface of the reflector by code in Blender is that it allows us to parameterize the roughness of the reflector precisely. The design process of each surface of the reflector has an iterative approach, where depending on the diffuse reflection of each surface and the proposed design guidelines, slight changes in its morphology are applied to each surface to adjust its behavior.

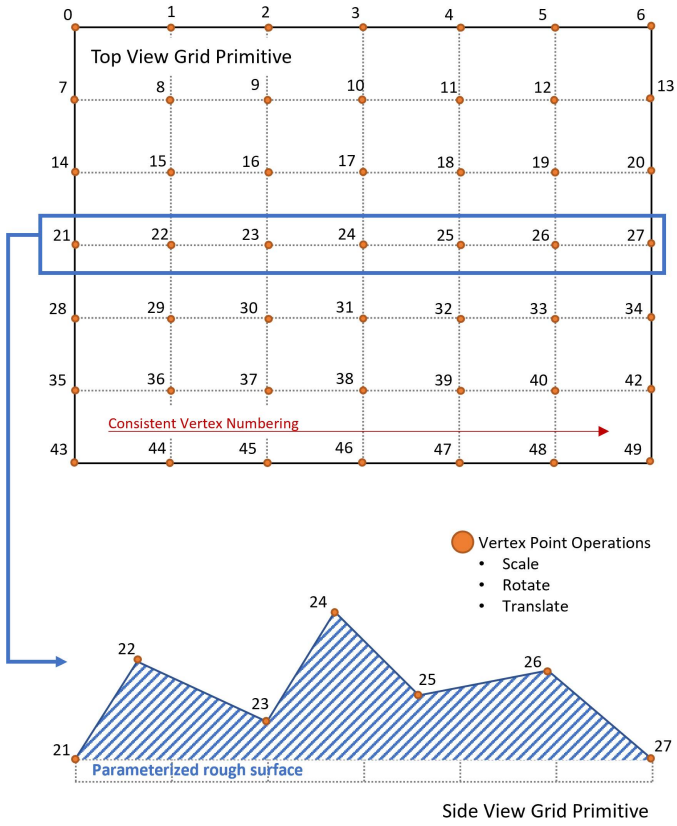

Figure 4.7: Design strategy of a parameterizable rough surface with basic operations on the mesh vertices.

Taking into account the design parameters of the reflector, one of the most important considerations is that the dispersion of the energy reflected by the reflector is as independent as possible of the angle of incidence of the radiation from the transmitting antenna, in order to always provide coverage in the same area, regardless of the position of the base station. To illustrate this idea, figure 4.8 shows the cross section of a reflector where it is impacted by the radiation of a transmitting antenna, where, depending on the angle of incidence of the rays on the reflector, each reflection goes to unwanted directions (Path B, C), and directions of interest (coverage area) (Path A).

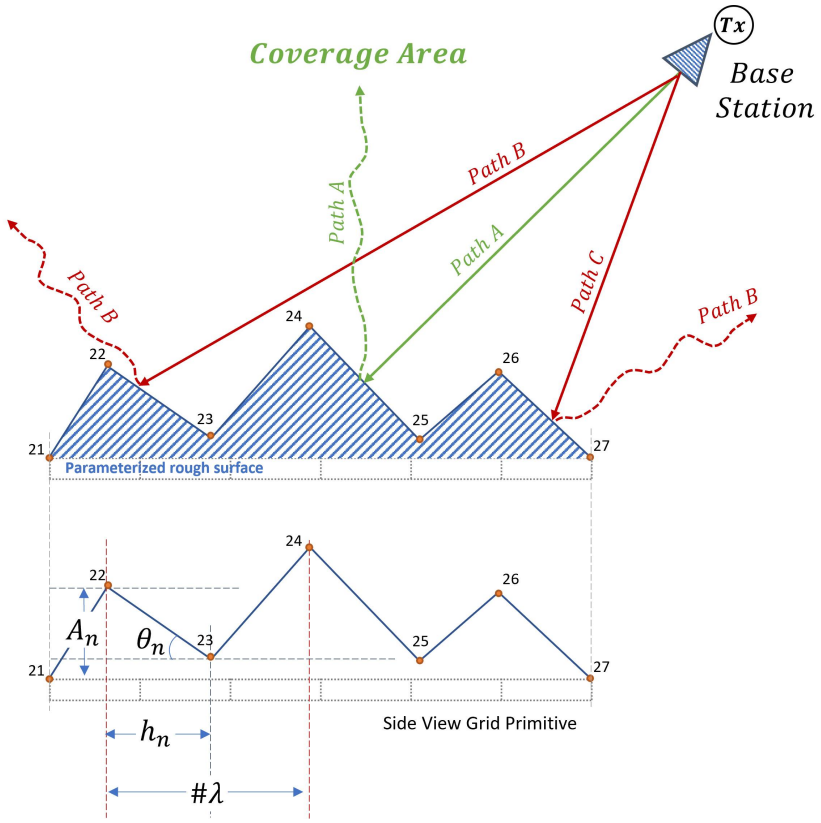

Figure 4.8: Design considerations for the passive mmWave reflector.

The design of this type of reflectors requires multiple iterations, where different types of reflector morphologies with different parameters (θ_n , A_n , h_n , λ_n) are tested, where these rely on the basic operations of scaling, translation and rotation on each vertex of the mesh of each primitive 3D model in Blender.

The design parameters were adjusted using ray tracing logic, predicting where each ray would go based on its specular reflection individually, and then compositing a diffuse reflection from the set of all incident rays on the reflector [122]. Therefore, different types of reflectors with different geometric shapes are designed and compared (See figure 4.9).

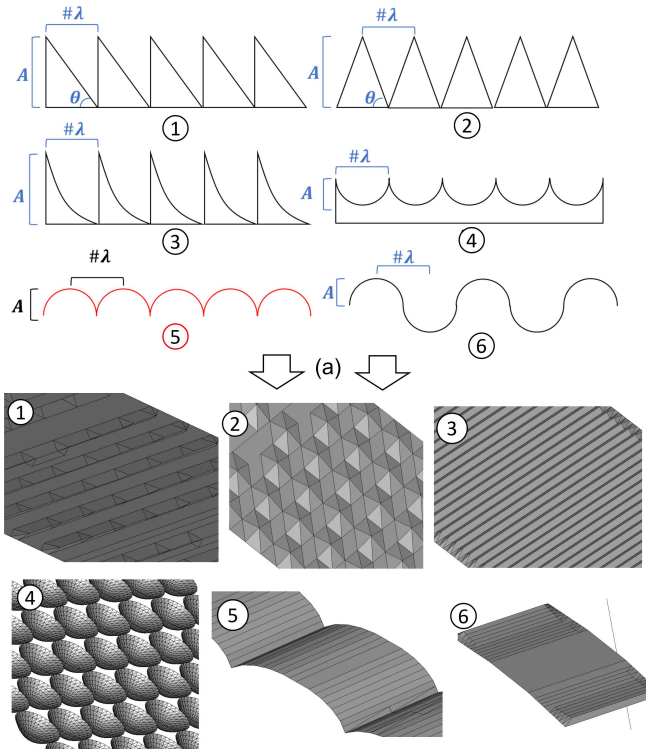

Figure 4.9: Testing proposals of geometrical shapes for reflector design.

The above surface proposals for the reflector are only a small sample of all the designs that were evaluated in simulation through CST Studio Suite [108]. Some surfaces are more difficult to model by coding and parameterizing than others, because this depends on the primitive to be used and, particularly, the task becomes more difficult when dealing with a composite surface created by merging several modified primitives.

For each model provided in figure 4.9.a, about 33 reflectors were modeled by code. Depending on the viability of the reflector, some proposed geometries had dramatic modifications in their morphology and minor alterations in other cases. Approximately 70% of the 200 reflectors designed had drastic changes. Those with slight changes were reflectors that had the potential to improve broadband energy dispersion. After a series of tests, the most promising reflector morphology for designing our diffuse reflector was number 5, as shown in figure 4.9.

4.5 Simulation strategies

This section discusses the simulation methodology used to electromagnetically analyze each designed reflector in order to evaluate its effectiveness as a passive diffuse reflector in mmWaves. The simulations were performed with the electronic analysis platform "CST (Computer System Technology)"[108]. The simulation approach is to place the reflector in the far-field region of the transmitter, so that the incident radiation on the reflector can be treated as a plane wave, as seen in the setup in figure 4.10. The transmitting antenna used was a horn antenna in the Ka-band from 26 GHz to 40 GHz [109]. The reflector has an irregular all-metal surface that has been previously designed with the Python API in Blender, and this surface has to be large enough to capture the maximum possible amount of energy coming from the transmitter.

The reflector cannot be too big, because it will be electrically large and this would cause unnecessary computational load at the beginning of the analysis. In order to more accurately calculate the field radiated by the reflector, the resolution of the grid used by the CST to perform the surface current analysis will be raised when each suggested design becomes more likely to be viable. Once the transmitting antenna and the reflector are positioned (See figure 4.10), the equivalent far field of the two elements as a whole is simulated, since the CST electromagnetic analyses are made taking into account a volumetric mesh, where the two elements are contained. As a result, at bigger volume sizes, simulations will require more system resources to run a single simulation.

The size of the volumetric mesh will depend mainly on the size of the reflector and the relative distance between transmitter and reflector. And, as mentioned above, the initial designs of each reflector are simulated with basic CST configuration, but good enough to have an initial insight into the frequency and radiation response. And, as mentioned above, in case of good potential results, the mesh resolution is improved to increase the accuracy.

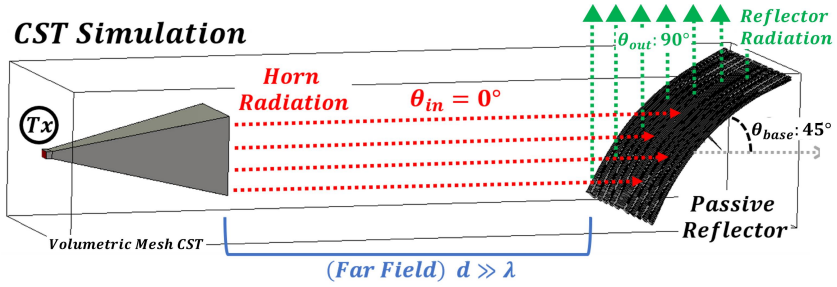

Figure 4.10: Simulation setup used to analyze reflector performance.

The following example of reflector prototype evaluation summarizes the process for each surface, consisting of three clearly differentiated stages:

1. Design the irregular diffuse reflective surface with Python API in Blender (figure 4.11).

2. The designed surface is loaded in CST for validation and adjustment of the appropriate electrical dimensions, then the reflector is fed by a horn antenna at a distance above the far field limit to ensure that the incident wave can be treated as plane (figure 4.12.a).

3. The simulation is run according to the scheme in figure 4.12.a, and the far-field results are analyzed in the cross sections of the radiation pattern in two dimensions ($\phi = 90°$ and $\theta = 0°$) (figure 4.12.b), and then the radiated far-field in three dimensions is evaluated to look at the results as a whole. (figure 4.13)

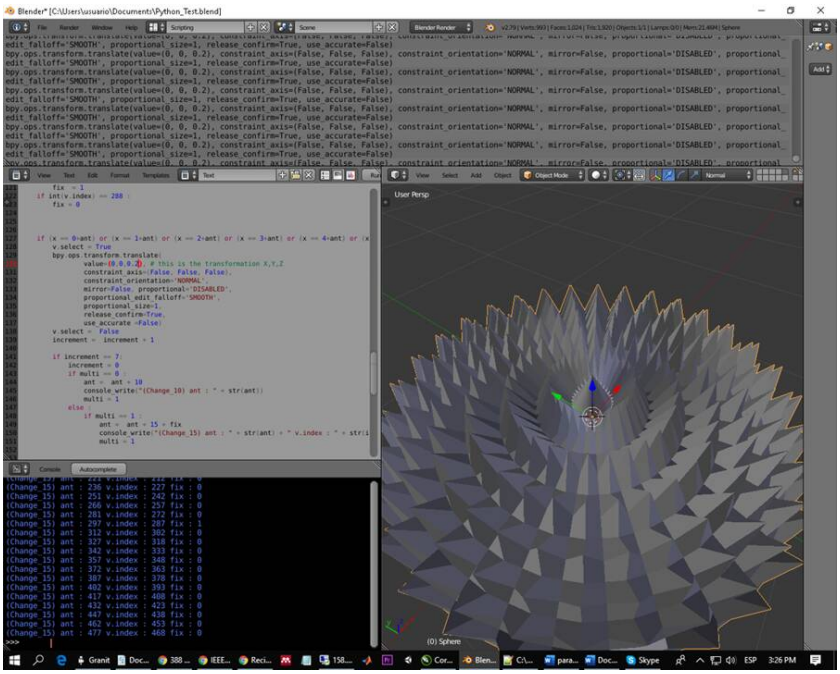

Figure 4.11: Design process in Python API in Blender.

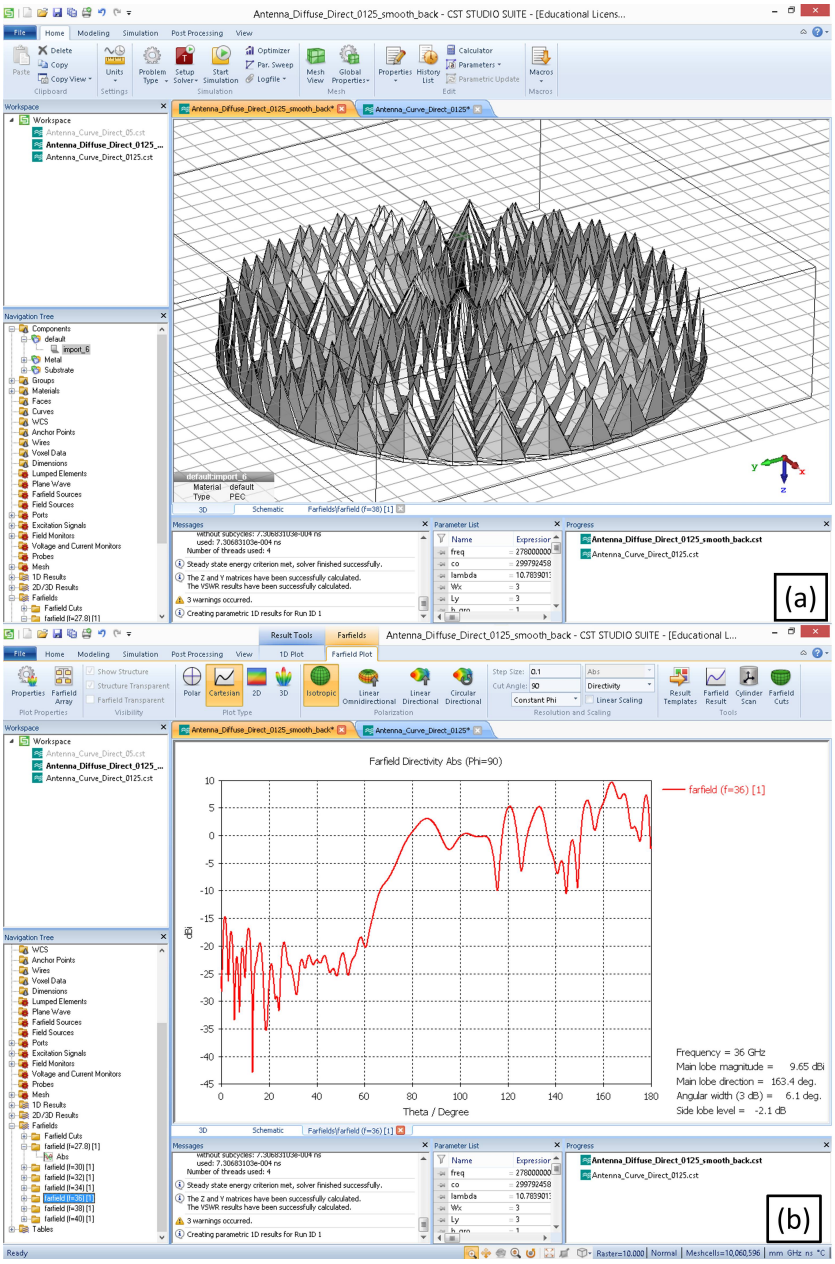

Figure 4.12: (a) surface loaded in CST and adjusted for simulation, (b) Simulation result of the far field simulation of the cross section $\phi = 90°$.

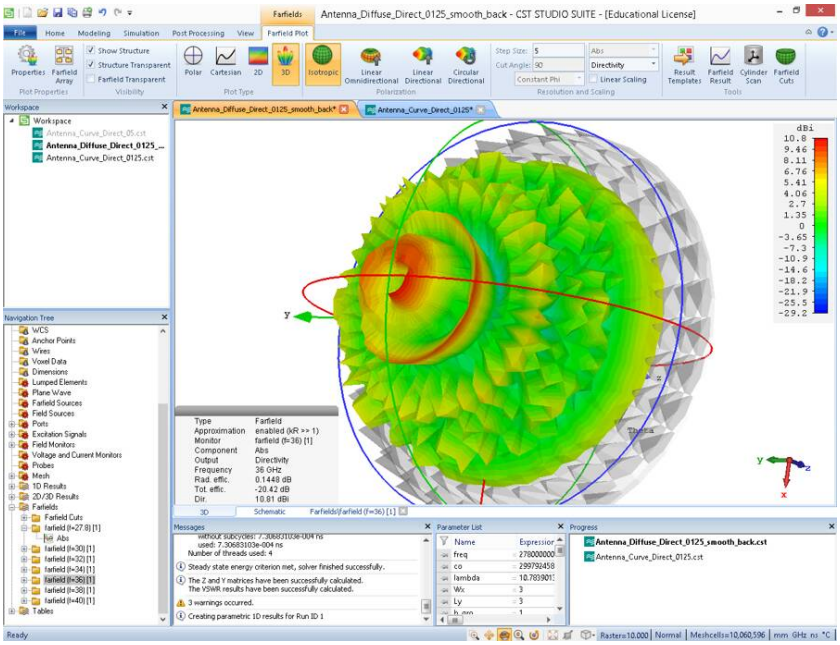

Figure 4.13: 3D Radiation pattern of the test reflector.

After the preliminary analysis of the test reflector designed surface, it can be observed that the reflector radiation has a reflection with a fading of 15 dB in the coverage area of interest ($\phi = 90$, with $\theta = 90°$ to $180°$) (see figure 4.12.b), so this reflector design can be immediately discarded and we will proceed to test another type of morphology by modifying the vertices of the reflector in Blender.

The previous steps are iterative according to the scheme of figure 4.10, where the reflector is initially simulated with an orientation of $\theta = 45°$ with respect to the direction of propagation of the transmitting horn antenna. The data are analyzed considering that the diffuse reflection must be as homogeneous as possible, with a maximum fading of 5 dB as our design criteria, taking into account that the angular zone of maximum reflection must be centered at $\theta = 90°$.

Once a reflector meets the condition that the radiation is homogeneous in the area of interest($\theta_{coverage}$), the reflector is gradually tilted to analyze its behavior with other angles of incidence, and thus to ensure one of the most restrictive design criteria. This design criterion is that the reflector can operate with different relative positions of the transmitter (different angles of incidence

θ_{margin}), when the reflector will always be in a fixed location such as on the ceiling of an indoor environment as shown in figure 4.4.

4.6 Parameterized design approach

In this section of the chapter, an example of how to design irregular surfaces with parametrizable wedges based on reflectarray techniques for emulating Fresnel's reflectors is presented. The objective of the design of this type of reflectors is to emulate concave and convex parabolic reflectors, with a surface as flat as possible, according to the research [122].

But in the case of this section we discuss briefly the design process of a flat reflector with slope wedges, based on the Blender grid primitive. This type of surfaces were designed with a matrix of coefficients (See figure 4.14), where each coefficient determines the operation on each vertex that characterizes a wedge, based on the design parameters (θ_n , A_n , h_n , λ_n) defined in the figure 4.8.

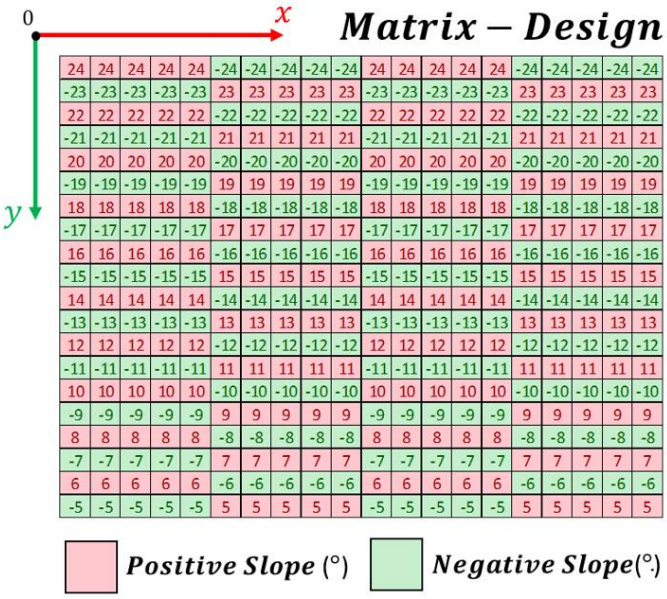

Figure 4.14: Coefficient matrix of an irregular planar reflector created with a Blender grid.

In this example, the matrix of coefficients of the previous figure contains the values of the slope in degrees of each wedge, which is indicated as a cell in the matrix. Each section of the matrix has different slope values, where the cells with green color are have negative slopes, corresponding to a wedge down or a notch, while the cells with red color represent the positive slopes of the wedge. Each wedge has different slope values with a well-defined pattern, as in the example case, where every cell has a positive slope and negative. As the reflector's goal is to diffuse energy in an angular range in order to produce a dispersed reflection, each wedge has a different slope.

The resulting reflector after programming the matrix of coefficients is shown in figure 4.15, where one can clearly see the difference in the slope as a function of the value of each matrix coefficient. This type of coefficient matrix strategies to parameterize an irregular parametrizable surface are also used in surfaces with revolution symmetry, as when using other types of Blender primitives such as the UV sphere and the cone.

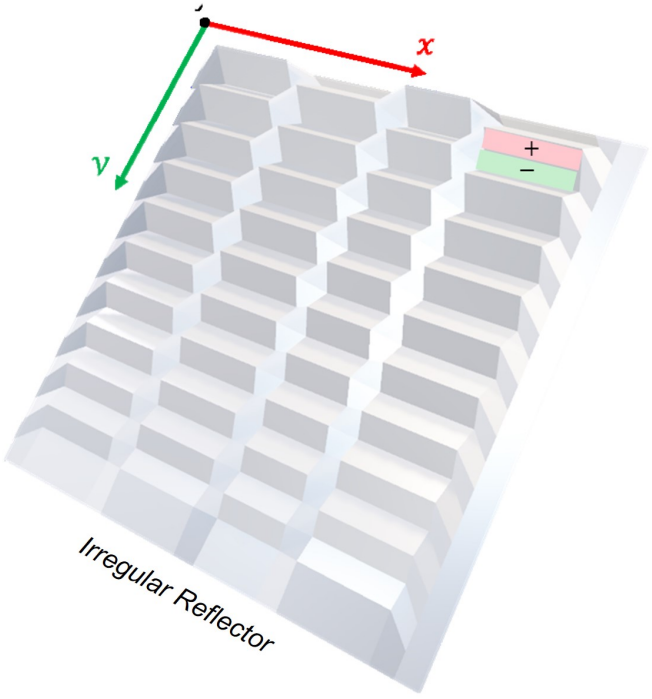

Figure 4.15: Irregular Reflector created with the coefficient Matrix.

Figure 4.16 shows the field radiated by the reflector that has been designed (See figure 4.15) with the coefficient matrix (Yellow Line). This result is compared with the field radiated by a completely flat reflector (Red Line), where its maximum radiation follows a fully specular behavior $\theta_{out} = 90°$. Also in these results the radiation pattern of the horn antenna is plotted (Blue Line) $\theta_{in} = 0°$.

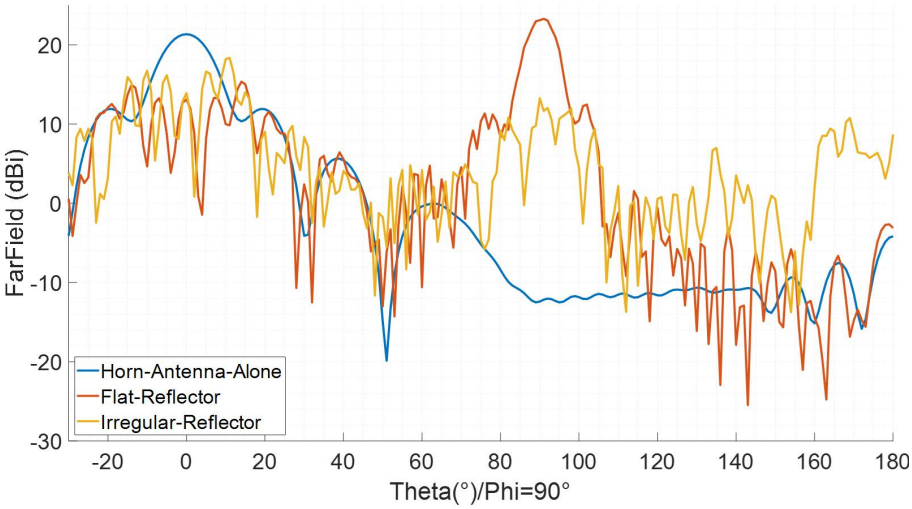

Figure 4.16: Results of the radiation pattern of the irregular reflector proposed with the coefficient matrix.

Following the results obtained not only from this example design but also from several designs previously considered with different coefficient matrices, it is concluded that, according to the previously established design guidelines, the diffuse reflection generated by the reflector should be as homogeneous as possible in the coverage area. As for the surfaces created with flat slopes, all of them have a strong specular behavior, although each wedge has a gradual and complementary slope with respect to its adjacent wedges.

These surfaces cause phase problems in each of their specular contributions, which generate strong fading in the resulting radiation pattern as clearly seen in figure 4.16 (yellow line "Irregular Reflector"). And, when the other most important design guideline is considered, which is that the transmitter feeding the reflector can be anywhere in the environment, the phenomenon of strong fading in the coverage area is aggravated.

4.7 Final Simulation Results

As concluded in the previous section, the design of a diffuse reflector with flat slopes causes phase inconsistencies, which in turn cause power fading in the diffuse reflection. Thus, after several unsuccessful attempts to design a reflector with various types of configurations, due to its parameterization simplicity and its compact morphology, it was decided to design surfaces with wedges with a smooth transition between them, and with curved slopes instead of linear slopes. For this reason the surfaces with curved slopes (See figure 4.9.a surfaces 4-5-6) were proposed, as the most suitable for the design of our reflector.

The strategy used was to ensure that the reflector has a radiation pattern as broad as possible, to maintain a fixed coverage area regardless of the angle of incidence, to be within the proposed design margins (θ_{margin}). With this strategy, power is traded for coverage: the wider the coverage, the less the power density. As the reflector is a passive element, its unique purpose is to distribute the energy efficiently, so it is important that this reflector operates with highly directive antennas in the mmWave band.

The final proposed design is detailed in figure 4.17 and figure 4.18, which is composed of two different types of smooth surfaces. The first surface is a concave surface, modeled with a cosine function with a period from 0° to 90°, with an amplitude (Z axis) of 15 mm, and with dimensions of its base (X-Y axis) of 100mm x 100mm.

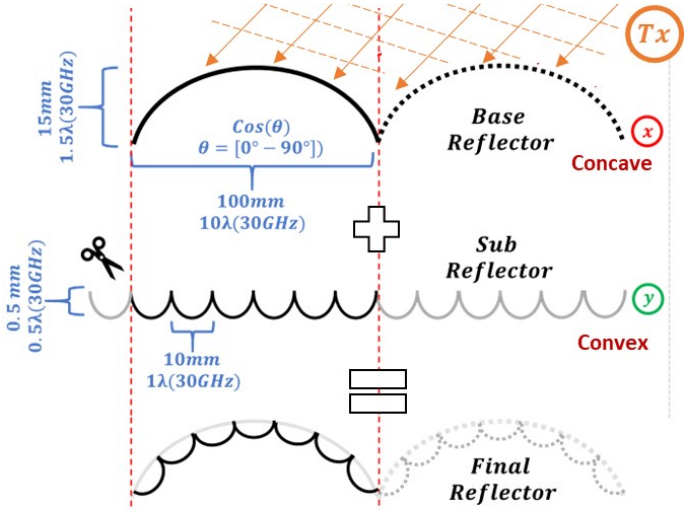

Figure 4.17: Final proposed reflector design strategy.

This surface is not designed with a coefficient matrix because this surface is composed entirely of sinusoidal functions, so the design system proposed above for flat slope surfaces in figure 4.15 is not applicable, because smooth transitions between slopes are indispensable to avoid fading in the resulting radiation pattern. Although the proposed design with flat slopes in figure 4.15 was only one example of the iterative design process where multiple types of rough surfaces were tested.

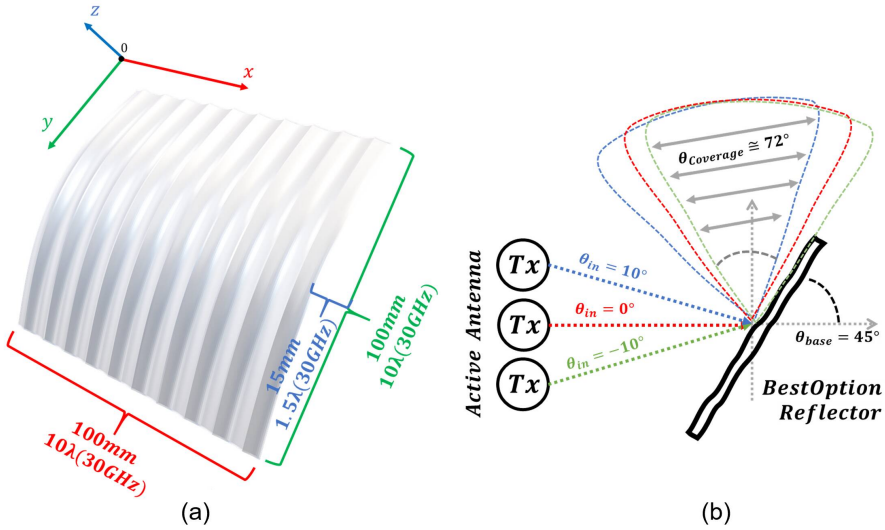

Figure 4.18: Final proposed design to improve indoor coverage.

The reflector has been designed with a periodic surface, which means that a larger reflector can be built by positioning many of such elements one after the other. The purpose of making a larger reflector is to capture more energy of the radiation received by the transmitting antenna; the size of the reflector will be inversely proportional to transmitting antenna directivity. This reflector design prevents scattering components from being in counter-phase and therefore allows to reduce unwanted power fading in the coverage area.

Figure 4.19 shows the field radiated by the final reflector design at 30 GHz, with different positions of the transmitting antenna, as detailed in figure 4.18.b. Depending on the position of the transmitter, it is incident on the reflector with different arrival angles $\theta_{in} = 0°, 10°, -10°$. Therefore, and according to the most important design guidelines, the transmitter should not be in a fixed

position, but could be positioned so that it could be incident with an input range of $\theta_{margin} = 20°$.

Results of the radiation pattern are plotted in figure 4.19, where a specular reflection at 90° is used as a reference. The final diffuse reflector increase the coverage area ($\theta_{coverage}$) from 15° at -12dB of the specular reflector to 100° at -12dB, homogeneously distributing the energy throughout the coverage range, for any fixed position of the transmitter.

If the incoming angle varies in a range of 20°, the beam width of the reflected pattern keeps being 100°, pointing slighthy different directions, but maintaing a range of 72° of angles of departure always covered (see figure 4.19). Summarizing, this reflector's peak gain was traded for coverage and flexibility.

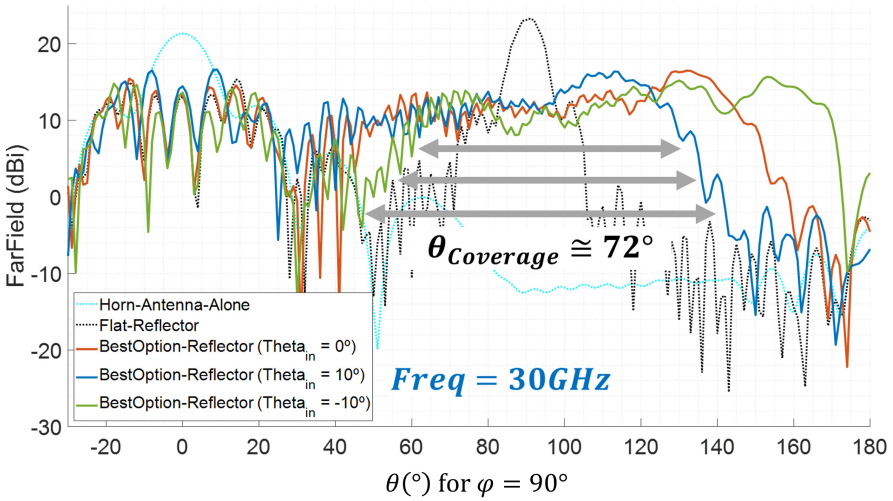

Figure 4.19: Radiation pattern of the final prototype reflector.

4.8 Conclusions

In this chapter a solution for efficient power distribution in indoor environments in the mmWave range was presented. To achieve this, a passive reflector has been designed to homogeneously distribute the received power, increasing the coverage area by 450% in exchange for a maximum gain reduction of approximately 10 dB in an operating bandwidth of 10 GHz (30 GHz - 40 GHz). This aims to solve coverage problems in 5G systems in indoor environments, in order to avoid losses due to obstacles.

One of the limitations of this reflector that is solved in the following chapter is the incapacity to disperse the energy homogeneously in all directions equally, which is due to the orientation of the predominant concave surface.

Chapter 5

Analysis and Design of Diffuse Modular Honeycomb Passive Reflector

This chapter presents the design process of the hexagonal modular diffuse reflector for coverage optimization for fifth generation (5G) systems. The objective of the reflector is to provide greater coverage to radio systems in the mmWave band, giving the radiowaves an alternative path to propagate. As a result, it prevents high gain and high directivity antenna arrays to radiate directly into the indoor environment, being the radiating system oriented to the diffuse reflector, so to distribute the energy homogeneously within the environment. This simplifies the planning and avoids unexpected fading of the radio channel.

To this aim, this chapter has been divided into the following sections:

- Section 5.1 presents a brief introduction on the relevance of including a reflector in radio access network (RAN) systems.
- Section 5.2 presents the design considerations for the mmWaves diffuse modular reflector.
- Section 5.3 describes the iterative simulation strategies used to determine the best broadband reflective surfaces for the proposed reflector.
- Section 5.4 describes the initial design considerations to be taken into account for designing a modular passive reflector in the mmWave band.

- Section 5.5 describes the final surfaces proposed for diffuse broadband reflector performance.
- Section 5.6 describes the reflector measurement campaigns.
- Section 5.7 presents the conclusions of this chapter.

5.1 Introduction

As described in chapter 4, passive reflectors have been extensively studied to optimize the communication links [122] and radars [123], [124], whereas to the best of our knowledge there are no publications on the design and application of millimeter-wave reflectors. In [122] the concave parabolic reflector geometry is adapted to an irregular planar surface, based on the low-profile Fresnel zonal plate antenna (FZP) [125] and also called reflectarray. The resulting reflector retains almost the same efficiency and performance, but its volume is much smaller.

This basic approach is used as a guide for the design of the modular reflector developed in this PhD. This chapter describes the design of a passive reflector that uniformly distributes the incident radiating wave in fixed NLOS zones, regardless of the angle of the incoming wave. Simulations of the reflector are performed and verified with measurements. The ultimate goal of the reflector is to improve indoor wireless system deployments. In addition, the reflector will have a modular design that gives the flexibility to increase its operating area to suit any indoor environment and radiating source location.

5.2 Reflector design considerations

Some years ago when there was no commercial software for electromagnetic analysis, designers used to build their own codes to characterize and design reflectors. But now we can rely on industry standard commercial codes, as many companies have made them a standard. In the past, studies were limited to efficiency analyses [126], [127], used to predict reflector gains and main and lateral lobe apertures. These analyses gave the designer a first approximation of the relevance and efficiency of each parameter. Today, on the contrary, it is possible to create reflectors with customized radiating patterns using commercial software. However, only in the case of traditional reflector design where only the design parameters need to be changed, engineers can adapt the design to the needs of their application.

Since reflectors are normally electrically very large, optical analysis tools are generally used to characterize reflectors such as: physical optics combined

with PO/PTD physical diffraction theory and geometrical optics combined with GO/GTD geometrical diffraction theory. For this type of analysis the best tool on the market is TICRA's GRASP [128], which is mainly focused on reflector analysis.

To analyze electrically smaller reflectors one can apply the method of moments (MoM), time domain analysis, or frequency domain analysis; with such methods, not only the basic parameters such as directivity and radiating pattern are analyzed, but also the electromagnetic interaction of the surface currents with all the elements of the reflector is taken into account, including interactions with the sub-reflector and its supporting elements. This type of analysis can be performed by various software suites in the industry such as GRASP [128], Ansys HFSS [129] and CST studio suite [108].

These programs are sold by commercial vendors that continuously improve their computational times through algorithm improvements, graphics processing units (GPUs) or out-of-core solutions to reduce RAM requirements. These techniques can now be used in a reasonable way thanks to computing improvements. Although different techniques may have different execution times, the most important factor is the accuracy of the results.

The objective of this chapter is to design a diffuse reflector in the mmWave band, and since there are no design precedents for this type of reflector, the CST electromagnetic analysis simulation tool was used, allowing greater precision in the radiating pattern analysis. Furthermore, the proposed modular reflector is not electrically very large.

The purpose of the proposed reflector is to homogeneously distribute the energy of a transmitting antenna over a non-line-of-sight (NLOS) region. This approach is opposite to the traditional one, because the commonly used reflectors are intended to collimate the energy in a region of the space to increase the directivity of a fixedly located source.

In our case, from a highly directive source, the aim is to disperse the energy in a fixed region, in order to provide coverage in the shadow zones, as the antennas in the mmWave band are highly directive to counteract the high propagation losses in free space. Therefore, this highly directive radiating source is used for beam-forming and beam-steering techniques.

On the other hand, the proposed passive reflector cannot be flat, because it would have a strong specular behavior and, consequently, a high dependence on on the angle of incidence θ_{in}, as seen in figure 5.1.a.

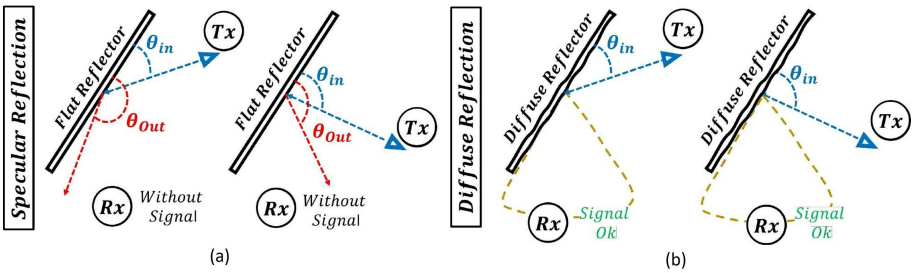

Figure 5.1: (a) Specular reflector vs (b) Diffuse reflector for mmWave coverage.

Therefore, the main design requirement will be that the diffuse reflection does not depend on the angle of incidence of the radiating source (θ_{in}). This consideration is important for practical applications, because it offers flexibility in the installation of indoor wireless 5G network systems. It so, the location of the reflector is independent of the location of the radiating source TX.

5.2.1 General Design Guidelines

As noted above, the proposed approach for the design of this type of reflector is a hybrid one, making use of some concepts from phased array and conventional reflector technologies. Like the phased array, it is composed of a set of elements that are placed in an irregular grid configuration on a convex surface. Its similarity with the conventional reflector (See figure 5.2(a)) lies in the fact that both structures are fed by the planar wavefront incident on it, so it is defined as a passive element. The proposed reflector differs from the phased array in that its elements are quasi-periodic. This means that the dimensions of its elements are not similar. However, our diffuse reflector differs from the traditional reflector by the use of a phase-front transformation mechanism that adjusts the dimensions and shapes of its elements. This is in contrast to the conventional reflector which uses the Euclidean geometry laws as well as the direct reflections of incoming light to achieve it.

The proposed reflector, in its most basic form, is composed of a group of quasi-periodic wedge elements that overhang the reflector surface, where the entire surface is fully metallized, as shown in figure 5.2(c). The metallic surface causes all incident energy to be repelled by the reflector.

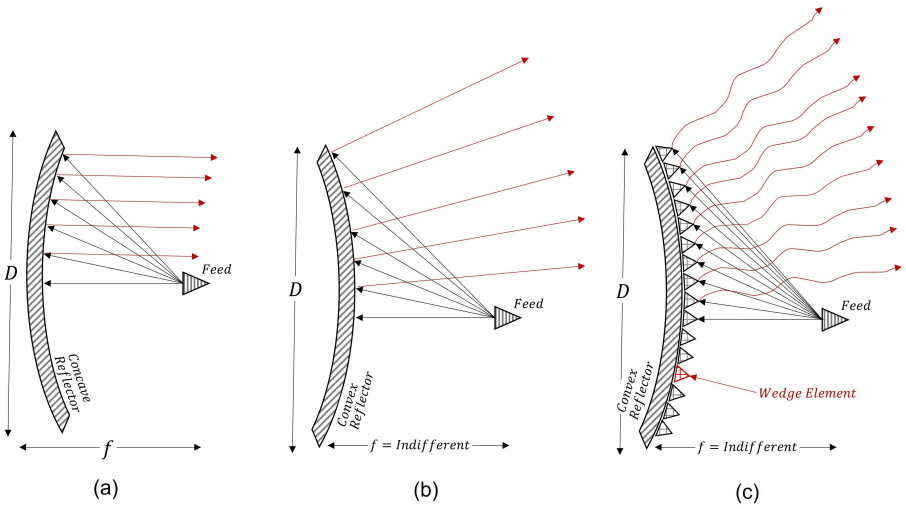

Figure 5.2: (a) Concave traditional reflector, (b) Convex base reflector, (c) Convex reflector with wedges.

The dimensions of the wedge are adjusted to realize a random aperture field distribution, in order to have a homogeneous diffuse field orthogonal to the reflector. To achieve this goal, each wedge is positioned in a randomly programmable manner such that the phase of each reflected beam has a slightly different phase from that of neighboring wedges.

Figure 5.3, shows how the phase of wedge φ_{11} should be slightly different from that of wedge φ_{21}. This strategy should try to be independent of the phase of the incoming wave, which depends on the bandwidth of the incident signal.

The relative phase shifts of each of the wedges are controlled by the W and L dimensions of each wedge and by their L_x and W_y spacing. The diffuse scattering or reflection generated by each wedge should be slightly different from the adjacent wedge, so that they are phase compensated, in order to avoid unwanted power fading in the resulting radiating pattern of the reflector. The phasing strategy of each wedge is valid only to determine the roughness of the base convex reflector.

In practice, however, each wedge of this reflector is not designed as a discrete taper. It is designed taking into account a sinusoidal function, which depends on the radial distance of the reflector and in some cases also varies angularly. The fact that it is not a discrete design as in the case of the reflectarray, is because the reflective surface is continuous and fully metallized, in order to

reduce the manufacturing costs of the reflector, because designing a reflectarray with discrete elements that change the impedance of each one to alter the phase is more complicated to manufacture and measure. Note that our intention from the beginning is not to collimate the energy to increase the directivity of the reflector but the opposite.

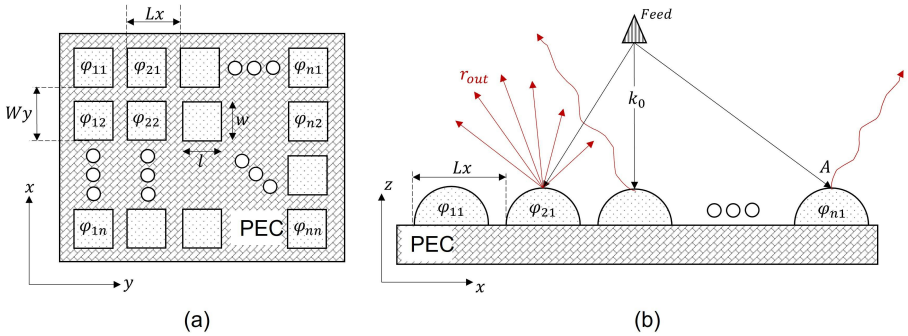

Figure 5.3: Views of the pseudo-random rough surface formed by discrete wedges (a) Top-view (b) Side-View.

For this reason, the design of the reflector is subdivided into two parts:

- Determine the optimum convex curvature that allows us to have a diffuse base reflector (See figure 5.2(b))
- Determine the pseudo-random roughness that minimizes the sudden fading of the reflected power (See figure 5.2(c))

The design process of the reflector was an iterative process. The reflector surface was parameterized with a continuous sinusoidal function designed and created using the open license 3D modeling software called Blender. Using this software, each of the surfaces was designed with different types of roughness variables.

Each designed surface was created based on the Python programming language, in order to parameterize each of the predominant dimensions of the convex base reflector and the rough surface with continuous wedges. The surface of the reflector is modeled in the 3D modeling software called Blender, in order to create a coherent mesh, with the previously programmed instructions in Python.

Every reflector prototype is loaded into the electromagnetic analysis software CST in order to analyze the behavior of the currents induced on the

reflector by a standard broadband horn, and consequently its resulting broadband radiating pattern from 30 to 40 GHz.

These steps were repeated several times, where in each iteration the behavior of the currents on the reflector and the resulting radiating pattern were analyzed. As a consequence of these results, the sinusoidal function of the reflector roughness was modified slightly. Also depending on the results obtained in every iteration, the relative dimensions of the convex base surface were changed. This was an arduous process, because our objective was to have a reflector with the following design parameters as shown in figure 5.4.

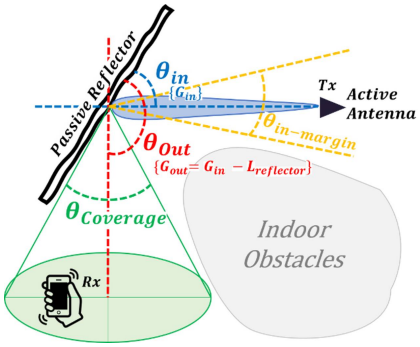

Figure 5.4: Diffuse reflector design parameters.

Therefore, the design requirements for the proposed modular diffuse reflector are as follows:

- Reflector Morphology: It has to be as flat as possible, in order to assemble it and cover large areas.
- θ_{in}**:** Incident angle on the reflector of 45°.
- $\theta_{in-margin}$**:** Incident angular range to the reflector at 20°.
- $L_{reflector}$**:** Reduced by a maximum scattering loss of $12dB$ in the $\theta_{coverage}$.
- Bandwidth: The operating frequency range has to be in the millimeter band between 30 to 40 GHz.
- θ_{out}**:** Angle of departure of the scattered radiating of 90 °.
- $\theta_{coverage}$**:** coverage angular aperture of the reflector around the specular dispersion of 80°.

5.3 Iterative simulation procedure

In order to study the electromagnetic and radiating characteristics of the reflector in indoor environments, it is always necessary, in a first phase, to carry out a detailed analysis of the plausible simulations in the software tools, to properly characterize the proposed reflector, in an iterative process. Therefore, these sets of simulations should cover a multitude of different conditions, to prevent a bias in the results obtained. Once the simulation process started, it was impossible to determine the number of simulations to be performed, Because in an iterative process, the results of each reflector prototype determined the next prototype to be simulated.

As a result, the process of obtaining a viable prototype was a very costly and slow, mainly due to the technical limitations of simulating a reflector in the mmWave band, where any type of reflector with dimensions of the order of centimeters is electrically very large. Therefore, each simulation was very computationally expensive, because for each prototype of a proposed reflector several simulation approaches were used in order to obtain as reliable results as possible.

The simulation campaign was carried out in a three-dimensional free-space scenario, where the only active element is the Ka band (26-40 GHz) horn antenna [109] located in front of the reflector, as in the example of figure 5.5, where a flat reflector is illustrated. The environment simulation variables are the angular orientation of the reflector, θ_r, which is varied from 0 to 90 degrees with steps of 5 degrees per simulation, and the distance between the reflector and the horn is F_r, whose change from 1 to 10 m with steps of 0.5 m. With this minimum distance F_r of 1m we always guarantee that the reflector is located in the far field zone with respect to the horn antenna.

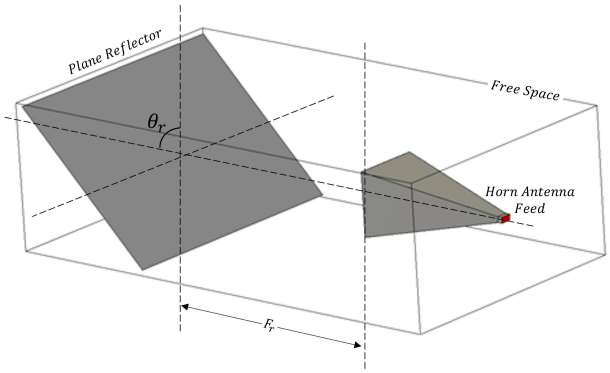

Figure 5.5: Reflector simulation schematic in the CST simulation tool.

For each simulation run, the behavior of the currents induced in the reflector by the radiating source was visually analyzed. This analysis consisted in ensuring that no anomalous concentration of energy was found in specific regions of the reflector, because, if the currents in the reflector are not homogeneously distributed, the energy radiating from the reflector will not be homogeneous. Consequently, the proposed roughness of the reflector cannot have abrupt discontinuities (See figure 5.6(a)), since in that case the induced energy will not be distributed homogeneously (See figure 5.6(b)).

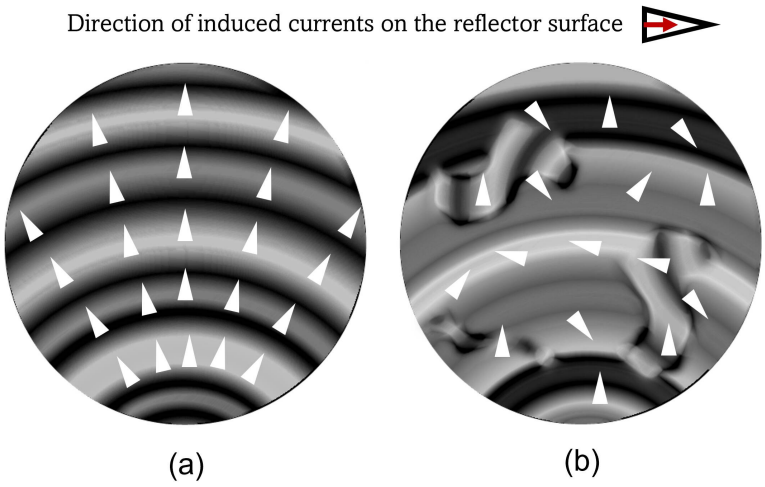

Figure 5.6: Propagation of currents on the reflector surface, (a) Homogeneous, (b) Irregular.

All simulations have been performed taking into account the intrinsically three-dimensional character of both the proposed reflector and the radiating source. But, for practical purposes, the results of the radiating pattern of the reflector have been analyzed only for the axial slices at $\theta = 90°$ and $\phi = 90°$, orthogonal to each other. To analyze the radiating pattern of the reflector, a relatively homogeneous reflection must be ensured, with an angular aperture of 80 degrees and with a maximum scattering loss of 12dB. A prototype will be discarded or approved according to the above criteria. Figure 5.7 shows a small example of the results obtained after rotating on its axis a completely specular flat reflector.

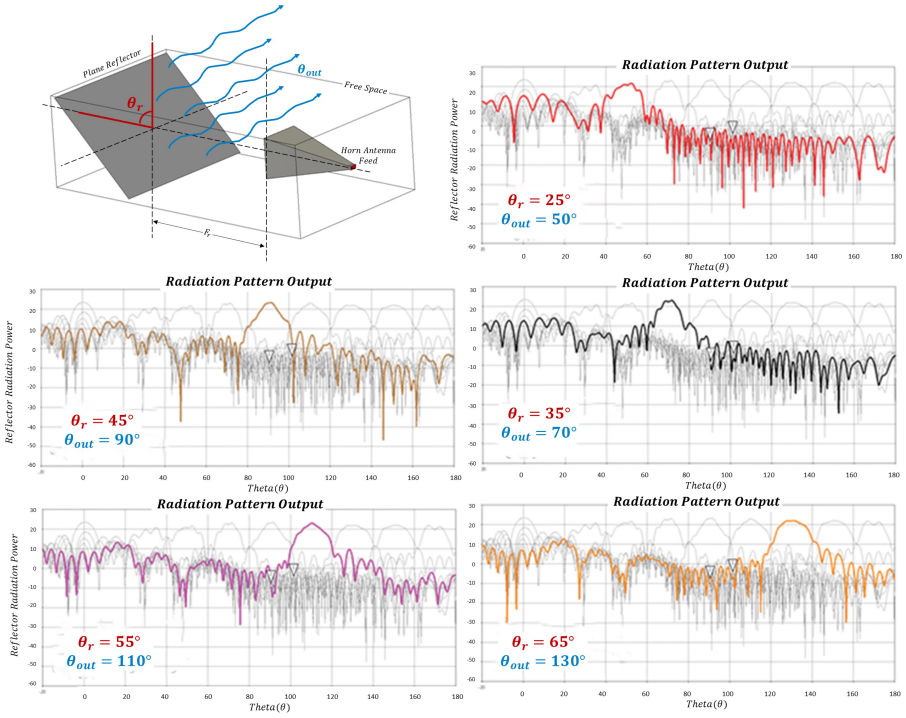

Figure 5.7: Example radiating pattern results for a flat reflector.

In each iteration, only one reflector prototype is analyzed. Then, in each iteration results are obtained from several angular positions of the reflector with different separations between antenna and reflector. And in each of these positions the surface currents induced in the reflector by the antenna are obtained, as well as the radiating patterns from the reflector. Therefore, for each reflector type, about 360 data sets are being analyzed. This amount of data is exorbitant because the design requirements of the reflector are very demanding.

5.4 Modular reflector prototype design

According to the above design guidelines, an initial base reflector had to be designed. The base reflector has a geometrical structure larger than the wavelength. This geometrical structure is the most critical, because it will allow to design the reflector to operate in a modular way. Where "*modularity*" refers to the ability of the base reflector to replicate indefinitely without losing the reflective properties for which it was designed. For this reason, throughout the design process, different types of reflector prototypes were simulated with different geometric shapes that could be adapted to a modular design, as shown in figure 5.8.

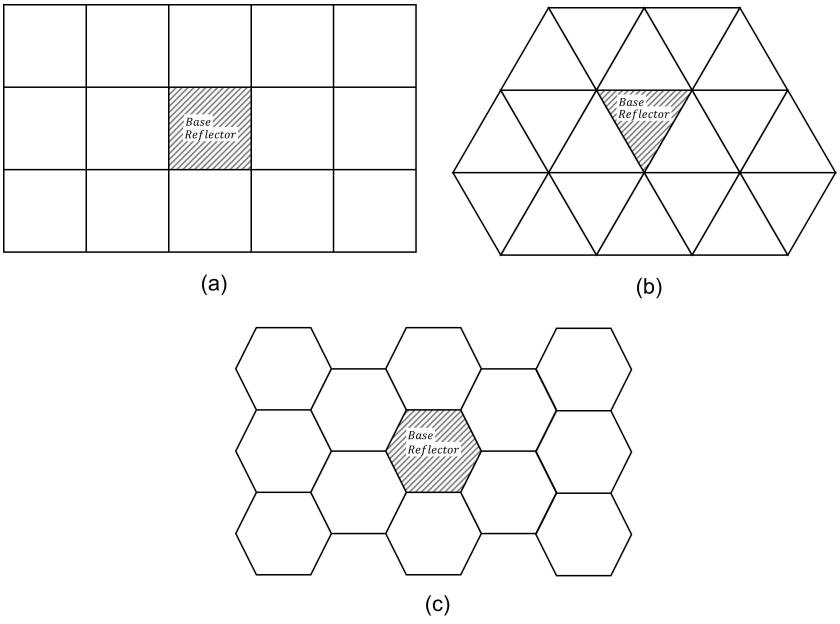

Figure 5.8: Prototype of modular patterns for base reflectors.

According to the geometrical patterns previously proposed, base reflectors were designed with three types of basic geometrical shapes such as square, triangular and hexagonal. From this basic geometrical shape, a smooth convex surface was designed initially. It has to be a convex surface to disperse the energy when it hits the reflector, because the radiating field comes from a very directive source.

After testing a large number of designs of convex surfaces adapted to the geometric shapes, it was concluded that the best geometric shape to fit the convex surface was the one shown in figure 5.8(c), in which radial revolution symmetry is obtained by building the base reflector with hexagonal segments. This allows us to adapt a circular convex reflector without causing discontinuities in the base reflector junction when assembled.

These discontinuities would causes abnormal energy concentrations, causing the resulting reflection from the set of base reflectors to be difficult to predict and parameterize. This phenomenon causes strong energy fading in the radiating pattern, which totally distorts the performance of the proposed reflector.

For this reason, triangular and square geometrical shapes are not suitable to design the base reflector, and therefore they were discarded. The first one because it was very complicated to build a convex surface with triangular shapes without discontinuities, and the second one because it did not adapt faithfully to a circular shape, causing many flat spaces, making the reflector to have highly specular contributions.

In conclusion, the optimal modular base reflector with a smooth surface to operate in the 30 to 40 GHz band, according to the design criteria of section 5.2.1, is the one proposed in figure 5.9. The final design consists of a semi-spherical convex section, with the optimal size of the convex part 60% of the cross section of the curvature of the semi-sphere, and with a radius of 7.8 cm, as shown in figure 5.9(c).

Each of the sides of the hexagonal section has a length of 4.543 centimeters. This dimension must be very precise, because this type of broadband mmWave reflectors are very sensitive due to their wavelength, which has also been observed with fine adjustments in simulations. These dimensions correspond to each base reflector that can operate as an individual or modular reflector as seen in figure 5.9(a)-(b). It can be observed that in the proposed base reflector the flat spaces in the transitions among base reflectors are very small, which allows to avoid strong specular behavior in the reflection; therefore, its effect can be omitted. It should be noted that one of the design parameters of the reflector was that it should be as flat as possible, in order to have a design as modular as possible, so it can be easily adapted to any type of built surface in any indoor environment.

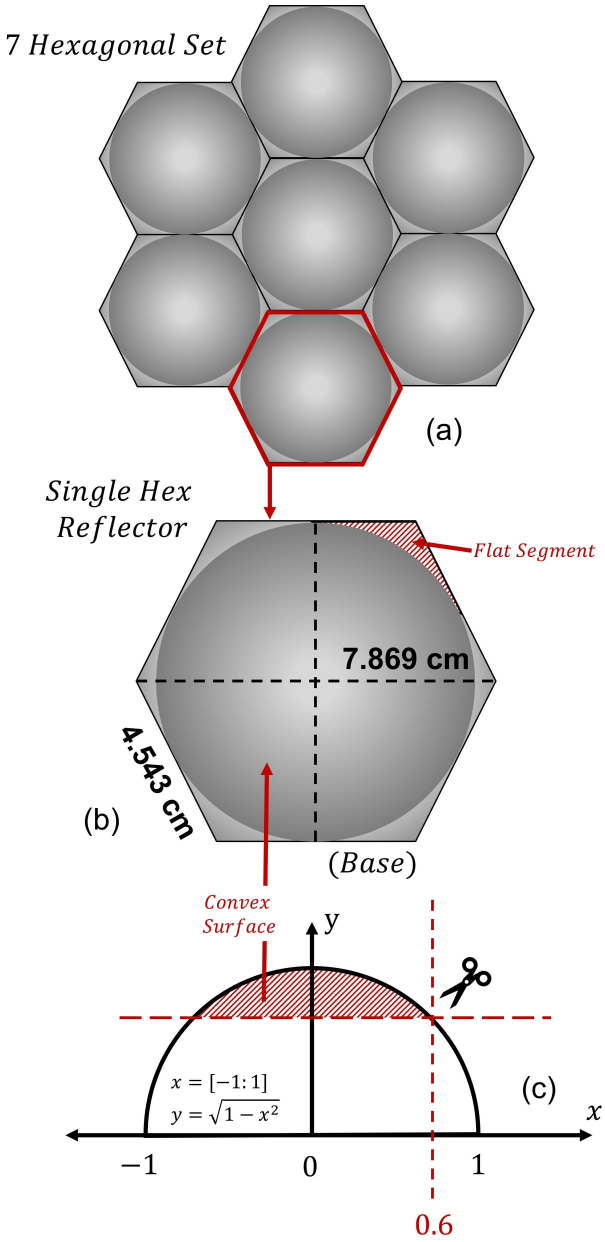

Figure 5.9: Design of the base geometric shape of the modular reflector. (a) Set of 7 assembled reflectors, (b) Individual reflector, (c) Design of the base reflector from a convex Semi-Sphere.

Figure 5.10 shows the distribution of surface currents induced by the Ka band horn antenna. It can be seen that there is a total continuity in the current distribution, and therefore a relatively homogeneous radiating pattern has been obtained in the target bandwidth. Recall that it was important to ensure homogeneity in the currents distribution especially at the intersection of the base reflectors, to get broadband performance.

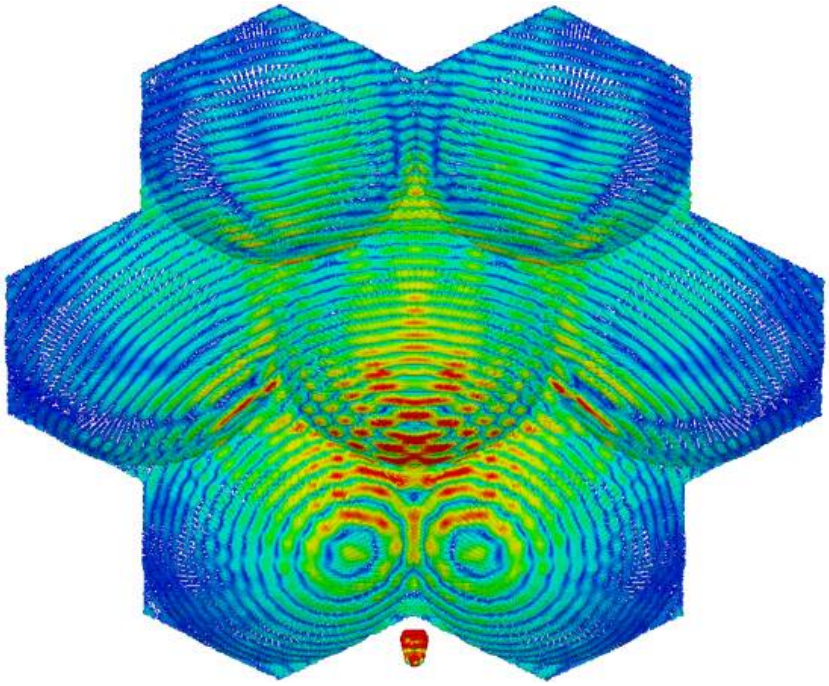

Figure 5.10: Current behavior on the reflector surface, Base Reflector (35 GHz).

Figure 5.11 shows the final results of the simulations obtained for seven segments of the modular base reflectors as a whole. The simulations were obtained after several iterative processes in the CST simulation tool [108]. The results show the radiating pattern in two axial cuts at $\theta = 90°$ and $\varphi = 90°$ of the 3D radiating pattern of the reflector, which is compared with the radiating pattern of the reflection obtained by a flat reflector to highlight the differences. For practical purposes, only the radiating pattern is shown at three different frequencies at 30, 35 and 45 GHz, but the complete analysis was performed in all this frequency range with 1 GHz steps.

Finally, it is concluded that the radiating pattern changes marginally as a dependence of frequency, causing sudden fades of 20dB and approximately 4° wide. Despite this, it was still possible to increase the broadband coverage from approximately 20° to 85° with a reduction in peak gain of 15dB respect to the specular reflection of the plane reflector(Blue one). In the proposed configuration each piece of the hexagonal reflector is relatively small (53.62 cm^2) and flat with a profile height of 1.46 cm.

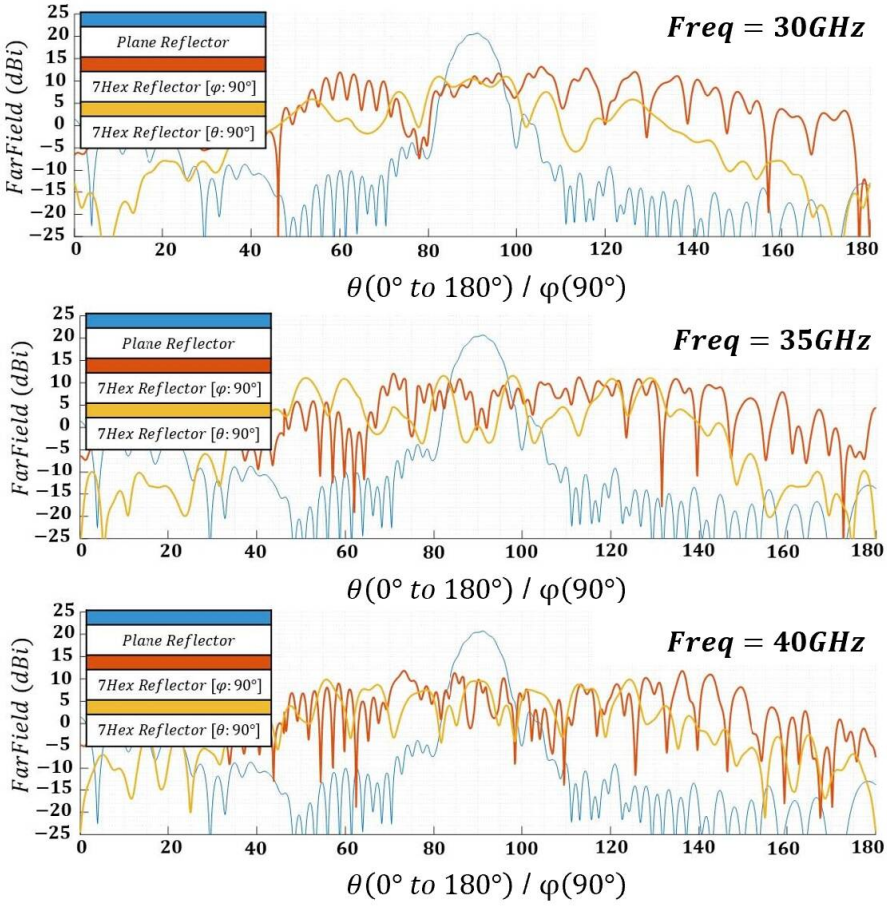

Figure 5.11: radiating pattern of the 7-hexagonal reflector and the specular plane reflector (Simulation of base reflector N°1 with CST).

5.5 Irregular surface design on base hexagonal reflector

As seen in figure 5.11, when the radiating pattern of the reflector is emulated with a smooth convex surface, some sudden power fades of about 20dB are present. In order to ensure that the radiating pattern is as homogeneous as possible, a pseudo-random rough surface should be designed to replace the smooth surface, so that most of the reflected contributions will be slightly different in phase, and not counteract each other within phase in the design frequency range.

The roughness was designed with a concentric periodic pattern in the cross section of the convex circular surface of the reflector (see figure 5.12(a)). The roughness has a radial variation ($\triangle r(mm)$), starting from the center of the circumference towards the outside of the circumference, and an angular variation ($\triangle \varphi(^\circ)$). The angular or radial variation refers to a slight discrete change in the height of the smooth surface of the base reflector. The change is made on the vertex of the mesh that forms the geometrical structure of the surface in three dimensions in the Blender software [130]. The mesh of the convex surface of the reflector has a revolution symmetry with an angular resolution of 0.1 degrees between vertices, and at 30 GHz $\lambda = 10mm$, so 0.1mm is 0.1λ.

This approach intends to design a surface as pseudo-random as possible, but with some design consistency, in such a way that it allows us to parameterize the rough surface, so to calibrate it with CST simulations to operate in broadband.

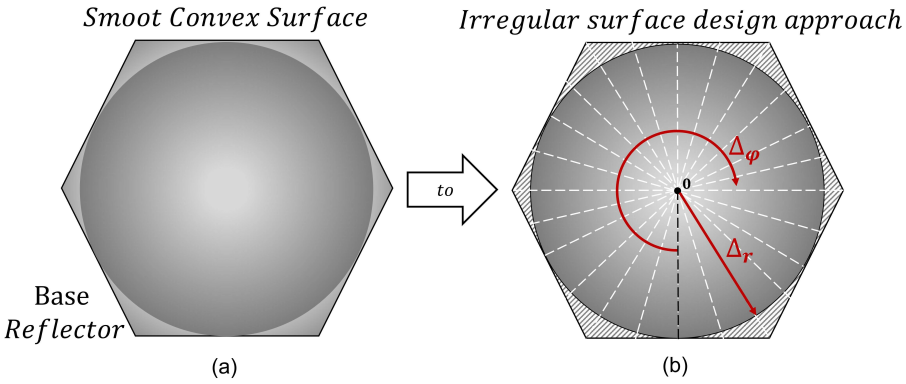

Figure 5.12: Hexagonal reflector Design Scheme.

All proposed irregular surfaces were initially evaluated just considering a single hexagonal segment. After this initial evaluation, the best performing surfaces were chosen, to evaluate the same irregular surface, but replicating it seven times as shown in figure 5.9(a). This was done in order to evaluate the reflector performance on a modular surface of larger electrical dimensions.

This part of the analysis was the most critical, because most of the surfaces that satisfied the design requirements individually, when evaluated as a larger modular reflector drastically decreased their performance and had to be discarded. This selection process was a very iterative and slow process, considering that when electrically larger reflectors are analyzed, as in the case of groups of 7 reflectors, the simulation times and hardware resource requirements increase drastically.

In the end, after countless simulations and surface design rectifications, four surfaces were chosen to improve the radiating pattern of the base hexagonal reflector. This process was really very tedious, since it is a broadband reflector in the mmWave range, and any subtle change in its irregular profile would greatly change its behavior. Finally, the proposed reflectors have the following mathematical formulation:

- **Prototype 1**
  - This is the base reflector, and its surface is smooth as seen in figure 5.9(b) , $\triangle r = 0$, $\triangle \varphi = 0$.
- **Prototype 2**
  - $\triangle r = 1.3 * sin\left(\frac{r\pi}{5}\right)$
  - $\triangle \varphi = 0.8 * cos\left(\frac{\varphi\pi}{23}\right)$
- **Prototype 3**
  - $\triangle r = 1.8 * |sin\left(\frac{r\pi}{12}\right)|$
  - $\triangle \varphi = 0$
- **Prototype 4**
  - $\triangle r = 0.87 * |sin\left(\frac{11r\pi}{80\varphi^{(0.22)}}\right)|$
  - $\triangle \varphi$ Depend on $\triangle r$
- **Prototype 5**
  - $\triangle r = -0.75 * |sin\left(\frac{r\pi}{14}\right)|$
  - $\triangle \varphi = 0$

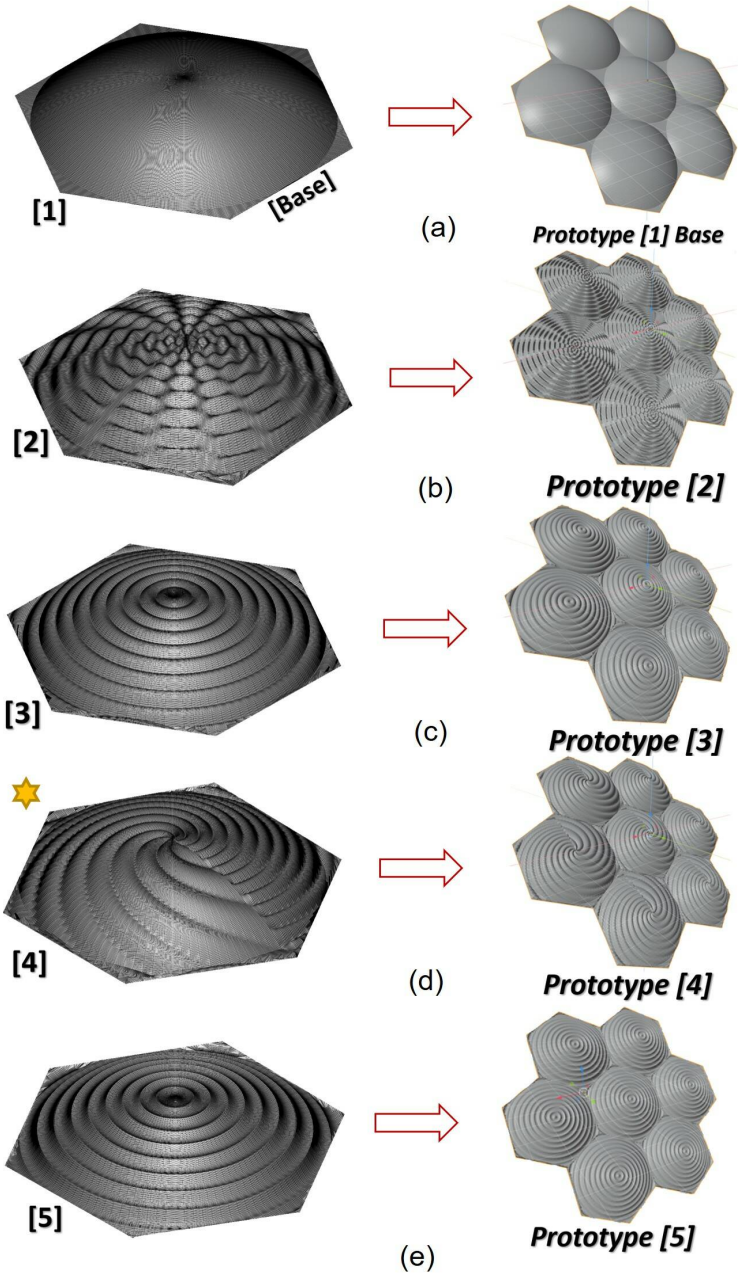

Figure 5.13: Hexagonal reflector Surfaces Prototypes.

The design of prototype 4 has a particularity, because it has a spiral design. With this approach it is achieved that each sector (Q_n) has a different irregular profile in front of it, when the modular reflector is composed of more than one base reflector, as shown in figure 5.14.

For example, the irregular surface of the reflector in sector (Q_2) of reflector 0, is different from the irregular surface of the reflector assembled next to sector (Q_4) of reflector 1. This applies to all sectors without the need to change the reflector design or orientation. This strategy is similar to the spatial diversity gain in mobile network coverage planning of past generations.

With this design strategy the contributions in each sector of the hexagonal reflector (Q_n) are diversified, so that the final sum of the adjacent contributions is as random as possible, and this results in a more homogeneous radiating in the area of interest.

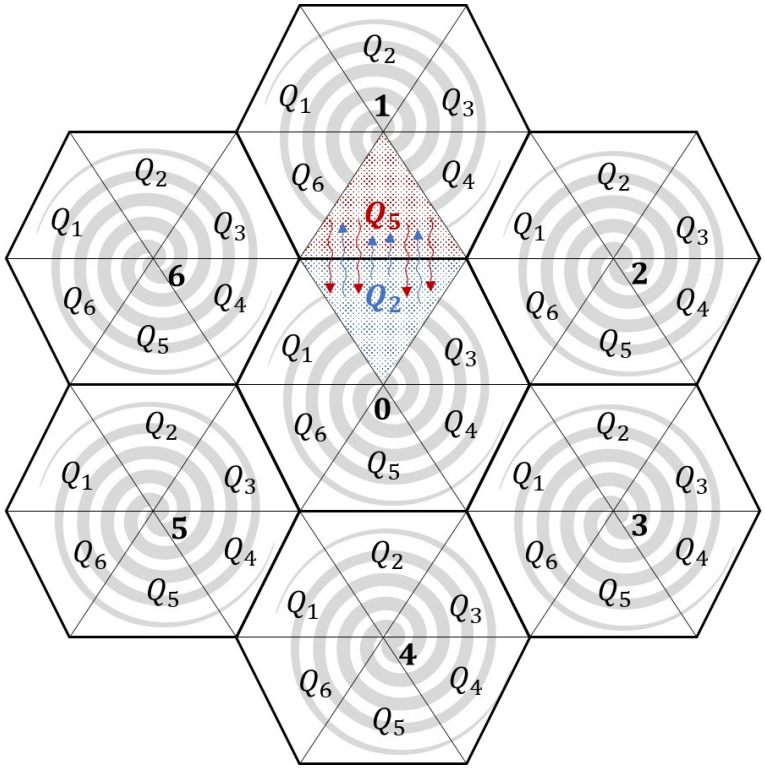

Figure 5.14: Spatial diversity design strategy for prototype 4.

5.6 Measurement campaigns

Once the prototypes were designed to improve the frequency response and radiating characteristics, the reflectors were manufactured with a professional large format 3D resin printer [131]. The use of a resin printer instead of a filament printer was a decision that was taken along the way, because the reflector of the previous chapter was built with a filament printer, which does not allow printing surfaces with great detail in the order of millimeters, and because the prototype proposed in this chapter has a more detailed surface, so it was decided to use a better quality printer.

Once the reflectors were made, they were metallized with a special paint with a surface resistance of 5 ohms, which is very similar to an all-metal aluminum surface [132]. The advantages of manufacturing this type of reflector with plastic is that it reduces manufacturing costs and allows for greater scalability.

The measurement setup is shown in figure 5.15, using a vector network analyzer (VNA), with two Ka-band horn antennas [109] and high-performance low-loss cables. The frequency response of the (S_{21}/S_{12}) channel was measured in a certified semi-anechoic chamber as shown in figure 5.16. Each reflector is made up of seven hexagonal reflectors as shown in figure 5.9.a, and both the transmitter and receiver are located 50 cm away from the reflector.

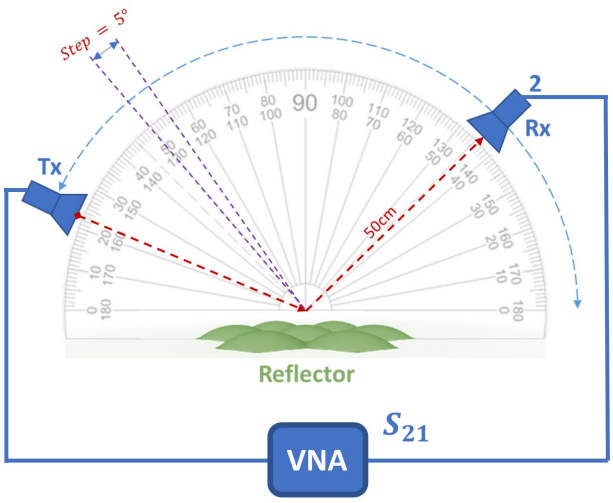

Figure 5.15: Measurement setup scheme for TX and RX positions.

The horn antennas are always oriented to the center of the reflector, while the receiving antenna will be radially displaced with 5° steps until reaching the whole angular range of the reflecting field, that will depend on the relative angular position of the transmitting antenna.

Different sets of measurements were taken for various angular positions of the TX antenna, of which 25° and 45° are used in this chapter in order to compare the results, with one of the design requirements of the input angular range of $\theta_{in-margin} = 20°$.

The measurements were performed in two groups. The first group of measurements set the T_x at 25° and gradually moved the RX every 5° between 170° to 45°. And in the second group of measurements set the T_x at 45° and gradually moved the R_x every 5° between 170° to 70° (See figure 5.16).

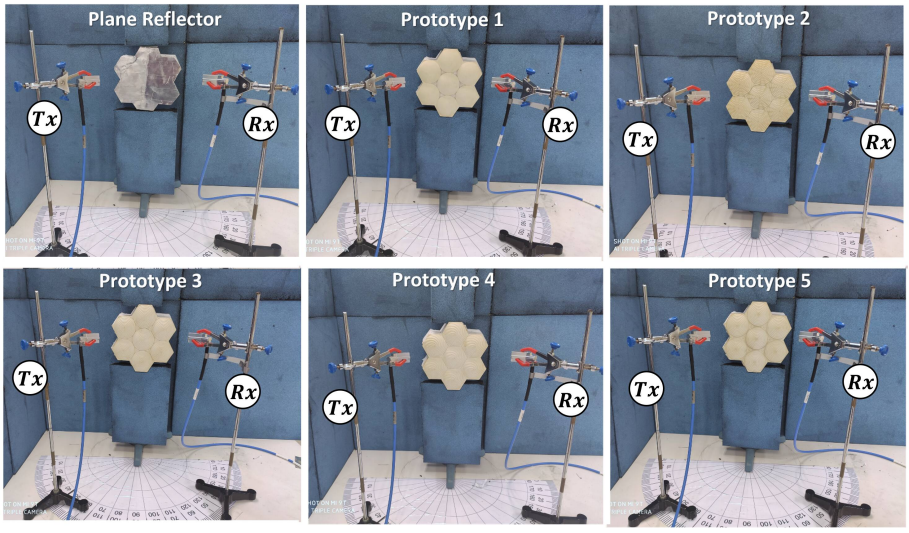

Figure 5.16: Measurement Setup in anechoic chamber.

The results in the figures 5.17 and 5.18, show the frequency response of the channel S_{12} measured $(x-axis)$ at different angular positions of the $T_x/R_x(y-axis)$. To compare the results, the prototype channel frequency responses have been normalized with the maximum power value obtained from the specular reflection over a flat metal reflector $(T_x : 25°(57dB)/T_x : 45°(56dB))$. The reference flat reflector has the same dimensions as the set of seven hexagonal reflectors, to evaluate the same RF energy incident on the prototype area.

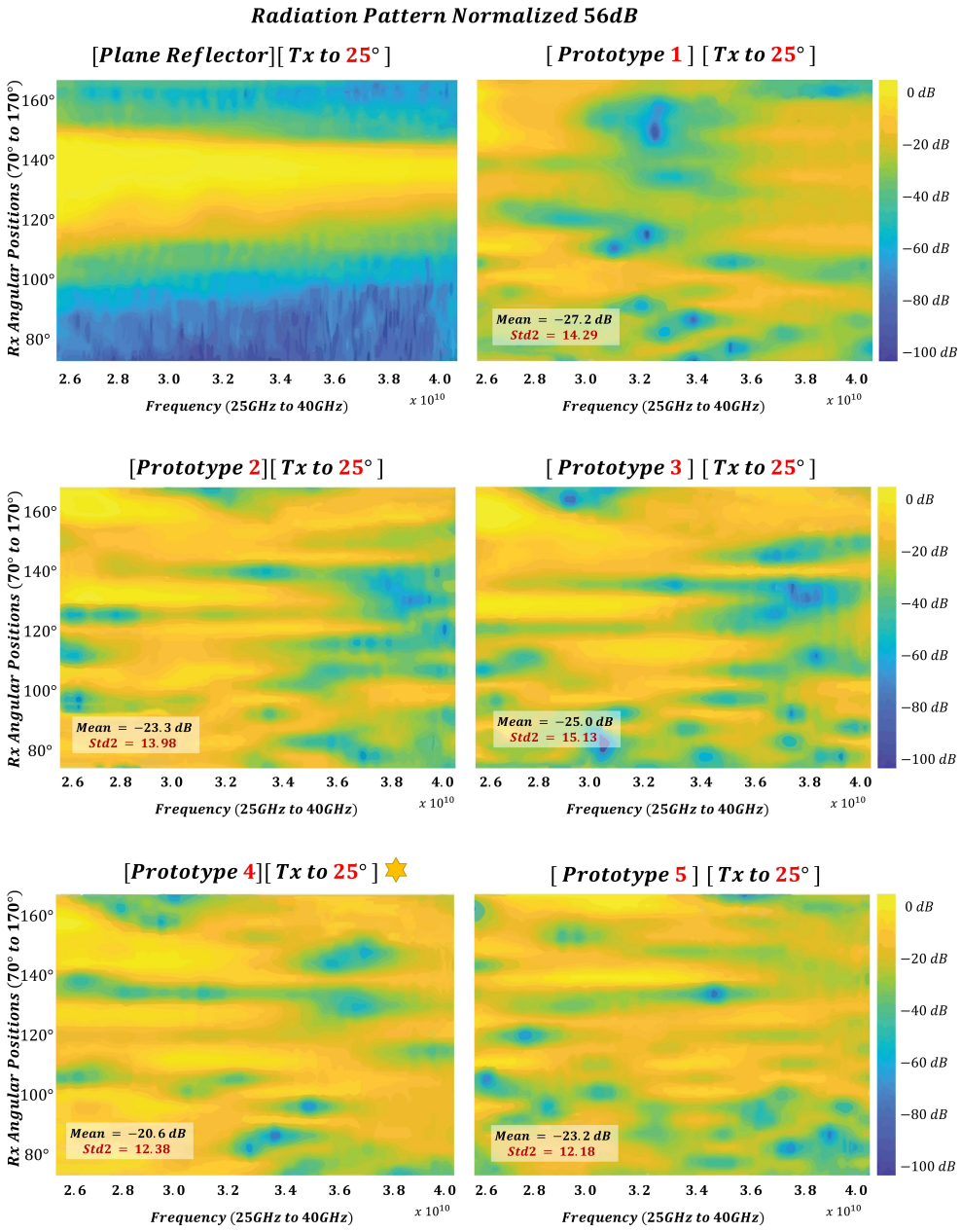

Figure 5.17: Measurement results at 25 degrees.

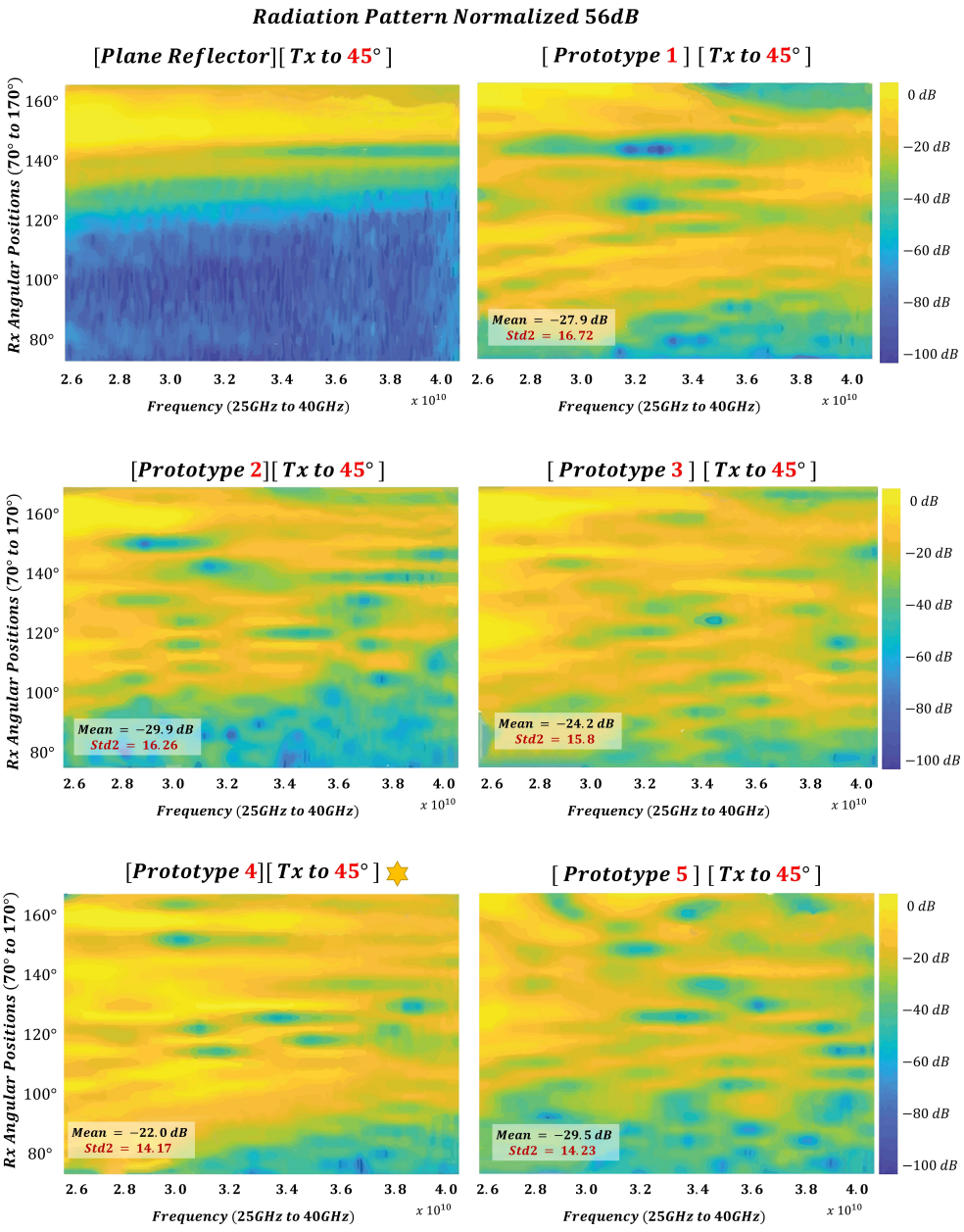

Figure 5.18: Measurement results at 45 degrees.

Figures 5.17 and 5.18 show graphically the results of the normalized directivity of each of the proposed reflector prototypes in the frequency range of 26 to 40 GHz. In order to evaluate the best performing prototype, a statistical analysis of the results was proposed. One of the parameters to be calculated is the mean of all the power values over the entire bandwidth of the study, as well as its standard deviation.

According to these measurements, the prototype $N°1$ has the worst performance, because, despite being a design with a convex surface, it has a smooth surface. This causes many of the reflected contributions to be countersubtracted in phase, and reflection radiating pattern fading (blue notches) appears in certain frequency ranges and incidence angles.

These results, which are easily observed, are also reflected by the value of their $Mean$, which is the lowest of the two groups of measurements with $-27.9dB$ and $-27.2dB$ respectively, also with the worst standard deviation 16.72 and 14.39 respectively.

On the other hand, the $N°4$ prototype has the best homogeneous energy spreading over the whole angular range and broadband, because it has the highest mean $-22dB$ and $-20.6dB$ respectively, and the smallest standard deviation 14.17 and 12.38 respectively. It is also concluded that the energy is dispersed in the proposed coverage range, which is approximately $\theta_{coverage} \approx 80°$ as seen from the results.

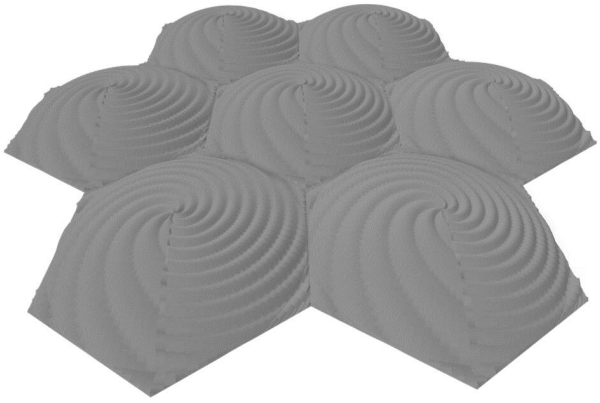

Figure 5.19: Prototype N-4 with the best performance in terms of dispersion.

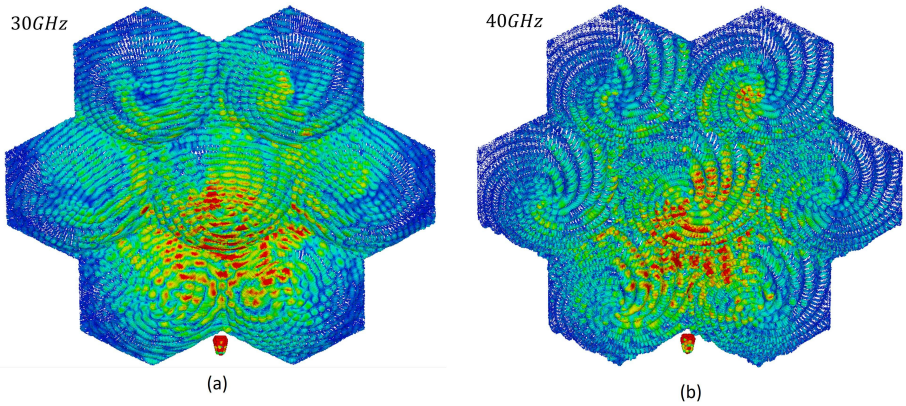

Figure 5.20: Current behavior on the reflector surface, Prototype 5 (30-40 GHz).

To complete the analysis of the reflective scattering behavior of the best performing prototype, we analyzed the simulation of the surface currents induced in the reflector (See figure 5.20), which propagate superficially following a spiral pattern, as the designed surface. Furthermore, a homogeneous distribution is observed in all the modular reflectors, ensuring the homogeneity of the radiating pattern throughout the design frequency range.

5.7 Conclusions

This chapter has presented a cost-benefit solution to optimize RF channel coverage in indoor environments at millimeter-wave frequencies by using passive reflectors. A modular reflector, composed of hexagonal convex rough surface elements, has been designed and tested. The proposed reflector is built with a 3D resin printer and then metallized with spray painting techniques, so the fabrication cost is low.

Its modular design allows to adapt the reflector size to each scenario in order to meet the coverage requirements, which is done by adjusting the number of hexagonal reflectors to be assembled. This passive reflector works independently of the position of the radiating source, as it has been designed to have no focal point, allowing unbeatable flexibility.

Among the configurations designed and tested, the $N°4$ prototype (figure 5.19) showed the best performance, offering homogeneous scattering with slight fading in the reflection pattern, depending on the operating frequency. This was possible due to the intentional non-homogeneity of the hexagonal surfaces of the proposed reflector.

The proposed reflector distributes the incoming field power nearly homogeneously over a coverage area of 80°, with a bandwidth of 30 to 40 GHz.

Compared to the use of planar reflectors, coverage in the NLOS regions can be increased by $\approx 400\%$, of course with a maximum reflector gain reduced by around 20 dB, which is still well above the human body blocking losses at mmWaves frequencies, which can easily reach 35 dB, as discussed in chapter 3.

Chapter 6

Antenna beam steering prediction in dynamic indoor environments

This chapter presents the design and implementation process of a predictive steering system for mmWaves communications, to operate in highly dynamic indoor environments, using Ray-Tracing techniques. The objective of this system is to predict the optimal antenna steering in order to minimize mmWave propagation losses when the visibility of the radio link is obstructed by people or moving obstacles in the environment. In addition, the technique could also be used to find the optimal configuration to maximise performance of MIMO antennas or distributed MIMO systems.

The system must characterize the environment in real time as efficiently as possible, so to predict alternative routes to the propagation of the signal in mmWaves, and anticipate the best beam steering. To achieve this, all physical phenomena that affect the propagation of a plane wave when it is obstructed are considered in a simulation environment.

To this aim, this chapter has been divided into the following sections:

- Section 6.1 presents a brief introduction.
- Section 6.2 presents the state of the art of artificial intelligence algorithms used to identify and track persons from video information.
- Section 6.3 presents the hardware configuration used to capture the environment information of the predictive beam steering system.

- Section 6.4 presents a step-by-step methodology used as design guidelines for the predictive beam steering system.
- Section 6.5 presents the initial draft implementation of the predictive beam steering system on the Unity video game platform.
- Section 6.6 describes an overview of the Unreal Engine video game platform used to implement the final version of the predictive beam steering system.
- Section 6.7 presents the definitive implementation of a real-time predictive beam steering system using video information from a stereographic camera.
- Section 6.8 presents the procedure used to calibrate the ray-tracing algorithm employed to characterize the mmWaves radio channel in the predictive beam steering system.
- Section 6.9 presents the conclusions of this chapter.

6.1 Introduction

The promise of ultra-high-speed connections demands larger bandwidths in the next-generation mobile networks, such as 5G and beyond 5G networks. Although mmWave bands have a lot of available free spectrum, they are more susceptible to path and penetration losses than sub-6 GHz options.

In the case of an indoor environment with several obstacles, inadequate received signal power (mainly in non-line-of-sight NLOS areas) can become the biggest problem in the mmWave bands, because it degrades coverage and forces operators to deploy additional base stations, which is often very costly and therefore impractical for them to implement. Hence, it is of vital importance to understand the mmWave channel propagation characteristics to predict their behavior.

The characterisation of the mmWave channel has been studied in a number of simulation- and measurement-based studies in the literature. In [133] Ray-Tracing simulations and imaging methods are jointly used to model the propagation of the broadband channel at 60 GHz. Based on the outdoor-to-indoor path measurements, propagation loss and delay characteristics of mmWave signals in the 32 GHz spectrum are examined in [134]. In [135], a variety of 5G channel characteristics are examined in a real office setting using channel probe measurements and contrasted with current 3GPP and ITU models. In [136], a real-time experiment platform is suggested, that facilitates real-time multiband

and closed-loop evaluations for sub-6 GHz MIMO and mmWave systems. In [137], the authors experimentally study the building entry loss and environmental clutter loss models that ITU-R adopted for the 3.5 GHz and 27 GHz bands and demonstrate that the loss behavior is not multiplicative as indicated by ITU-R. In [138], 3D ray-tracing simulations of large urban environments were conducted in the 2 GHz and 28 GHz bands with the use of radio channel model parameters such as path loss exponent, angle spread and delay spread. In [139], three-dimensional ray-tracing simulations were performed for an outdoor scenario in mmWaves, where simulations and channel measurements were compared to evaluate the importance of diffuse scattering as in the works of [140], [141]. Note that throughout this Thesis the diffuse scattering generated by the human body is studied in detail (Chapter 2 and 3), so this effect is also considered in the development of the proposed predictive beam steering system.

Therefore, throughout this chapter, we investigated how to implement proprietary ray-tracing techniques on video game simulation environments in both Unity [142] and Unreal Engine [143].

The use of these simulation environments allows to easily reconstruct any complex indoor environment and thus efficiently simulate how the wave propagates at mmWave frequencies, and to obtain the inputs needed to predict the alternative signal paths, when the signal has been obstructed by any dynamic obstacle in the environment. The main dynamic obstacle identified and evaluated in a complex environment will be the human body, because it is the one that most affects the propagation of the signal, since statistically it is always very close to the mobile terminal.

6.2 Human Body Recognition

One of the objectives of our system is to actively track the human body and its posture, in order to evaluate its effect on signal propagation in the mmWave band in complex indoor environments. Human body posture recognition has been used extensively in smart tracking, computer-human communication, video recording, virtual reality, and so on. This has always been an important research direction in the field of computer vision, because of the large number of applications that make use of this technology. The first human body posture recognitions are mostly based on multiple sensors on different areas of the human body [144]. The use of sensors in smartphones and other wearable technology, such as wristbands and watches, to recognize human body posture has already gained significant adoption [145]-[146]. Time and frequency domain analysis, SVM (Support Vector Machine), Bayesian networks and other

conventional machine learning techniques are used in [147]-[148]. For feature extraction, these machine learning techniques require expert knowledge in the field of human body posture.

There have been two main trends in recent years regarding the identification of human body posture. One is to train, identify, and categorize human body postures using Convolutional Neural Network (CNN) object identification methods that are based on deep learning. For instance, some researchers have used deep learning and neural networks, but artificial feature extraction is still necessary [146]-[149]. CNN were employed in [150], where only one layer was used, although this is not a sufficient learning depth to correctly extract the posture characteristics of the human body. Smart watches and deep CNN were utilized in literature [151] to recognize and categorize human activities in various contexts.

The other trend is the identification of important features such the body, hands, face, and evaluation of body position. For the purpose of identifying 2D poses of numerous persons in an image, Zhe Cho introduced a technique called OpenPose in 2016 [152]. In this method, the essential points are first identified using a bottom-up algorithm, and then the backbone is identified. It can accurately estimate how the human body is posed in the image. A 2D OpenPose-based human gesture grading system was described in literature [153] using monocular images. The remarkable OpenPose in three dimensions was used to construct a bi-manual teleoperation system that was controlled by a human through 3D skeleton extraction in literature [154].

6.2.1 Convolutional Neural Network (CNN)

One of the most important tools used by artificial intelligence technologies for object detection is the use of convolutional neural networks (CNN). Convolutional neural networks, usually referred to as CNNs or ConvNets, are a category of feed-forward artificial neural networks whose connectivity structure is modeled following the way that animal visual cortices are set up. The visual cortex contains small clusters of cells that are sensitive to specific regions of the visual field. Only when specific edge orientations are present, do individual neuronal cells in the brain respond or activate. Some neurons are triggered when edges are displayed vertically, while others are triggered when edges are displayed horizontally or diagonally. A kind of artificial neural network called CNN is used in deep learning to assess visual data. These networks are capable of handling a variety of media-related tasks involving images, sounds, text, videos, and other forms of media. In the late 1990s, Bell Labs professor Yann LeCunn developed the first functional convolutional networks.

In a CNN, each input image will technically go through a series of convolution layers with filters (Kernels), Pooling, fully connected layers (FC), and apply the Softmax function to classify an object with probabilistic values between 0 and 1. This is how CNN deep learning models work for training and testing. A complete CNN flow is shown in the following figure 6.1, which processes an input image and classifies objects based on values.

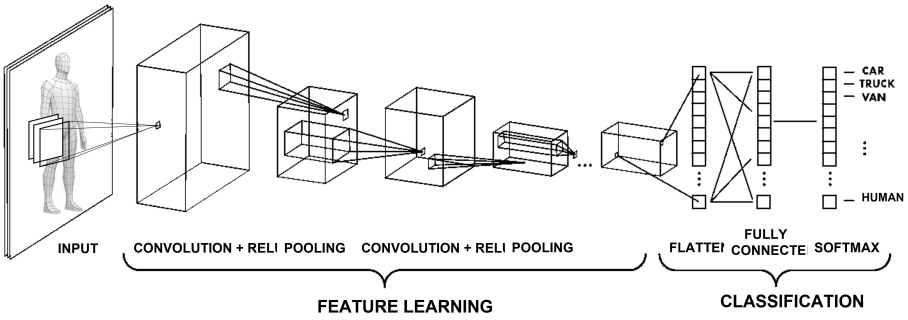

Figure 6.1: Neural Network with many Convolutional layers.

The method of convolution involves combining two functions to create the result of the combined function. After CNNs apply filters to a complicated input image, a feature map is created. The network vectors that make up the weights and biases of filters are generated at random. Instead of being different for each neuron, CNN uses weights and biases that are the same for all neurons. There are many different filters that may be created, and each one extracts a different quality from the input. Sometimes, filters are referred to as *kernels*.

6.2.2 Region Convolutional Neural Networks (R-CNN)

The fully connected layer structure of a convolution neural network (CNN) causes inability to handle many items and frequency of occurrence. To solve it, one method would be to use a sliding window brute force search to choose a region (figure 6.2) before applying the CNN model to it [155]. However, this approach has the drawback that the same item might be represented in an image with various sizes and aspect ratios. These considerations have resulted in a large number of proposed regions, and if deep learning (CNN) were to be applied to all of them, the computational cost would be very high.

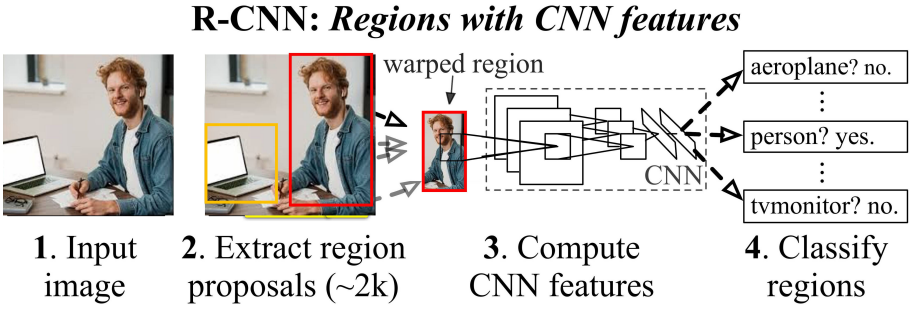

Figure 6.2: R-CNN Architecture.

Therefore, the R-CNN technique is based on the following concepts:

- **Region Proposals**: Simply defined, region recommendations are the smallest areas of the input image that may contain the things we are looking for. R-CNN uses a greedy technique called selective search to decrease region proposals.

- **Selective Search**: In order to generate region proposals, the greedy method of selective search joins smaller segmented regions. This algorithm uses an image as its input and output region suggestions on it. This algorithm's benefit over random proposal generation is that it keeps the total number of suggestions to around 2000, and the region proposals it generates have a good recall rate.

- **Algorithm**:

  1. Create the initial picture sub-segmentation.
  2. Recursively combine similar bounding boxes to create larger ones.
  3. Create region proposals for object detection using these larger boxes.

Then, according to the specifications of the CNN model, these areas are deformed into a single square of regions of smaller dimensions than the original image information. The CNN model we utilized here is a pre-trained version of AlexNet, which at the time was the most advanced CNN model for image categorization.

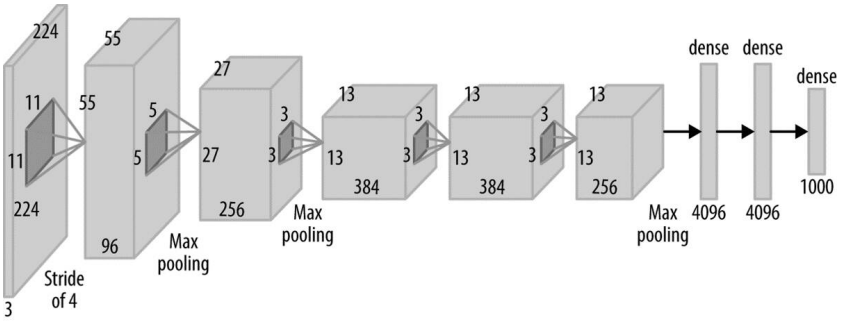

Figure 6.3: R-CNN AlexNet architecture.

The fact that the AlexNet receives the same input size (224, 224, 3) every time is another crucial consideration. However, the image suggestions have various shapes. Numerous of them are either smaller or larger than what is needed. We must therefore resize each region suggestion.

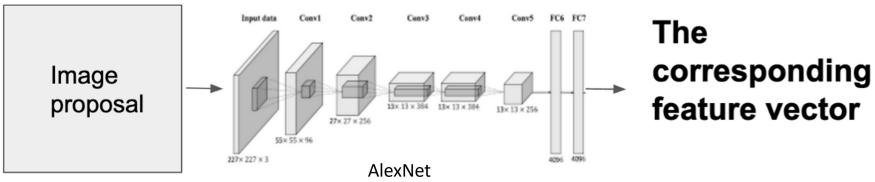

Figure 6.4: R-CNN AlexNet SVM.

SVM (Support Vector Machine): the binary SVM is trained on each class separately, then it consumes the feature vector generated by the CNN. With the help of the feature vector produced by the CNN architecture above, this SVM model generates a confidence score for the presence of an object in that area. However, there is a problem with training the SVM because the AlexNet feature vectors need to train the SVM class. As a result, AlexNet and SVM cannot be trained simultaneously. Therefore, with future iterations of R-CNN, we address the performance issue as with Fast R-CNN.

With this R-CNN technique, different types of objects can be efficiently identified from the video information, although with the Fast R-CNN technique the detection performance is considerably increased, especially if this information is used to detect mainly the human body in a complex indoor room.

6.2.3 Detectron2 Algorithm

One of the major complexities of training a convolutional network is the large amount of images that would be needed to train it properly; the training also needs a lot of computational power especially for the Graphics Processing Unit(GPU) of the video cards. For this reason, today there are pre-trained detection algorithms using artificial intelligence and one of the most powerful and versatile is Detectron2.

The newest library from Facebook AI Research is Detectron2 [156], which offers cutting-edge segmentation and detection techniques. It is the replacement for Detectron and maskrcnn-benchmark. It supports a variety of Facebook production apps as well as computer vision research projects. Some of Detectron's results can be seen in figure 6.5.

Figure 6.5: Detectron2 Detection Results.

Pytorch, a programming language used in the development of Detectron2, has a thriving community and is constantly updated and bug-fixed. Currently, the Facebook AI research team actually paid attention to the difficulties and gave relatively simple setup instructions for installations. A very simple API was also made available for extracting scoring results.

Pytorch is a language that relies on Python [156], therefore to use Detectron it is mandatory to program in Python. In fact, most of the latest implementations of artificial intelligence is based on a Python core, which makes it an indispensable programming language when implementing any development that involves the use of this technology.

As previously mentioned, Detectron2 is an object detection algorithm, not only of persons, that is widely used in the industry for many applications, so we will also use it to detect people in our adaptive beam steering system, and to determine the exact position of people in real time.

6.3 Stereographic vision to capture the environment

To detect the people inside a space and to determine at the same the dimensions of that space, it is necessary to have a hardware element that allows us to read any complex environment efficiently. Initially one could think of using a traditional video camera, with the limitation that it only allows to acquire images in two dimensions. This is beneficial in the first instance because it will allows to identify people in an environment, since artificial intelligence technology always uses two-dimensional images to identify if there is any type of object in a video capture. With this approach, the identified obstacle can be located in a two-dimensional plane, which for most applications is more than enough, because the aim is only to know the type of the identified objects and their number in the scene. But in our case it's also very important to know in detail in which place of the scene is the identified object.

For this reason it was necessary to use depth cameras or stereographic cameras to read not only the two-dimensional information of the environment, but also to consider the depth information. This is vital because it will allow us to properly evaluate the mmWave radio channel, which is highly dependent also on the positions of all the obstacles, and especially of human bodies, in the environment.

6.3.1 Stereo Vision System

One of the most often used methods of computer vision is the stereo vision system. The goal is to take advantage of parallax error. The depth is inferred from the parallax error measurement after the identical scene is recorded from two distinct viewing angles. The parallax error, also known as the disparity between the pixels of the image frames, is inversely proportional to depth and simplifies it to a single basic equation, yet estimating the parallax error is a very alluring non-trivial issue to manage. Only overlapping fields of view between the two viewpoints, as shown in figure 6.6, allow for depth estimation.

To accurately extract findings from stereoscopic systems, numerous researchers and mathematicians have developed novel algorithms in this subject [157]. This method has been used for more than a century and has demonstrated its value in numerous applications. In the field of robotics, this system is especially beneficial, because robots will know the depth of objects, and will have a three-dimensional understanding of their environment, in which they interact.

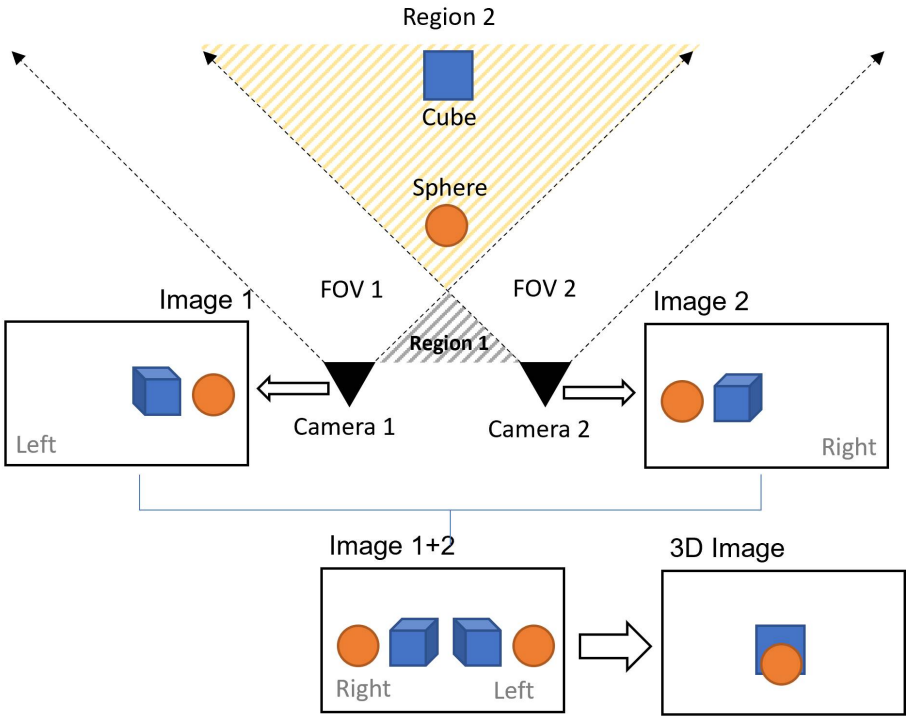

Figure 6.6: Visual Stereo Setup.

As a result of these two superimposed images from each camera (right, left), we obtain the scene information that is visible in the right frame and not in the left frame, as shown in figure 6.6.

It's impossible to find directly a disparity between these pixels to form a scene with depth information. But there are techniques with intelligent interpolations that help us to determine the similarity between the frames to extract the distance information.

Many of these interpolation techniques depend on the manufacturer and are therefore proprietary techniques. And, depending on the technique, better results can be got in the resolution of detecting the depth of the objects on the stage, and on the max range.

Additionally, some leading companies in this type of technology use complementary LiDAR techniques that help to improve their performance.

6.3.2 Hardware Settings Used

Throughout the development of the predictive beam steering system explained in this chapter, two different types of hardware were used, namely RealSense D435 by Intel [158] and ZED2i from Stereolabs [159]. These are considered among the best depth cameras on the market with the best possible performance.

Intel RealSense cameras are the most widely used cameras today for industrial and research applications, therefore they have the largest community of developers working on this platform, which makes the initial learning curve for this type of camera very fast. In contrast are the ZED cameras that are the most powerful on the market, for the speed of stereographic image processing that allows low latency applications, in addition to having twice the range of its closest competitor, the Intel RealSense. Throughout the development of the research of this chapter the two cameras were used, where initially a tracking system was implemented with the Intel RealSense D435 within the Unity video game platform.

Later, due to the latency and range limitations of the Intel cameras, it was decided to use the ZED cameras to develop the system in a more professional way through the Unreal Engine video game platform.

Keep in mind that, with the two types of hardware used, one can make applications in various programming languages such as C++, *C#* and Python, but the artificial intelligence algorithms used to detect the relative position of people within the scenario are fully developed in Python. Both Intel and Stereolab cameras were programmed using Python in order to facilitate the implementation and training of artificial intelligence algorithms.

The cameras used have the following technical characteristics:

Stereo Cameras		
Features	**RealSense D455**	**ZED2i**
Use Environment	Indoor	Indoor/Outdoor
Ideal Range	0.6 to 6m	0.4 to 15m
Depth Field of View (FOV)	87° x 58°	110° x 70°
Depth output resolution	Up to 1280 x 720	Up to 4416 x 1242
Depth frame rate	Up to 50 fps	Up to 100 fps
Depth technology	Stereoscopic	Native video resolution
RGB frame resolution	Up to 1280 x 800	Up to 4416 x 1242
RGB frame rate	50 fps	100 fps
RGB sensor FOV (H x V)	90 x 65°	110° x 70°
Additional Sensors	none	Accelerometer, Gyroscope, Barometer, Magnetometer, Temperature sensor
Programming Language	C++, C#, Python, Matlab	C, C++, C#, Python, Linux, Jetson L4T
Connectivity	USB-C* 3.1 Gen 1*	USB 3.1 Type-C
Dimensions	124 x 26 x 29 mm	75.25 x 30.25 x 43.10 mm
Weight	100 g	166 g
Power	USB 5V / 230mA	USB 5V / 380mA
Operating Temperature	0°C to +40°C	-10°C to +50°C

The following figure shows the physical cameras used.

Figure 6.7: Stereo Cameras Hardware.

6.4 Predictive steering System Implementation Methodology

The objective of this chapter is to design a predictive radio beam steering system to support beam-forming and beam-steering systems in the mmWave band, in order to optimize coverage in complex indoor environments especially in non-line-of-sight (NLOS) areas and to avoid unwanted fading of signal quality.

For this purpose, as explained in the previous sections, it was essential to have a technology that allows to identify the relative positions of people in an environment, because the human body is the main propagation obstacle in the mmWave band, due to its random movement around the indoor scenario and its proximity to the mobile terminal. To analyze the scattering effect of the human body, the research carried out in chapter 2 and 3 was used.

To evaluate radio channel with Ray-Tracing techniques through video game simulation platforms, it was also necessary to have a tool that enables to have real time characterisation of the three-dimensional scenario. For this, we used stereographic cameras that enable to map onto a three-dimensional scenario the position of people detected by video information in a two-dimensional scenario, and to determine the position of obstacles in the environment.

The proposed methodology comprises several steps that will be explained taking into account the example scenario in figure 6.8 of an office with furniture and people, seen from a zenithal point of view.

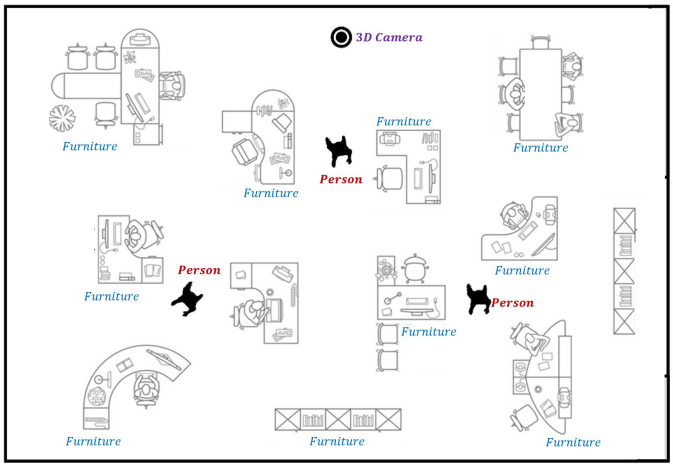

Figure 6.8: Example Indoor Office from a zenithal point of view.

From this point we begin to structure the methodology proposed in our system in eight clearly differentiated steps, as shown below.

The objective of **step one** is to identify all fixed obstacles in the environment using a stereographic camera, as shown in figure 6.9, where the identification scope depends on the Field of View (FOV) of the camera. Everything outside the FOV of the camera is unknown to our system. Let's keep in mind that the idea of this system is to analyse the environment in real time, for which it is important to initially discriminate between furniture and people.

Therefore, in **step two** the objective is to effectively discriminate between people in the environment and furniture. For this purpose we use the artificial intelligence algorithm called Detectron2, which is one of the most versatile nowadays. This identification is done on the two-dimensional video information and then extrapolates its position onto three dimensions, according to the information of the position of each pixel that is associated with a depth value. The identification of the furniture in step 1 is done once in a while, but the identification of people has to be done in real time, since they are constantly changing their relative positions.

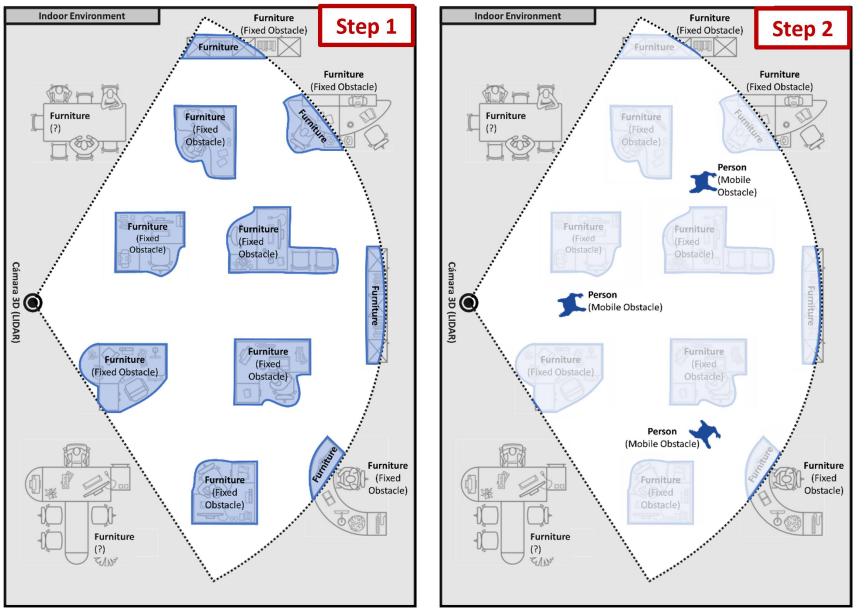

Figure 6.9: Steps one and two, detection of fixed and dynamic obstacles.

In **step three** the system has to identify all potencial entrances and exits that will depend on the camera's Fiel of Viewv (FOV). The identification of the positions of the plausible exits and entrances will be discrete, and will depend on the relative positions of all the scenario furniture. Then, for example, these points will determine the possible entrances and exits through which a person will enter and exit the visibility of the camera, and will be those areas that will not have any obstructions for each person to move through them.

And in **step four**, the system should calculate all possible viable paths to each of the entry and exit points based on the visibility of the camera. These will be the same possible routes that people will take when they move along the indoor scene. This step is very important because it must not only take into account the entry and exit positions, but also the relative positions of all the furniture on the scenario and thus calculate the optimal routes among all the possible combinations of routes in the scenario.

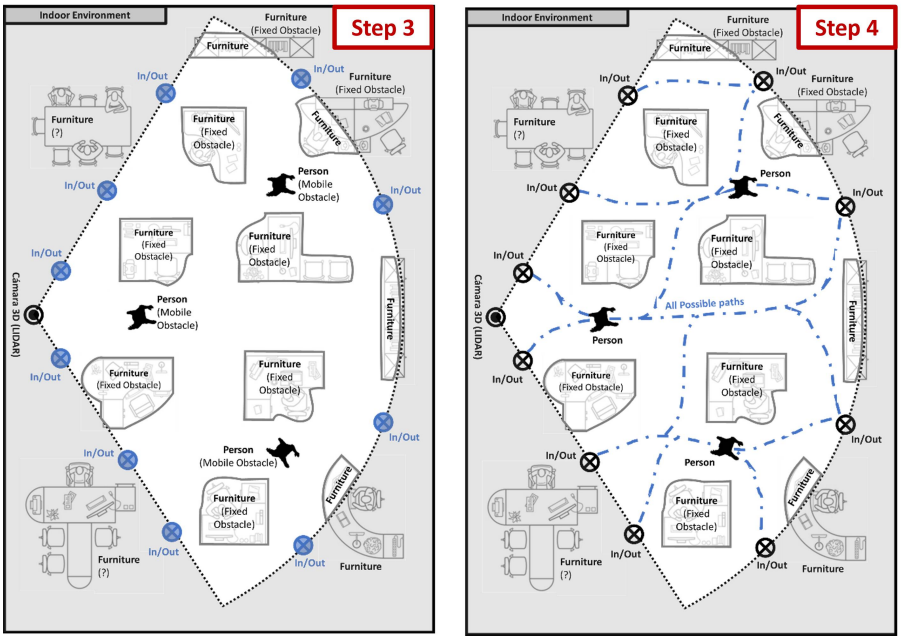

Figure 6.10: Steps three and four, analysis of entry and exit points with their trajectories.

In **step five**, the system analyzes the relative movement of all the people in the scenario, in order to determine the most probable trajectory that each person in the scenario could take, according to the routes previously identified in step four. This procedure allows the system to identify the most likely path a person could take in order to predict future radio channel behavior along that path.

In **step six**, our system has the objective to identify all those areas where there is line of sight (LOS), as well as those where there is no line of sight (NLOS). This is done in order to provide our system with the ability to identify which of these areas are more likely to have a poorer signal quality, since are in NLOS, and so to reinforce the multi-path contributions in those areas, to mitigate the propagation losses in mmWaves. In addition, temporary NLOS concealment zones, which are produced by the obstruction of the human body, are also considered. These zones are constantly changing as the person moves through the environment.

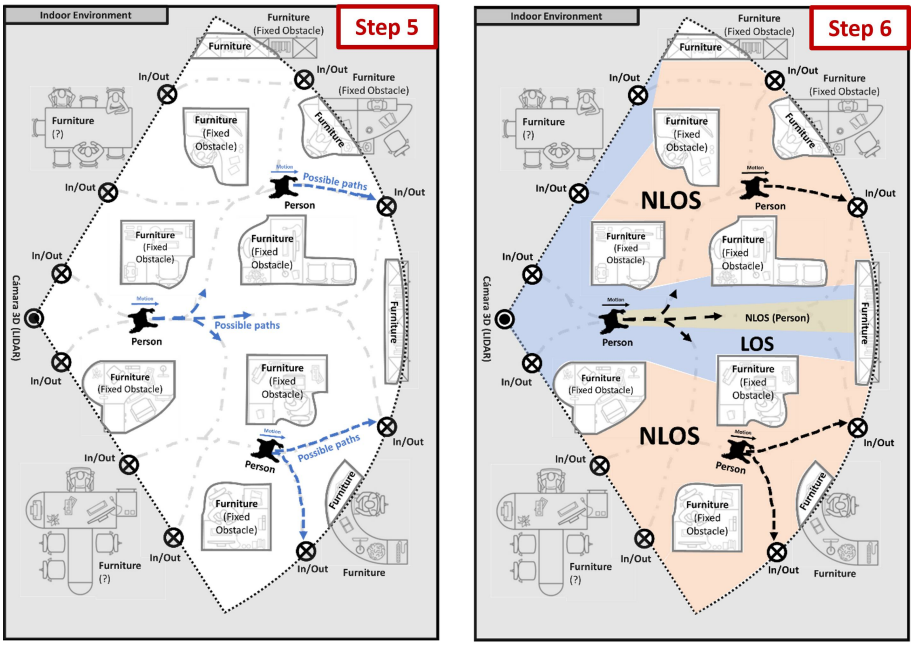

Figure 6.11: Steps five and six, analysis of the possible routes of each person in the scenario and classification of the zones according to their visibility.

In **step seven**, the proprietary Ray-Tracing system is used to calculate the physical phenomena of reflection, diffraction and transmission. Based on the multi-path contributions of these physical phenomena, the optimal orientation of the beam along the predicted trajectory of each person is deduced in order to improve its coverage. Note that providing coverage at the person's location is equivalent to providing coverage to the mobile terminal, due to the physical proximity. In this step, before considering the movement and relative location of each person in the environment, all contributions caused by all fixed obstacles such as furniture, walls, ceilings etc., are pre-calculated in order to optimize system performance. When the complete analysis is done in **step eight**, only the effects generated by the human body as it moves through the scenario have to be analyzed in real time. Therefore, in step eight only the prediction is updated according to the interaction with people in the scenario and the contributions of the static scenario previously calculated in step seven. With the information on the dynamic and static multi-path contributions, as the person moves along the scenario, our system will have the capability to suggest the optimal beam steering to improve coverage especially in NLOS areas.

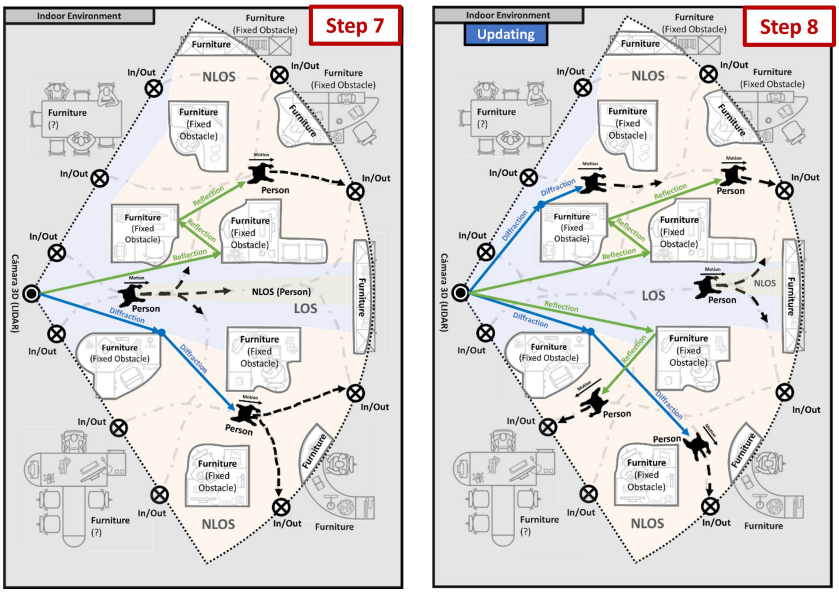

Figure 6.12: Steps seven and eight, final analysis of the used methodology, where Ray-Tracing techniques are used to deduce the optimal multi-path contributions.

6.5 Sketch implementation of predictive steering system in Unity

In this section we discuss the draft implementation of the predictive steering system for coverage optimization in the video-game platform called Unity. This platform was used in chapter 3 to implement the Double Knife-Edge model to evaluate the scattering effects of the human body on mmWaves.

First, we defined the camera to be used in this implementation, which was the Intel RealSense D455. This camera was chosen for being the most flexible of the two previous proposals, besides being the easiest to learn to program together with artificial intelligence tools in Python. This stereo camera works in conjunction with LiDAR technology, which allows us to obtain information about the depth of the scene as well as video. From the video information, the Detectron2 artificial intelligence algorithm can be applied to track the relative positions of the human body in the indoor scene. One of the features of this camera is that it automatically calibrates itself according to the environment, which makes it easy to set up the system quickly.

The D455 camera was configured to automatically calibrate itself according to the lighting conditions of the environment, where the resolution, range and frames per second settings are self-configured to be optimal. The range of this type of camera depends to a large extent on the illumination of the scene, so for well-lit scenes the range will be the maximum, which in the case of the D455 is 6 meters. We must take into account that the artificial intelligence algorithm used to detect people is also very sensitive to lighting.

In this type of camera the field of view (FOV), which is the angular range of view of the camera is fixed (Azimuth: 87°, Elevation: 58°). The visual limit of the camera is relevant, because depending on how big is the environment to be characterized, this type of camera can be useful or not. So, for large scenarios such as conference rooms this type of camera is not a good solution due to the limited field of view, as well as the 6m max range in optimal lighting conditions.

In this draft implementation the programming languages used were C++, C# and Python. These languages were used separately to create our system as a whole, because each one has its own advantages and limitations depending on where it is used; in our case, the choice of one language or another was depending on the platform.

The C++ language is the native low-level language of the camera D455. Therefore, it was used to calibrate the camera and make fast readings of the camera information. With this language we read all the information from the

camera quickly and send it directly through sockets to the Unity platform for processing.

Python is the most widely used language for developing applications with artificial intelligence, so it is the language with the largest number of libraries and tools to identify objects only with color video information. This is important because Detectron2 identifies people independently of the depth information of the scene, considerably reducing the computational load, which is indispensable in any real-time system. With Python, initially we were also able to identify all the furniture in the scenario, like chairs, tables, cabinets, etc. But this information did not provide any useful information for the system, since it can be easily deduced that a fixed obstacle is furniture. So, with the depth information obtained with C++ we can have that information in addition to the wall and ceiling information. When the artificial intelligence algorithm identifies one or more people in the scenario, it sends the coordinates of each part of the human body through sockets to the Unity platform.

The C# language is the native high-level language used in the Unity platform. This language is organized so that all the information received through the C++ sockets (Reading the camera scenario) and Python (Identification of the person in the scenario). Once all information is received, we integrate it in a three-dimensional environment. This three-dimensional environment is used as a starting point to carry out the methodology explained in section 6.4. In the end, the system is fully integrated in Unity, since the core of our system is in the proper processing of the data received to compose our predictive steering algorithm created mostly with Unity C#.

6.5.1 Scenario measured with the stereo camera

The tests were performed in a room of 4x4 meters where there was no office furniture. These tests were performed in such a small room mainly due to the range limitations of the D455 camera. As shown in figure 6.13.a, the camera was placed in an upper corner of the room in order to have the maximum visibility.

Figure 6.13.b shows the scenario recreated with the camera where, according to the field of view of the camera only the corner opposite to the camera's location can be observed. Since there was no furniture, an office environment was emulated by placing obstacles (artificial furniture) in different positions within the field of view of the camera. Recall that people moving within this scenario should avoid colliding with these artificial furniture in order to move from one side to the other, as seen in step four of the previous section.

Note that even if the furniture is emulated to create a more complex scenario, this does not invalidate the results of the draft system, as it is designed

to adapt to any environment, without the need to preload any scenario, because it is automatically calibrated to identify fixed and dynamic obstacles as well as the possible routes that a person can take in the environment.

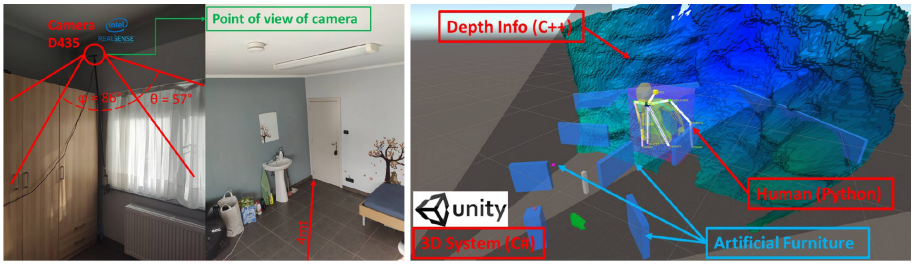

Figure 6.13: (a) Measured room with the stereo camera and (b) its equivalent in the Unity implementation.

6.5.2 Identification of the obstacles in the scenario (Step One)

The identification of obstacles in the scenario is essential to describe the routes that exist in a conference room or in an office, since people tend to walk avoiding the obstacles in the scenario, which usually have a fixed position. It is important to keep this in mind because our system was designed to automatically calibrate itself only per scenario, at the first run of the program. The program has not been designed for frequent changes in the environment, but although this could easily be implemented for more dynamic environments where furniture is often moved, for practical reasons it is only calibrated once at the beginning of the program.

The obstacles in the scene are located by mapping the entire scene with a hexagonal mesh with the same dimensions as the camera field of view, as shown in figure 6.14, where the scene in this context is the depth information obtained directly from the D455 camera. The hexagonal mesh used is discrete, i.e, each hexagon of the mesh is an independent object. The hexagonal shape was used because it is the most efficient geometric shape for filling spaces in nature and allows us to reliably map the complex shapes of obstacles in the environment. The hexagon can adequately map the environment without the need to decrease their size, and therefore place more elements unnecessarily that drastically affect the performance of each simulation, because in Unity each element or GameObject has an independent life cycle, with libraries, etc.

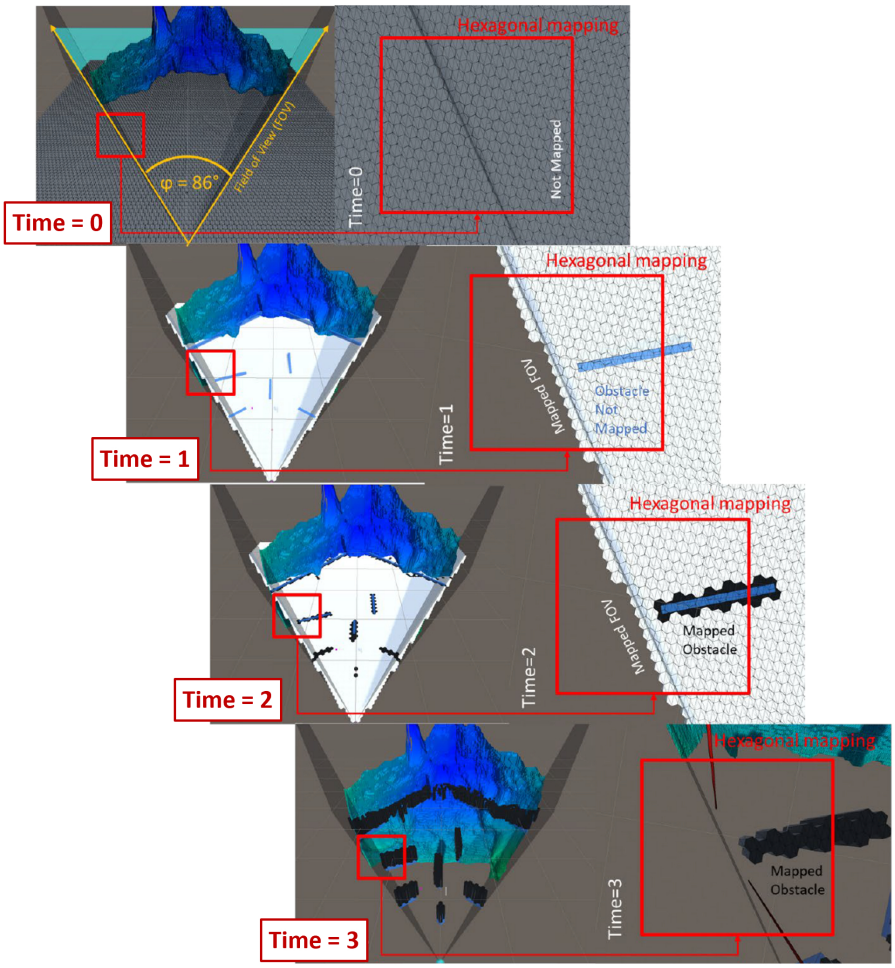

Figure 6.14: Steps of the hexagonal mapping carried out in Unity of the obstacles of the scenario, read by the Intel RealSense D435 camera (C ++).

To understand how the mapping process is carried out, we briefly explain step by step the scenario mapping carried out to identify the obstacles, which is shown in figure 6.14.

- **At time = 0** : We create a mesh with independent hexagonal gray elements, building a rectangular surface over the entire scenario, where

the scenario is determined by the limits of the camera's field of view (FOV).

- **At time = 1** : We eliminate the hexagonal elements that were not within the FOV of the camera, because these elements were outside the scenario.
- **At time = 2** : An angular sweep is performed from bottom to top, with the meshing of white hexagonal elements to map the scene according to the location of the obstacles in the environment. The obstacles in the enviroment are mapped from the depth information of the D455 camera (using C++) including the artificial obstacles that had been placed to emulate a complex environment. Note that when the environment mapping is executed, there must not be any person on the stage, otherwise it will be recognized as a static obstacle. When the stage obstacles are mapped, the hexagons change color from white to black indicating that there is an obstacle on the stage.
- **At time = 3** : We eliminate all the white hexagons that did not trace any obstacle, so these spaces will be possible paths between entry and exit points.

With the procedure described above, the entire scenario was mapped efficiently, without the need to read the depth information from the D455 camera constantly in real time, because it is more computationally expensive, especially to be processed by a high-level platform such as Unity.

6.5.3 Identification of the Human Body (Step two)

The predictive steering system was designed to avoid the harmful effects of the human body on the signal propagation in the mmWaves band that causes significant fading in complex indoor scenarios. For this reason, it is essential to identify the human body in the scenario in an efficient way and for this purpose we used the pre-trained algorithm called Detectron2, which allows us to identify the skeleton of the human body only with video information, without having to resort to depth information. This algorithm is quite versatile, but has the problem that it is too robust and heavy to be applied to a real-time identification of the human body only. Therefore, it was necessary to manipulate the root code of the Detectron2 GitHub to simplify it, in order to make it work in real time. After simplification, the identification time was reduced from about 10 s to 5 ms per frame, by eliminating the need of the algorithm to identify hundreds of objects. With this modified artificial intelligence algorithm, each part of the human body was identified as an independent element,

which is quite useful because it allows to adapt the 3D model of the human body to the identified body parts, and make the 3D model of the human body as close to reality as possible, as shown in figure 6.15.

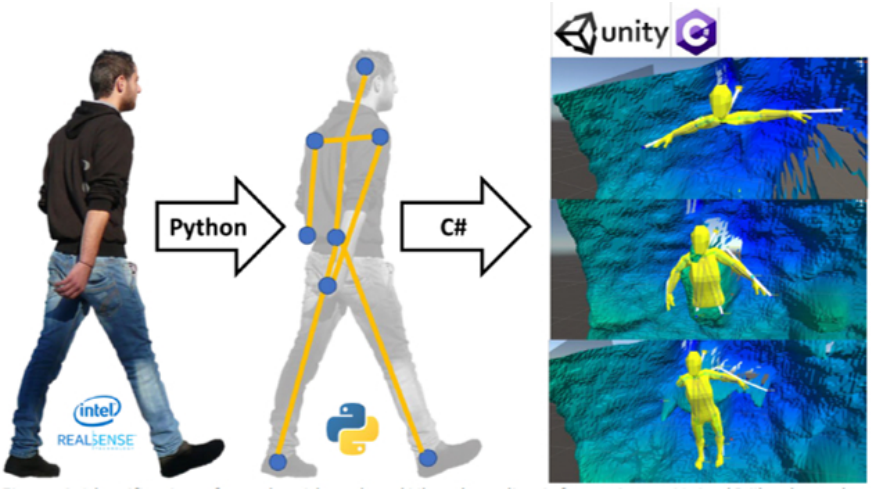

Figure 6.15: Identification of people with Python (AI) and transmission of this information to Unity (C#), where persons can be identified according to their visibility.

6.5.4 Identification of the Scenario Routes (Steps Three-Four-Six)

Once the positions of the obstacles in the scenario have been identified, the routes that a person could take through the scenario must be identified. Therefore, it is essential to understand what we mean by a "*path*" in the scenario. According to figure 6.16, we can define a path as the route that a person travels among all the obstacles of the scenario from points A to points B, where points A refer to the potential entrances and exits on the left boundary according to the field of view of the camera, and points B refer to those on the right boundary.

The number of paths is not directly proportional to the number of points A/B, since it depends directly on the placement and shape of the obstacles. For example, it can be seen in figure 6.16 that between point A1 and B1 there is only one valid path, while other paths are not possible due to the furniture blocking the passage of people. In reality there are other paths from A1 to B1, but they are out of the scope of the camera, so they are not taken into account

by the algorithm. Another option would be passing through subsequent points A2/B2, but they are considered independent from the viewpoint of the camera, hence they are not considered. As in the process of identifying obstacles in the scenario in the previous section, it should be noted that when the system is identifying the scenario routes, there should be no person in the scene, because the system will recognize the person as a fixed obstacle, and will substantially change the predefined routes.

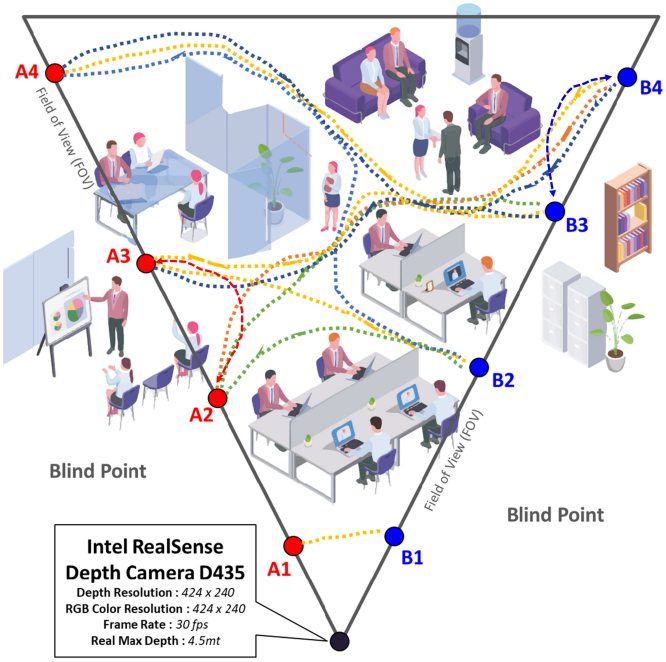

Figure 6.16: Explanatory diagram of the concept of routes according to the field of vision of the D455 camera and how it is handled in the implemented system.

Before identifying the routes, the first thing to identify are the start/end points of the routes (the A/B points); therefore, an algorithm was created that automatically identifies these points at the boundaries of the camera viewpoint that do not have any obstacles nearby, i.e., they are corridors where people can start or end their route.

Once the A/B points were identified, the next step was to create a system of independent bots. The goal of each bot is to find the optimal path between

point A to B, where a proprietary maze guide ray tracing algorithm was created in Unity with C# (See figure 6.17). Each bot will leave the A/B points and evaluate all possible routes available, regardless of the number of obstacles and their dimensions. This is the longest process in the whole system and its duration is directly proportional to the number of A/B points, which depends on the number of bots looking for the shortest routes in the scenario .

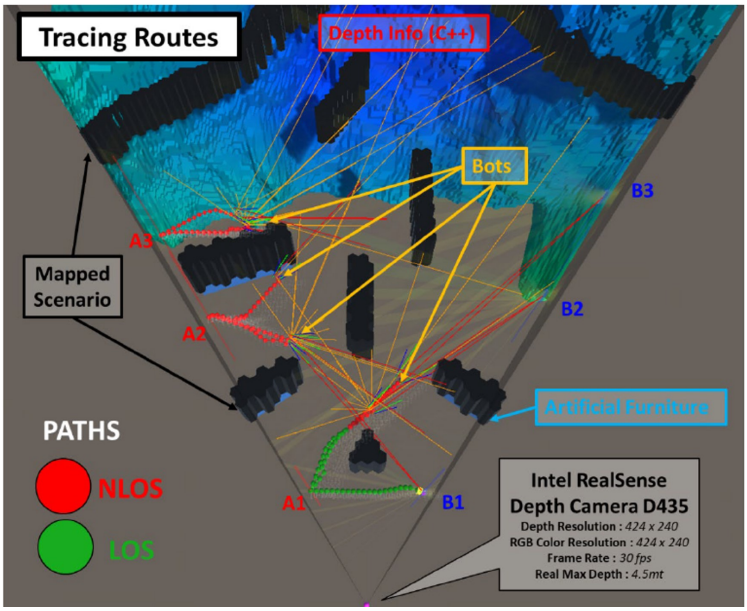

Figure 6.17: How the routes are created by bots and what are the final resulting routes.

Another important objective of each bot is to identify whether there is visibility (LOS) or not (NLOS) of the camera to the section that the bot travels (See figure 6.18). This is done in order to identify in which segments of the path traversed by the bot the mmWaves signal will experience fading, caused by the concealment produced by obstacles. In those areas, the multipath components will have to be reinforced to offer better quality of service.

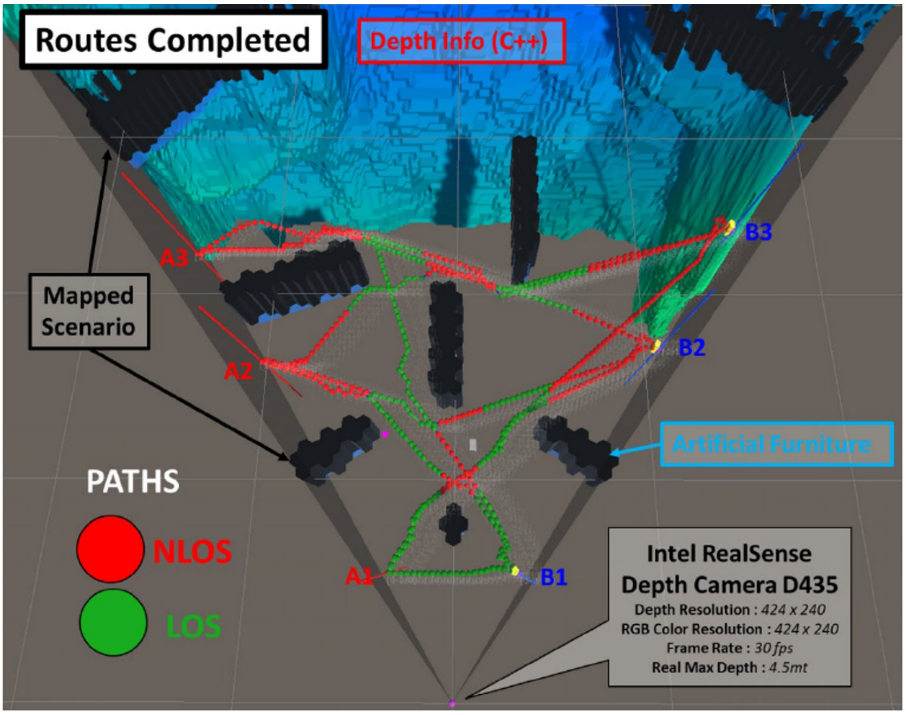

Figure 6.18: Final routes with NLOS and LOS identification.

6.5.5 Beam steering Prediction draft system in NLOS areas (Steps Five-Seven-Eight)

Once all possible routes that a person can take between the entry and exit points and their respective visibility (LOS / NLOS) in each segment of the route have been identified, the next step in the system is to deduce which potential route that person will take to reach an exit point from the camera's field of view. Once the most likely path a person will take has been determined, the multipath contributions will be calculated with the proprietary Ray-Tracing technique, to identify the possible reflections and diffractions in each segment of the path in the NLOS areas.

Once we know the possible route that each person is going to take and the possible multipaths that the signal can take to provide coverage in those NLOS areas, the system only has to suggest to the antenna radiating system which should be the optimal future beam steering according to the movement of the person in the environment.

Figure 6.19 shows the step-by-step evolution of the system in the Unity simulation environment.

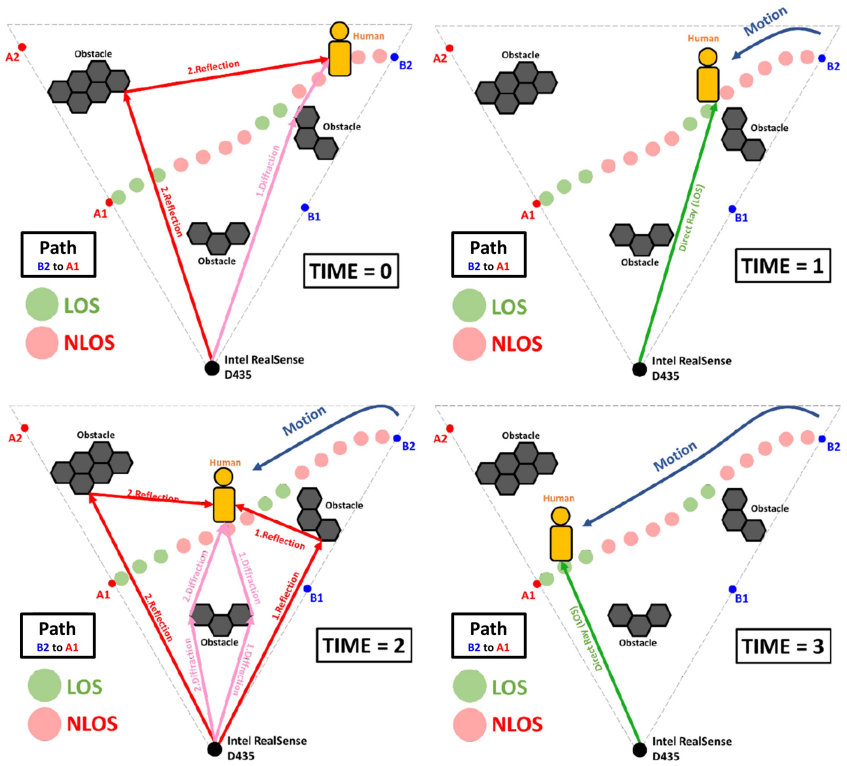

Figure 6.19: Operation of the predicted beam steering system, considering various positions of a person on stage and the different responses of the system (Reflection + Diffraction).

In figure 6.19 we can see, at **time = 0**, the initial position of the persons entering the camera field of view through point B2. This position, according to the route previously calculated by the bots, is in an NLOS area with respect to the camera location, which in future will be occupied by the mmWave radiating system that controls the beam steering. As the person is in a NLOS area, the system knows in advance which are the possible paths through which it can provide coverage in that initial position, which in the presented case example could be either by a reflection or a diffraction path

At **time=1** event, the person has moved and is in a coverage area (LOS) for which neither reflections nor diffractions are considered to provide coverage, although in the case of MIMO antennas, these contributions could to be considered as well, which is not the case in this implementation.

At **time = 2** instance, we see that the person is now in a shadow zone again so, according to the system, four possible paths are offered through which coverage can be provided, either by redirecting the beam or by doing a specific beam-forming to the direction of interest, where we have two contributions by reflection and two by diffraction.

And finally, at **time = 3**, we are back in the coverage area (LOS) so no alternative paths are proposed. In summary, this is how the adaptive beam steering system works.

The following figures 6.20 and 6.21 illustrate the operation of the real-time system, which has been explained in figure 6.19 above.

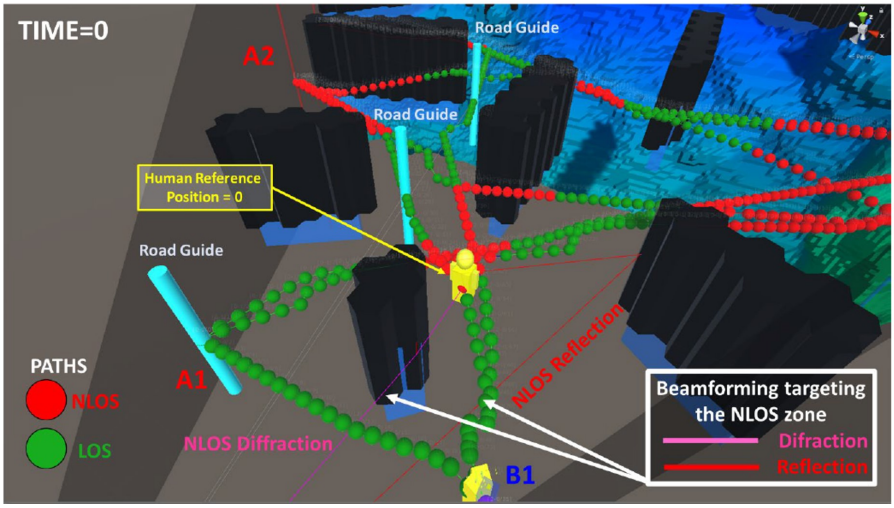

Figure 6.20: Real-time emulator of the predicted beam steering system developed in Unity, at Time = 0.

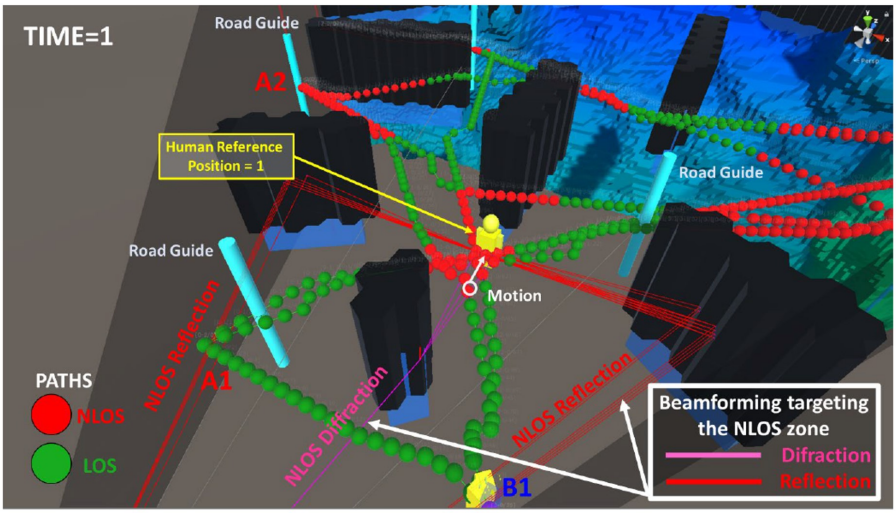

Figure 6.21: Real-time emulator of the predicted beam steering system developed in Unity, at Time = 1.

6.5.6 Conclusion Beam steering Prediction draft system

Based on the research conducted for the implementation of the draft beam steering system in Unity, the following conclusions can be drawn:

- One of the great difficulties in the implementation of this system was the integration of three programming languages in a single system, since each language has its advantages and disadvantages. As mentioned above, the use of C++ is essential to use to have a fast reading of the data directly from the camera; also the use of Python programming language is very well adapted to work with artificial intelligence, and therefore it was essential mainly to identify the human body in the scenario, and finally the use of C# is essential to work with Unity where the whole system was consolidated and own algorithms were designed for the implementation of predictive beam-steering.

- One of the most important challenges throughout the development of this system was the manipulation of the information coming from the camera (depth + color), due to the amount of information that had to be manipulated. Therefore, this was initially unfeasible due to the low computational capability but, after countless tests and debugging in all

phases of development, a reliable real-time system was achieved. In future, the algorithm could be further optimized to run on computers with lower computational capability, or alternatively the simulation platform could be replaced by a more powerful one.

- Due to the pandemic circumstances the system was only tested with one person, which was a drawback in the development of the system, since in conference rooms and office environments there is usually more than one person and in constant movement. After several tests, it was found that the maximum range of the D455 camera is only 4.5m, so its use it in a real environment would have been unfeasible. In addition, lighting conditions would have to be ideal, both to achieve this limited range and to use the Detectron2 algorithm to identify people. Therefore, it was concluded that this type of camera is not the most recommended for this type of implementation, so for the next section it was decided to use a camera with much better performance than the Intel RealSense D455.
- Other limitations of this draft implementation is that it was only possible to make the beam steering system in a two-dimensional plane. It would had been very complicated to synthesize a three-dimensional scenario, due to the limitations of the camera to fully recognize the scenario, as well as the inability of the Unity simulation platform to simulate hundreds of objects simultaneously, and be part of the synthesized three-dimensional scenario.
- The most significant finding from this implementation is that it showed that a beam steering system to dynamically reorient a radiation system based on video data can be implemented.

6.6 Advanced Game Engine Simulation Tool

The platform used to design the beam steering prediction system assisted by video information is called Unreal Engine 4 (UE4) which is explained in detail in Annex (Section A.4). In this platform, the ray tracing techniques used in the Unity gaming platform were redesigned in order to improve performance in order for the system to work in real time. This allows not only to evaluate the scattering effect of the human body with the DKE model, but also to predict the radio channel in mmWaves in a complex and realistic indoor environment.

All the design considerations on the ray-tracing techniques learned in the previous implementations in Unity were taken into account, to evaluate both the human body and the physical phenomena, as well as to design the predictive steering system in concealment zones.

The decision to change the simulation platform was based on the need of a more robust and faster platform. One of the major limitations of implementing this predictive steering system in Unity was the difficulty of having a real-time system, because the logic of this platform is supported in a high-level language like C#, and this kind of platform is not adapted to operate simultaneously with hundreds of GameObjects.

Although Unreal Engine has many advantages over its closest competitor Unity, it also has a number of disadvantages that are not negligible, where the one that stands out is the complexity of learning, because it is a professional platform that until recently was released under an open source license, so its community is very small and the detailed knowledge of the use of this platform was limited to industry professionals for the development of last generation video games.

The following table explains comparatively the strengths and weaknesses of each Open-Source videogame platform, which also includes a platform called Godot, that also allows the creation of videogames and simulation environments.

Comparison of Simulation Platforms			
Features	**Unreal**	**Unity 3D**	**Godot**
Learning Curve	⊕ ⊕ ⊕ ⊕ ⊕⊕	⊕⊕	⊕ ⊕ ⊕
Documentation	⊕⊕	⊕ ⊕ ⊕⊕	⊕
Community	⊕⊕	⊕ ⊕ ⊕⊕	⊕
Performance	⊕ ⊕ ⊕ ⊕ ⊕⊕	⊕ ⊕ ⊕	⊕⊕
Programming	C++, Blueprint	*C#*	GDScript
License Use	Free	Free	Free
Graphics Engine	⊕ ⊕ ⊕ ⊕ ⊕⊕	⊕ ⊕ ⊕	⊕⊕
Tools	⊕ ⊕ ⊕ ⊕ ⊕⊕	⊕ ⊕ ⊕	⊕
Pricing (Free)	Yes	Only the basic version	Yes
Cross-platform	⊕ ⊕ ⊕ ⊕ ⊕⊕	⊕ ⊕ ⊕	⊕⊕
Pc Requirements	⊕ ⊕ ⊕⊕	⊕⊕	⊕
Versatility	⊕ ⊕ ⊕ ⊕ ⊕	⊕⊕	⊕⊕
Open Source Code	Yes	No	Partially

By comparison with other platforms, Unreal Engine is the best in performance, programming language, graphics engine, tools, cross platform implementation, versatility and open source. Therefore, Annex presents Unreal Engine in detail, as well as the development framework using C++ and Blueprints.

Unreal Physics and Raycasting

To implement the Ray-Tracing logic in Unreal Engine, the physics of the 3D objects "*actors*" in the 3D scenario "*level*" and the EU4 *Raycasting* are used. These two techniques are essential to implement the predictive beam steering algorithm in mmWaves.

The Unreal Physics system monitors any movement and collision of the "*actors*" in the "*level*", as well as the force exerted on him. Any interaction of these physical phenomena triggers a set of events that are used to know where a ray has hit, in the case of the ray tracing algorithm.

The EU4 Raycasting is a method that allows us to throw an invisible ray between two points within the "*level*" and judge if this ray has impacted on some "*actor*" (also known as "trace"). This method is very similar in Unity, where, if knowing on what the ray has impacted, one can know the characteristics of the "*actor*", as its name, location, properties, texture etc.

Every object in Unreal that supports collision is given an object kind which governs how it communicates with other object kinds. Certain object kinds have the ability to block, overlap, and ignore. Using trace channels, an object can specify how it should respond to traces.

The configuration of the collisions is done by means of the graphical interface of each Blueprint associated to an "*actor*". The events associated to each collision are also associated to a "*Blueprint Node*", therefore this type of implementation has to be done by this visual programming method, as shown in figure 6.22.

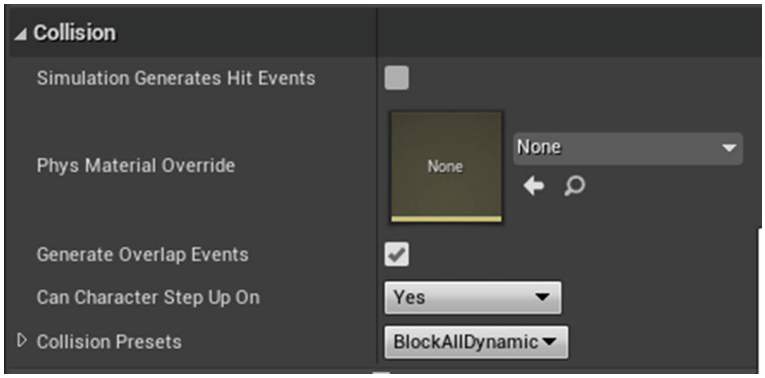

Figure 6.22: Collision properties of static mesh in an Actor.

This is opposite to the Raycasting, which can be implemented in both ways with blueprint as well as by code in C++, where the code that supports this implementation is as follows:

bool ***LineTraceSingleByChannel*** *(OutHit, Start, End, TraceChannel)*

If the function "*LineTraceSingleByChannel*" returns TRUE, it means that the ray has successfully hit some component of an actor in the channel defined by "*TraceChannel*". Where:

- **OutHit**: The first blocking hit found
- **Start**: The starting point of the ray
- **End**: The last point of the ray
- **TraceChannel**: This ray's "channel," which is utilized to choose which components to hit

6.7 Implementation of predictive steering system in Unreal Engine

In this section the implementation of the predictive steering system with video information to optimize the channel model in mmWaves in Unreal is discussed. One of the main advantages of using UE4 is its processing speed, since it is designed to work with a low level language like C++. In addition to performance, the transition to work with the C++ libraries of the ZED2 stereo camera is more fluid, and therefore no bottlenecks occur in the exchange of information depth of the scenario, which is great for real-time system design.

It is important to emphasize that all the previous experience in the design in Unity, as well as the implementation of Ray-Tracing techniques to emulate the physical phenomena of reflection, diffraction and transmission on the indoor scenario for the human body, are all applicable to the implementation made in Unreal. Anyway, there is no backward compatibility between the platforms, because they are radically different.

As previously mentioned, the camera used in this implementation was the ZED2 of StereoLab. This camera has much better performance than the Intel Realsense D455, especially for the range, which is more than twice that of the D455, in addition to providing a wider field of view, as well as not being dependent on lighting to obtain the information of the depth of the scene. This camera is the best stereo camera in the market today, although there are also LiDAR radars that allow to have greater ranges, but not having the option at getting the video signal with the same hardware limits the possibilities of people detection. This detection is done with artificial intelligence algorithms; in our case we use a pre-trained algorithm called Detectron2 as explained at the beginning of the chapter. This Detectron2 algorithm can only be used with Python, because it is the standard programming language in the industry and most implementations and libraries with this type of technology are only available through it.

6.7.1 Hardware Implementation

In order to obtain real-time information from the environment, a hardware system was designed. It is composed of a ZED2 stereo camera, which has a scanning system with servomotors, controlled by an Arduino microcontroller. In addition, the system has a laser pointer, which is intended to emulate the beam steering of a radiating system.

The complete hardware system can be seen in figure 6.23; it is composed of two azimuth and elevation positioning systems for both the ZED2 camera and the laser pointer. The positioning systems are controlled through a serial communication through the Arduino, where it receives instructions from the Unreal Engine simulator.

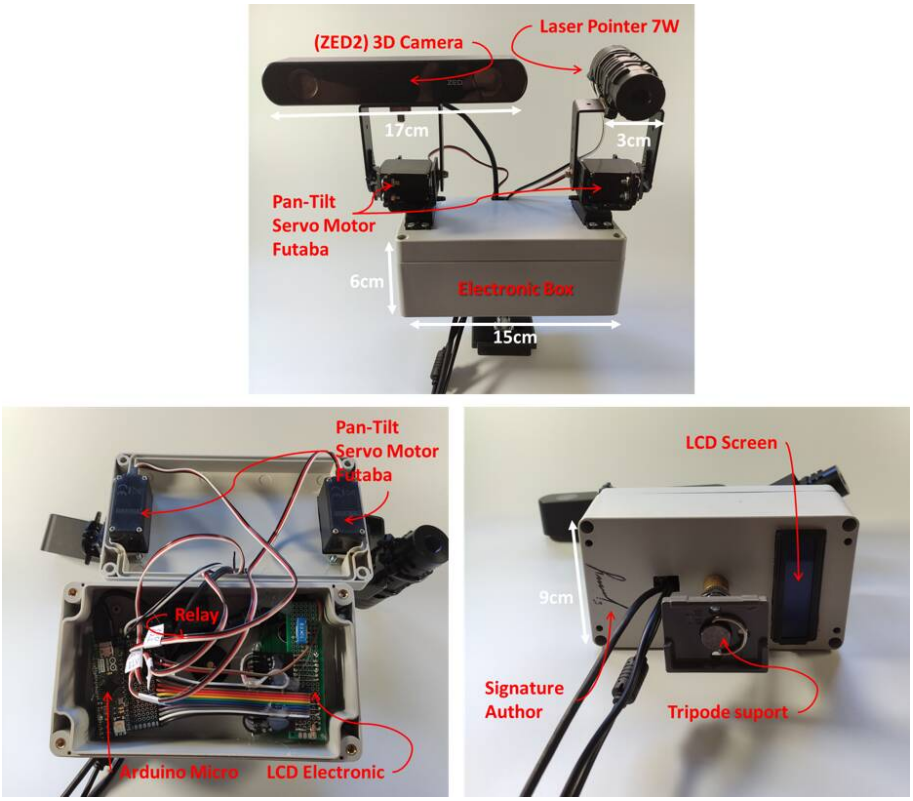

Figure 6.23: Video Assisted Beam Steering Hardware Setup.

The scheme of interaction between the hardware and software systems is explained in figure 6.24. In our system, we have two sources of input information coming exclusively from the ZED2 stereographic camera.

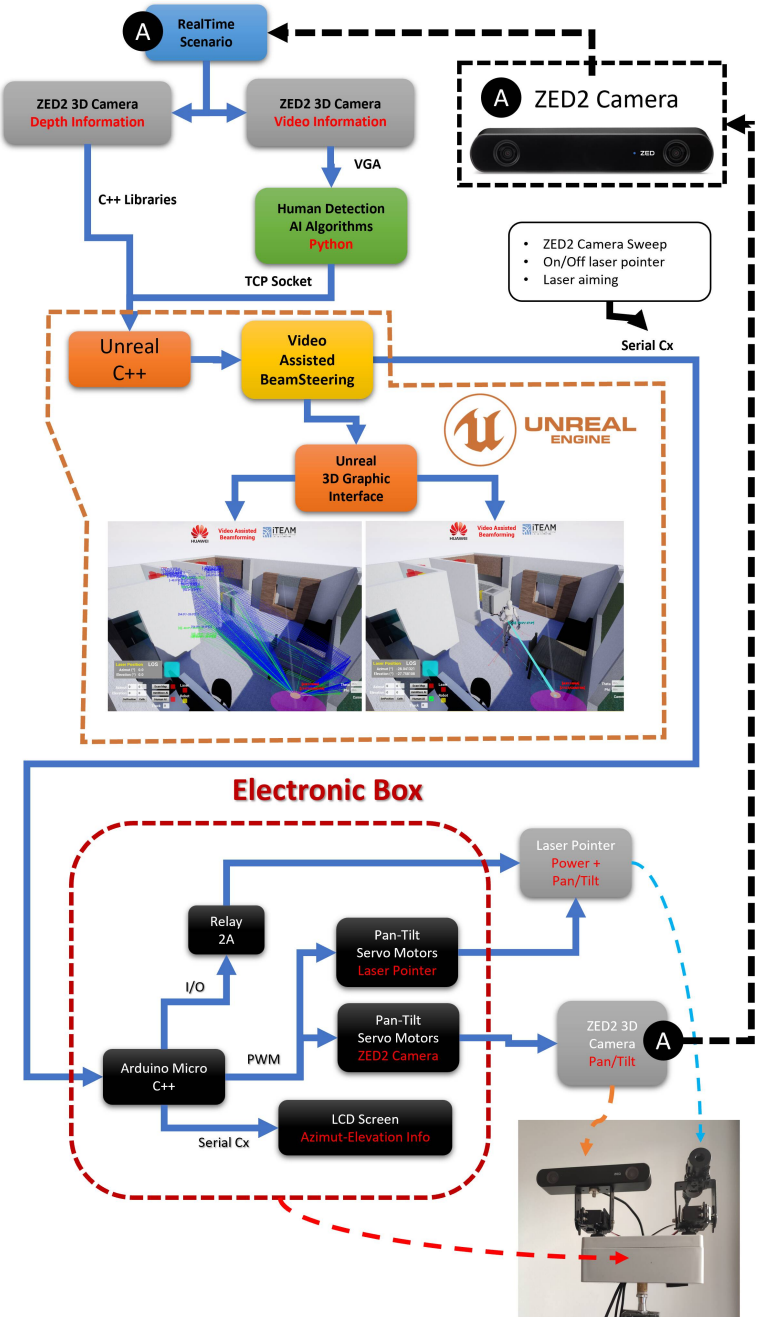

Figure 6.24: Video Assisted Beam Steering Hardware Software Scheme.

The first source of information coming from the camera is the two-dimensional and color video information. This information is processed by the artificial intelligence algorithm programmed in Python to detect people.

Once the morphology of the people is identified, the information of the two-dimensional coordinates of each segment of the human body identified as head, shoulders, arms, waist, legs is sent through a TCP Socket to the Unreal system.

This information is processed in Unreal together with the scenario depth information, in order to locate each segment of the human body in a three-dimensional scenario in real time.

The scenario depth information is read directly from the camera into Unreal, since both use C++ language, thus avoiding bottlenecks in the scenario depth matrix acquisition, which is quite dense to read and process.

The input data is processed and positioned in a 3D scenario previously designed or reconstructed with the depth information.

A series of proprietary algorithms will be run, which will be explained in more detail later in this section, and which follow the guidelines of section 6.4. The video-assisted beam steering system in Unreal, once the data has been processed and the algorithms corresponding to the beam direction prediction have been executed, sends a series of instructions to move the camera and the laser. The objective of moving the camera is to increase the field of view to have a more complete view of the scene and thus a more accurate reconstruction of the scenario, while the laser steering intends to emulate and visualize in real time the pointing suggested by the system to optimize the coverage in NLOS areas.

The following sections explain step by step how the predictive system has been implemented in Unreal Engine, and show the obtained results.

6.7.2 Mapping/Creation of the 3D scenario.

In this step, the first thing the system has to do is to rebuild the scenario or manually preload the scenario created with any external modeling software, such as Blender, SkecthUp, Maya, 3ds Max, etc. Each of these tools has its advantages and disadvantages when it comes to reconstructing the scenario information.

In the first approach, we seek to reconstruct the scenario based exclusively on the depth information obtained from the proprietary C++ libraries of the ZED2 camera. The depth information comes in the format of a point cloud, where each point has the three-dimensional information of the distance from the camera to the nearest obstacle. As stereo cameras, like LiDAR sensors, obtain depth data in this way, there will always be gaps in the point cloud readout. These gaps are impossible to reconstruct with only one camera from

a single point of view. In addition, depending on the lighting conditions of the scene, as well as the orientation of the obstacles, there may also be misreadings of the depth that result in the absence of this information.

This is very important because losing scenario information means losing valuable propagation channel information obtained with our Ray-Tracing techniques. This is the major disadvantage of reconstructing the scenario exclusively with the depth information from the camera (See figure 6.24).

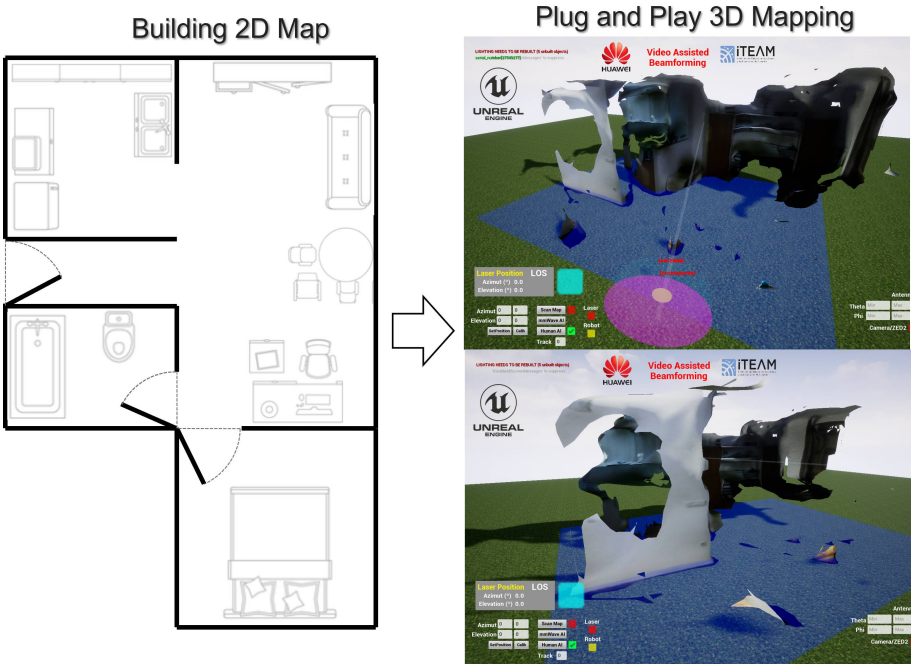

Figure 6.25: Scenario reconstruction with the point cloud information obtained from the ZED2.

The depth information has the same resolution as the two-dimensional video information. Therefore, depending on the camera's reading refresh time, our system will have to process in real time a three-dimensional matrix to reconstruct the scene. Because this process is very computationally expensive, the reconstruction is only done at the beginning of the system execution; updates can be programmed very often, but not in real time.

The other approach of reconstructing the scenario is manual, although at first it seems to be the most complicated to do, because it would be necessary

to have the map of the scene, or to alternatively reconstruct it ourselves from the measurements directly done on the scene.

This medium-term approach is the best way to have the scenario as close to reality as possible (see figure 6.26), because it does not depend on factors such as illumination, obstacle orientation and camera range to reconstruct the scenario. Note that in the case of the ZED2 its maximum range with optimal lighting conditions is 15 meters, which is fine for small indoor spaces, but in the case of large scenarios it is still too short. It is important to emphasize that a reliable reconstruction of the scenario is essential to provide reliable beam steering predictions.

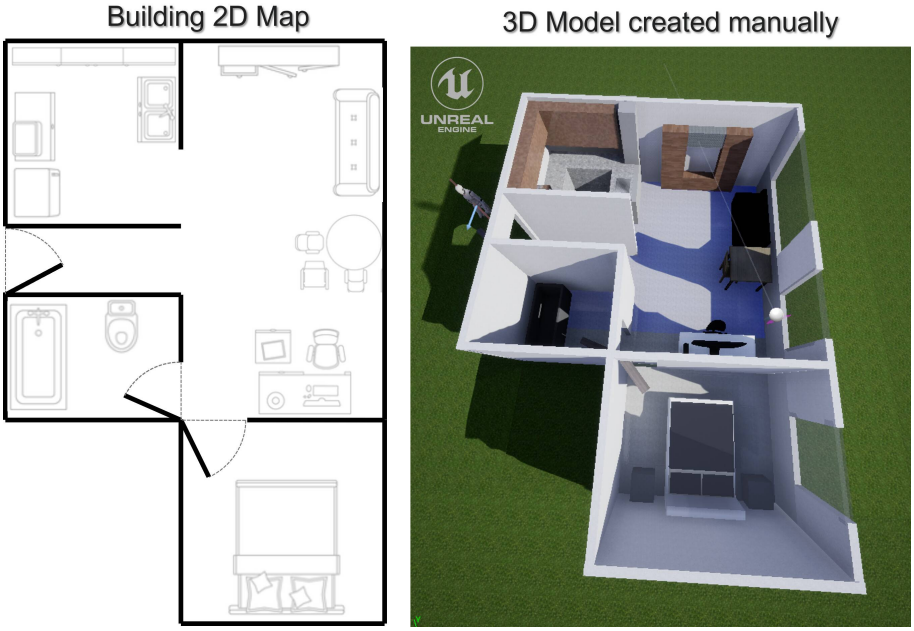

Figure 6.26: Manual Scenario reconstruction.

6.7.3 Delimit the areas of interest (Voxels) for ray tracing analysis.

Once the scenario has been reconstructed satisfactorily, in this step what we do is to fill with voxels the previously reconstructed scenario in three dimensions.

Each voxel has the geometric mesh of a cube, and it is associated to an Actor in Unreal, where it has an independent collision event logic. The objective of

building these voxels is to cover all the spaces where the analysis is going to be executed, in order to identify potential shadow zones, in NLOS. Therefore, each voxel has to be an independent object with parameterizable dimensions, because depending on the complexity of the scenario, more or less voxels will be needed to cover the same volume.

All the above can be seen in the example of figure 6.27 for the small apartment, where we omitted to analyze the signal propagation in mmWaves in the bedroom but not in the rest of the apartment.

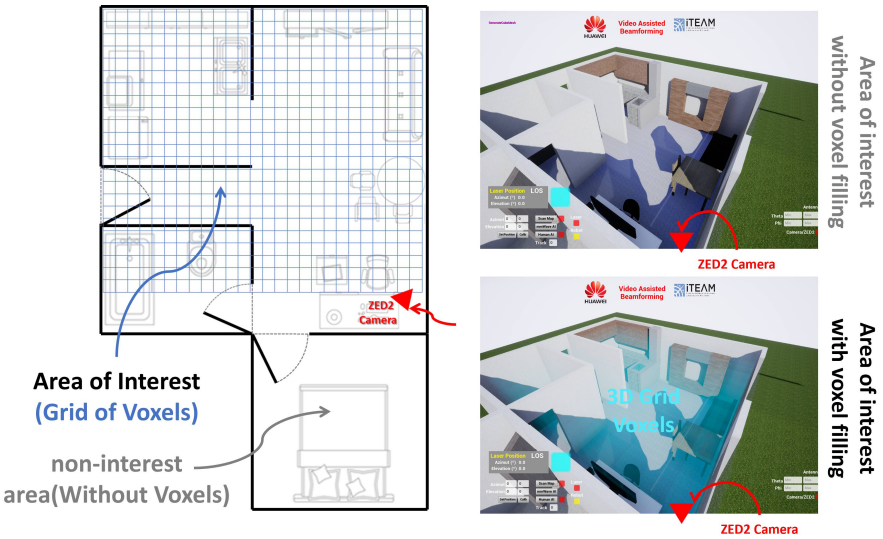

Figure 6.27: Delimitation of system analysis with voxels in a small apartment.

The strategy of delimiting the scene where the channel will be analyzed, allows omitting those areas where there is no visibility from the camera, and therefore there will be no detection of people, and it will not be possible to suggest any beam steering in those blind spots of our system.

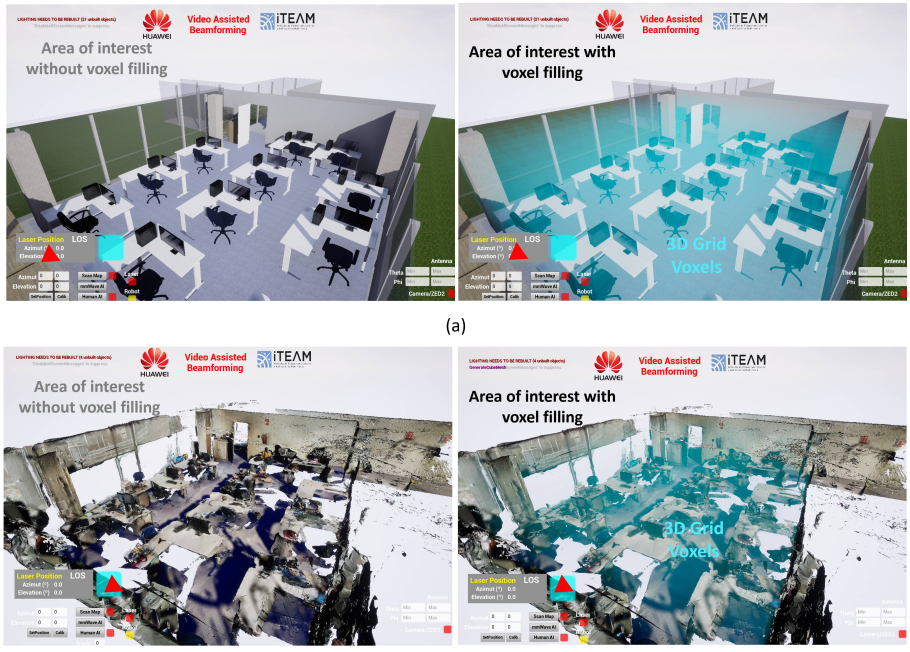

Figure 6.28: (a)Manually reconstructed scenario, (b)Scenario reconstructed with a portable stereo camera with local sweep.

Figure 6.28 shows an example of an office twice the size of the apartment, which has been filled with voxels in the area of interest. Figure 6.28.a shows the manually created scenario and figure 6.28.b shows the scenario reconstructed with a portable stereographic camera of a mobile phone, where to reconstruct this scenario it is necessary to make a tour and a sweep of the whole environment. Although it is possible to observe more details than in the reconstruction with the ZED2, it is still a very irregular reconstruction, which is very inconvenient for the Ray-Tracing system.

6.7.4 Identification of LOS and NLOS zones

Once the voxels have filled the areas of interest in the reconstructed scenario, the next step is to filter the voxels in each area of interest, where we only leave those voxels that are in regions without line of sight (NLOS). To do this, we emulated an onmidirectional antenna at the camera location, where a set of rays

are launched in all directions with the command "*LineTraceSingleByChannel*", in order to hit the voxels.

With this strategy only those voxels that are in direct line of sight are hit. And once the voxels have identified a collision coming from the omnidirectional voxel filtering antenna, they are removed. With this, only those voxels that are in NLOS zones will remain active from the perspective of the stereo camera position as seen in figure 6.29.

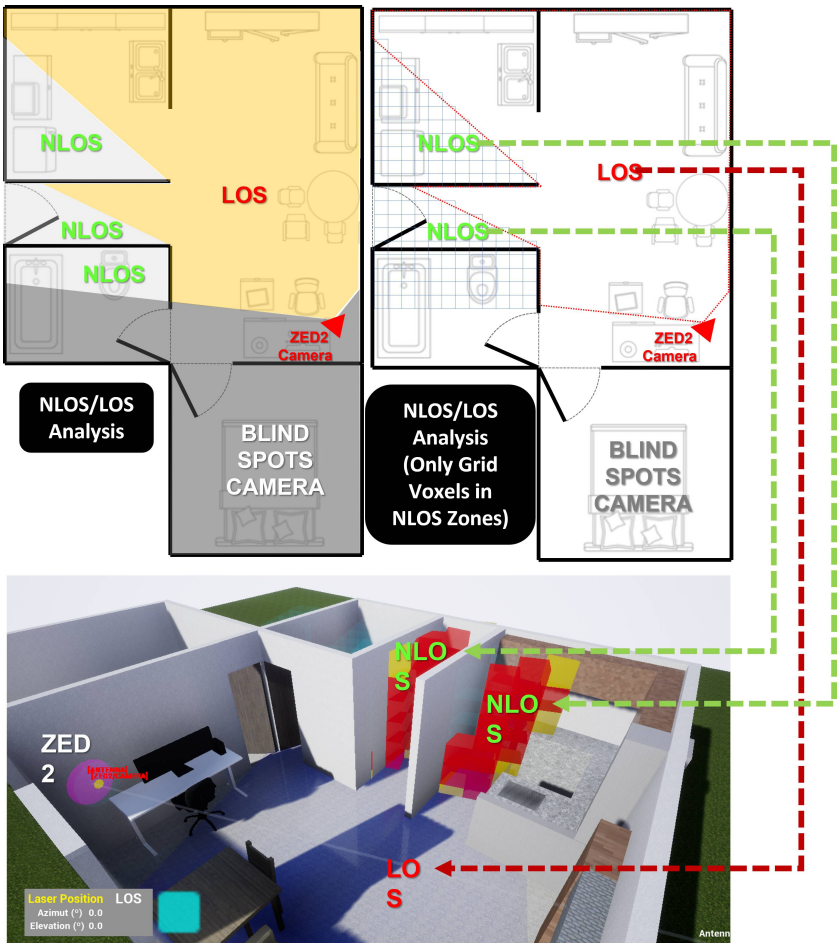

Figure 6.29: Classification of coverage areas by means of voxels in a three-dimensional scenario.

Recall that the future location of the radiation system in mmWaves will be the same as the stereo camera. This strategy identifies those regions where line-of-sight (LOS) RF coverage cannot be provided. Therefore, to improve coverage in those areas it will be necessary to consider multipath contributions that will be obtained by Ray-Tracing techniques.

6.7.5 Analysis of Ray-Tracing in the NLOS zones

Once the voxels have been identified in the NLOS zones in the reconstructed 3D scenario, the next step is to run the proprietary ray-tracing system, which aims to reach those voxels that are in the shadow zone. For this purpose an omnidirectional radiation is emulated similar to that of the previous subsection, but in this case each ray interacts with the entire reconstructed scenario, not only with the voxels.

In the interaction with the scenario we emulate only the two most important physical phenomena. The first physical phenomenon emulated is the specular reflection, taking into account that it strongly depends on the normal vector of the face of the geometric mesh surface, where the ray has hit. Therefore, in order to simulate this physical phenomenon as accurately as possible, we must have a geometric mesh of the scenario as close to reality as possible. This is one of the most important considerations to take into account when reconstructing the scenario with the point cloud or manually.

The other physical phenomenon emulated with Ray-Tracing techniques is the edge diffraction at obstacles. An obstacle is any object electrically large enough to obstruct the straight-line propagation of a plane wave in the far field. This physical phenomenon was simulated in a similar way to how the scattering effects on human body were characterized in Chapter 3. If we take into account the applicability limits of the mathematical model of Double Knife-Edge proposed in Chapter 2, we will be able to emulate the scattering quite accurately over any obstacle regardless of whether it is the human body or part of the furniture, or any other object.

When physical phenomena are simulated with ray-tracing techniques, the predictive beam steering system identifies each of the multipath contributions that can enhance coverage in those voxels that are in the NLOS zones. These contributions are classified in each voxel and are visually distinguished in the simulator by the color that each voxel takes, as shown in figure 6.30.

Red voxels are impacted only by reflection contribution, while yellow voxels have both reflection and diffraction contributions. Each voxel has the information of each contribution that reaches it, such as the position of the radiation source, azimuth and elevation of the angle of arrival of the ray that has im-

pacted the voxel, as well as how many reflections or diffractions the ray has had to suffer to reach the voxel, and the length of the path it has traveled.

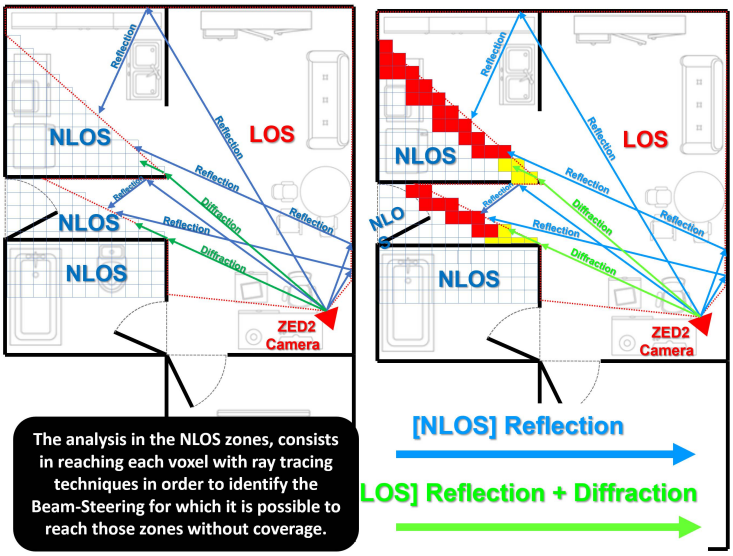

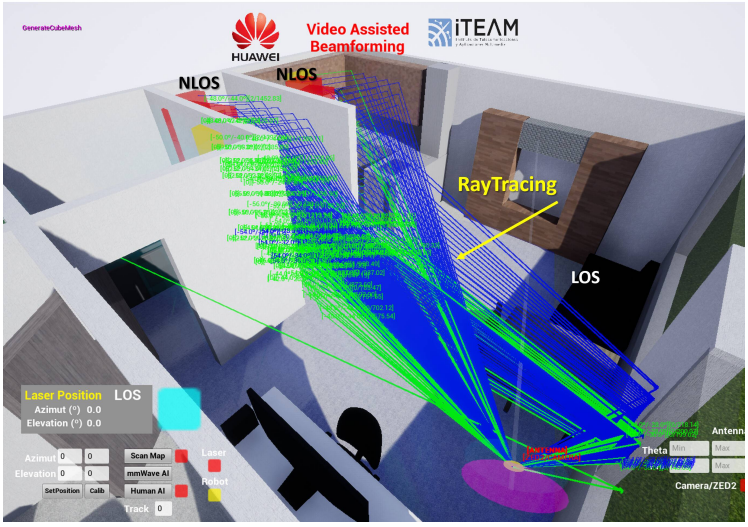

Figure 6.30: Multipath contributions on voxels in NLOS zones of the manually reconstructed apartment scenario.

With this classification strategy, the system knows which physical phenomena reach a certain voxel that is located in an area without direct coverage, so we have characterized the multipath contributions exclusively in those most critical areas.

These contributions are updated in real time, especially when there are people inside the scenario, because these people obstruct some contributions that had previously been calculated in the empty scene. This update also takes into account the evaluation of the scattering effects of the human body as explained in chapter 3.

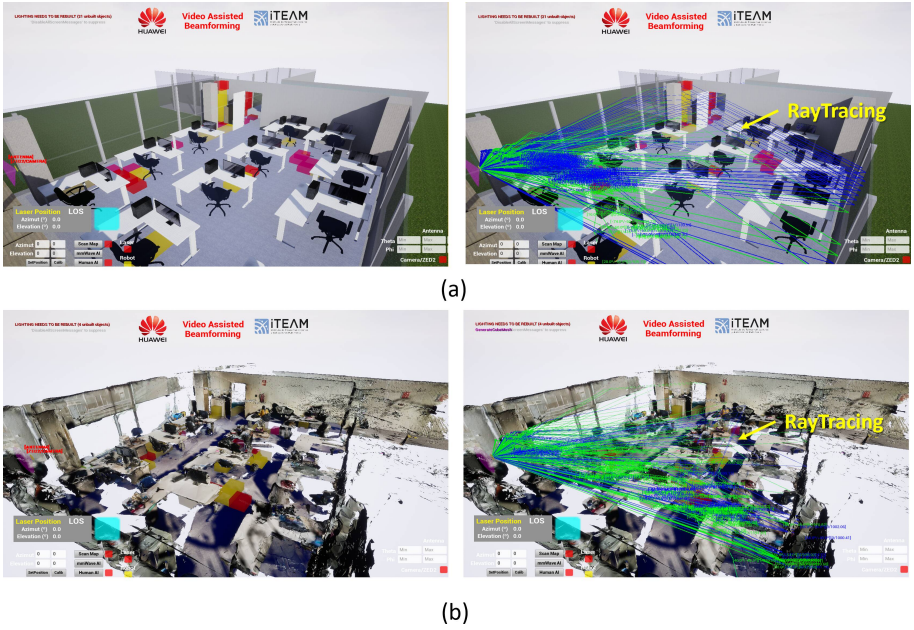

Figure 6.31: (a) Ray-Tracing analysis of the manually reconstructed scenario., (b) Ray-Tracing analysis of the scenario reconstructed with a portable stereo camera.

Figure 6.31 shows an example of the predictive raytracing system on NLOS voxels in a larger and more complex scenario. It simulates the multipath contributions in the office scenario reconstructed manually as well as by a portable stereo camera. At first glance it seems that there are few differences, but when observed in detail, the multi-path contributions of the two examples are quite different, mainly due to the geometric morphology of each scenario.

6.7.6 Selection of beam steering based on the prediction of people trajectory in a shaded area

Once that the voxels in the NLOS zones have been determined of the reconstructed scenario, the next step is to perform three analyses. First of these analyses is to identify the people in the scenario. As discussed in previous sections, people are identified using the two-dimensional color video information obtained from the ZED2 stereo camera, which is processed independently of the depth information. The identification of persons is done with Detectron2, which is modified in such a way that the detection of persons is as efficient as possible. Once the person has been identified in a two-dimensional plane from the video information, the position of the persons in three dimensions is extrapolated from the point cloud information obtained from the depth information of the camera.

Second analysis to be performed is that once we know the position of the persons in the scenario in three dimensions and in real time, we extract information about their velocity and relative positions in order to predict their trajectories. With the prediction of a person's trajectory, it can be deduced where the person is likely to be in the near future and, based on this information, it can be deduced if the person is going to enter the non-line-of-sight regions that have been previously identified with NLOS voxels.

With this information we determine if a person is not going to have coverage in the near future, and where that person is going to be once we stop detecting her/him. One of the most important purposes of building NLOS voxels is to estimate where persons will be once they have disappeared from the camera's field of view. Before the person disappears from the tracking it collides with the NLOS voxels, and therefore we will know in which voxel the person will most likely be. Therefore, we will also know which are the multipath contributions that will provide coverage to that specific voxel and therefore we will be able to suggest a beam steering according to that information. Then this information is sent to the laser pointer of the hardware system that we have previously designed (see figure 6.23), to re-orient the laser pointer, so to see in real time the results obtained by our system.

Figure 6.32 shows how the position of the persons inside an indoor environment affects the performance of the step-by-step beam steering prediction algorithm along time.

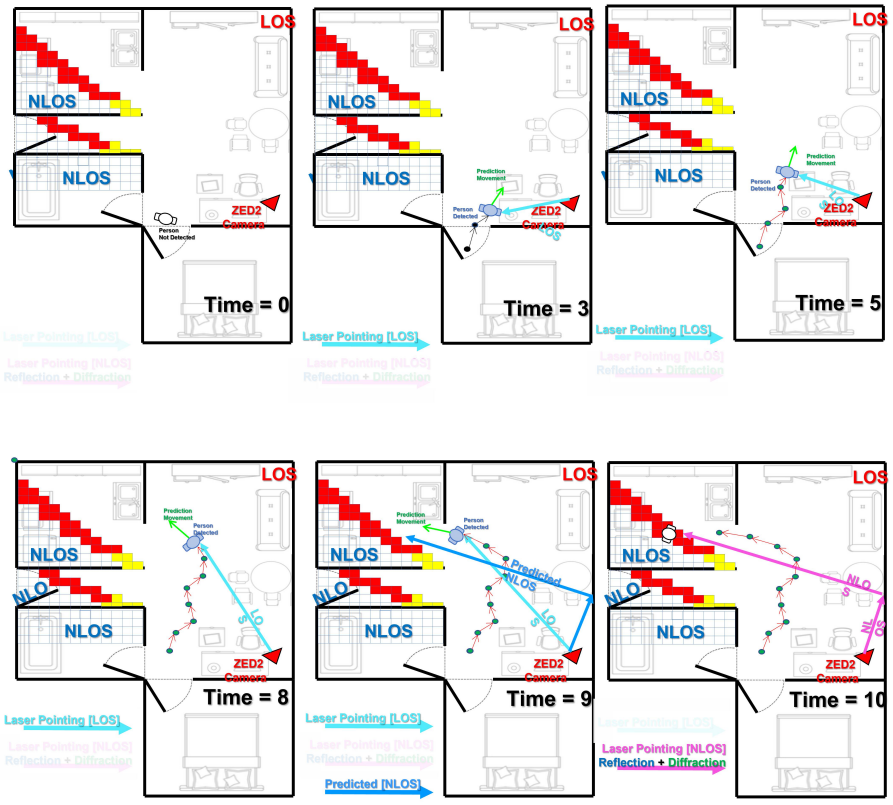

Figure 6.32: Time-step execution of the predictive beam steering system to optimize coverage in NLOS areas.

Figure 6.32 shows how at **time = 0**, the system has already detected which are the zones without direct line of sight according to the positions of the NLOS voxels of the previously reconstructed scenario. In addition, it also knows which are the multipath contributions that reach those specific voxels. Although at this time it has not been possible to detect the person, it is because it is in a blind spot of the camera.

At **time = 3** the person has already been identified and located in the reconstructed 3D scenario. Moreover, its velocity and potential trajectory have already been calculated according to its immediately preceding movement (Green Arrow). At this time, the system knows that the person is not near a shadow zone and not expected to enter it any time soon, so the beam steering follows the person in line of sight (LOS) (Blue Arrow).

At **time = 5** the person continues to walk within the scenario, and the system continues to predict his or her trajectory, to be alert to act when the person is likely to move to NLOS areas, while the beam is directed towards the person at LOS (Blue Arrow).

At **time = 8**, the system is still predicting the trajectory of the person, and pointing at LOS.

At **time = 9**, according to the prediction of the person's trajectory, the system detects that the person is likely to hide soon. Therefore our algorithm suggests to the radiation system, which in our case is emulated by the laser pointer, that it should steer the beam to give coverage in the shadow zone, with the multipath contributions previously calculated and constantly updated with the obstruction of the person inside the scenario.

Finally at **time = 10** the person has disappeared from the scene, because it has hidden in a blind spot of the camera, but our algorithm already knows in advance where it should have steered the beam to further enhance the coverage where the person is possibly hidden (Magenta Arrow).

The previous example can be seen in the following figures directly in the Unreal simulator, where the situation at **time=5** is shown in figure 6.33, and that at **time=10** is shown in figure 6.34.

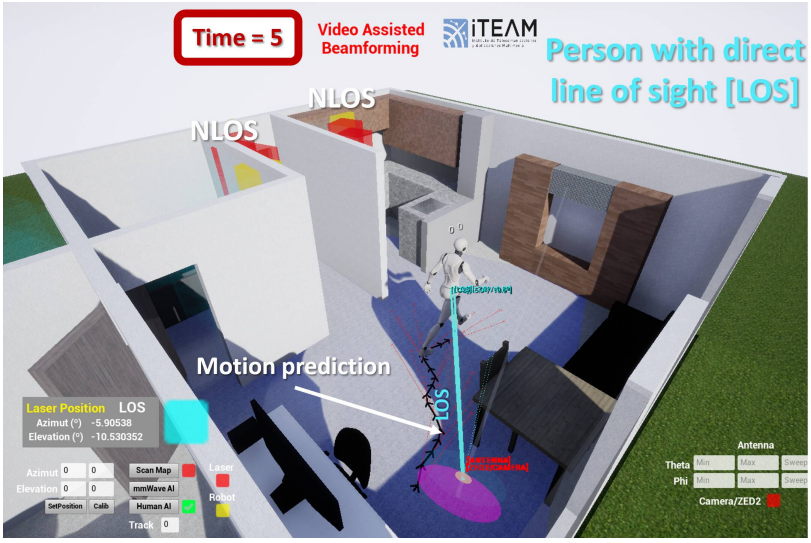

Figure 6.33: Screenshots of the predictive beam steering system run at time=5, equivalent to figure 6.32.

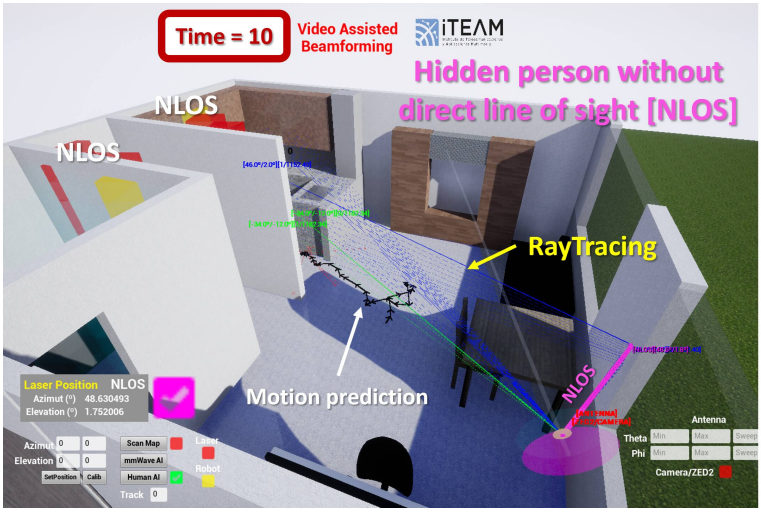

Figure 6.34: Screenshots of the predictive beam steering system at time=10.

The predictive beam steering system was also run with the reconstructed scenario in real time, with the point cloud information from the stereo camera (See figure 6.35). The results change quite a lot because this reconstructed scenario has quite a lot of missing information, especially a missing wall on the right side of the scene, which is where most of the multipath contributions of the manual reconstructed scenario come from.

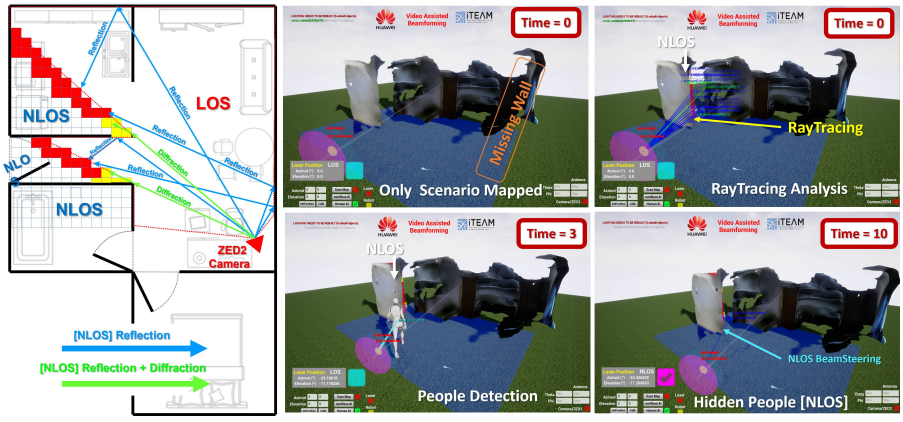

Figure 6.35: Screenshots of the system with the depth reconstructed scenario.

Therefore, since losing scenario information means losing reliability in the system's prediction, the best way to run our algorithm is to use manually reconstructed scenarios.

Figure 6.36, shows the screen shots of the system operating in real time, where the system is running with two people simultaneously and our system has the ability to predict the optimal beam steering for each person, when they leave the field of view of the camera or when they enter in a shadow zone.

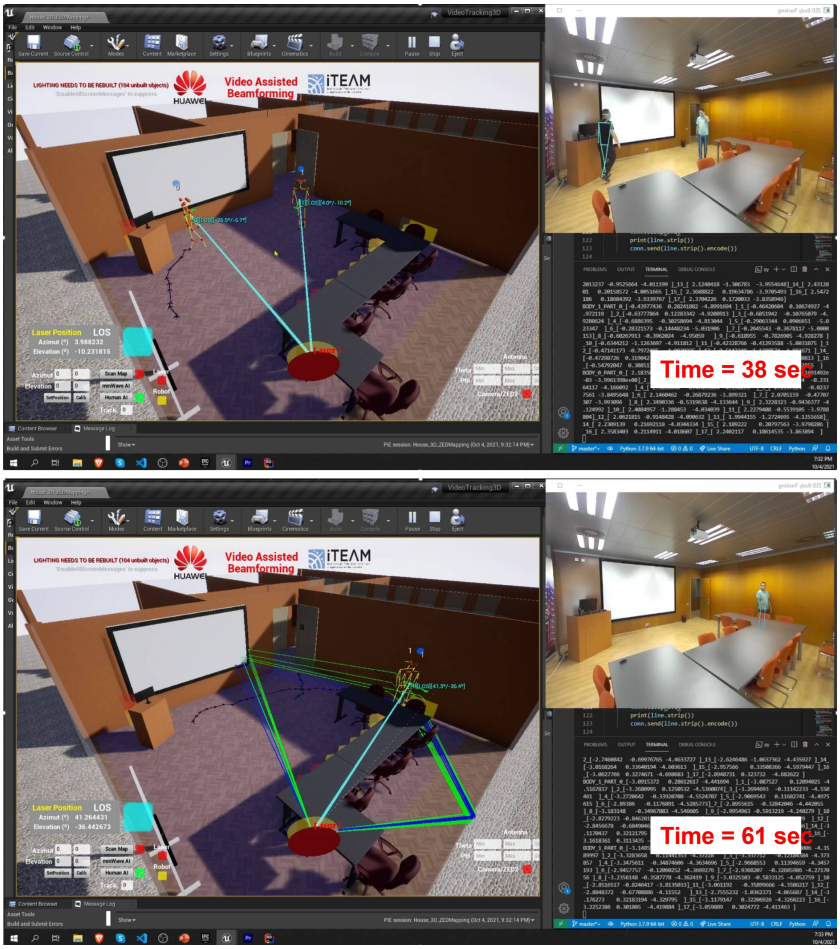

Figure 6.36: Screenshots of the predictive beam steering system run with two people simultaneously.

6.7 Implementation of predictive steering system in Unreal Engine

Figure 6.37 shows how our system has been tested with a wide range of environments, both in indoor and outdoor scenarios.

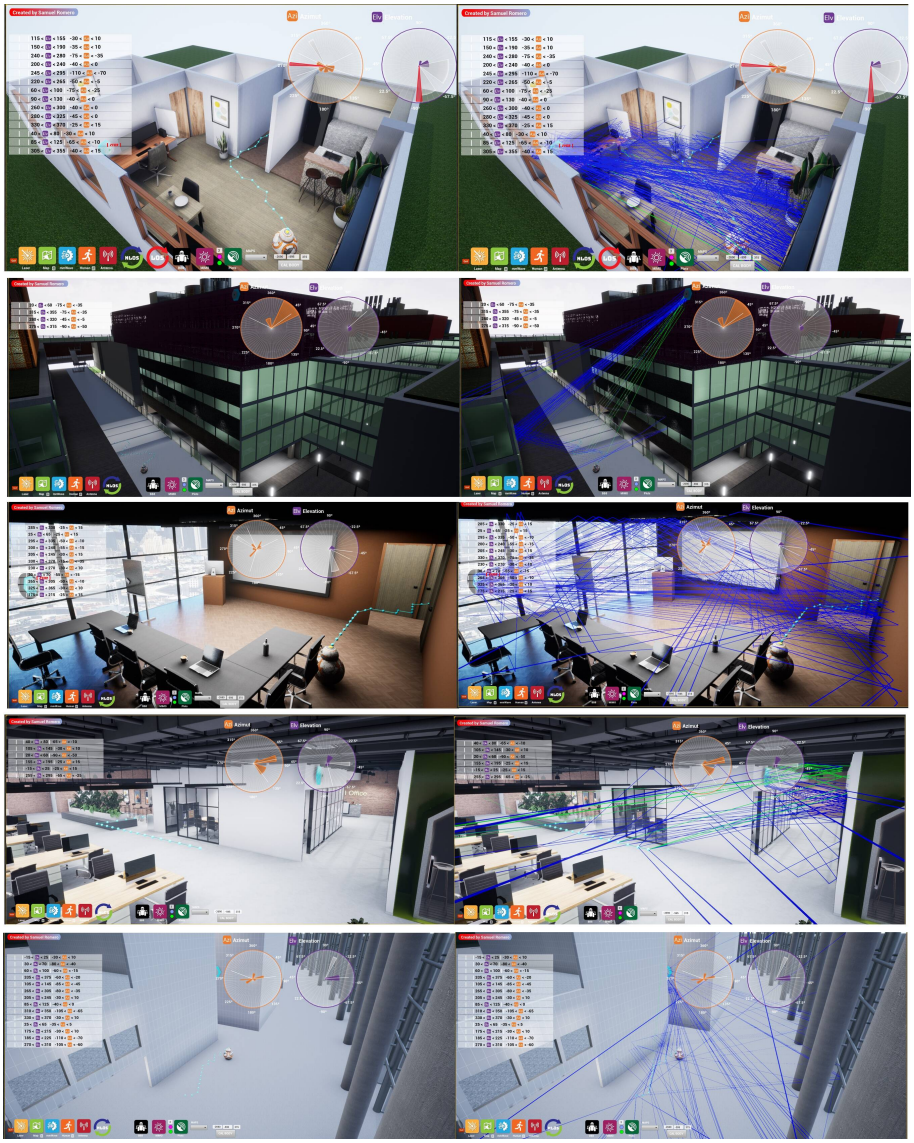

Figure 6.37: Simulated scenarios with the predictive beam steering system.

6.8 Calibration of Ray-Tracing algorithm with measurements

This section deals with the calibration of the Ray-Tracing algorithm used for the beam steering prediction system. The calibration was done using simulator results in conjunction with measurements.

The Ray-Tracing algorithm used so far has only taken into account the physical phenomena of specular reflection and edge diffraction. These two physical phenomena are the most important to consider according to the literature [160–168], because they are the ones that contribute the most energy to the received power, although this statement depends on the materials of the scenario where the mmWaves propagation channel is being evaluated [169–173].

So the objective of this section is to insert some additional physical phenomena into the Ray-Tracing algorithm such as transmission, diffuse scattering and diffuse reflection. These physical phenomena can have an important impact depending on the scenario and the relative positions of both the transmitter and receiver. In addition, material losses are also included in this analysis, resulting from the interaction of the plane wave with the material of which the obstacle is composed.

The multipath contribution also depends on the order that we want to simulate, i.e. the number of bounces (Reflexions/Diffractions/Transmissions) that a ray can experience after leaving the radiation source.

The example scenario of this analysis is the one shown in figure 6.38.a, where the receiver, which is in position 9, and the transmitter are not in line of sight.

The calibration study of the Ray-Tracing algorithm was done in all the points of the scenario shown in figure 6.38.a; in this section we present only results for position 9, which is one of the most interesting to analyse.

Additionally, figure 6.38.b shows the composition of the materials of the whole scenario, where the predominant material is chipboard. This type of material has relatively low penetration losses in mmWaves [170], so it will allow very important transmission contributions to be considered.

(a)

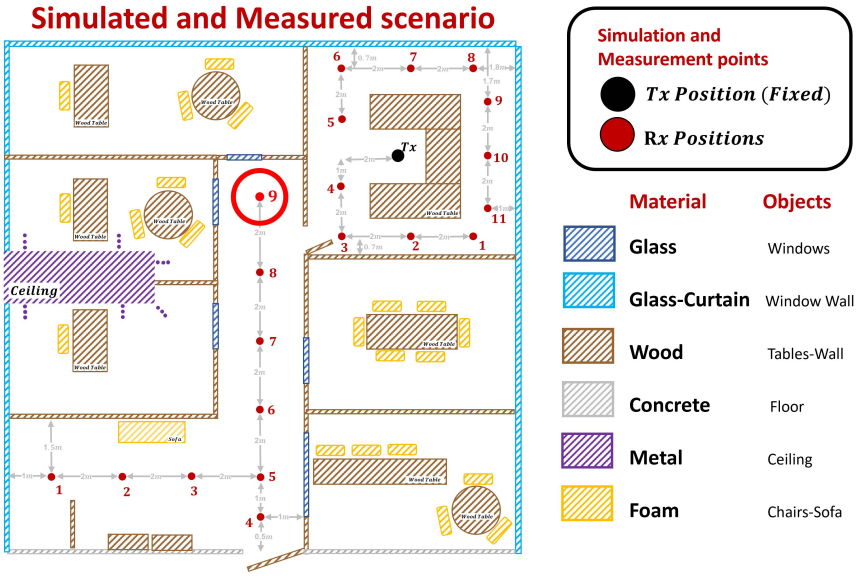

(b)

Figure 6.38: (a) Scenario simulated with ray-tracing algorithms used in the predictive steering system, (b)Material compositions present in the simulated and measured scenario.

Figure 6.39 shows the visual results of the mmWaves propagation channel simulation with the Ray-Tracing algorithm where all the additional physical phenomena such as transmission, diffuse scattering and diffuse reflection are taken into account.

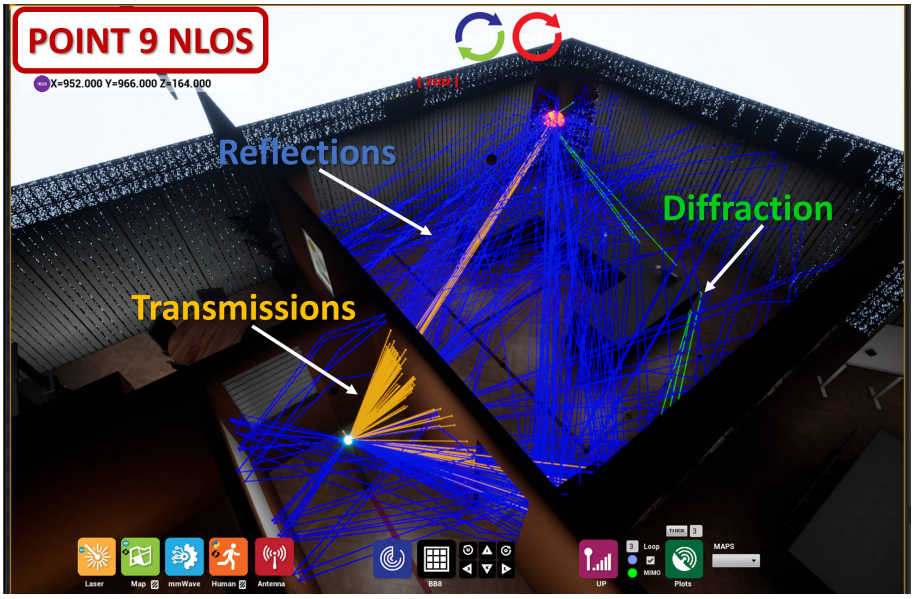

Figure 6.39: RaytracingMateriales.

According to these results it is observed that the transmission contributions are very important in this particular scenario, so omitting this information as many scientific studies have done [160–168] may lead to inaccurate results, although it also depends on the type of scenario simulated.

This conclusion can also be appreciated when we compare the simulation results with the measurements (See figure 6.40). Both measurements and simulations were done with omni-directional antennas to evaluate all the multipath contributions that our ray-tracing algorithm can handle.

Keep in mind that this Ray-Tracing algorithm, which considers more physical effects, is usually much slower to execute than the Ray-Tracing algorithm used in the previous section. But this algorithm is highly parameterizable, so, depending on the type of scenario to be simulated, it can be configured to be more or less accurate to save computational load.

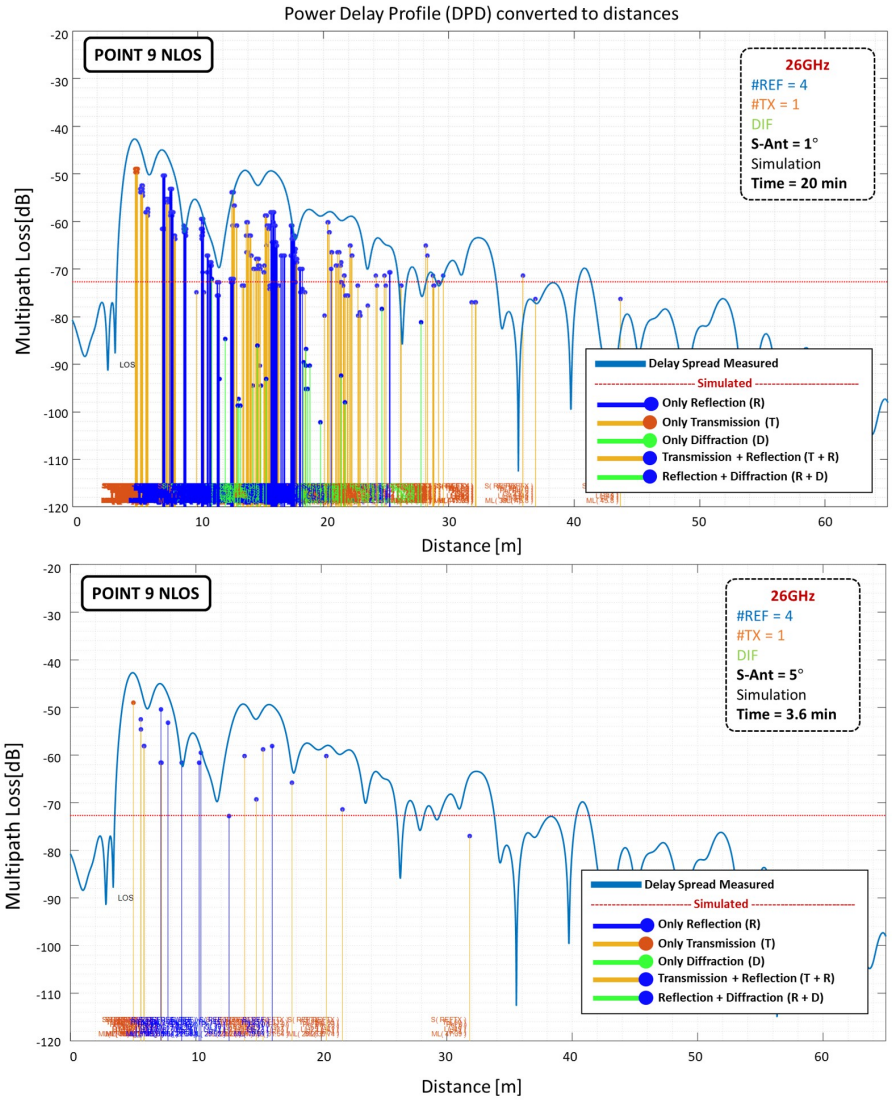

Figure 6.40: Comparison of delay profile measurements and simulations.

Figure 6.40 shows the comparison between measured and simulated results. In the measurements the TX/RX were equipped with the identical omni antenna, which has been manufactured by Steatite, model QOM-SL-26-40-K-SG-

R manufactured by Steatite, operating at frequencies from 26 to 40 GHz, with a gain of 4 dBi [174]. The RX and TX are connected to ports 1 and 2 respectively of the vector network analyzer (VNA), model RS-ZNB40, by Rohde-Schwarz.

The VNA measures the frequency response and obtains the power delay profile at the center frequency of 26 GHz with a bandwidth of 400 MHz. The bandwidth is wide in order to discriminate as much as possible each of the multipath contributions measured by the VNA.

The measurement results are shown as a continuous blue line, and the simulation results are discrete vertical lines, where the height of each line is related to the power level of each contribution. Each of these lines is an independent multipath contribution, whose color identifies to which physical phenomenon the contribution belongs to. This allows us to filter and analyze which physical phenomenon is the predominant in a particular scenario, and therefore to decide which physical phenomenon we can use to improve the performance of the Ray-Tracing algorithm.

Based on the simulation results, we can affirm with total certainty that the physical phenomenon of transmission is crucial in the power contribution at the receiver, and therefore in this scenario it has to be taken into account.

It is also observed how the simulated contributions adapt quite well to the measured contributions, in the sense that, where there is an increase of power in the measurements, there are multipath contributions that contribute to that increase of power at that given delay, while in the opposite case, where there is a fading at a given delay, simulated multipath contributions do not appear.

Another important conclusion that can be obtained from these results is that, apart from discriminating a physical phenomenon to accelerate the Ray-Tracing algorithm, we can also decrease the order of computational analysis.

For example, the results shown in figure 6.40.a were obtained with an angular resolution of the omni-directional antenna of 1 degree, a maximum number of reflections of 4, and only 1 transmission per launched beam. This provides quite good results by comparison with the measurements, but on the other side it takes a simulation time of 20 minutes just to evaluate a single position of transmitter and receiver.

This time is fine to do analyses on fixed positions, but it is not efficient at all to do analyses like the one we did in the previous section, where the Ray-Tracing algorithm must run in real time to suggest a beam steering based on the video information.

Because of this issue it is important to reduce the execution time of the Ray-Tracing algorithm, and this is achieved either by avoiding some physical phenomena, or by reducing the order of the algorithm, as well as decreasing the angular resolution of the simulated antenna.

This is the case of figure 6.40.b, where only by reducing the resolution of the antenna from 1 degree to 5 degrees, we reduce the calculation time from 20 minutes to 3.6 min. In this case we obviously obtain less contributions; nevertheless, the most important ones, which are the ones that provide more power, are still present in the simulated results.

In summary, the calibration process has been carried out successfully, taking into account the amplitude and displacement similarity of the peaks and valleys of the simulated multipath contributions compared to the delay profile measured, although as we have seen, the reliability of the results depends on many factors, such as the complexity of the scenario, the materials involved or the interaction of people. Therefore, it is recommended that the calibration process be carried out in a particular way for each type of scenario, in order to obtain as reliable results as possible.

6.9 Conclusions

In this chapter the feasibility of using a predictive beam steering system with video information was evaluated. According to the results obtained, it is totally feasible to implement this type of intelligent predictive systems to adapt the radio channel propagation model at mmWaves to optimize the coverage in complicated areas of complex indoor scenarios. Nevertheless, there are some considerations to be taken into account in the system implementation, such as the following ones:

- The Unreal engine platform is a very robust, complete and much more efficient platform than its Unity counterpart. But this platform requires a lot of system resources to run and a high programming knowledge to operate with it, apart from knowledge in 3D modeling to reconstruct the scenarios.
- Both the detection of people and the reading of the depth of the stereo camera depend on the lighting conditions to ensure a correct reading, and this is detrimental because it is not always possible to guarantee it, which means that our system has a limited scope of application. Apart from the fact that current depth cameras have a reduced range of maximum 15 meters, this is the major drawback of this type of technology, and limits the applicability of our system.
- The reconstruction of the scenario in the simulation platform is crucial to obtain reliable results with the Ray-Tracing algorithms designed for this purpose. For this reason it is essential to switch from stereographic camera technology to LiDAR, because it avoids the limitations of range and scenario replicability that do not depend on the illumination conditions of the environment.
- The core of the system is the Ray-Tracing algorithm, which, as was shown in the previous section, can obtain good results. But this also implies to reduce the performance of the algorithm, limiting the use of this system in real time. It is possible to improve its performance by sacrificing accuracy, which in many cases depends on the complexity of the scenario to be characterized.

Chapter 7

Conclusions and Future Work

7.1 Concluding Remarks

This doctoral Thesis had three main objectives. The first was to characterize the scattering effect that an incident electromagnetic field at millimetre-waves (mmWaves) frequencies experiences on human body, in order to propose a simplified mathematical and geometrical model to reliably evaluate this phenomenon.The second was to design a modular millimeter-wave passive reflector, whose objective is to optimize coverage in indoor environments in an efficient and cost-effective way. The third objective was to design a predictive beam steering system for the mmWaves radiation system, in order to reduce propagation losses in dynamic and complex indoor environments.

Regarding the first objective, a set of applicability guidelines to use the Double Knife-Edge mathematical model to evaluate the scattering effects of the human body was proposed, along with geometric simplifications to facilitate the evaluation of these effects and their implementation in a simulation platform. This mathematical and geometrical model was evaluated in conjunction with simulations and measurements in order to confirm its reliability. According to the analysis performed, the proposed mathematical and geometrical model is not only valid to characterize the human body, but it can also be used to evaluate the scattering effects of any type of obstacle, whether its material is fully absorbing or reflective in the frequency band from 30 GHz to 40 GHz. One of the most important guidelines is that the smallest cross section of the

obstacle should be greater than 6λ and the minimum gap distance between the radiation source and the obstacle should be at least 15λ. Therefore, to implement it in a simulation environment only the geometrical limits of the obstacle from the point of view of the radiation source must be calculated, as well as the electrical distances.

Concerning the second objective, a modular passive reflector was designed in mmWaves, whose main motivation was to optimize the coverage of the radio access network (RAN) in future mobile systems, where it is quite vulnerable to any type of obstacle in the environment, especially the human body due to its physical proximity to the mobile terminal. To carry out the design of this reflector, a considerable number of reflectors with a parameterizable rough surface were designed and tested. The purpose of this surface was to cause a homogeneous diffuse reflection in an area of interest, with the energy incident on the reflector. The reflection must be diffuse because future mmWaves systems will tend to be highly directive to mitigate propagation losses in free space, thus this energy has to be distributed over the environment efficiently. One of the design goals of the reflector was that it should be modular, in order to compose a larger reflective surface according to the coverage needs of the environment.

With respect to the third objective, a predictive radiation beam steering system was designed and implemented with information from a stereographic camera. The objective of this system is to evaluate in real time the behavior of the propagation channel in mmWaves in dynamic and complex environments. Proprietary Ray-Tracing techniques are used to propose an optimal multipath steering to reinforce those areas with coverage problems due to lack of visibility. For this it is essential to have both the information on the scenario and the relative positions of the people in it. For this purpose, we used the depth information of the camera for the scenario, and the video information to identify the people with an artificial intelligence algorithm.

In the following we evaluate each of the hypotheses proposed in this Thesis and indicates how this research work has satisfied each one of them:

- **HypoThesis 1:** In indoor scenarios, people cause a considerable power level degradation of about 40dB in the mmWave radio propagation channel, due to dispersive effects on them; furthermore, these effects are exacerbated by the unpredictability of the movement of people in these environments and the proximity of the mobile terminal to the human body.

- **HypoThesis 2:** The mathematical models proposed in literature adequately evaluate the scattering effect of the human body in mmWaves and are in good agreement with measurements taken in controlled environments, but most of them are quite complex and expensive to implement. For this reason, it was decided to use the Double-Knife Edge model to evaluate the scattering effects and to identify the applicability limits of this model in order to guarantee its reliability for estimating propagation losses in the shadow zone.

- **HypoThesis 3:** Due to the applicability limits of the double knife edge model proposed to evaluate the scattering effects of the human body in mmWaves, it was discovered that it is feasible to simplify its implementation by using a simplified geometrical model of the body, where only the body geometrical limits and the relative distances to the transmitter and receiver are needed to characterize its scattering effect in an efficient way.

- **HypoThesis 4:** Due to the geometrical simplification of the human body and keeping in mind the applicability limits of the Double Knife-Edge model, it is possible to implement the characterization of the scattering effects of the human body in a complex real-time simulation environment.

- **HypoThesis 5:** A low-cost alternative to optimize mmWave coverage has been achieved by designing a passive diffuse modular reflector. This strategy consists of offering alternative propagation paths to the radio signal through the reflector, in order to avoid additional propagation losses caused mainly by the scattering effects of the human body. This radio signal propagation approach will allow us to offer a homogeneous coverage in broadband (30 GHz to 40 GHz) with a directive radiation source. As it is a modular reflector with a low and flat profile, it can be installed on any surface with no size limit, in order to offer the best coverage in complex indoor environments.

- **HypoThesis 6:** With the stereographic information from the camera it is possible to reconstruct the scenery. However, this reconstructed scenario is not suitable for estimating the radio channel propagation deterministically with the ray tracing technique, because the depth information does not allow to represent faithfully the morphology of the scenery. Furthermore, the reconstructed surfaces have an unwanted roughness, which causes inconsistencies in the reflection calculation with our proprietary ray tracing system. Therefore the most feasible solution is to reconstruct the scenery manually with its plans, in order to guarantee the reliability

of the reconstructed scenery surfaces and hence to get reliable channel propagation results.

- **HypoThesis 7:** According to the designed predictive beam steering system, it is possible to estimate the propagation channel in real time considering the effects of people, thanks to the simplifications proposed to implement the Double Knife-Edge model to evaluate the dispersive effects of the human body, provided that the proposed applicability limits to use this model are respected.

- **HypoThesis 8:** Throughout the Thesis two simulation platforms were discussed, Unity 3D and Unreal Engine. Each of them has its advantages and disadvantages, but in the end the most suitable simulation platform to evaluate the propagation channel in mmWaves in real time was Unreal Engine. In this platform it is possible to integrate in a more efficient way the external logic to read and process the information of the cloud of points of the scenario, as well as the people detection with artificial intelligence. In this platform, the radio channel propagation in mmWaves can be effectively evaluated with Ray-Tracing techniques in a complex and dynamic environment. It is also intuitive to visually analyze the obtained results.

7.2 Future Research Lines

There are numerous other study areas that might be explored after this Thesis. The following elements should be emphasized in particular:

- In order to improve the autonomy of the predictive beam steering system with video information, it will be necessary to address the problem of scenario reconstruction more seriously. As a matter of fact, with current stereographic cameras it is impossible to reconstruct the scenery properly due to the large amount of depth errors obtained from stereo cameras, which become more acute as the camera moves away from the obstacles, and also because these systems are very susceptible to the environment illumination. Therefore, two approaches are suggested to improve the reconstruction of the scenario. The first approach would be to use a LiDAR radar to reconstruct the scenery because it has a much longer range than cameras and does not depend on illumination to reconstruct the scenery. The other approach would be to use several stereographic cameras simultaneously placed strategically in the environment. However, this approach makes the reconstruction of the scenery very complex

because it will be necessary to synchronize the point cloud of several cameras simultaneously and it will require a cumbersome installation of the system.

- It is necessary to better evaluate the diffuse modular reflector. To this aim, it will be necessary to test the reflector with a larger composition than the one tested in the laboratory, where this reflective surface was only composed of seven hexagonal modular sections, whose dimensions were not larger than a few centimeters. These new tests will be need to determine whether the reflective surface can be effective even when irradiated by a poorly directive source instead of a highly directive one. The results of this study will give guidelines to include the dispersive behavior of the reflector in the predictive beam steering system in Unreal. The integration of this crucial feature that will help us to determine the best beam steering to reinforce areas with poor or no coverage.

- Throughout its development, the predictive beam steering system was tested several times in real environments and with real people dynamics, but the predictive steering was emulated exclusively with laser pointers. This was useful to determine how the system actually worked, but insufficient to determine how the coverage was actually optimized. Therefore, one of the most important validations to do would be to test the predictive system with an external mmWave directive radiation system, which we can control through Unreal Engine as it was done with the laser pointer. This validation will give us the necessary guidelines to further optimize and correct some deficiencies that could be in our system. So far, our system was successfully calibrated with a static scenario without people in it, because the human body scattering effect was evaluated individually with measurements and simulations.

- This Thesis has also demonstrated the great potential of using game engines for the emulation of mmWaves communications in cellular systems for future research. A large number of additional tools can be integrated into the game engines, such as MIMO functionalities, evaluation of active and passive smart reflective surfaces, as well as traffic analysis according to the dynamic behavior of the radio access channel, etc. These game engines are very flexible and allow a high adaptability to the latest technologies.

Appendix A

Software used in the Thesis research

A.1 CST Microwave Studio

CST is a full-featured software suite for electromagnetic design and analysis in the high frequency range. This tool simplifies the process of creating the physical structures to be analyzed by providing a powerful graphical solid modeling front end that is based on the ACIS modeling kernel. Once the 3D solid model is built, a fully automatic meshing procedure is applied, on which the electromagnetic simulation engine is based.

A key feature of CST is to be able to choose the analysis method to be used in the simulator or the type of mesh that best suits the type of electromagnetic analysis sought, that depends on the complexity of the 3D model and the frequency range to be simulated.

As there is no method that works well for all electromagnetic analyses, the software has different simulation techniques (transient solver, frequency domain solver, integral equation solver, multilayer solver, asymptotic solver and eigenmodes solver) to best suit different applications and system simulation resources. Each electromagnetic analysis method adapts its meshing to best suit every simulation technique. Hexahedral meshes can be used in combination with the Perfect Boundary Approximation (PBA) function and some solvers using the hexahedral mesh also support the Thin Sheet Technique (TST) extension. The application of such advanced techniques often increases the accuracy of the results obtained substantially better than other conventional simulators such as ANSYS HFSS [129]. In addition to the hexahedral mesh, the frequency

domain solver also supports a tetrahedral mesh. Surface or multilayer meshes are available for the integral equation solver and multilayer solver, respectively.

The most flexible CST tool is the **transient solver** using a hexahedral mesh, capable of obtaining the entire broadband frequency behavior of the simulated device from a single calculation (in contrast to the frequency step by step approach of many other simulators). This solver is notably efficient for most high-frequency solutions, such as connectors, transmission lines, filters and antennas, etc. For geometrical models that are electrically considerably smaller than the shortest wavelength, the transient solution is less effective. In these circumstances, it is useful to use the frequency domain solver to deal with the issue.

The **frequency domain solver** is most suitable for narrow band problems, such as filters, or when tetrahedral meshes are desired. This solver is general purpose (because it supports hexahedral and tetrahedral grids), plus it has alternatives for fast computation of the S-parameters of highly resonant structures.

In the case of large electrical structures, volumetric discretization methods (transient and frequency domain solver) tend to have inaccuracies in their results, so they will have to have a very fine mesh, to improve the quality of the results. But, as the mesh becomes finer, the required system resources increase exponentially, making it unfeasible to simulate large structures with these methods. Therefore, CST provides an **integral equation solver** that is well suited for such solutions. The integral equation solver adopts a triangular surface mesh that is more efficient for electrically large structures.

Another technique used by CST for large structures is the **fast multilevel method solver** (MLFMM) technology, which provides good scaling of solver time and memory requirements with increasing frequency. For lower frequencies, where MLFMM is not very effective, it becomes essential to make use of the iterative method of moment solving. Despite its excellent scalability, even the MLFMM solver is inefficient for electrically very large structures.

These very high frequency problems are best solved using the CST **asymptotic solver**, which is based on a ray-tracing technique.

In the case of mainly planar structures, such as microfiber filters or printed circuit boards, this particular property of the **multilayer solver** method can be exploited to gain computational efficiency, because this solver, based on the method of moments, does not need to discretize the dielectric and metallic material into subsections transversely. Therefore, this solver can be more efficient than general-purpose 3D solvers for this specific type of two-dimensional application.

Another solver available from CST is the **eigenmode solver** which allows efficient filter design that often requires direct calculation of the operating modes in the filter instead of S-parameter simulation.

And finally, one of the most relevant features of CST is the complete parameterization of all the settings that compose a 3D model or structure to be analyzed, where the user can parameterize its dielectric properties as well as its dimensions. So that in combination with the built-in optimizer and parameter sweeping tools, CST Microwave Studio is able to perform sequential analysis by modifying each of its parameters, as well as being useful for the design of electromagnetic devices, according to established design limits.

Simulations performed in CST to evaluate the feasibility of using the Double Knife-Edge model were performed with the **transient solver**, since it is the best fit for electrically large obstacles at millimeter frequencies.

A.1.1 CST Microwave Studio Interface

CST Microwave Suite works with two main interfaces, one of them is the entry interface to the tool (see figure A.1), and the other one is the workflow interface (see figure A.2) which will depend on the type of electromagnetic analysis we are going to perform.

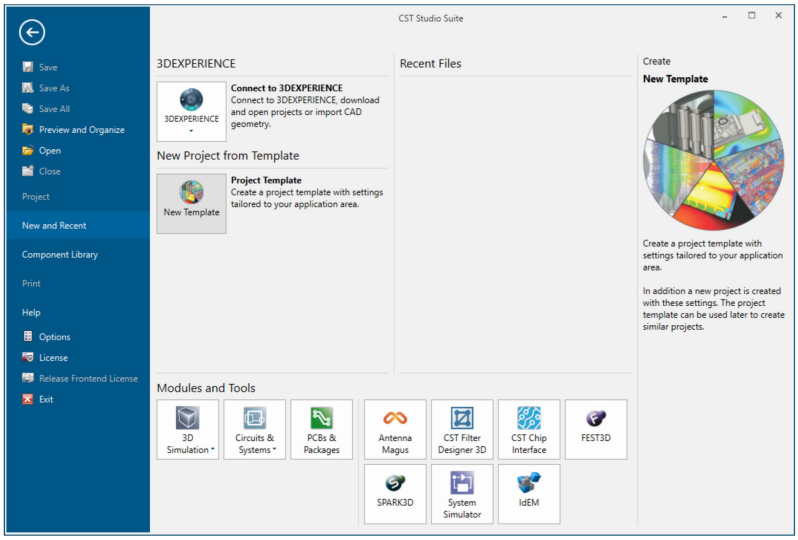

Figure A.1: CST Microwave Studio entry interface.

This is the application's default display when no projects are open. Selecting the File tab will enable it at any time. You get immediate access to common file-related options like Open, Save, and Print in the left pane. The options listed below, in addition to these common controls, are:

- **Project**: The project page provides a short summary of the currently active project and offers project-related actions, such as File As or quick access to the project folder in Windows Explorer.

- **New and Recent**: The New and Recent page is the main place to start a new project or to quickly load one of the recent projects.

- **Component Library**: On the component library page you manage and share your existing reusable projects with your partners.

- **Help**: From the Help page you can launch online help, access your support account or get copyright and version information.

- **New Template**: This option will allow us to create a new project. This will launch the template wizard, which will guide you through a sequence of questions to determine the application area of your new project.

- **Connect to 3DExperience**: Allows to easily open projects or import CAD geometry from 3DExperience, which will simplify the process of importing external models in any format such as .fbx, .obj, etc.

Next step is to create a new project. Click the File: New and Recent → New Template button to start the template wizard. Then a wizard will open and guide us step by step to create our project according to our needs (See figure A.2). According to our field of study, to simulate the scattering over obstacles to validate the requirements to use the double knife-edge mathematical model; the project will be based on the "Antennas" template which is suitable for simulating scattering in free space.

This type of workflow can use an antenna as an active element and an obstacle as a passive element in the same set-up and simulate it as the same structure, where they only interact through the free space. As we will work with the antenna template, the radiation pattern resulting from the interaction of an active element (transmitter) with a passive obstacle (obstacle) can be obtained. This is useful for our purpose, because the double knife edge model gives us the final scattered field beyond the obstacle(See figure 2.3).

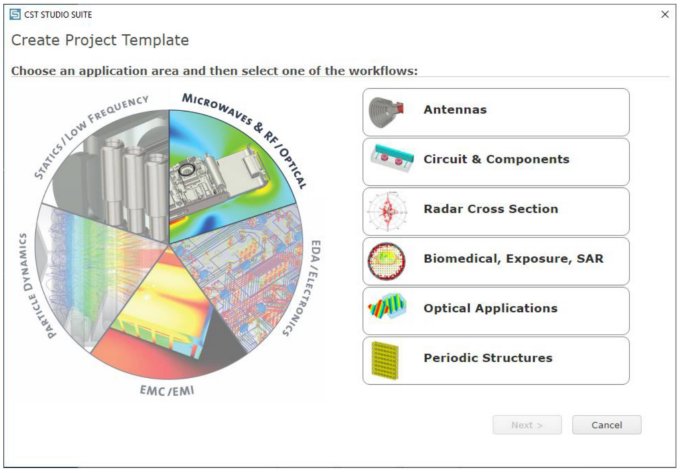

Figure A.2: CST workflow template wizard

The following interface is the main interface in our workflow, where you operate with the structure (passive and active elements) on which the electromagnetic analysis will be performed and define the meshing of the structure to be simulated with the transient solver(Time Domain).

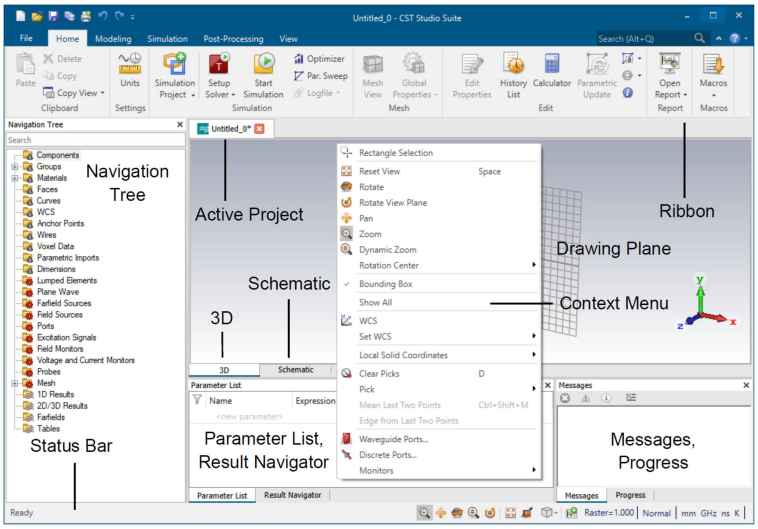

Figure A.3: CST Main workflow interface.

The user interface elements are:

- **Active Project**: Use the tabs at the top of the central main window to toggle between the currently loaded projects.
- **Navigation Tree**: The navigation tree is an essential component of the user interface. It provides information about the structural components and the results of the simulation.
- **Context Menu**: This is a convenient and flexible way to access the most frequently used menu commands in the context of the current configuration. The information in this menu (which can be accessed by clicking the right mouse button) changes dynamically.
- **Drawing Plane**: Use the drawing plane to sketch the 2D part of the 3D geometry. In this window you can change the orientation of the drawing plane and using various tools, you can design 3D geometric structures from scratch. You can also change the location of each of the passive and active elements of the scenario to compose a geometrical structure to be simulated.
- **3D, Schematic and Assembly**: Using the tabs at the bottom of the central main window you can switch between the 3D modeling view, the schematic view and the assembly view. In addition to these main views, you also have access to other temporary views, e.g. the result view, the user interface for the Schematic and Assembly view etc.
- **Parameter List**: The parameter list window shows a list of all parameters previously defined with their actual values.
- **Result Navigator**: This window shows a list of all previously calculated parametric results. It allows you to browse for all available results inside the current result view.
- **Messages and Progress**: The message window displays informational text (e.g. solver output) if applicable. In the progress window, a progress bar is shown for each simulation in progress, even if there is another active project.
- **Status Bar**: The status bar gives useful details about the current project settings. You can click on the status bar text to get access to these values. Furthermore, you can modify the way you handle the view with the mouse.

A.1.2 Structure Modeling in CST Microwave Studio

This section deals with the procedure of creating simple structures. Most complex structures are made up of very simple elements, or so-called primitives.

These types of structures (3D geometries to be electromagnetically analyzed) are the ones that will be used to build our simulation scenario, that will be composed of one active and one passive element.

The active element is a horn antenna in the Ka-band [109] and it comprises several cube primitives that compose the horn and an active primitive which is a predetermined patch radiation source at the bandwidth of interest from 30 to 40 GHz. The passive element is a metallic obstacle, which is composed exclusively of base primitives such as planes, cubes and cylinders.

As an example, we will draw one of these primitives, a brick (Cube) according to figure A.4.

Create a First Brick(Cube)

1. Use the Modeling tab and enable the Brick tool via Modeling: **Shapes** → **Brick**. Then you can choose the first location of the brick base in the drawing plane.

2. **Point 1**: You can set a starting point by double-clicking on a position in the drawing plane.

3. **Point 2**: The opposite corner of the brick base can now be selected on the drawing plane by double-clicking on it.

4. **Point 3**: Then set the height of the brick by dragging the mouse. Double-click to set the brick height.

5. A dialog box will finally appear that shows the numerical values of all the coordinate locations you have entered. Press OK to save the settings and generate your first primitive.

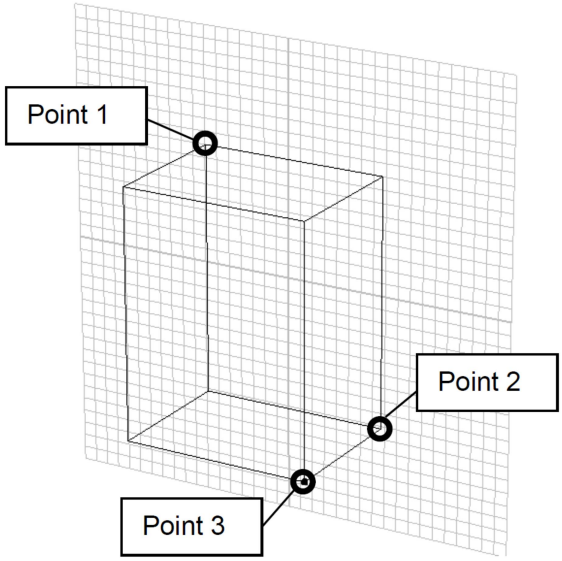

Figure A.4: Starting points for creating a primitive brick structure (Cube).

Figure A.5 gives a brief summary of all the basic shapes that can be generated similar to the brick (cube) described above.

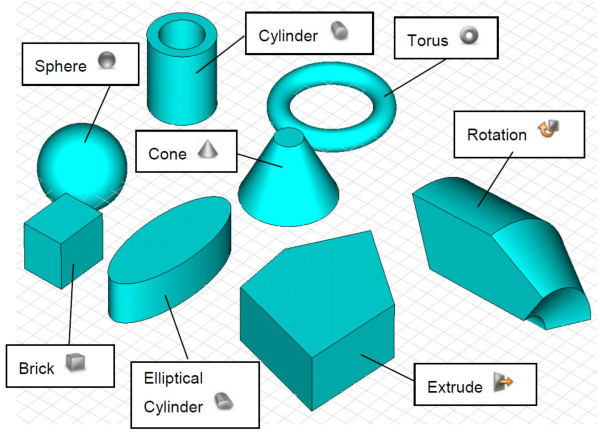

Figure A.5: Primitives available in CST Microwave Studio.

Once a shape is created, it is cataloged by default in the navigation tree. You can locate all shapes in the Components folder. If you open this folder, you will see a sub-folder called component1, containing all the defined shapes. Each primitive's name is assigned in the final shape dialog box when the shape is created. The default names begin with "solid" followed by an increasing number: solid1, solid2, etc. A shape can be selected by clicking on the corresponding element in the navigation tree (See figure A.6).

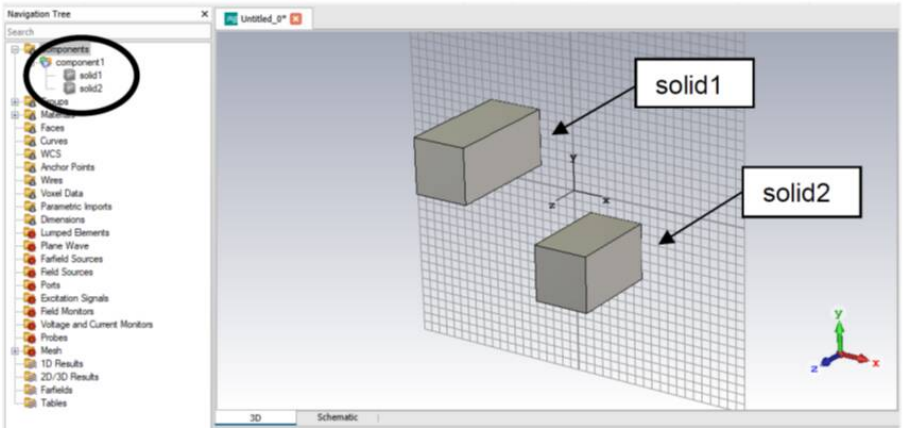

Figure A.6: Organizational structure of objects created by brick primitives(Cube).

Once a shape has been created, the next most important thing to determine the electromagnetic properties of that material is to assign it a material. Thus the assignment of a component to a shape has nothing to do with the physical properties of its material, but is more a way of organizing the shapes. When a shape is associated with a particular component, its material is defined by its color visualization. In other words, the material properties (and colors) do not belong to the shapes directly, but to the respective material. It means that all shapes made of a specific material are displayed with the same color.

To change the electrical properties of the material of any individual shape, one can drag the solid in the navigation tree to the target material or vice versa, as shown in figure A.7.a.

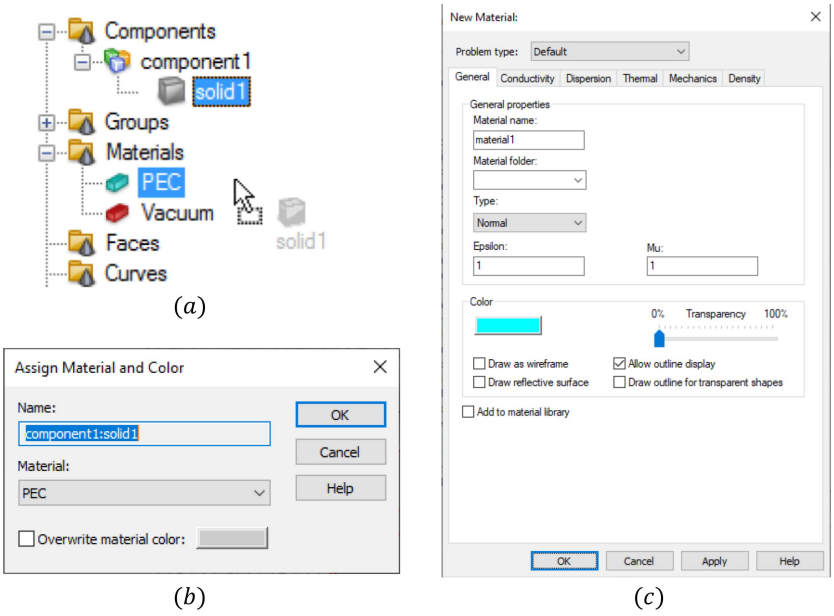

Figure A.7: (a) drag and drop to change material, (b) Dialog box to Assign Material, (c) Create New Material box.

Another method is to select the shape and choose Modeling: Materials → New/Edit → Assign Material and Color (this is also possible in the context menu of the selected shape). The dialog box will open as in the figure A.7.b. In this dialog box, one can choose an available material from the list or create a new one by selecting the [New material...] item in the list. In the last case, a new dialog box will open as shown in figure A.7.c.

In the dialog box in figure A.7.c, the material name and the material type (e.g. perfect electrical conductor (PEC), normal dielectric (Normal), etc.) must be specified. Note that the available material types, as well as the corresponding options, depend on the CST Microwave Studio material library (see figure A.8). However, we can also customize our own materials, if we have characterized their electromagnetic properties. To load the database of standard materials defined by CST, access it by selecting Modeling: Materials → Material Library → Load from Library. This operation will open the following dialog box showing the database contents of all materials available in the tool.

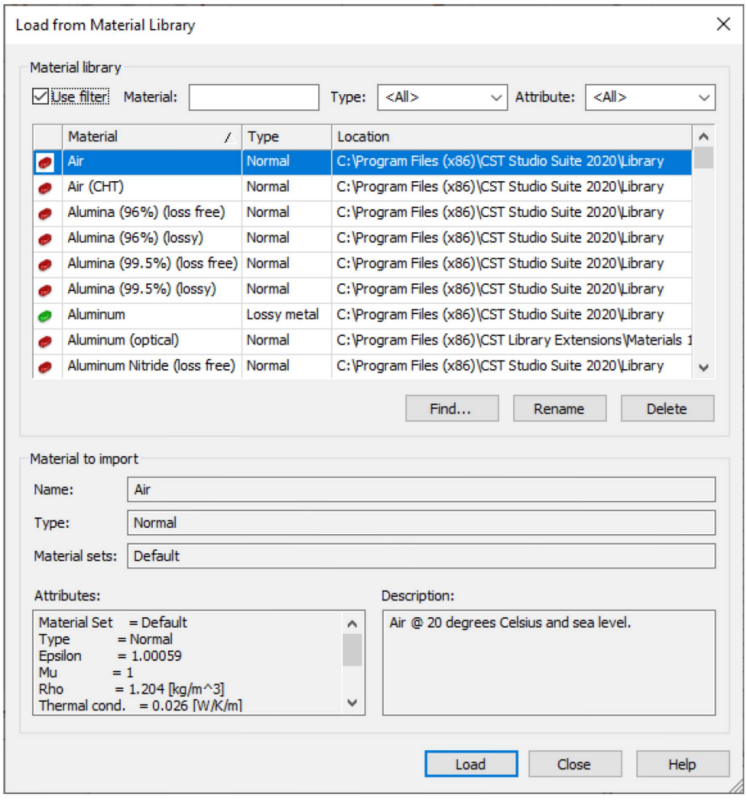

Figure A.8: Standard Material Library CST.

In our case study, the material used to build both the horn antenna (active element) and the blocking object (passive element) will be the Perfect Electrical Conductor (PEC). The use of the PEC material for the blocking object is due to the fact that it guarantees that it is totally absorbent in transmission. This decision has been made to have an equivalent reference point for the measurements.

Since it is impossible to have a totally absorbing flat material at mmWave frequencies, it was decided to use a metallic plane; as this is a totally reflective material, the transmitted field through the material is null at the frequencies of interest. Therefore we can use it as an equivalent to validate the Double Knife-Edge model in both simulations and measurements.

A.2 Blender

Blender is a free and open source 3D modeling program. It enables modeling, rigging, animation, simulation, rendering, compositing and motion tracking, as well as video editing and game production. It is one of the most popular 3D modeling tools today, because it is one of the most complete tools, allowing to create content that has nothing to envy to professional commercial platforms such as Maya, 3ds Max, SketchUp, Cinema 4D, etc. It is a cross-platform program that works on Linux, Windows, and Mac computers. Its user interface is built with OpenGL to ensure a consistent experience.

Blender is free and open source, so you can download the full tool for free from its website (www.blender.org).

Blender is a suitable application for small animation studios, freelance 3D artists, independent filmmakers, students learning about 3D computer graphics, and committed computer graphics enthusiasts. It is also used, albeit covertly, by major animation, visual effects and video game companies because it is reasonably easy to modify, has a responsive development team, no licenses management is required.

Blender, like many other 3D computer graphics programs, has a reputation for being difficult to learn for newcomers but, although it is true that the learning curve is very slow, it is a very versatile tool that allows expert users great freedom to carry out their projects quickly once the tool is mastered.

Blender was published under the GNU General Public License on October 13, 2002 as a result of the community's fervor and willingness to invest time, money, and effort when there was an opportunity to compete with their paid competitors in the sector. With the community in control of the source code, Blender experienced an explosion of development and new feature additions in a relatively short period of time, including both common and cutting-edge innovations.

One unique aspect of Blender programmers is that many of them use the program on a daily basis. They produce code not because they have to, but because they want to enhance Blender for their own needs. Many Blender developers began as artists who wanted to make Blender accomplish something it couldn't do previously. Part of the programmers' motivation stems from the open source nature of Blender, but it also stems from the fact that Blender was initially an in-house production tool designed by artist programmers, who worked exclusively on new features that directly benefited artists.

One of the most innovative features was to include Python as part of its source languages, which for the time was very revolutionary, because high-level languages were often looked down upon because they tend to be computationally inefficient. Although it was a risky bet at the time, today it has brought

a great competitive advantage, because Python has become the most used language to implement artificial intelligence systems and one of the most popular because of its low barrier to entry.

After two decades, the Blender community is stronger and larger than ever. Blender is a cutting-edge, potent piece of software that can compete in quality with similarly priced, high-end alternatives. Screenshots of Blender from its beginnings to the present day are shown in figure A.9.

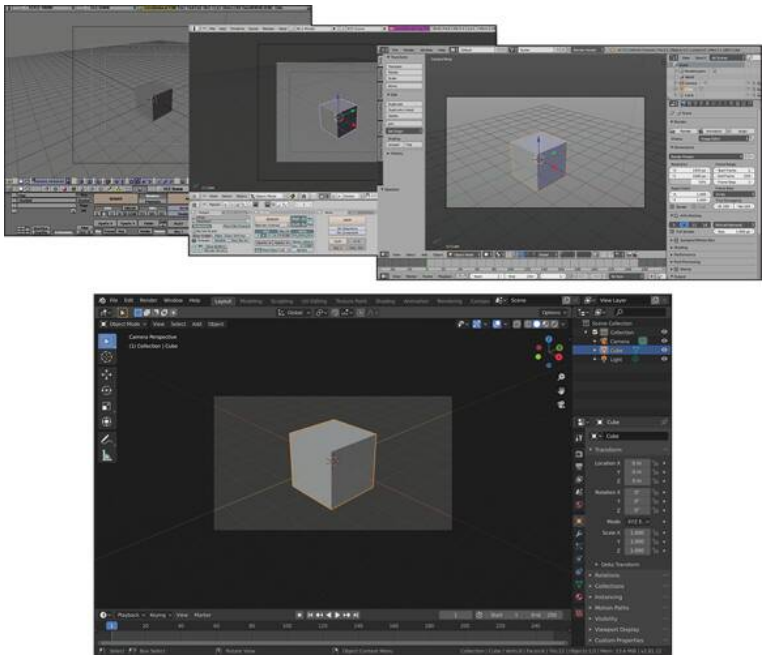

Figure A.9: The evolution of the blender: Blender 1.8 (top left), Blender 2.46 (top middle), Blender 2.72 (top right), today's Blender 3.2.1 (bottom).

A.2.1 Blender Interface

The Blender interface is divided into nine parts [175] (see figure A.10).

1. **Topbar**: This area is where you manipulate the project files, as well as edit and/or change the graphical interface of the work approach, such as: Modeling, Sculpting, Texturing, Animating and Scripting etc.

2. **Status Bar** : The status bar is located at the bottom of the Blender window and is used to display information about the mouse keymap, which

is indispensable in Blender; it also displays information about currently running tasks or tools and information about system resources.

3. **Header**: This is a small horizontal banner that is placed at the top or bottom of a 3D View. All editors have a header that supports the most commonly used menus and tools. The menus and buttons will change depending on the type of editor and the chosen object and mode.

4. **Main Region**: This is the region that is always visible. It is called the main region and is the most prominent part of the editor. In this area the 3D models you are working on are displayed.

5. **Toolbar**: It shows the buttons of each of the most used tools, related to a direct action on the 3D model displayed in the main region.

6. **Outliner**: In this area you can see the list of all the objects present in your workspace. Each object is classified according to its type, such as: lighting objects, 3D models, cameras, layers, animations, etc.

7. **Tabs**: Are used to regulate overlapping portions of the user interface. A single tab's content is displayed at a time. Each component of this tab has a collection of tools for modifying the properties of the selected object.

8. **Panels**: A panel is the smallest organizational element in the user interface. Each panel shows the properties that can be modified on each selected object type.

9. **Timeline**: This section provides the user with a full view of a scene's animation, including the current frame, the keyframes of the active object, the start and finish frames of its animation sequence, as well as the user-defined markers.

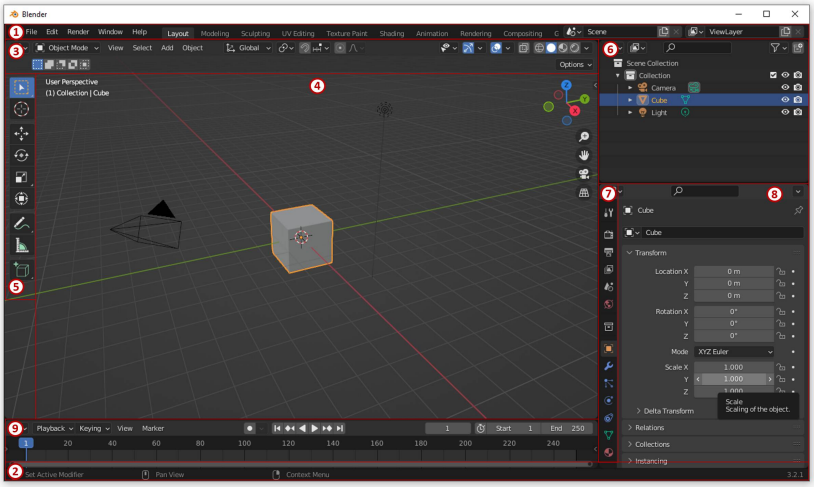

Figure A.10: Blender Interface segments.

A.2.2 Geometry in Blender

A 3D scene requires at least three main components, which are as follows: Models, Materials and Lights. In the research focus of this thesis, Blender has been used only to model and characterize the millimeter waves 3D reflector. Modeling is simply the art and science of creating a surface that mimics the shape of a real world object or expresses a shape for a particular need. Several modeling modes are available depending on the purpose of the object to be represented. The types of modeling are determined by the accuracy of the model to be created and by the way the object meshes are modified. The modeling modes are as follows:

1. **Object Mode**: Basic operations such as object generation, object joining, shape key management, and UV/color layers are supported.

2. **Edit Mode**: This simple mode is used for the vast majority of mesh editing tasks.

3. **Sculpt Mode**: Instead of dealing with individual mesh elements, this modeling relies on brushes to sculpt the 3D model, this type of modeling is the most artistic and is only recommended for professional modelers.

4. **Scripting Mode**: This is the most accurate, but also the most complex to approach of all modes, because it is necessary to have excellent

knowledge in Python programming, as well as to master the modeling manually.

Before getting into Blender modeling it is fundamental to know what is a mesh in a 3D model, and what are the elements that compose it. With meshes, everything is built with three basic structures, which are: vertices, edges and faces (see figure A.11).

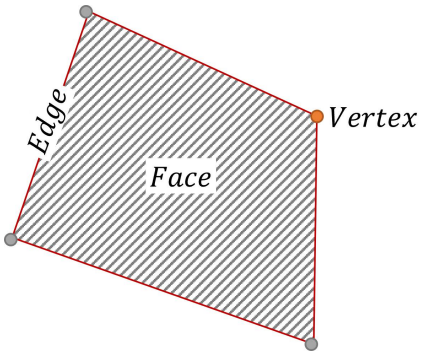

Figure A.11: Blender Mesh structure.

- **Vertices**: The vertices, which are ingle points or locations in 3D space, are the basic component of a mesh. In edit mode, vertices are shown as little dots in the 3D viewport. A coordinate matrix is used to store an object's vertices.
- **Edges**: An edge is always a straight line that links two vertices. When viewing a mesh in wireframe view, the edges are the "wires." They are typically undetectable in the displayed picture. They are used to make faces.
- **Faces**: Faces are utilized to construct the object's physical surface. They are visible when the mesh is rendered. If this region does not have a face, the produced picture will simply be translucent or non-existent. A face is defined as the region with an edge on each side between three (triangles), four (quadrangles), or more (n-gons) vertices. Faces are frequently shortened to tris, quads, and n-gons.
- **Normal**: A normal in geometry is a direction or line that is perpendicular to something, usually a triangle or surface, however it can also be relative to a line, a tangent line for a point on a curve, or a tangent plane for a point on a surface.

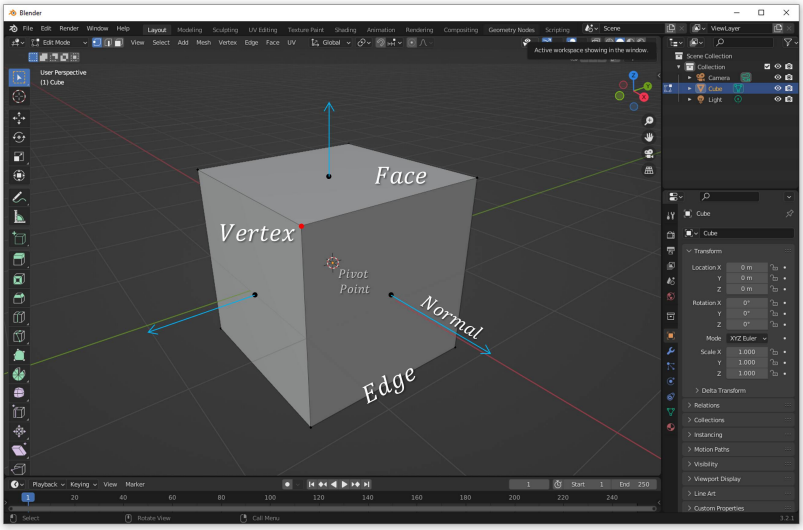

Figure A.12: 3D Cube with Vertices, Edges, Faces and Normals.

Geometry primitives with Blender

The 3D primitives in blender are all those geometric objects that are essentially simple and can be used as a base for the creation of more complex elements, as in our case a mmWave reflector. In other words, primitives are basic and elementary models from which a more complex model can be developed with the composition of several primitives. The primitives come from their analogous 2D geometric shapes, such as a sphere or a cylinder from a circle, a cube from a square, a tetrahedron from a triangle, etc. In the figure A.13 are some 3d primitives created in Blender.

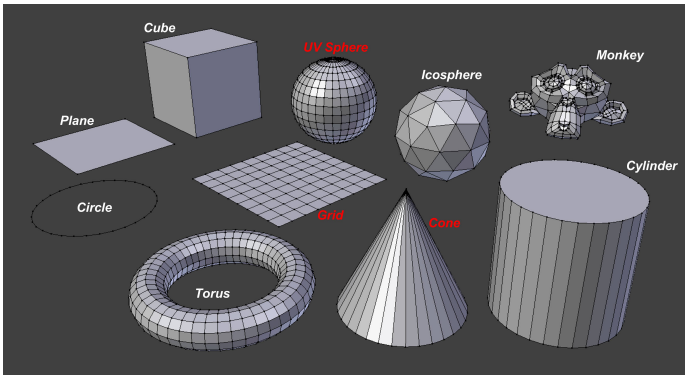

Figure A.13: Blender's standard primitives.

When you create a primitive in Blender from scratch, you have to specify a number of parameters to create the object, some of which are radius, size, location, rotation, segments, rings, etc. The Blender primitives used to design the millimeter waves passive reflector were mainly the following: UV Sphere, Grid and Cone. The particularity of these primitives with respect to the rest is that they allow us more flexibility to modify them symmetrically and by code in a comfortable way.

- **UV Sphere**: A quadrilateral UV sphere has triangular mesh at the top and bottom and quadrilateral faces in the middle. Config: Segments, Rings.
- **Cone**: Cones may be made of spikes or pointed caps, among other things. Config: Vertices, Radius, Depth.
- **Grid**: a split plane with a regular square grid. Config: X/Y Subdivisions .

A.2.3 The Blender Python API

There are many individual interfaces that make up Blender. The main interfaces are highly programmable because almost every possible user interaction is tied directly to a Python function. This Blender feature makes it possible to replicate almost everything that can be done in Blender manually, with an automated equivalent in Blender via the Python API. This is Blender's biggest competitive advantage because it makes it much easier for designers to create models with the highest precision, if they have programming knowledge.

Before we start getting into the Python API it is necessary to identify which scripting interface Blender uses for this purpose. To enter the scripting interface, select the Scripting option from the drop-down menu to the right of the Help button within the Header menu. Throughout the text, we will present instructions like this with bold directives, such as: Header Menu → Scripting. See figure A.14.a for the location of the menu. The Blender layout will change to appear as in figure A.14.b.

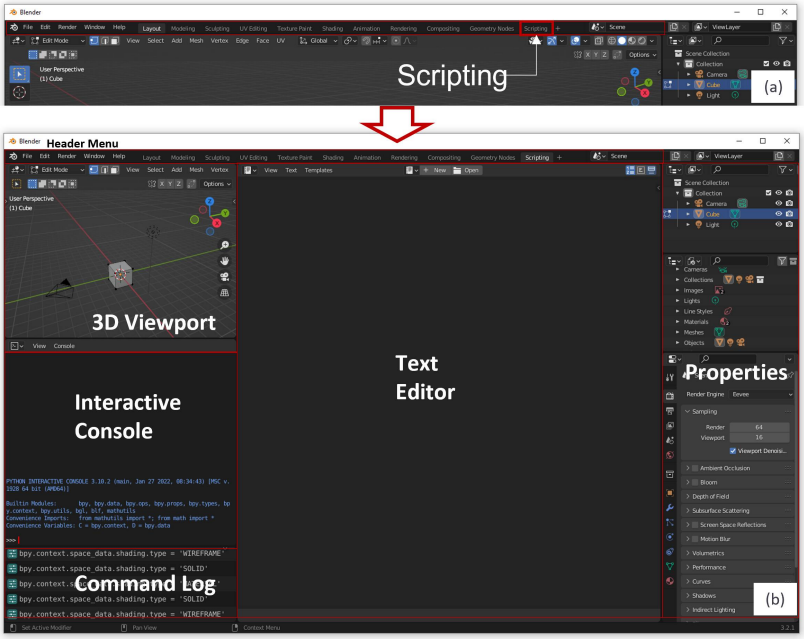

Figure A.14: (a) Selecting the Scripting interface, (b) The Scripting interface.

According to the interface in figure A.14, the most important segments for coding with the Python API are described:

- **Text Editor**: The Text Editor allows us to edit text files, including Python scripts. The New and Open buttons can be used to create and launch scripts, respectively. The menu bar at the bottom of the Text Editor will alter to allow saving and switching between files after the scripts have been loaded. There are certain unique features of the Blender Text Editor that relate to imports, system paths, and linked files in Python.

- **Command Log**: The function calls performed by the Blender interface throughout the session are displayed in the command log. When playing with scripts and learning about the API, this window is quite helpful. For instance, if we use the red arrow to move the cube in the 3D Viewport, we get the next output in the Command Log:

```
bpy.ops.transform.translate(value=(3.05332, 0, 0),
        constraint_axis=(True, False, False),
        constraint_orientation='GLOBAL',
        mirror=False, proportional='DISABLED',
        proportional_edit_falloff='SMOOTH',
        proportional_size=1, release_confirm=True)
```

  This output shows that the *translate()* function was called from the transform class of the *bpy.ops* submodule. The parameters are quite verbose and often redundant in the calls made from the interface, but they are straightforward enough that we can figure out what they mean and experiment with the function.

- **Interactive Console**: The Python environment known as the Interactive Console resembles the IPython consoles that are often seen at the bottom of IDEs (interactive development environments). Text Editor scripts have access to the same global Blender data that is stored in *bpy* and its submodules, but the Interactive Console does not share any local or module-level data with Text Editor scripts. As a result, the console won't be able to read or change the local variables used by the scripts, but changes made to *bpy* are shared.

The aforementioned three Python scripting windows are used to program a 3D model in Blender. It is significant to note that the Python API allows for the execution of any 3D model action that can be performed manually, including scaling, placing, extruding, rotating, merging, and constructing primitives. All of the actions that will be carried out using Blender's Python API will only employ the 3D model primitives.

A.3 Unity Game Engine

Unity is a group of technologies and tools with the goal of helping developers create interactive software products, mostly games, but also AR applications and simulators, collectively referred to as Unity. Simply put, Unity is a game creation program. But further explanation is needed in order to avoid the false

impression that knowing Unity is sufficient in and of itself for game development. This is a false assumption because games are made up of a wide variety of elements from several fields, ranging from scripting and programming to graphics and music.

Unity's scope only includes some of these elements. In the strictest sense, Unity is not an asset development tool like Blender, 3DS Max, Maya, Photoshop or FL Studio. Graphics, music, sounds, ideas, concepts, voices, animations, movies and other game elements are not typically created by developers using Unity.

Usually, musicians, artists, and other developers produce these materials in advance using programs and methods other than Unity. While a vehicle manufacturing factory will assemble a car from a variety of ready-made components or pieces, Unity's purpose is to take those precreated assets as individual files, add more information to them, and make them work together in a synthesis that is a final game product.

Unity is a game-making tool in that more specific meaning. It is software that designers and programmers mostly utilize to develop the final game from pre-made components. For this reason, this section will not discuss techniques for creating models and graphics in 3D software or creating music and sound. Rather, it assumes that such assets have already been created and then explores how Unity can help.

The three main sections or components that make up Unity as a tool are: 1) the engine; 2) the publishing or distribution modules; and 3) the editor. Together, these three components make up Unity's core and are the reason why it is such a powerful game development tool. In the following, we present a concise but thorough analysis of these elements.

The Engine

Although Unity is frequently referred to as a "game engine", this label really only emphasizes one of its three parts. Similar to how the heart and brain are among the essential components of the body, the engine is the fundamental component, or the core, of the Unity package and any games made with it. The Unity engine is a piece of software that operates constantly in the background and is not immediately apparent to the user or developer. It is included or incorporated without being specifically indicated in all Unity-created games. There, it serves as the game's logical foundation or invisible framework.

The engine might be compared to a template that is altered to create several games, much as a car engine is connected to various frames to create various car models. As we will see, the engine differs from the editor and distribution modules, which make up the other two parts of Unity. Additionally, it differs

from game assets. The images, sounds, animations, and models that are present in the game's universe are referred to as an asset. The world exists and functions because of the engine, on the other hand. It serves as the "rules of the game universe" and allows us a blank environment to fill with our resources and creativity.

The Distribution Modules

Unity is distinguished by its "Build once, deploy everywhere" approach to cross-platform development. In other words, Unity aims to be a development tool that allows game developers to create games for a variety of platforms and systems with a single project or set of code. Windows, Mac, Linux, Web, Android, iOS, Flash, Xbox SeriesX, Wii U and PlayStation 5 are all supported by Unity. Regardless of Unity compatibility, distribution modules are the parts of Unity that enable the compilation and deployment of games using the engine. The engine and game data created with the editor can be combined using distribution modules to create a standalone, independent game. Standalone denotes the fact that it can be supplied to and used by customers without the need for them to have the Unity software.

The Editor

The component of the software that is most noticeable is the Unity editor (see figure A.15). When using Unity, it is the place where most developers will spend the most of their time; in contrast, a player don't even see the editor when playing a game, unless they are also Unity devs, of course. But even then, they won't be aware of it because it is a part of any completed game; rather, they will only be aware of it because they have used the editor to make their own games. Only game developers use the editor during the game development phase. It covers all the interface elements, windows, tools and messages that make up Unity. The Unity editor is used by the developer when he launches Unity from his desktop and starts using the tools to create a game. The editor provides access to a variety of Unity-bundled or add-on-expandable tools, windows, and modules.

A.3.1 Unity Interface

The Unity user interface is divided into eight sections [176] (see figure A.15).

1. **The Toolbar** gives access to your Unity user account, Unity Cloud services, play, step controls and pause, and Unity find, a layer display menu, and the editor layout menu (which gives you some alternative

layouts for the editor windows as well as allowing you to save your own layout customization).

2. **The Hierarchy window** is a text representation that shows the hierarchy of each **GameObject** in the **scene**. The two windows are inextricably linked since every component of the scene has an entry in the hierarchy. The hierarchy shows the organization of the connections between the GameObjects.

3. **The Game view** emulates the final game as rendered through the scene **cameras**. When you click the Play button, the rendering simulation begins.

4. **The Scene view** enables you to explore and edit your Scene visually. Depending on the type of project you are working on, the **scene view** can offer a 3D or 2D perspective.

5. **Overlays** include the fundamental controls for working with the scene view and the game objects It containss. Additionally, you can include unique Overlays to improve your process.

6. **The Inspector Window** allows you to examine and modify each of the game object's properties that is currently chosen. Every time a different GameObject is selected, the layout and contents of the **Inspector** window change because different GameObject types have different sets of properties.

7. **The Project window** reveals the Assets in your library that are available for use in your project. These assets show up here after you import them into your project.

8. **The status bar** gives rapid access to relevant tools and settings, as well as notifications on various Unity processes.

Figure A.15: Unity Editor Interface.

A.3.2 Key concepts in Unity

To design game mechanics, you need to understand some key concepts, which will be necessary to implement any kind of game or simulation in Unity by code.

1. **Scenes**: In Unity, scenes are where you work with content. They are resources that may fully or partially contain a game or program. One scene, for instance, may be used to create a straightforward game, whereas one scene, one level, each with its own setting, characters, obstacles, decorations, and UI, could be used to create a more sophisticated game. A project can contain any number of scenes. Unity opens a sample scene with just a Camera and a Light when you initially create a new project and open it.

2. **Unity Component**: Components are the functional parts of each GameObject. Components contain properties that you can edit to define the behavior of a GameObject and one of its components is the "Transform", which allows us to change the position, rotation and scale of the GameObject.

   Another of the most important components is "Rigidbody-Collider" that allows us to define the limits in which the GameObject acts in case of a collision with another object in the scenario. This component is fundamental to identify when an object is hit by another object and this

component is very important because it defines the equivalent edges to implement the DKE model.

A list of the components attached to a GameObject can be seen through the Inspector window by selecting that GameObject.

3. **GameObject**: Each of the objects that constitute the scene in Unity is known as a GameObject. It contains different components according to their functionality. For example every element of your game, from people and collectibles to lights, cameras, and special effects, is a GameObject. A GameObject, however, is powerless on its own; you must give it features in order for it to take on the characteristics of a character, an environment, or a special effect.

   Within each gameObject you can load physical objects which are composed of a set of interconnected two-dimensional triangular polygons, known as meshes. Each mesh is composed of vertices, edges and faces, which together constitute the morphology of an object in three dimensions in Unity. Additionally, 3D primitive objects such as the cube, the sphere, the capsule and the cylinder are also available in Unity. These objects are often used to create simple objects such as walls, furniture etc.

   But in the case of objects with a complex morphology, it is necessary to import them, because Unity does not have the capacity to model complex 3D objects, as Blender, Maya, Cinema 4D. do. In our case the geometric model of the human body was downloaded from the internet.

4. **Prefabs**: It allows us to create, configure and package a complete GameObject with all its components, property values and child GameObjects as a reusable Asset. The Prefab Asset works as a template from which you can create new Prefab instances in the Scene.

5. **Layers**:These are a tool that allows us to separate each GameObject into different scenes. These can be used through the UI and with scripts to modify how the GameObjects interact with each other in a scene.

6. **Constraints**: This component binds the position, rotation or scale of a GameObject to another GameObject. A constrained GameObject moves, rotates or scales like the GameObject to which it is linked. So any change on the GameObject will directly affect all its children.

7. **Rotation and orientation in Unity**: Quaternions and Euler angles can both be used in Unity to express rotations and orientation. Although both

representations are identical, they have different applications and constraints. The Transform component, which shows orientation as an Euler angle, is typically used to rotate items in your scene. To avoid gimbal lock, Unity internally records rotations and orientations as quaternions, which might be helpful for more complicated motions.

8. **Lights**: Each scenario needs lighting to be effective. Lights determine the color and mood of a 3D environment, whilst meshes and textures form the shape and appearance of a scene. In each scene, you'll probably use more than one light. It takes some practice to get them to cooperate, but the effects can be pretty astounding.

9. **Cameras**: Similar to how cameras are used in movies to tell the tale to the audience, cameras are utilized in Unity to show the player the game world. A scene will always contain at least one camera, but there may be more.

A.3.3 Scripting in Unity

One of the best cross-platform game engines is Unity3D, which has a strong rendering engine and support for Augmented Reality (AR) and Virtual Reality (VR). The assets shop allows to download both free and paid assets. In most cases, when an asset is needed, for instance one that allows us to communicate via UDP socket, its implementation is already available for purchase. However, many of these assets, once in use, prove not to be what they claim to be and may have some or many limitations, which cannot be solved just by buying more assets.

Therefore it is important that the developer has advanced programming knowledge, which allows him to design his own asset according to his needs. This is one of the advantages of using such a consolidated high-level language as *C#*.

The drawback of a high-level programming language is that it can be very slow in some applications, such as the implementation of the ray-tracing system.

Therefore, Scripting is an indispensable component in all games developed in Unity. Most games need scripts to react to player input and to organize game events in a timely manner. In addition, scripts can be used to generate graphical effects, control the physical behavior of gameobjects or even implement a custom AI system for in-game characters.

In order to develop interactive programs in Unity it is necessary to use an integrated development environment (IDE), whose function is to facilitate the development of other proprietary pieces of software such as classes, functions

and structures. Unity supports the following IDEs: Visual Studio, JetBrains Rider and Visual Studio Code.

Using the *C#* scripting framework, you can handle GameObject instantiation, manipulation, user interactions, and UI control management. The simplicity of GameObject access through inspector and the MonoBehaviour life cycle techniques are the standout features of Unity scripting.

The entity that directs the behavior and interaction of the game elements in the scenario is called scripting. The life cycle techniques and APIs for gameObject manipulation make Unity scripting effective. Everything in the Unity scene may be thought of as a GameObject, and you can use the inspector or the ***GetComponent*** method in the script to refer to it.

The major scripting language for Unity is *C#*. Although Javascript is an option, most programmers prefer *C#* because of its simplicity. Only object-oriented scripting languages are supported by Unity. The fundamental units of any language are variables, functions, and classes.

Here is a simple Unity script with a log message:

```
using System.Collections;
using System.Collections.Generic;
using UnityEngine;

public class HelloWorld: MonoBehaviour
{
    //Variables
    //Functions
    //Classes

    // Start is called before the first frame update
    void Start()
    {
        Debug.Log("Hello World");
    }

    // Update is called once per frame
    void Update()
    {

    }
}
```

A Unity project's main building block is the GameObject. All objects, including lighting, UI, and 3D models, are descended from the GameObjects class. All the objects we use in a Unity scene belong to this parent class.

GameObject Manipulation

In Unity, there are two ways to interact with GameObjects: through the inspector, and through scripts. If you want to move an object, you can do so quickly and efficiently using the inspector window. In addition, the inspector allows you to add additional elements such as Rigidbody and custom scripts, as well as modify rendering properties. If you wish, you can perform the same task using a single script, as seen in the following code fragment.

```
// Create a GameObject
Instantiate(GameObject prefab);
Instantiate(GameObject prefab, Transform parent);
Instantiate(GameObject prefab, Vector3 position,
                                Quaternion rotation);
Instantiate(bullet);
Instantiate(bullet, bulletSpawn.transform);
Instantiate(bullet, Vector3.zero, Quaternion.identity);
Instantiate(bullet, new Vector3(0, 0, 10),
                          bullet.transform.rotation);

// Destroy a GameObject
Destroy(gameObject);

// Finding GameObjects
GameObject myObj = GameObject.Find("NAME IN HIERARCHY");
GameObject myObj = GameObject.FindWithTag("TAG");

// Accessing Components
Example myComponent = GetComponent<Example>();
AudioSource audioSource = GetComponent<AudioSource>();
Rigidbody rgbd = GetComponent<Rigidbody>();
```

Physical Events

The physics implementation system in Unity is highly advanced. It gives the game objects different physical characteristics including gravity, acceleration, collision, and others. In the following code example, both objects have activated

the Collider and the RigidBody component, so that the events indicated with the private function "OnCollision" work.

```
private void OnCollisionEnter(Collision hit) {
  Debug.Log(gameObject.name + " hits "
                                + hit.gameObject.name);
}
private void OnCollisionStay(Collision hit) {
  Debug.Log(gameObject.name + " is hitting "
                                + hit.gameObject.name);
}
private void OnCollisionExit(Collision hit) {
  Debug.Log(gameObject.name + " stopped hitting "
                                + hit.gameObject.name);
}

// Trigger must be checked on one of the Colliders
private void OnTriggerEnter(Collider hit) {
  Debug.Log(gameObject.name + " just hit " + hit.name);
}
private void OnTriggerStay(Collider hit) {
  Debug.Log(gameObject.name + " is hitting " + hit.name);
}
private void OnTriggerExit(Collider hit) {
  Debug.Log(gameObject.name + " stopped hitting "
                                        + hit.name);
}

// For 2D Colliders
private void OnCollisionEnter2D(Collision2D hit) { }
private void OnCollisionStay2D(Collision2D hit) { }
private void OnCollisionExit2D(Collision2D hit) { }
private void OnTriggerEnter2D(Collider2D hit) { }
private void OnTriggerStay2D(Collider2D hit) { }
private void OnTriggerExit2D(Collider2D hit) { }

// Ray casting to detect the collision
Ray ray = Camera.main.ScreenPointToRay(Input.mousePosition);
RaycastHit hit;
```

```
if (Physics.Raycast(ray, out hit, 100)){
  Debug.DrawLine(ray.origin, hit.point);
  Debug.Log("Hit: " + hit.collider.name);
}
```

Physical events are to be used extensively in the implementation of the double Knife-Edge model. Both the "OnCollisionEnter" event and the "Physic.Raycast" functions were used for the implementation of the proprietary RayTracing system, as well as for the implementation of the DKE model to characterize the scattering effects of a 3D model of the human body. These two physical events will be briefly explained below:

- **Collider.OnCollisionEnter(Collision)**: OnCollisionEnter is called when this collider/rigidbody has begun touching another rigidbody/collider. More precisely, this event is triggered on the GameObject script when it is hit by another GameObject, or when it is hit by a "Ray", which is controlled by the "Physics.Raycast" function. When this event is triggered, the parameter received in this event is the Collision class. The Collision class contains information, for example, about the contact points on the mesh of the GameObject, and who (GameObject) or what (Raycast) hit it, and mainly where this GameObject is at the impact time. This information is vital to implement the ray-tracing system, because with this simple information, you can deduce where the source of radiation is and if it has hit close to a potential equivalent edge, which will be used to implement the DKE model.

- **Physics.Raycast**: This function launches a ray, of length maxDistance, from the origin point towards all colliders (GameObject) of the Scene. This function was used to emulate the antenna, which is the entity tha emanates the rays that will hit the whole scenario, and in particular the three-dimensional geometric model of the human body.

A.4 Unreal Engine

Unreal Engine (UE) is a 3D graphics game engine developed by Epic Games, first introduced in 1998 in the first-person shooter game Unreal. Initially developed for PC first-person shooter games, it has since been used in a variety of game genres and has been adopted by other industries, such as film, television and architecture. Written in C++, the Unreal engine features a high degree of portability and performance as it supports a wide range of desktop, mobile, console and virtual reality platforms.

Since the original 1998 version, several generations of the software have been released. Unreal Engine 2 was released in 2002, UE3 in 2006, UE4, in 2014, and finally the recent version UE5 released in 2022. This latest version is unique in its kind, due to the large amount of tools available and the photo realistic quality of results, where this platform gave a blow to the table with the intentions of revolutionizing the simulation and video game industry. Since version 4 of Unreal Engine, this is not focused exclusively on the creation of video games, which makes it the most versatile tool today. As this is not a modeling tool, to create any kind of scenario one needs to resort to software like Blender, SketchUp or 3DMax etc.

Unreal Engine is free to download and use, however there are some restrictions because it is open source. You must consent to Epic Games' licensing terms, which call for you to give them a small portion of your income, in order to download and utilize the engine. A 5% royalty must be paid to Epic Games for any sales exceeding $3,000 if you produce something with the engine that generates more than $3,000 in a single quarter (i.e., a quarter of a year).

In the development of our beam steering system we used Unreal Engine version 4.27, which is more robust than the most recent version 5.0, especially in the integration of functions with C++.

A.4.1 Unreal Basic Concepts

The following are the basic concepts that must be taken into account when developing any implementation within the Unreal Engine development environment.

- **Projects**: In the Unreal Engine context, a project is the entity that contains all of the information for an individual game. This means that each individual game you create will be stored in its own project. In Unreal there are two types of projects, the first type of project are those that operate entirely with "Blueprint", which is a visual programming language focused on interconnecting blocks as subsystems in Unreal, and the other type of project is a hybrid project where some portions of the game are programmed with "Blueprint" or another portion with C++.

- **Levels**: A level is the whole or part of the "world" of your game. Environments, usable objects, other characters and other elements are contained in a level for the player to see and interact with. In video games, multiple levels with distinct transitions between them are typical (e.g., once the final boss of one level is defeated, you move on to the next). In other interactive experiences created with Unreal Engine, different levels can be used to switch between various exposures or environments.

- **Actor**: Any item that can be inserted into a Level, such as a camera, a static mesh, or the player's starting position, is considered an Actor. 3D transformations like translation, rotation, and scaling are supported by actors. Through the use of gameplay code (C++ or Blueprints), they can be generated (spawned) and destroyed. The actor is equivalent to the GameObject in Unity, therefore each actor has its own life cycle and its own logic within it. In Unreal there are different types of Actors that depend on the interaction that the Actor will have within the Level; for example, simple Actors that usually have low computational load by having fewer functions and events, are called StaticMesh Actors, while in the opposite case, Actors with more interaction and functions are called Character Actors, which are usually the ones that have the main characters in video games. Within each Actor we load the physical objects that determine the geometrical limits of our object, and these are composed of a set of two-dimensional triangles interconnected by vertices, called StaticMesh.

- **Components**: In Unreal, Actors can be assigned to certain types of objects called Components. Actors can actually be thought of as simple containers that hold Components. For instance, an Actor that contains a Static Mesh Component is referred to as a Static Mesh Actor.

- **Blueprint**: The Blueprint Visual Scripting system is a complete game scripting system based on the concept of using an interface based on nodes to create interaction with all the Level Actors, where Depending on the type of interaction, for instance a collision, the components of each Actor are modified. In Unreal the use of Blueprint is mandatory because it is the only way to interact with the graphical interface, so even though most of the logic of a simulation system is programmed in C++, it is essential to use Blueprint to display the results of the interaction visually.

A.4.2 Unreal Editor Interface

The Unreal Engine is an application used to run games, where algorithms are used to determine how objects are rendered frame by frame, how lighting should affect them, how objects interact with collisions, etc. But in Unreal Engine there is the Unreal Editor which is the application where the engine is used to create games and simulations step by step.

The scenes that you use to create your gaming experience are known as levels in the Unreal Editor. Consider a level as a three-dimensional setting where you can arrange various items and geometrical elements to create the scenario your users will encounter. Any item that is introduced into your

environment, whether it be a character, a mesh, or a light, is referred to as an actor. In the Unreal Engine, an actor is a programming class that is used to define an object with its own logic as well as information about its location, rotation, and scale. Any object that may be inserted into your levels can be thought of as an actor.

Therefore where we create a level with actors is known as Level Editor and is the main sub-editor in Unreal Editor, where depending on the logic that is being done in our code it alternates between Sub-Editors like the Blueprint Editor, Sound Editor, Animation Editor etc. However, in the development of our system we use only the level editor and the blueprint editor.

The Level Editor interface is divided into seven parts as shown in figure A.16.

1. **(a)Tab Bar and (b)Menu Bar**: (a) The name of the current level is displayed in a tab along the top of the Level Editor. Similar to a web browser, tabs from other editor windows may be docked next to this tab for quick and simple navigation. (b) Access to the standard tools and commands used while interacting with levels in the editor is provided through this menu.

2. **Toolbar**: A list of commands is displayed on the Toolbar panel, giving users easy access to frequently used tools and functions.

3. **Place Actor / Modes**: You can switch the Level Editor's mode to a number of settings that make different activities easier using the Modes Panel. These activities involve dragging and dropping things into your level, giving them color and texture, changing their geometry, customizing the level's landscape, and including foliage, or plant life, in your level.

4. **Viewports**: You can see a visual representation of your game with the Viewport. Along with characters and items that players will see in the game, you will see a representation of the setting you design. Additionally, you will be able to see several items in the Viewport that you won't be able to see in-game, including cameras, event triggers, and invisible boundaries. Additionally, using the Viewport, you can directly manipulate items.

5. **Content Browser** : The Content Browser is where you save and organize any content you want to include in your game. Meshes, materials, music, sound effects, visual effects, and other types of content are included in this. The Unreal Editor allows users to directly create several forms of content.

6. **World Outliner**: The World Outliner is used to list and organize the items in your Level so that they are simple to identify and pick when you want to update them.

7. **Details**: The details of the currently selected object, including the object's size and placement, can be seen and modified in the Details Panel.

Figure A.16: Unreal Level Editor Interface.

A.4.3 Scripting in Unreal Engine

For developing new game assets, Unreal provides two techniques: Blueprint Visual Scripting and C++. A level or game's custom gameplay can be created using C++'s underlying game systems, on top of which designers can develop. In these scenarios, the designer works in the Blueprint Editor in Unreal Engine 4, while the C++ programmer utilizes a text editor (like Notepad++) or IDE (often Microsoft Visual Studio).

Both systems have the game API and framework classes, which can be used individually, but show their true potential when used together to support each other. Unreal's goal is for programmers to implement all the most important functionalities in C++; then, these functionalities will be used by designers as blueprint sub-systems, where they give the appropriate functionality to the proposed simulation.

Having said that, let's look at an example of a typical C++ programmer's work flow when producing design-related building blocks. The fundamental

design of an Actor code is demonstrated in the code below. In C++ the structure of the code is segmented in two parts, the first one is the header (.h) which is where the classes, functions and variables are defined.

```
#pragma once
#include "CoreMinimal.h"
#include "GameFramework/Actor.h"
#include "MyActor.generated.h"
UCLASS()
class BOOKTEMPLATE_API AMyActor: public AActor
{
    GENERATED_BODY()
public:
    // Sets default values for this actor's properties
    AMyActor();
protected:
    // Called when the game starts or when spawned
    virtual void BeginPlay() override;
public:
    // Called every frame
    virtual void Tick(float DeltaTime) override;
};
```

The other part is the source code (.cpp) which is where the implementation of the code previously defined in the header is done.

```
#include "MyActor.h"
AMyActor::AMyActor()
{
    PrimaryActorTick.bCanEverTick = true;
}
void AMyActor::BeginPlay()
{
    Super::BeginPlay();
    UE_LOG(LogTemp, Warning, TEXT("Hello World"));
}
void AMyActor::Tick(float DeltaTime)
{
    Super::Tick(DeltaTime);
}
```

All code created in C++ to be used in Unreal Editor must be associated to a Blueprint. This Blueprint must be associated to an Actor element within each Unreal Editor Level. Finally, the result of each functionality implemented in C++ has to be read through a Blueprint to be seen in the graphical interface of the Level at the time of execution of the simulation.

Unreal Blueprints

A Blueprint is an asset in the Unreal Engine that includes information and instructions. Blueprints can be divided into two categories: level blueprints and blueprint classes.

A **Level Blueprint** is used to store information and guidelines for that Level. It may contain information on how much time is left to finish the Level, how many keys you have gathered so far, and so forth. Additionally, instructions specific to that Level are stored there.

Blueprint Classes are a way to transform any Actor or asset into a Blueprint. The engine comes with several pre-defined Blueprint Classes, such as Pawn, Character, Player Controller, Base Game Mode, etc. However, you can also create your own Blueprint Classes, by means of C++ classes, where we can create additional functionalities to each actor to interact with the environment as it is more convenient for us.

As in the case of the Unreal Editor, there is also a Blueprint Editor in which the only thing that changes is the Viewport interface for a canvas called Event Graph, in which each functionality will be graphically invoked as a node.

The section of a Blueprint where the logic is scripted is called the **Event Graph**. The logic can be written in C++ pure code if you're a programmer. However, Epic Games has created a visual scripting system that can be useful even for seasoned programmers and enables non-programmers to script logic.

The scripting system works by using a variety of **Nodes**, each of which has a different function, and connecting them together. Figure A.17.a illustrates how the Level Blueprint initially has two widely used Nodes, which compose the life cycle of each Actor, such as the *Event BeginPlay*, which is executed only once the game is started, and the *Event Tick,* which is the loop where the Actor's functionality is implemented within the Level. These are initially deactivated, and can be used directly by joining them to another Node. These same nodes are equivalent to the C++ classes with the same name.

Depending on the type of Node, they have one or several inputs or outputs, which can be sequentially interconnected with each other, if they are the same type of variables as shown in figure A.17.b.

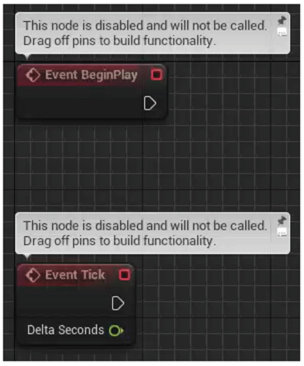

(a)

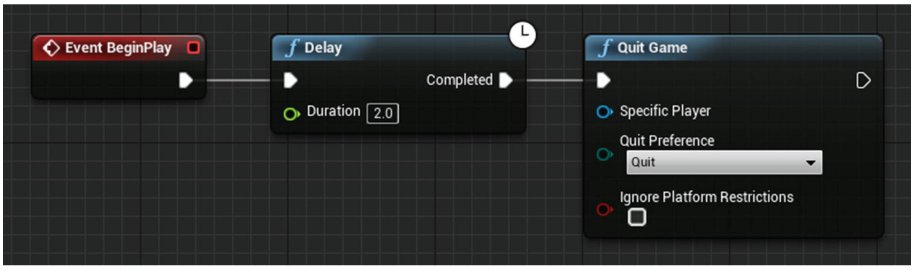

(b)

Figure A.17: (a) illustrates starting Blueprint Nodes, and the (b) illustrates sequentially Interconnected Nodes.

Blueprint logic is much more difficult to control than in C++, because as methods with more complex functionality are implemented, the connection of the nodes becomes too convoluted (see figure A.18), which makes it very difficult to debug the code. Therefore, it is recommended to use Blueprint only when it is strictly necessary, and to use C++ classes for most of the logic, both for performance and order reasons.

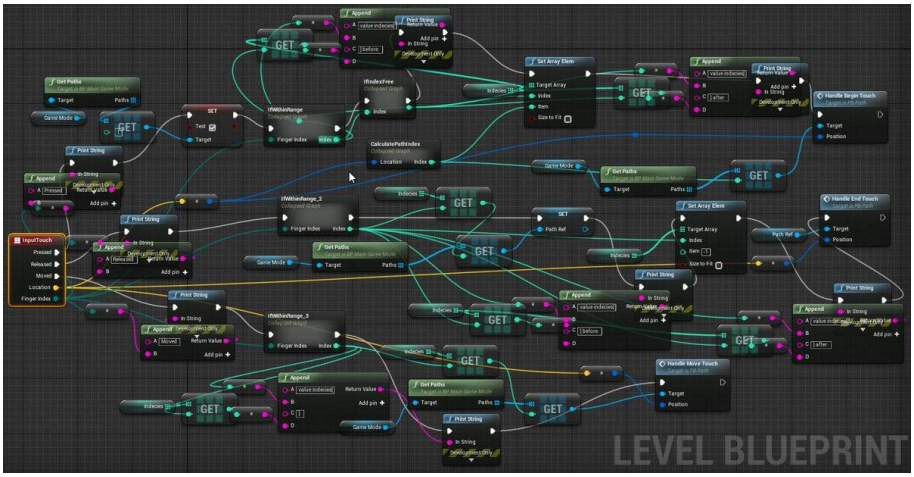

Figure A.18: Example of a complex logic with BluePrints.

References

[1] INE, URL https://www.ine.es, 2022.

[2] ITU-R, "IMT vision – framework and overall objectives of the future development of IMT for 2020 and beyond," ITU, Recommendation M.2083-0, Sep. 2015.

[3] M. Shafi, A. F. Molisch, P. J. Smith, T. Haustein, P. Zhu, P. De Silva, F. Tufvesson, A. Benjebbour, and G. Wunder, "5G: A tutorial overview of standards, trials, challenges, deployment, and practice," *IEEE Journal on Selected Areas in Communications*, vol. 35, no. 6, pp. 1201–1221, Jun. 2017.

[4] T. S. Rappaport, Y. Xing, G. R. MacCartney, A. F. Molisch, E. Mellios, and J. Zhang, "Overview of millimeter wave communications for fifth-generation (5G) wireless networks—with a focus on propagation models," *IEEE Transactions on Antennas and Propagation*, vol. 65, no. 12, pp. 6213–6230, Aug. 2017.

[5] F. Boccardi, R. W. Heath, A. Lozano, T. L. Marzetta, and P. Popovski, "Five disruptive technology directions for 5G," *IEEE Communications Magazine*, vol. 52, no. 2, pp. 74–80, Feb. 2014.

[6] P. Marsch, Ö. Bulakci, O. Queseth, and M. Boldi, *5G System Design: Architectural and Functional Considerations and Long Term Research*. Wiley, 2018.

[7] ITU-R, "Spectrum requirements for international mobile telecommunications 2000 (IMT-2000)," ITU, Recommendation M.2023, May 2000.

[8] ITU-R, "Minimum requirements related to technical performance for IMT-2020 radio interface(s)," ITU, Recommendation M.2410-0, Nov. 2017.

[9] S. E. Elayoubi, M. Fallgren, P. Spapis, G. Zimmermann, D. Martín-Sacristán, C. Yang, S. Jeux, P. Agyapong, L. Campoy, Y. Qi *et al.*, "5G service requirements and operational use cases: Analysis and METIS II vision," in *2016 European Conference on Networks and Communications (EuCNC)*, Sep. 2016, pp. 158–162.

[10] A. Osseiran, J. F. Monserrat, and P. Marsch, *5G mobile and wireless communications technology*. Cambridge University Press, 2016.

[11] ITU-R, "Future technology trends of terrestrial IMT systems," ITU, Recommendation M.2320-0, Nov. 2014.

[12] S. M. Razavizadeh, M. Ahn, and I. Lee, "Three-dimensional beamforming: A new enabling technology for 5G wireless networks," *IEEE Signal Processing Magazine*, vol. 31, no. 6, pp. 94–101, Nov. 2014.

[13] G. Fodor, N. Rajatheva, W. Zirwas, L. Thiele, M. Kurras, K. Guo, A. Tolli, J. H. Sorensen, and E. d. Carvalho, "An overview of massive MIMO technology components in METIS," *IEEE Communications Magazine*, vol. 55, no. 6, pp. 155–161, Jun. 2017.

[14] E. Björnson, J. Hoydis, and L. Sanguinetti, "Massive mimo has unlimited capacity," *IEEE Transactions on Wireless Communications*, vol. 17, no. 1, pp. 574–590, 2018.

[15] M. G. Sarret, G. Berardinelli, N. H. Mahmood, M. Fleischer, P. Mogensen, and H. Heinz, "Analyzing the potential of full duplex in 5G ultra-dense small cell networks," *EURASIP Journal on Wireless Communications and Networking*, vol. 2016, article no. 284, pp. 1–16, Dec. 2016.

[16] F. M. Kabonzo and M. U. Dilshad, "Impact of radio over fiber technology for integrated 5G front and back-haul applications," in *2017 IEEE 2nd Advanced Information Technology, Electronic and Automation Control Conference (IAEAC)*, 2017, pp. 1077–1081.

[17] K. Tekkouk, J. Hirokawa, M. Ando, and R. Sauleau, "Continuous beam steering antenna with large 2d coverage for 5G applications," in *2017 IEEE International Symposium on Antennas and Propagation USNC/URSI National Radio Science Meeting*, 2017, pp. 243–244.

[18] T. Pham, J. Weng, K. Pham, F. Gallée, and R. Sauleau, "V-band beam-switching transmitarray antenna for 5G mimo channel sounding," in *2019 13th European Conference on Antennas and Propagation (EuCAP)*, 2019, pp. 1–5.

[19] S. Rizvi, A. Aziz, M. T. Jilani, N. Armi, G. Muhammad, and S. H. Butt, "An investigation of energy efficiency in 5G wireless networks," in *2017 International Conference on Circuits, System and Simulation (ICCSS)*, 2017, pp. 142–145.

[20] J. Lee, E. Tejedor, K. Ranta-aho, H. Wang, K. Lee, E. Semaan, E. Mohyeldin, J. Song, C. Bergljung, and S. Jung, "Spectrum for 5G: Global status, challenges, and enabling technologies," *IEEE Communications Magazine*, vol. 56, no. 3, pp. 12–18, Mar. 2018.

[21] S. Chen and J. Zhao, "The requirements, challenges, and technologies for 5G of terrestrial mobile telecommunication," *IEEE Communications Magazine*, vol. 52, no. 5, pp. 36–43, May 2014.

[22] E. Dahlman, S. Parkvall, and J. Skold, *5G NR: The next generation wireless access technology*. Academic Press, Mar. 2018.

[23] Y. Wang, J. Li, L. Huang, Y. Jing, A. Georgakopoulos, and P. Demestichas, "5G mobile: Spectrum broadening to higher-frequency bands to support high data rates," *IEEE Vehicular Technology Magazine*, vol. 9, no. 3, pp. 39–46, Sep. 2014.

[24] G. Ancans, V. Bobrovs, A. Ancans, and D. Kalibatiene, "Spectrum considerations for 5G mobile communication systems," *Procedia Computer Science*, vol. 104, pp. 509–516, 2017, iCTE 2016, Riga Technical University, Latvia. [Online]. Available: https://www.sciencedirect.com/science/article/pii/S1877050917301679

[25] METIS, "METIS channel models," METIS, Deliverable D1.4, Feb. 2012.

[26] M. S. Kumari and N. Kumar, "Channel model for simultaneous backhaul and access for mmwave 5G outdoor street canyon channel," *Springer Science+Business Media,*, 2018. [Online]. Available: https://link.springer.com/article/10.1007/s11276-020-02421-0#citeas

[27] S. Sun, T. S. Rappaport, S. Rangan, T. A. Thomas, A. Ghosh, I. Z. Kovacs, I. Rodriguez, O. Koymen, A. Partyka, and J. Jarvelainen, "Propagation path loss models for 5G urban micro- and macro-cellular scenarios," in *2016 IEEE 83rd Vehicular Technology Conference (VTC Spring)*, 2016, pp. 1–6.

[28] L. Wang, L. Ma, Z. Bao, Y. Hou, Y. Li, and X. Wang, "Research on d2d communication technology in the 5G smart grid scenario," in *2021 IEEE 4th International Conference on Computer and Communication Engineering Technology (CCET)*, 2021, pp. 345–349.

[29] 3GPP, "Study on channel model for frequencies from 0.5 to 100 GHz (release 14)," in *3GPP, report TR 38.901 V14.1.1*, 2017.

[30] J. Kunisch and J. Pamp, "Ultra-wideband double vertical knife-edge model for obstruction of a ray by a person," in *2008 IEEE International Conference on Ultra-Wideband*, vol. 2, 2008, pp. 17–20.

[31] M. Jacob, S. Priebe, T. Kürner, M. Peter, M. Wisotzki, R. Felbecker, and W. Keusgen, "Extension and validation of the IEEE 802.11ad 60 GHz human blockage model," in *2013 7th European Conference on Antennas and Propagation (EuCAP)*, 2013, pp. 2806–2810.

[32] P. C. J. S. Lu, D. Steinbach, "Modeling human blockers in millimeter wave radio links," in *ZTE Commun*, vol. 10, 2012, pp. 23–28.

[33] G. R. MacCartney, S. Deng, S. Sun, and T. S. Rappaport, "Millimeter-wave human blockage at 73 GHz with a simple double knife-edge diffraction model and extension for directional antennas," in *2016 IEEE 84th Vehicular Technology Conference (VTC-Fall)*, 2016, pp. 1–6.

[34] M. Jacob, S. Priebe, A. Maltsev, A. Lomayev, V. Erceg, and T. Kürner, "A ray tracing based stochastic human blockage model for the IEEE 802.11ad 60 GHz channel model," in *Proceedings of the 5th European Conference on Antennas and Propagation (EUCAP)*, 2011, pp. 3084–3088.

[35] X. Chen, L. Tian, P. Tang, and J. Zhang, "Modelling of human body shadowing based on 28 GHz indoor measurement results," in *2016 IEEE 84th Vehicular Technology Conference (VTC-Fall)*, 2016, pp. 1–5.

[36] N. Tran, T. Imai, and Y. Okumura, "Study on characteristics of human body shadowing in high frequency bands: Radio wave propagation technology for future radio access and mobile optical networks," in *2014 IEEE 80th Vehicular Technology Conference (VTC2014-Fall)*, 2014, pp. 1–5.

[37] R. Luebbers, "Finite conductivity uniform gtd versus knife edge diffraction in prediction of propagation path loss," *IEEE Transactions on Antennas and Propagation*, vol. 32, no. 1, pp. 70–76, 1984.

[38] H. Wang and T. Rappaport, "A parametric formulation of the utd diffraction coefficient for real-time propagation prediction modeling," *IEEE Antennas and Wireless Propagation Letters*, vol. 4, pp. 253–257, 2005.

[39] M. Jacob, S. Priebe, R. Dickhoff, T. Kleine-Ostmann, T. Schrader, and T. Kurner, "Diffraction in mm and sub-mm wave indoor propagation channels," *IEEE Transactions on Microwave Theory and Techniques*, vol. 60, no. 3, pp. 833–844, 2012.

[40] M. Ghaddar, "Human body modelling for prediction of effect of people on indoor propagation channel," *Ieexplore Journal*, vol. 40, pp. 1592–1594, 2004.

[41] M. Ghaddar, L. Talbi, T. A. Denidni, and A. Sebak, "A conducting cylinder for modeling human body presence in indoor propagation channel," *IEEE Transactions on Antennas and Propagation*, vol. 55, no. 11, pp. 3099–3103, 2007.

[42] M. Jacob, S. Priebe, T. Kürner, M. Peter, M. Wisotzki, R. Felbecker, and W. Keusgen, "Fundamental analyses of 60 GHz human blockage," in *2013 7th European Conference on Antennas and Propagation (EuCAP)*, 2013, pp. 117–121.

[43] M. Peter, M. Wisotzki, M. Raceala-Motoc, W. Keusgen, R. Felbecker, M. Jacob, S. Priebe, and T. Kürner, "Analyzing human body shadowing at 60 GHz: Systematic wideband mimo measurements and modeling approaches," in *2012 6th European Conference on Antennas and Propagation (EUCAP)*, 2012, pp. 468–472.

[44] G. L. James, "Geometrical theory of diffraction for electromagnetic waves." in *Stevenage, U.K.: Peregrinus*, 1976, p. 6.

[45] M. Abramowitz and I. A. Stegun, "Ahandbook of mathematical functions with formulas, graphs, and mathematical tables," *Ieexplore Journal*, vol. 4, 1964.

[46] H.-T. Kim and N. Wang, "Utd solution for electromagnetic scattering by a circular cylinder with thin lossy coatings," *IEEE Transactions on Antennas and Propagation*, vol. 37, no. 11, pp. 1463–1472, 1989.

[47] T. B. A. Senior and J. L. Volakis, "Approximate boundary conditions in electromagnetics." in *Institution of Electrical Engineers, London, U.K*, 1995.

[48] B. R. Levy, "Diffraction by an elliptic cylinder," in *[Online]. Available: http://www.jstor.org/stable/24900530*, vol. 9, no. 2, Nov. 1960, p. 147–165.

[49] M. Yokota, T. Ikegamai, Y. Ohta, and T. Fujii, "Numerical examination of em wave shadowing by human body," in *Proceedings of the Fourth European Conference on Antennas and Propagation*, 2010, pp. 1–4.

[50] A. G. Aguilar, P. H. Pathak, and M. Sierra-Pérez, "A canonical utd solution for electromagnetic scattering by an electrically large impedance circular cylinder illuminated by an obliquely incident plane wave," *IEEE Transactions on Antennas and Propagation*, vol. 61, no. 10, pp. 5144–5154, 2013.

[51] P. Karadimas, B. Allen, and P. Smith, "Human body shadowing characterization for 60-GHz indoor short-range wireless links," *IEEE Antennas and Wireless Propagation Letters*, vol. 12, pp. 1650–1653, 2013.

[52] G. R. MacCartney, T. S. Rappaport, and S. Rangan, "Rapid fading due to human blockage in pedestrian crowds at 5G millimeter-wave frequencies," in *GLOBECOM 2017 - 2017 IEEE Global Communications Conference*, 2017, pp. 1–7.

[53] M. Peter, K. Haneda, S. Nguyen, A. Karttunen, and J. Järveläinen, "Measurement results and final mmmagic channel models," *Deliverable D2*, vol. 2, p. 12, 2017.

[54] 3GPP TSG RAN, "Study on channel model for frequencies from 0.5 to 100 GHz," 3GPP, TR 38.901 V14.0.0, May 2017.

[55] R. L. Haupt and Y. Rahmat-Samii, "Antenna array developments: A perspective on the past, present and future," *IEEE Antennas and Propagation Magazine*, vol. 57, no. 1, pp. 86–96, 2015.

[56] G. A. Deschamps, "Microstrip microwave antennas," *3rd USAF Symp.on Antennas*, vol. 1, no. 1, p. 1, 1953.

[57] D. Berry, R. Malech, and W. Kennedy, "The reflectarray antenna," *IEEE Transactions on Antennas and Propagation*, vol. 11, no. 6, pp. 645–651, 1963.

[58] D. Pozar, S. Targonski, and H. Syrigos, "Design of millimeter wave microstrip reflectarrays," *IEEE Transactions on Antennas and Propagation*, vol. 45, no. 2, pp. 287–296, 1997.

[59] J. Huang and J. A. Encinar, "Reflectarray antennas," *NY, USA: Wiley-IEEE*, vol. 1, no. 1, p. 1, 2008.

[60] C. Balanis, "Analysis of an array of line sources above a finite ground plane," *IEEE Transactions on Antennas and Propagation*, vol. 19, no. 2, pp. 181–185, 1971.

[61] C. A. Balanis, *Antenna theory: analysis and design*. John wiley & sons, 2015.

[62] G. James and V. Kerdemelidis, "Reflector antenna radiation pattern analysis by equivalent edge currents," *IEEE Transactions on Antennas and Propagation*, vol. 21, no. 1, pp. 19–24, 1973.

[63] C. Mentzer and L. Peters, "A gtd analysis of the far-out sidelobes of cassegrain antennas," *IEEE Transactions on Antennas and Propagation*, vol. 23, no. 5, pp. 702–709, 1975.

[64] L. LaLonde and D. Harris, "A high-performance line source feed for the aio spherical reflector," *IEEE Transactions on Antennas and Propagation*, vol. 18, no. 1, pp. 41–48, 1970.

[65] A. Rudge and N. Adatia, "Offset-parabolic-reflector antennas: A review," *Proceedings of the IEEE*, vol. 66, no. 12, pp. 1592–1618, 1978.

[66] P. Clarricoats and G. Poulton, "High-efficiency microwave reflector antennas - a review," *Proceedings of the IEEE*, vol. 65, no. 10, pp. 1470–1504, 1977.

[67] P. Castleberg and K. Xilouris, "The arecibo observatory," *IEEE Potentials*, vol. 16, no. 3, pp. 33–35, 1997.

[68] W. Lin, Y. Zhang, G. Gao, H. Liu, and X. Yuan, "Fast telescope optical transmission system based on delta-sigma modulation," in *2020 IEEE International Symposium on Broadband Multimedia Systems and Broadcasting (BMSB)*, 2020, pp. 1–5.

[69] O. Hachenberg, B. Grahl, and R. Wielebinski, "The 100-meter radio telescope at effelsberg," *Proceedings of the IEEE*, vol. 61, no. 9, pp. 1288–1295, 1973.

[70] M. S. Gatti, "A phased array antenna for deep space communications," in *2008 IEEE Aerospace Conference*, 2008, pp. 1–8.

[71] R. J. Mailloux, "Phased array antenna handbook," *2nd Edn, Artech House*, vol. 1, no. 1, p. 1, 2005.

[72] M. I. Skolnik, "Radar handbook,," *3rd Edn, McGraw-Hill*, vol. 1, no. 1, p. 1, 2005.

[73] R. Munson, "Microstrip reflectarray for satellite communication and radar cross-section enhancement or reduction," *U.S. patent 4684952, Washington D. C*, vol. 1, no. 1, p. 1, 1987.

[74] Z. Pi and F. Khan, "An introduction to millimeter-wave mobile broadband systems," *IEEE Communications Magazine*, vol. 49, no. 6, pp. 101–107, 2011.

[75] J. S. Romero-Peña and N. Cardona, "Applicability limits of simplified human blockage models at 5G mm-wave frequencies," in *2019 13th European Conference on Antennas and Propagation (EuCAP)*, 2019, pp. 1–5.

[76] T. S. Rappaport, S. Sun, R. Mayzus, H. Zhao, Y. Azar, K. Wang, G. N. Wong, J. K. Schulz, M. Samimi, and F. Gutierrez, "Millimeter wave mobile communications for 5G cellular: It will work!" *IEEE Access*, vol. 1, pp. 335–349, 2013.

[77] H. Zhao, R. Mayzus, S. Sun, M. Samimi, J. K. Schulz, Y. Azar, K. Wang, G. N. Wong, F. Gutierrez, and T. S. Rappaport, "28 GHz millimeter wave cellular communication measurements for reflection and penetration loss in and around buildings in New York city," in *2013 IEEE International Conference on Communications (ICC)*, Jun. 2013, pp. 5163–5167.

[78] K. Du, O. Ozdemir, F. Erden, and I. Guvenc, "Sub-terahertz and mmwave penetration loss measurements for indoor environments," in *2021 IEEE International Conference on Communications Workshops (ICC Workshops)*, 2021, pp. 1–6.

[79] T. Singal, "Wireless communications." *Tata McGraw-Hill Education,*, vol. 1, no. 1, p. 1, 2010.

[80] A. Kajiwara, "Line-of-sight indoor radio communication using circular polarized waves," *IEEE Transactions on Vehicular Technology*, vol. 44, no. 3, pp. 487–493, Aug. 1995.

[81] J. Pascual-García, J. Molina-García-Pardo, M. Martínez-Inglés, J. Rodríguez, and N. Saurín-Serrano, "On the importance of diffuse scattering model parameterization in indoor wireless channels at mm-Wave frequencies," *IEEE Access*, vol. 4, pp. 688–701, Feb. 2016.

[82] F. Sheikh, D. Lessy, M. Alissa, and T. Kaiser, "A comparison study of non-specular diffuse scattering models at terahertz frequencies," in *2018 First International Workshop on Mobile Terahertz Systems (IWMTS)*, Jul. 2018, pp. 1–6.

[83] J. Jürvelüinen and K. Haneda, "Sixty gigahertz indoor radio wave propagation prediction method based on full scattering model," *Radio Science*, vol. 49, no. 4, pp. 293–305, Apr. 2014.

[84] Y. Yaman and P. Spasojevic, "A ray-tracing intracluster model with diffuse scattering for mmwave communications," *IEEE Antennas and Wireless Propagation Letters*, vol. 20, no. 5, pp. 653–657, 2021.

[85] V. Degli-Esposti, "A diffuse scattering model for urban propagation prediction," *IEEE Transactions on Antennas and Propagation*, vol. 49, no. 7, pp. 1111–1113, Jul. 2001.

[86] V. Degli-Esposti, F. Fuschini, E. M. Vitucci, and G. Falciasecca, "Measurement and modelling of scattering from buildings," *IEEE Transactions on Antennas and Propagation*, vol. 55, no. 1, pp. 143–153, Jan. 2007.

[87] N. Blaunstein and J. B. Andersen, *Multipath Phenomena in Cellular Networks*. Artech House, Jun. 2002.

[88] M. M. Ahamed and S. Faruque, "Propagation factors affecting the performance of 5G millimeter wave radio channel," in *2016 IEEE International Conference on Electro Information Technology (EIT)*, May 2016, pp. 728–733.

[89] Y. Rahmat-Samii, "GTD, UTD, UAT and STD: A historical revisit," *2012 IEEE-APS Topical Conference on Antennas and Propagation in Wireless Communications (APWC)*, pp. 1145–1148, Oct. 2012.

[90] J. G. Andrews, S. Buzzi, W. Choi, S. V. Hanly, A. Lozano, A. C. Soong, and J. C. Zhang, "What will 5G be?" *IEEE Journal on selected areas in communications*, vol. 32, no. 6, pp. 1065–1082, Jun. 2014.

[91] M. K. Samimi, T. S. Rappaport, and G. R. MacCartney, "Probabilistic omnidirectional path loss models for millimeter-wave outdoor communications," *IEEE Wireless Communications Letters*, vol. 4, no. 4, pp. 357–360, Aug. 2015.

[92] ITU-R, "Guidelines for evaluation of radio interface technologies for IMT-2020," ITU, Recommendation M.2412-0, Oct. 2017.

[93] S. Jaeckel, M. Peter, K. Sakaguchi, W. Keusgen, and J. Medbo, "5G channel models in mm-wave frequency bands," in *European Wireless 2016; 22th European Wireless Conference*, 2016, pp. 1–6.

[94] C.-. WINNER+, "Winner+ final channel models," *Deliverable 5.3 Version 1*, vol. 1, no. 1, p. 1, 2010.

[95] F. Ademaj, M. Taranetz, and M. Rupp, "Implementation, validation and application of the 3GPP 3D MIMO channel model in open source simulation tools," in *2015 International Symposium on Wireless Communication Systems (ISWCS)*, 2015, pp. 721–725.

[96] M. Döttling, W. Mohr, and A. Osseiran, "Winner ii channel models," *Radio Technologies and Concepts for IMT-Advanced*, pp. 39–92, 2010.

[97] G. Liang and H. L. Bertoni, "A new approach to 3-D ray tracing for propagation prediction in cities," *IEEE Transactions on Antennas and Propagation*, vol. 46, no. 6, pp. 853–863, Jun. 1998.

[98] M. project. MiWEBA project homepage. [Online]. Available: http://www.miweba.eu(FP7-ICT-2013-EU-Japan,projectnumber:608637)

[99] METIS, "METIS Simulation Resources," 2015. [Online]. Available: URL{https://metis2020.com/documents/simulations/index.html}

[100] L. R. S. Jaeckel and L. Thiele, "Quasi deterministic radio channel generator user manual and documentation (v2.2.0)," *https://quadriga-channel-model.de*, vol. 1, no. 1, p. 1, 2019.

[101] T. S. Rappaport, G. R. MacCartney, S. Sun, H. Yan, and S. Deng, "Small-scale, local area, and transitional millimeter wave propagation for 5G communications," *IEEE Transactions on Antennas and Propagation*, vol. 65, no. 12, pp. 6474–6490, Dec. 2017.

[102] M. Tesanovic and M. Nekovee, "mmwave-based mobile access for 5G: Key challenges and projected standards and regulatory roadmap," in *2015 IEEE Global Communications Conference (GLOBECOM)*, 2015, pp. 1–6.

[103] C. Gustafson and F. Tufvesson, "Characterization of 60 GHz shadowing by human bodies and simple phantoms," in *2012 6th European Conference on Antennas and Propagation (EUCAP)*, 2012, pp. 473–477.

[104] U. T. Virk and K. Haneda, "Modeling human blockage at 5G millimeter-wave frequencies," *IEEE Transactions on Antennas and Propagation*, vol. 68, no. 3, pp. 2256–2266, 2020.

[105] B. Davis and G. Brown, "Diffraction by a randomly rough knife edge," in *IEEE Antennas and Propagation Society International Symposium. 1998 Digest. Antennas: Gateways to the Global Network. Held in conjunction with: USNC/URSI National Radio Science Meeting (Cat. No.98CH36*, vol. 2, 1998, pp. 892 vol.2–.

[106] X. Zhao, Q. Wang, S. Li, S. Geng, M. Wang, S. Sun, and Z. Wen, "Attenuation by human bodies at 26- and 39.5-GHz millimeter wavebands," *IEEE Antennas and Wireless Propagation Letters*, vol. 16, pp. 1229–1232, 2017.

[107] J. S. Romero-Peña and N. Cardona, "Applicability limits of simplified human blockage models at 5G mm-wave frequencies," in *2019 13th European Conference on Antennas and Propagation (EuCAP)*, 2019, pp. 1–5.

[108] 3DS. CST electromagnetic suite studio. [Online]. Available: https://www.3ds.com/products-services/simulia/products/cst-studio-suite/

[109] sagemillimeter. SAR-2309-28-s2, WR-28. [Online]. Available: https://www.sagemillimeter.com/content/datasheets/SAR-2309-28-S2.pdf

[110] N. Wiener, *Extrapolation, Interpolation, and Smoothing of Stationary Time Series: With Engineering Applications*. John wiley & sons, 1964.

[111] C. J.Barder, *Wave propagation modeling in closed enviroment within the mmWave band*. Institut fur Hochstfrequenztechnik und Electronik, 1995.

[112] J. McKown and R. Hamilton, "Ray tracing as a design tool for radio networks," *IEEE Network*, vol. 5, no. 6, pp. 27–30, 1991.

[113] T. Bai, A. Alkhateeb, and R. W. Heath, "Coverage and capacity of millimeter-wave cellular networks," *IEEE Communications Magazine*, vol. 52, no. 9, pp. 70–77, 2014.

[114] A. Ghosh, T. A. Thomas, M. C. Cudak, R. Ratasuk, P. Moorut, F. W. Vook, T. S. Rappaport, G. R. MacCartney, S. Sun, and S. Nie, "Millimeter-wave enhanced local area systems: A high-data-rate approach for future wireless networks," *IEEE Journal on Selected Areas in Communications*, vol. 32, no. 6, pp. 1152–1163, 2014.

[115] J. Bae, Y. S. Choi, J. S. Kim, and M. Y. Chung, "Architecture and performance evaluation of mmwave based 5G mobile communication system," in *2014 International Conference on Information and Communication Technology Convergence (ICTC)*. IEEE, 2014, pp. 847–851.

[116] A. I. Sulyman, A. T. Nassar, M. K. Samimi, G. R. MacCartney, T. S. Rappaport, and A. Alsanie, "Radio propagation path loss models for 5G cellular networks in the 28 GHz and 38 GHz millimeter-wave bands," *IEEE communications magazine*, vol. 52, no. 9, pp. 78–86, 2014.

[117] D. D. Falconer and J.-P. DeCruyenaere, "Coverage enhancement methods for LMDS," *IEEE Communications Magazine*, vol. 41, no. 7, pp. 86–92, 2003.

[118] T. S. Rappaport, S. Sun, R. Mayzus, H. Zhao, Y. Azar, K. Wang, G. N. Wong, J. K. Schulz, M. Samimi, and F. Gutierrez, "Millimeter wave mobile communications for 5G cellular: It will work!" *IEEE access*, vol. 1, pp. 335–349, May 2013.

[119] Y. Azar, G. N. Wong, K. Wang, R. Mayzus, J. K. Schulz, H. Zhao, F. Gutierrez, D. Hwang, and T. S. Rappaport, "28 GHz propagation measurements for outdoor cellular communications using steerable beam antennas in new york city," in *2013 IEEE international conference on communications (ICC)*. IEEE, 2013, pp. 5143–5147.

[120] Q. Wu, Y. D. Zhang, F. Ahmad, and M. G. Amin, "Compressive-sensing-based high-resolution polarimetric through-the-wall radar imaging exploiting target characteristics," *IEEE Antennas and Wireless Propagation Letters*, vol. 14, pp. 1043–1047, 2014.

[121] F. Chatzigeorgiadis, "Development of code for a physical optics radar cross section prediction and analysis application," NAVAL POSTGRADUATE SCHOOL MONTEREY CA, Tech. Rep., 2004.

[122] V. Manohar, J. M. Kovitz, and Y. Rahmat-Samii, "Synthesis and analysis of low profile, metal-only stepped parabolic reflector antenna," *IEEE Transactions on Antennas and Propagation*, vol. 66, no. 6, pp. 2788–2798, 2018.

[123] J. Bjornholt, G. Hamman, and S. Miller, "Electronic fence using high-resolution millimeter-wave radar in conjunction with multiple passive reflectors," Oct. 15 2002, uS Patent 6,466,157.

[124] C. Bredin, J. Goutoule, R. Sanchez, B. Richards, D. Hall, J. Aguttes, and T. Amiot, "High resolution sar micro-satellite based on passive reflectors," in *IGARSS 2004. 2004 IEEE International Geoscience and Remote Sensing Symposium*, vol. 2, 2004, pp. 1196–1199.

[125] J. Gómez, A. Tayebi, J. de Lucas, and F. Cátedra, "Metal-only fresnel zone plate antenna for millimetre-wave frequency bands," *IET Microwaves, Antennas & Propagation*, vol. 8, no. 6, pp. 445–450, 2014.

[126] S. K. Sharma, S. Rao, and L. Shafai, *Handbook of reflector antennas and feed systems volume I: theory and design of reflectors.* Artech House, 2013.

[127] T. A. Milligan, *Modern antenna design.* John Wiley & Sons, 2005.

[128] Ticra. GRASP - analysis and design of reflector antenna systems. [Online]. Available: https://www.ticra.com/software/grasp/

[129] Ansys. HFSS - 3D electromagnetic field simulator for rf and wireless design. [Online]. Available: https://www.ansys.com/products/electronics/ansys-hfss

[130] B. Foundation. Blender- open source 3D creation suite. [Online]. Available: https://www.blender.org/about/

[131] Formlabs. FORM3L- 3D resin printer. [Online]. Available: https://formlabs.com/es/3d-printers/form-3l/

[132] Cuptronic. Cuptronic is an adhesion-promotion company. [Online]. Available: http://cuptronic.com/applications/printed-circuit-boards/high-frequency/

[133] S. Li, Y. Liu, L. Lin, D. Sun, S. Yang, and X. Sun, "Simulation and modeling of millimeter-wave channel at 60 GHz in indoor environment for 5G wireless communication system," in *2018 IEEE International Conference on Computational Electromagnetics ([ICCEM).* IEEE, 2018, pp. 1–3.

[134] J. Lee, K.-W. Kim, M.-D. Kim, and J.-J. Park, "32-GHz outdoor-to-indoor channel measurement of propagation losses and delay spread," in *2019 IEEE International Symposium on Antennas and Propagation and USNC-URSI Radio Science Meeting.* IEEE, 2019, pp. 2071–2072.

[135] G. R. Maccartney, T. S. Rappaport, S. Sun, and S. Deng, "Indoor office wideband millimeter-wave propagation measurements and channel models at 28 and 73 GHz for ultra-dense 5G wireless networks," *IEEE access*, vol. 3, pp. 2388–2424, 2015.

[136] J. O. Lacruz, R. R. Ortiz, and J. Widmer, "A real-time experimentation platform for sub-6 GHz and millimeter-wave MIMO systems," in *Proceedings of the 19th Annual International Conference on Mobile Systems, Applications, and Services*, 2021, pp. 427–439.

[137] R. Rudd, X. Meng, V. Ocheri, D. Wu, and M. Nekovee, "Joint statistics of urban clutter loss and building entry loss at 3.5 GHz and 27 GHz-from measurement to modelling," in *2020 14th European Conference on Antennas and Propagation (EuCAP)*. IEEE, 2020, pp. 1–5.

[138] S. Hur, S. Baek, B. Kim, J. Park, A. F. Molisch, K. Haneda, and M. Peter, "28 GHz channel modeling using 3d ray-tracing in urban environments," in *2015 9th European Conference on Antennas and Propagation (EuCAP)*. IEEE, 2015, pp. 1–5.

[139] K. Kimura and J. Horikoshi, "Prediction of millimeter-wave multipath propagation characteristics in mobile radio environment," *IEICE transactions on electronics*, vol. 82, no. 7, pp. 1253–1259, 1999.

[140] V. Degli-Esposti, F. Fuschini, E. M. Vitucci, M. Barbiroli, M. Zoli, L. Tian, X. Yin, D. A. Dupleich, R. Müller, C. Schneider *et al.*, "Ray-tracing-based mm-wave beamforming assessment," *IEEE Access*, vol. 2, pp. 1314–1325, 2014.

[141] M.-T. Martinez-Ingles, D. P. Gaillot, J. Pascual-Garcia, J.-M. Molina-Garcia-Pardo, M. Lienard, and J.-V. Rodríguez, "Deterministic and experimental indoor mmw channel modeling," *IEEE Antennas and Wireless Propagation Letters*, vol. 13, pp. 1047–1050, 2014.

[142] Unity 3D, URL https://unity.com/, 2019.

[143] Unreal Engine, URL https://www.unrealengine.com/, 2022.

[144] W. Wu, S. Dasgupta, E. E. Ramirez, C. Peterson, G. J. Norman *et al.*, "Classification accuracies of physical activities using smartphone motion sensors," *Journal of medical Internet research*, vol. 14, no. 5, p. e2208, 2012.

[145] J. R. Kwapisz, G. M. Weiss, and S. A. Moore, "Activity recognition using cell phone accelerometers," *ACM SigKDD Explorations Newsletter*, vol. 12, no. 2, pp. 74–82, 2011.

[146] L. Zhang, X. Wu, and D. Luo, "Recognizing human activities from raw accelerometer data using deep neural networks," in *2015 IEEE 14th International Conference on Machine Learning and Applications (ICMLA)*. IEEE, 2015, pp. 865–870.

[147] A. Anjum and M. U. Ilyas, "Activity recognition using smartphone sensors," in *2013 IEEE 10th consumer communications and networking conference (CCNC)*. IEEE, 2013, pp. 914–919.

[148] H. Martín, A. M. Bernardos, J. Iglesias, and J. R. Casar, "Activity logging using lightweight classification techniques in mobile devices," *Personal and ubiquitous computing*, vol. 17, no. 4, pp. 675–695, 2013.

[149] Y. Kwon, K. Kang, and C. Bae, "Analysis and evaluation of smartphone-based human activity recognition using a neural network approach," in *2015 International Joint Conference on Neural Networks (IJCNN)*. IEEE, 2015, pp. 1–5.

[150] M. Zeng, L. T. Nguyen, B. Yu, O. J. Mengshoel, J. Zhu, P. Wu, and J. Zhang, "Convolutional neural networks for human activity recognition using mobile sensors," in *6th international conference on mobile computing, applications and services*. IEEE, 2014, pp. 197–205.

[151] M.-C. Kwon, H. You, J. Kim, and S. Choi, "Classification of various daily activities using convolution neural network and smartwatch," in *2018 IEEE International Conference on Big Data (Big Data)*. IEEE, 2018, pp. 4948–4951.

[152] Z. Cao, T. Simon, S.-E. Wei, and Y. Sheikh, "Realtime multi-person 2d pose estimation using part affinity fields," in *Proceedings of the IEEE conference on computer vision and pattern recognition*, 2017, pp. 7291–7299.

[153] S. Qiao, Y. Wang, and J. Li, "Real-time human gesture grading based on openpose," in *2017 10th International Congress on Image and Signal Processing, BioMedical Engineering and Informatics (CISP-BMEI)*. IEEE, 2017, pp. 1–6.

[154] E.-J. Rolley-Parnell, D. Kanoulas, A. Laurenzi, B. Delhaisse, L. Rozo, D. G. Caldwell, and N. G. Tsagarakis, "Bi-Manual Articulated Robot Teleoperation using an External RGB-D Range Sensor," in *2018 15th International Conference on Control, Automation, Robotics and Vision (ICARCV)*. IEEE, 2018, pp. 298–304.

[155] R. Girshick, "Fast R-CNN," in *Proceedings of the IEEE International Conference on Computer Vision (ICCV)*, December 2015.

[156] Meta Research, URL https://research.facebook.com/downloads/detectron/, 2022.

[157] R. A. Hamzah, A. F. Kadmin, M. S. Hamid, S. F. A. Ghani, and H. Ibrahim, "Improvement of stereo matching algorithm for 3d surface reconstruction," *Signal Processing: Image Communication*, vol. 65, pp. 165–172, 2018.

[158] Intel RealSense, URL https://www.intelrealsense.com/depth-camera-d455/, 2022.

[159] StereoLabs, URL https://www.stereolabs.com/zed-2i/, 2022.

[160] E. Ozturk, F. Erden, K. Du, C. K. Anjinappa, O. Ozdemir, and I. Guvenc, "Ray tracing analysis of sub-6 GHz and mmwave indoor coverage with reflecting surfaces," in *2022 IEEE Radio and Wireless Symposium (RWS)*, 2022, pp. 160–163.

[161] H. T. P. da Silva, M. S. de Alencar, and K. D. R. Assis, "Path loss and delay spread characterization in a 26 GHz mmwave channel using the ray tracing method," in *2019 SBMO/IEEE MTT-S International Microwave and Optoelectronics Conference (IMOC)*, 2019, pp. 1–3.

[162] A. Karstensen, W. Fan, I. Carton, and G. F. Pedersen, "Comparison of ray tracing simulations and channel measurements at mmwave bands for indoor scenarios," in *2016 10th European Conference on Antennas and Propagation (EuCAP)*, 2016, pp. 1–5.

[163] S. Yang, J. Zhang, and J. Zhang, "Impact of foliage on urban mmwave wireless propagation channel: A ray-tracing based analysis," in *2019 International Symposium on Antennas and Propagation (ISAP)*, 2019, pp. 1–3.

[164] X. Francoeur, Y. de Jong, C. Jones, K. Gracie, and D. G. Michelson, "mmwave propagation prediction using hardware- accelerated monte carlo path tracing," in *2021 IEEE 19th International Symposium on Antenna Technology and Applied Electromagnetics (ANTEM)*, 2021, pp. 1–2.

[165] M. Sheeba Kumari, N. Kumar, and R. Prasad, "Performance of mmwave ray tracing outdoor channel model exploiting antenna directionality," in *2020 IEEE 3rd 5G World Forum (5GWF)*, 2020, pp. 607–612.

[166] C. Zheng, Z. Xu, D. He, K. Guan, B. Ai, and J. M. García-Loygorri, "Millimeter-wave channel measurement based ray-tracing calibration and analysis in metro," in *2019 IEEE International Symposium on Antennas and Propagation and USNC-URSI Radio Science Meeting*, 2019, pp. 1–2.

[167] V. Ravuri, M. V. Subbarao, S. K. Terlapu, and G. Challa Ram, "Path loss modeling and channel characterization at 28 GHz 5G micro-cell outdoor environment using 3d ray-tracing," in *2022 Second International Conference on Advances in Electrical, Computing, Communication and Sustainable Technologies (ICAECT)*, 2022, pp. 1–7.

[168] J.-H. Lee, J.-S. Choi, J.-Y. Lee, and S.-C. Kim, "28 GHz millimeter-wave channel models in urban microcell environment using three-dimensional ray tracing," *IEEE Antennas and Wireless Propagation Letters*, vol. 17, no. 3, pp. 426–429, 2018.

[169] C. A. L. Diakhate, J.-M. Conrat, J.-C. Cousin, and A. Sibille, "Millimeter-wave outdoor-to-indoor channel measurements at 3, 10, 17 and 60 GHz," in *2017 11th European Conference on Antennas and Propagation (EUCAP)*, 2017, pp. 1798–1802.

[170] C. E. O. Vargas, L. da Silva Mello, and R. C. Rodriguez, "Measurements of construction materials penetration losses at frequencies from 26.5 GHz to 40 GHz," in *2017 IEEE Pacific Rim Conference on Communications, Computers and Signal Processing (PACRIM)*, 2017, pp. 1–4.

[171] M. Khatun, C. Guo, D. Matolak, and H. Mehrpouyan, "Indoor and outdoor penetration loss measurements at 73 and 81 GHz," in *2019 IEEE Global Communications Conference (GLOBECOM)*, 2019, pp. 1–5.

[172] J. Lee, K.-W. Kim, M.-D. Kim, and J.-J. Park, "32-GHz outdoor-to-indoor channel measurement of propagation losses and delay spread," in *2019 IEEE International Symposium on Antennas and Propagation and USNC-URSI Radio Science Meeting*, 2019, pp. 2071–2072.

[173] S. Y. Jun, D. Caudill, J. Chuang, P. B. Papazian, A. Bodi, C. Gentile, J. Senic, and N. Golmie, "Penetration loss at 60 GHz for indoor-to-indoor and outdoor-to-indoor mobile scenarios," in *2020 14th European Conference on Antennas and Propagation (EuCAP)*, 2020, pp. 1–5.

[174] Steatite. QOM-SL-26-40-K-SG-R. [Online]. Available: https://www.steatite-antennas.co.uk/wp-content/uploads/2019/01/QOM-SL-26-40-K-SG-R.pdf

[175] Blender. Window system introduction. [Online]. Available: https://docs.blender.org/manual/en/2.80/interface/window_system/introduction.htm

[176] Unity. Unity's interface. [Online]. Available: https://docs.unity3d.com/Manual/UsingTheEditor.html